Dissertation

submitted to the

Combined Faculty of Natural Sciences and Mathematics

of the Ruperto Carola University Heidelberg, Germany

for the degree of

Doctor of Natural Sciences

Presented by

M. Sc. Gintvile Valinciute

Born in: Gargzdai, Lithuania

Oral examination: 12 October, 2020

Targeting MYC in

high risk medulloblastoma

Referees: PD. Dr. rer. nat. Odilia Popanda

PD Dr. med. Till Milde

For my Mom and Grandma

All that is gold does not glitter,
Not all those who wander are lost;
The old that is strong does not wither,
Deep roots are not reached by the frost. […]

J. R. R. Tolkien

Acknowledgements

I would like to thank the people who have inspired and supported me during the last 4 years and contributed to the completion of my PhD project:

Prof. Dr. Olaf Witt for an opportunity to work in the CCU Pediatric Oncology and in such a supportive and collaborative environment, for your invaluable scientific input and for keeping us all thinking of the translational aspects of every project.

PD Dr. Till Milde for being the best supervisor and mentor one could ask: Dear Till, thank you for believing in me, continuously inspiring me, and helping to find my path in science. Thank you for teaching me, when to stop pursuing the hypothesis, and for being so cool with my extra-curricular activities. Thank you for fun coffee breaks and crazy discussions, for your patience and for being an incredible leader. I consider myself very lucky to work with you.

PD Dr. Odilia Popanda for always providing invaluable scientific expertise as a TAC member and the first examiner of this project. **Dr. Marc Remke** for incredible collaboration and sharing all the data on medulloblastoma, and for his willingness to join the project as a TAC member. **Prof. Dr. Jeroen Krijgsveld** for his help with proteomics, constructive criticism during the development of this project and for his willingness to take part in my TAC.

Prof. Dr. Gislene Pereira and **Prof. Dr. Michaela Frye** for your willingness to participate in my thesis examination committee.

Our incredible collaborators who contributed to the completion of this study: **Thomas Hielscher** for his support with the analysis of our data and for his patience in teaching me how to do the analysis myself; **Dr. Gianluca Sigismondo** and **Prof. Dr. Jeroen Krijgsveld** for their help with co-IP optimization, mass spectrometry experiment and the analysis of this data; **Daniel Picard**, **Dr. Nan Qin** and **Dr. Marc Remke** for sharing their data, expertise, and the cell lines; **Dr. Christin Schmidt** for instructions on the CompuSyn software; **Dr. Kathrin Schramm**, **Dr. David Jones**, **Dr. Kai-Oliver Henrich** and **Dr. Frank Westermann** for sharing the cell lines; **Dr. Mirjam Blattner-Johnson** for helping with the INFORM dataset; **Dr. Tim Holland-Letz, Sonja Krausert** and **Dr. Marcel Kool** for their help with the animal experiment application and models; **Prof. Dr. Stefan Pfister** for the scientific input, inspiration, and fostering collaboration.

B310 lab family, i.e. the people who made my PhD journey an actually fun experience both, in the lab and out: **Ina**, **Sina**, **Jonas**, **Flo**, **Romain**, **Daniela**, **Nora**, **Johanna**, **Diren**, **Simon**, **Carina**, **Dani**, **Isabel**, **Heike**, **Johannes**, **Yannik**, **Lisa**, **Simay**, **Katharina**, **Till**, **Michael**, **Sara**, **Rabia**, **Aileen**, **Alex**, **Sonja**, **Charlotte**, **Clarissa** and **Ramona**. I would like to thank to **PD Dr. Ina Oehme** for her scientific input and constructive criticism and **Dr. Sina Oppermann** for her help with the PLK1 inhibitor evaluation. Special thanks to **Jonas** for introducing me to the *MYC*-amplified medulloblastoma, showing me the ropes in pediatric oncology, and for our afternoon scientific discussions staring at the western blot scans, and **Carina** for being so patient with my inexperience, teaching me all the lab techniques, and always helping with experiments. Thanks to the morning coffee gang: **Flo** for hilarious conversations and his help with transfection, **Romain** for scientific and non-scientific discussions, an occasional pub-night and the online Corona-Parties, **Lisa** for being an amazing friend, always ready to help and to have yet one more coffee, and **Daniela** for being a perfect online game master and a great addition to our so-called "Post-doc office". Thanks to **Johanna** for our nights out, great conversations, long days at the FACS Core facility, and going to salsa classes with me. Also, a big thank you to the B310 administrative assistants **Nicola** and **Natja** for all their help and organizational skills.

B310 lab family alumni: **Juliane**, **Jagoda**, **Fiona**, **Emily**, **Ramona**, and **Annika**. A special thanks to **Juliane** for always being there for me, for looking at the positive side of everything and for inspiring me to strive for my goals in Academia and outside of science, and to **Jagoda** for her calm and reassuring support at all times.

The Graduate School for financial and administrative support, as well as encouraging the extra-curricular activities of PhD students. The incredible 17/18 DKFZ PhD Council (**Maria**, **Lucie**, **Flo**, and **Michael**), the 17/18 **PhD Retreat team**, and the **organizing team of the 6th HFYLS**.

Finally, I would like to thank to my **Mom Nerija** and **Grandma Aldona**, as well as my **Uncle Vygantas**, **Aunt Birutė**, and **Cousin Elzė** for supporting me through the last 4 years and inspiring me to be a scientist. Also, a huge thanks to all my friends for being there for me through the thick and thin. I especially would like to thank the Fantastic Four ladies (**Aparna**, **Edurne**, **Shreya**), **Sandra**, **Žana**, **Pranas**, **Miglė**, **Vilmantė** and many others. I could not have done this without you!

Summary

Medulloblastoma (MB), arising in the cerebellum, is one of the most common malignant brain tumors in children. MB comprises four distinct molecular subgroups. One of them, Group 3, is enriched in oncogene *MYC* amplifications resulting in dismal prognosis and reduced survival rates. The treatment of MB includes surgical tumor-resection, cranio-spinal irradiation, and chemotherapy. However, even if the treatment is effective, a large population of surviving patients suffer from various sequelae. Therefore, there is a necessity for the development of therapeutics and their combinations targeted against the drivers of MB. In this thesis, a combination of two compounds indirectly targeting MYC is discussed.

We and others have previously demonstrated that *MYC*-amplified MB cells are highly susceptible towards treatment with class I histone deacetylase (HDAC) inhibitors, potentially due to MYC and HDAC2 co-localization in a protein complex in MB cells. We used a class I HDACi entinostat as the first compound in the combination. In order to determine the second candidate, we applied two target discovery techniques, elucidating the protein complex members by mass spectrometry and examining the potential targets in the transcriptional landscape changes induced by entinostat treatment. The elucidated candidate was tested for the selectivity for *MYC*-amplified MB cells assessing cell metabolic activity, cell cycle, cell death and viability. The interaction between entinostat and a second target inhibitor was examined and validated. Finally, the mechanism of interaction was investigated.

We determined that cell cycle regulator polo-like kinase 1 (PLK1) is a target for the combination therapy in *MYC*-amplified MB. PLK1 was found overexpressed in *MYC*-amplification-associated molecular subgroups and subtypes of MB underscoring the translational potential of PLK1 targeting. Moreover, *MYC*-amplified cells were more susceptible to the PLK1 inhibition as confirmed by cell metabolic activity, viability, and apoptosis induction. Entinostat and PLK1 inhibitors volasertib and GSK461364 were interacting synergistically in clinically relevant concentrations only in *MYC*-amplified MB cells. In addition, entinostat and volasertib synergistically induced apoptosis and reduced the cell viability in *MYC*-amplified cells only. Finally, we show that volasertib and its' combination with entinostat exert their activity via MYC axis. However, the details of interaction mechanism remain to be examined. The validation experiments involving on-target confirmation by PLK1 knockdown as well as *in vivo* assessment of the combination therapy are planned.

In summary, in this thesis, the synergistic interaction of entinostat and PLK1 inhibitors was demonstrated. This combination offers a potential for clinical development with *MYC* amplification serving as a predictive biomarker in MB and possibly other entities with *MYC* overexpression.

Zusammenfassung

Das im Kleinhirn auftretende Medulloblastom (MB) ist einer der häufigsten bösartigen Hirntumoren bei Kindern. MB umfasst vier verschiedene molekulare Untergruppen. Eine von ihnen, Gruppe 3, ist mit Amplifikationen des Onkogen MYC angereichert, was zu einer schlechten Prognose und verringerten Überlebensraten führt. Die Behandlung von MB umfasst chirurgische Tumorresektion, Bestrahlung der Schädel-Wirbelsäule und Chemotherapie. Selbst wenn die Behandlung wirksam ist, leidet eine große Anzahl überlebender Patienten an verschiedenen Spätfolgen. Daher besteht die Notwendigkeit Therapeutika und deren Kombinationen zu entwickeln, die gegen die Treiber von MB gerichtet sind. In dieser Arbeit wird eine Kombination zweier Verbindungen diskutiert, die indirekt auf MYC abzielen.

Wir und andere haben zuvor gezeigt, dass MYC-amplifizierte MB-Zellen sehr anfällig für die Behandlung mit Klasse I Histondeacetylase (HDAC) Inhibitoren sind, möglicherweise aufgrund der gleichzeitigen Lokalisierung von MYC und HDAC2 in einem Proteinkomplex in MB-Zellen. Wir verwendeten Entinostat – einen Klasse I HDACi – als erste Substanz der Kombination. Um den zweiten Kandidaten zu bestimmen, verwendeten wir zwei Techniken zur Targetidentifizierung: Die Mitglieder des Proteinkomplexes wurden durch Massenspektrometrie aufgeklärt und potenzielle Ziele in den Veränderungen der Transkriptionslandschaft, die durch Behandlung mit Entinostat induziert wurden, untersucht. Das ermittelte Target wurde auf die Selektivität für MYC-amplifizierte MB-Zellen getestet, wobei die Stoffwechselaktivität der Zellen, der Zellzyklus, der Zelltod und die Viabilität bewertet wurden. Die Wechselwirkung zwischen Entinostat und einem zweiten Inhibitor wurde untersucht und validiert. Schließlich wurde der Interaktionsmechanismus untersucht.

Wir haben festgestellt, dass der Zellzyklusregulator Polo-like-Kinase 1 (PLK1) ein Ziel für die Kombinationstherapie bei MYC-amplifiziertem MB ist. Es wurde festgestellt, dass PLK1 in molekularen Untergruppen und Subtypen von MB überexprimiert ist, die mit MYC Amplifikation assoziiert sind. Dies unterstreicht das Translationspotential von PLK1 als Angriffspunkt. Darüber hinaus waren MYC-amplifizierte Zellen anfälliger für PLK1-Hemmung, was durch Stoffwechselaktivität der Zellen, Viabilität und Induktion von Apoptose bestätigt wurde. Entinostat und die PLK1-Inhibitoren Volasertib und GSK461364 interagierten nur in MYC-amplifizierten MB-Zellen in klinisch relevanten Konzentrationen synergistisch. Darüber hinaus induzierten Entinostat und Volasertib synergistisch Apoptose und reduzierten die Zellviabilität nur in MYC-amplifizierte Zellen. Schließlich zeigen wir, dass Volasertib und seine Kombination mit Entinostat

ihre Aktivität über die MYC-Achse ausüben. Die Details des Interaktionsmechanismus müssen jedoch noch untersucht werden. Geplant sind die Validierungsexperimente mit Bestätigung des Ziels durch PLK1-Knockdown sowie In-vivo-Bewertung der Kombinationstherapie.

Zusammenfassend wurde in dieser Arbeit die synergistische Wechselwirkung von Entinostat mit PLK1-Inhibitoren gezeigt. Diese Kombination zeigt Potenzial für die klinische Entwicklung, wobei die MYC-Amplifikation als prädiktiver Biomarker bei MB und möglicherweise anderen Entitäten mit MYC-Überexpression dient.

Abbreviations

(co-)IP	(co-)Immunoprecipitation
ACTB	Actin β
AKT	RAC-alpha serine/threonine-protein kinase
AML	Acute myeloid leukemia
ANOVA	Analysis of variation
APC	Adenomatous polyposis coli
APC/C	Anaphase-promoting complex
APS	Ammonium persulfate
ARF	ADP-ribosylation factor
aRMS	Alveolic rhabdomyosarcoma
ATM	Ataxia-telangiectasia mutated protein kinase
ATP	Adenosine triphosphate
ATR	Ataxia-telangiectasia and Rad3-related protein kinase
ATRT	Atypical teratoid rhabdoid tumor
AURKA	Aurora A kinase
AURKB	Aurora B kinase
BBB	Blood-brain barrier
BCA	Bicinchoninic acid assay
BET	Bromodomain and extra-terminal motif
bFGF	Basic fibroblast growth factor
bHLH-LZ	Basic helix-loop-helix, leucine-zipper motif
BRD4	Bromodomain-containing protein 4
BSA	Bovine serum albumin
BTK	Bruton's tyrosine kinase
BUB	Budding uninhibited by benzimidazoles proteins
CAPN	Calpain
CBP	CREB Binding Protein
Cdc20	Cell-division cycle protein 20 homolog
Cdc25	Ras-specific guanine nucleotide-releasing factor 1
CDK	Cyclin-dependent kinase
cDNA	Copy deoxyribonucleic acid
CHD4	Chromodomain-helicase-DNA-binding protein 4
CHK1/2	Serine/threonine-protein kinase Chk1/2
CHX	Cycloheximide
CI	Combination index
CK1	Casein kinase 1
CK2	Casein kinase 2
CLIP-170	Cytoplasmic linker protein CLIP-170
CLL	Chronic lymphocytic leukemia
c_{max}	Maximal serum concentration
CNS	Central nervous system
CNV	Copy number variation
coREST	REST corepressor
CSA	Cranio-spinal axis
CT	Computed tomography
CT	Cycle of threshold
CTD	C-terminal domain
CTNNB1	Catenin beta-1

CUL1	Cullin-1
DDR	DNA damage repair
DHL	Double-hit lymphoma
DIPG	Diffuse intrinsic pontine glioma
DMEM	Dulbecco's modified Eagle's medium
DMP	Dimethyl pimelimidate
DMSO	Dimethylsulfoxide
DNA	Deoxyribonucleic acid
DNMT	DNA methyltransferase
DOX	Doxycycline
DSH	Disheveled
DTT	Dithiothreitol
EDTA	Ethylenediaminetetraacetic acid
EGF	Epidermal growth factor
EMEA	European Medicines Agency
Emi1	F-box only protein 5
EMT	Epithelial-mesenchymal transition
ER	Estrogen receptor
ERK	Mitogen-activated protein kinase/extracellular signal-regulated kinase
eRMS	Embryonic rhabdomyosarcoma
FACS	Fluorescence activated cell sorting/flow cytometry
FBXW7	F-box/WD repeat-containing protein 7
FCS	Fetal calf serum
FDA	Food and Drug Administration
FOXM1	Forkhead box protein M1
FSC	Forward scatter
GAPDH	Glyceraldehyde-3-phosphate dehydrogenase
GATAD2A	Transcriptional repressor p66-alpha
GBM	Glioblastoma
GCN5	Histone acetyltransferase KAT2A
GEP	Gene expression profile
GFI/GFI1B	Zinc finger protein Gfi-1/B
GFP	Green fluorescent protein
Gli(1/2/3)	Transcriptional activator GLI1/2/3
GliR3	Transcriptional activator GLI3 repressor
GluCN	Glutamatergic cerebellar nuclei
GO	Gene ontology
GSEA	Gene set enrichment analysis
GSK3(β)	Glycogen synthase kinase-3 beta
GTF2I	General transcription factor II-I
H_2O	Water
H3	Histone 3
HAT	Histone acetyltransferase
HDAC	Histone deacetylase
HDACi	Histone deacetylase inhibitor
HEPES	4-(2-hydroxyethyl)-1-piperazineethanesulfonic acid
HGG	High-grade glioma
Hh	Hedgehog
HIF-1α	Hypoxia-inducible factor 1-alpha
HMT	Histone methyltransferase

HP1	Heterochromatin protein 1
Hsp90	Heat-shock protein 90
iBAQ	Intensity-Based Absolute Quantitation
IC50	50 % inhibitory concentration
IgG	Immunoglobulin G
IMEM	Improved minimum essential medium
INR	Initiator
IQ	Intellect coefficient
IRES	Internal ribosome entry site
KBTBD4	Kelch repeat and BTB domain-containing protein 4
KDM6A	Lysine-specific demethylase 6A
KEGG	Kyoto encyclopedia of genes and genomes
LC/A	Large cell/anaplastic
LDHA	L-lactate dehydrogenase A chain
LFA-1	Integrin alpha-L
LFQ	Label free quantification
LRP6	Lipoprotein receptor-related protein 6
MAD	Mitotic spindle assembly checkpoint protein
MAX	MYC-associated factor X
MB	Medulloblastoma
MBEN	Medulloblastoma with extensive nodularity
MCA	Multiplex cell line authentication
McCT	Multiplex cell contamination test
MEF2	Myocyte enhancer factor 2
MEM	Minimum essential medium
MIZ-1	Zinc finger and BTB domain-containing protein 17
MMP	Matrix metalloproteinase
MRI	Magnetic resonance imaging
mRNA	Messenger ribonucleic acid
mSin3	Transcriptional regulatory protein Sin3
MTA2	Metastasis-associated protein MTA2
mTOR	Mammalian/mechanistic target of rapamycin
MYC	V-myc avian myelocytomatosis viral oncogene homolog
MYCL	V-myc avian myelocytomatosis viral oncogene lung carcinoma derived homolog
MYCN	V-myc avian myelocytomatosis viral oncogene neuroblastoma derived homolog
MYT1	Myelin transcription factor 1
NB	Neuroblastoma
N-COR	Nuclear receptor corepressor
NES	Nuclear export signal
NHL	Non-Hodgkin lymphoma
NLS	Nuclear localization signal
NOS	Not otherwise specified
NTD	N-terminal domain
NuRD	Nucleosome remodeling deacetylase complex
Omo	Omomyc
OS	Overall survival
OTX2	Homeobox protein OTX2
p15	Cyclin dependent kinase inhibitor 2B

p16	Cyclin dependent kinase inhibitor 2A
p18	Cyclin dependent kinase inhibitor 2C
p19	Cyclin dependent kinase inhibitor 2D
p21	Cyclin dependent kinase inhibitor 1A
p27	Cyclin-dependent kinase inhibitor 1B
p300	E1A Binding Protein P300
PA	Pilocytic astrocytoma
PAF1	Peroxisome biogenesis factor 2
PARP1	Poly [ADP-ribose] polymerase 1
PBS	Phosphate buffered saline
PBS-T	Phosphate buffered saline with Tween 20
PCA	principal component analysis
PCR	Polymerase chain reaction
PDAC	Pancreatic ductal adenocarcinoma
PDGF	Platelet-derived growth factor
PDK1	3-phosphoinositide-dependent protein kinase 1
PD-L1	Programmed cell death 1 ligand 1
PEI	Polyethylenimine
PEST	Proline, aspartate, serine, threonine-rich motif
PFS	Progress-free survival
PI	Propidium iodide
PI3K	Phosphatidylinositol 3-kinase
PLK	Polo-like kinase
PLK1i	Polo-like kinase 1 inhibitor
PNET	Primitive neuroectodermal tumor
PP2A	Serine/threonine-protein phosphatase 2A
PTCH	Patched
p-TEFb	Positive transcription elongation factor b
PTEN	Phosphatidylinositol 3,4,5-trisphosphate 3-phosphatase and dual-specificity protein phosphatase PTEN
PTM	Post-translational modification
PVDF	Polyvinylidene difluoride
qRT-PCR	Quantitative real time polymerase chain reaction
Rb	Retinoblastoma
RCC	Renal cell carcinoma
RNA	Ribonucleid acid
ROI	Region of interest
ROS	Reactive oxygen species
RPMI	Roswell Park Memorial Institute medium
RT	Room temperature
SA2	Cohesin subunit SA-2
SAC	Spindle attachment checkpoint
SCF	Skp, Cullin, F-box containing E3 ubiquitin ligase complex
SD	Standard deviation
SDS	Sodium dodecyl sulfate
SDS-PAGE	Sodium dodecyl sulfate-polyacrylamide gel electrophoresis
Sgt1	Protein SGT1 homolog
SHH	Sonic hedgehog
SIOP	The International Society of Pediatric Oncology
Skp2	S-phase kinase-associated protein 2

SMARCA4	Transcription activator BRG1
SMO	Smoothened
SMRT	Silencing mediator of retinoic acid and thyroid hormone receptor
SOC	Standard-of-care
SOX2	Transcription factor SOX-2
SSC	Side scatter
STAB	Stabilon
STAT1	Signal transducer and activator of transcription 1
SUFU	Suppressor of fused homolog
TAD	Transactivation domain
TAE	Tris-acetate-EDTA
TBL1X	F-box-like/WD repeat-containing protein TBL1X
TBS	Tris buffered saline
TBS-T	Tris buffered saline with Tween 20
TCF/LEF	T-cell factor/lymphoid enhancer factor
TCTP	Translationally controlled tumor protein
TEMED	Tetramethylethylenediamin
TERT	Telomerase reverse transcriptase
THY	Thymidine
TP53/p53	Cellular tumor antigen p53
TRRAP	Transformation/transcription domain-associated protein
TSM	Tumor stem medium
TSNE	T-stochastic neighbour embedding
TSS	Transcription start site
UBC	Unipolar brush cells
USP7	Ubiquitin carboxyl-terminal hydrolase 7
UT	Untreated
UV	Ultraviolet
Vol	Volasertib
VPA	Valproic acid
WEE1	Wee1-like protein kinase
WHO	World Health Organization
WNT	Wingless
YY1	Transcriptional repressor protein YY1
ZMYM3	Zinc finger MYM-type protein 3
ZNF217	Zinc finger protein 217
βTrCP	F-box/WD repeat-containing protein 1A

Table of contents

List of figures

List of tables

1. Introduction

1.1. Pediatric neuro-oncology and medulloblastoma

Worldwide, approximately 300,000 children and adolescents per year are diagnosed with cancer. Over the past decades, 5-year overall survival in childhood cancer increased from approximately 20 % to over 80 %[3,34] in developed world. This success can be attributed to the advancement of chemotherapy and radiotherapy regimen as well as the development of surgical techniques. Despite this improvement, cancer remains one of the main causes of death in children and adolescents. In the last decade, a plateau of childhood cancer survival improvement was observed. This is due to the fact that cancers that are curable with conventional techniques (standard of care therapy, SOC, including chemotherapy, radiation treatment and surgical resection of solid tumors) are being cured, while the remaining portion of cancers require other (improved) measures. The development of personalized medicine and targeted therapy is believed to be the key to further childhood cancer survival advancement. On the other hand, the numbers of patients with various treatment-induced conditions and diseases are increasing with enhanced survival. These include psychiatric, neurophysiological and developmental disorders, fertility issues, cardiovascular and other organ dysfunction-induced diseases as reviewed by Robison & Hudson[35]. In addition, secondary neoplasms have proven to be one of the main causes of premature death among childhood cancer survivors[8]. In this section, incidence, mortality rates of pediatric (CNS) tumors will be discussed. Since the main focus of thesis is on medulloblastoma, this entity will be described in more detail, including classification, diagnostics, prognostics and therapeutic options.

1.1.1. Incidence and mortality rates in pediatric neuro-oncology

The most common cancer entities in children are hematological malignancies (Figure 1) with leukemia and lymphoma comprising 32.9 % and 11.9 % of all cases, respectively. The second most common pediatric malignancies are the central nervous system (CNS) tumors with 20.7 % of all cancer cases worldwide[3]. The incidence data from

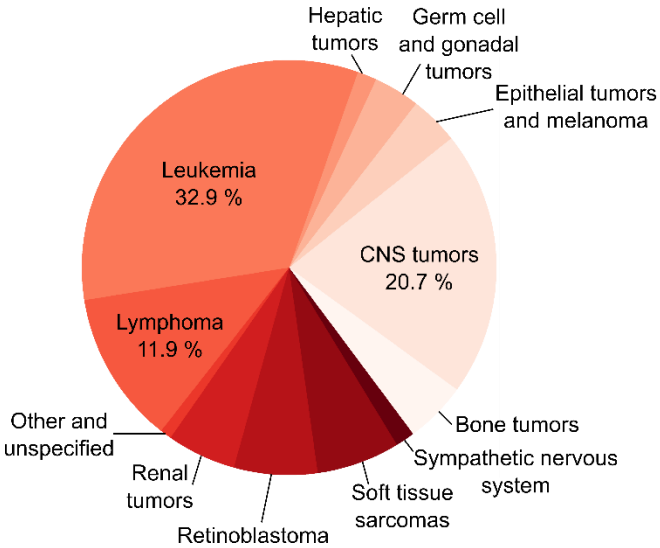

Figure 1 Incidence of tumor entities among children (age 0-14) worldwide in 2001-2010. Adapted from Steliarova-Foucher, et al (2017)[3]

National Childhood Cancer Registries in Germany, the United States and the United Kingdom are comparable in terms of entity distribution, with CNS tumors as the second most common entity. In addition, CNS tumors have some of the highest mortality rates in the UK[36], US[37] and Germany[8]. Here, CNS tumor mortality rates (29 %) are the second after leukemia[34]. However, 5-year overall survival (OS) of leukemia has been substantially improving in the last 20 years in contrast to the OS of CNS tumors indicating the importance of extensive tumor biology research.

Incidence and survival rates, however, differ substantially when comparing malignant to non-malignant CNS tumors as well as different entities within those groups. In Germany, based on the German Childhood Cancer Registry Annual Report 2016[8], the most common CNS cancer entity is astrocytoma comprising 45.6 % of all reported cases (Figure 2), with a 3.1 standardized mortality rate. Unfortunately, drawing meaningful comparisons on mortality and incidence rates is not possible since astrocytomas in this report include all grade entities from grade I pilocytic astrocytomas to grade IV glioblastomas, without further subdivision. The second most common entity in this dataset is medulloblastoma, with 17.4 % of all cases.

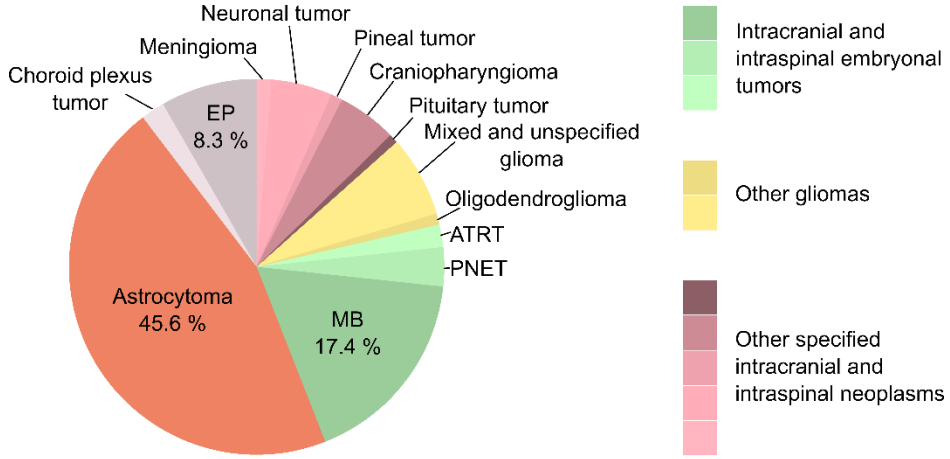

Figure 2 Incidence of CNS tumor entities in children (age 0-15) in Germany in 1980-2015. Adapted from German Childhood Cancer Registry Annual Report 2016[8]. MB: medulloblastoma. EP: ependymoma. ATRT: atypical teratoid rhabdoid tumor.

The Central Brain Tumor Registry of the United States state findings similar to those reported by German Childhood Cancer Registry in their recent report on CNS tumors in 2012-2016[21] (Figure 3). Here, grade I (non-malignant) pilocytic astrocytoma (PA) is the most common entity with 17.8 % followed by pooled various malignant gliomas (14 %). The third most common tumors similarly

to the data from Germany, are embryonal tumors with 13.1 %. The most common embryonal tumor is medulloblastoma (MB; 64.1 % of embryonal tumor cases or 6.6 % of all cases reported).

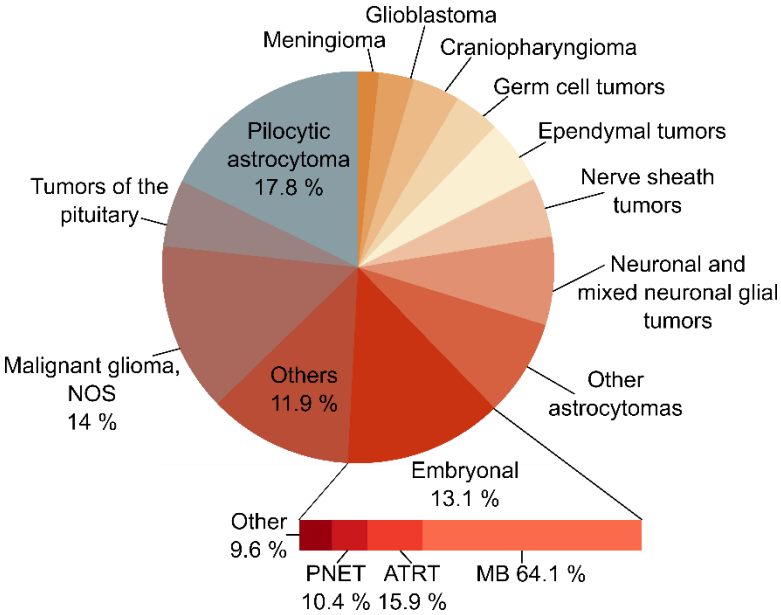

Figure 3 Incidence of CNS tumor entities in children (age 0-14) in the United States in 2012-2016. Adapted from CBTRUS Statistical Report[21]. MB: medulloblastoma. ATRT: atypical teratoid rhabdoid tumor. PNET: primitive neuroectodermal tumor. NOS: not otherwise specified.

MB is a heterogenous group of grade IV intracranial embryonal tumors, considered to be one of the most common malignant primary brain cancers in children, with some subgroups occasionally occurring in adults[38]. MB is arising in the posterior fossa inside or close to the cerebellum, grows fast and is prone to metastasis depending on the subgroup. In addition, MB is the principal cancer-related death cause in children[39]. Due to the rapid growth of the tumor, symptoms occur within weeks or months and include signs of cerebellar dysfunction (e.g. ataxia) as well as increased intra-cranial pressure. Children are diagnosed by neurological examination followed by magnetic resonance imaging (MRI) (or computed tomography, CT). MRI provides a better contrast of the soft tissue while sparing radiation, and thus is used more often. As exemplified in the Figure 4, T2-weighted contrast-enhanced sagittal magnetic resonance image shows an infratentorial tumor compressing cerebellum and medulla. The MB in the scan is obstructing the 4th ventricle and the flow of the cerebrospinal fluid (CSF). This leads to the obstructive hydrocephalus resulting in increased intra-cranial pressure and symptom development.

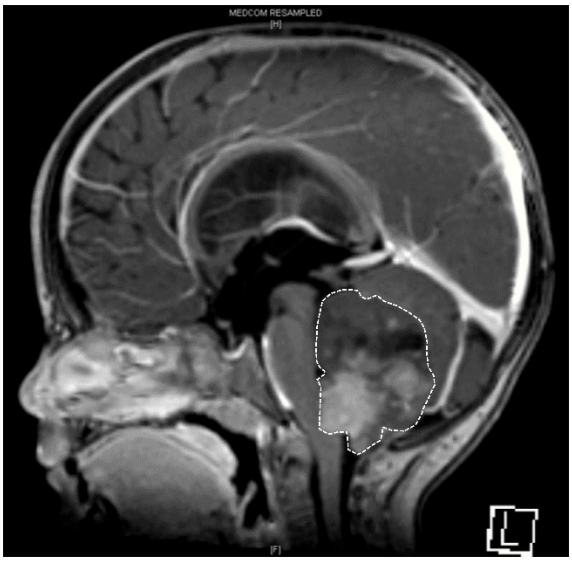

Figure 4 T2-weighted contrast-enhanced sagittal MRI scan showing medulloblastoma (encircled area).

The focus of this thesis is personalized medicine targeting features of MB biology. In the following section, histopathological and biological features of MB will be covered. The classic and molecular classification methods will be introduced. Finally, current treatment options, SOC therapy protocols and prognostic molecular components of different MB subgroups will be described.

1.1.2. Histopathological features and classification

MBs were first discovered by James Wright in the beginning of the 20th century and described consisting of undifferentiated nerve cells[40]. However, the term medulloblastoma was coined by Bailey and Cushing in 1925[41] where they suggested that the tumor arises from a hypothetical progenitor cell called the "medulloblast". For some time, MBs were even considered to be a class of “primitive neuroectodermal tumors” (“PNETs”) due to their suspected origin. Of note, the cell-of-origin of MB has been a center of debate throughout the last century. The current consensus is that there are different cells-of-origin for each of the molecular subgroups of MB, and some of them have already been found (as described below).

MBs have been classified based on immunohistochemistry by pathologists since the 70s when the first attempts at histopathological differentiation of MB were made[42], until as late as the first decade of the 21st century, when molecular subgrouping of MB was discovered[43-45] (further described in the following sections). MBs are distinguished by histopathology to be classic, desmoplastic/nodular, large cell/anaplastic medulloblastoma (LC/A) or medulloblastoma with extensive nodularity (MBEN)[10,23]. **Classic** MB is the most common histological subgroup with an overall incidence of around 65 % (Figure 5a). Classic MBs (Figure 5b) consist of dense uniform

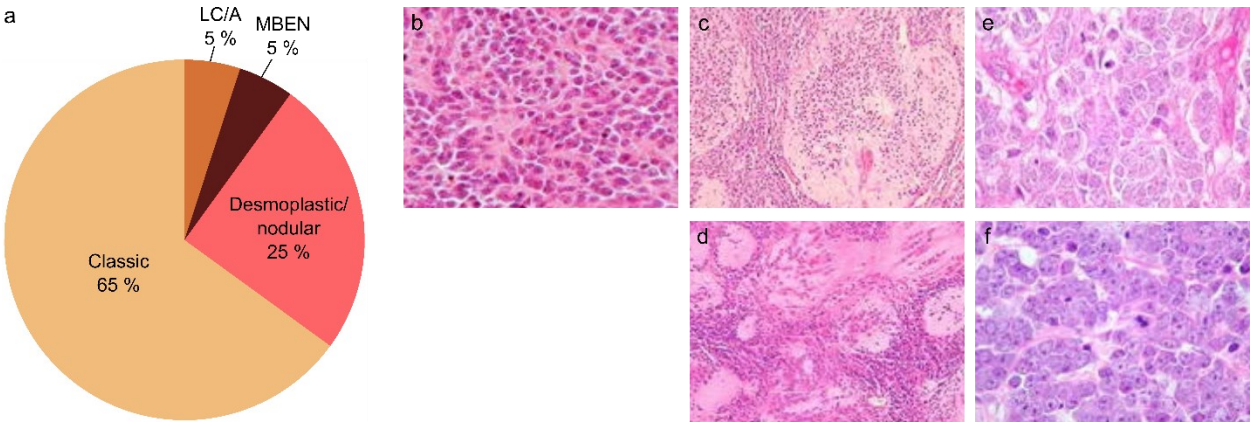

Figure 5 Histopathological classification of MB. a – distribution of histopathological types of MB[10]. b – example of classic type MB. c – example of desmoplastic/nodular MB. d – example of MBEN. e – example of anaplastic MB. f – example of large cell MB. LC/A: large cell/anaplastic. MBEN: medulloblastoma with extensive nodularity. Histology images adapted from Ellison (2010)[23].

small cells with high nuclear-to-cytoplasm ratio and occasional pattern-breaking rosettes. Those cells often show neuronal differentiation patterns. **Desmoplastic/nodular** MBs comprise approximately 25 % and are described by two observed patterns/types of cells (Figure 5c). There are dense nodules of neurocytic cells characterized by low growth rate, high grade of differentiation and expression of neuronal markers. Desmoplastic internodular regions consist of undifferentiated rapidly dividing embryonal cells with reticulin-rich extracellular matrix. Desmoplastic/nodular MBs are almost exclusively associated with the SHH molecular subgroup[46] (sections 1.1.3.1 and 1.1.3.3) and, in turn, Gorlin syndrome defined by germline-mutations in the sonic hedgehog (SHH) pathway[47,48]. An extreme variant of desmoplastic/nodular MBs are considered a separate type, namely **MBs with extensive nodularity (MBEN)**[49]. They have larger nodular regions with advanced neuronal differentiation and restricted internodular parts (Figure 5d). MBENs comprise 5 % of MB, are associated with SHH pathway mutations and carry a relatively good prognosis[49]. **Large cell/anaplastic** (LC/A) type, further subdivided in some publications, constitutes approximately 5 % of MBs (Figure 5e and f). These tumors are characterized by a low grade of differentiation, as well as regions of large cells with prominent nucleoli intersected by numerous anaplastic areas with atypic nuclei containing cells. LC/A MBs are associated with the worst prognosis of all histological types[49].

1.1.3. Molecular alterations and classification

Although histopathological analysis is a useful tool for routine diagnostics, in some cases, histopathological evaluation is not precise enough for MB heterogeneity and risk assessment. Newly developed microarray and high-throughput nucleic acid sequencing techniques have helped to elucidate the heterogeneity of MB and identify consensus molecular subgroups. Many research groups have contributed to the establishment of the four major molecular MB subgroups WNT, SHH, Group 3 and Group 4[43-45,50-54]. Even now, almost a decade after these discoveries, MB subgrouping is being remodelled and refined both on a subgroup as well as additional subtype level[2,55-57]. In this section, the molecular MB subgroups will be described in detail.

1.1.3.1. Molecular subgroups

Based on gene expression changes, copy-number variations (CNV) and methylation profiles, 4 molecular MB subgroups can be identified. Two of them, WNT and SHH, are very distinct as they cluster separately in the dimension reduction (principal component, PCA, or t-distributed

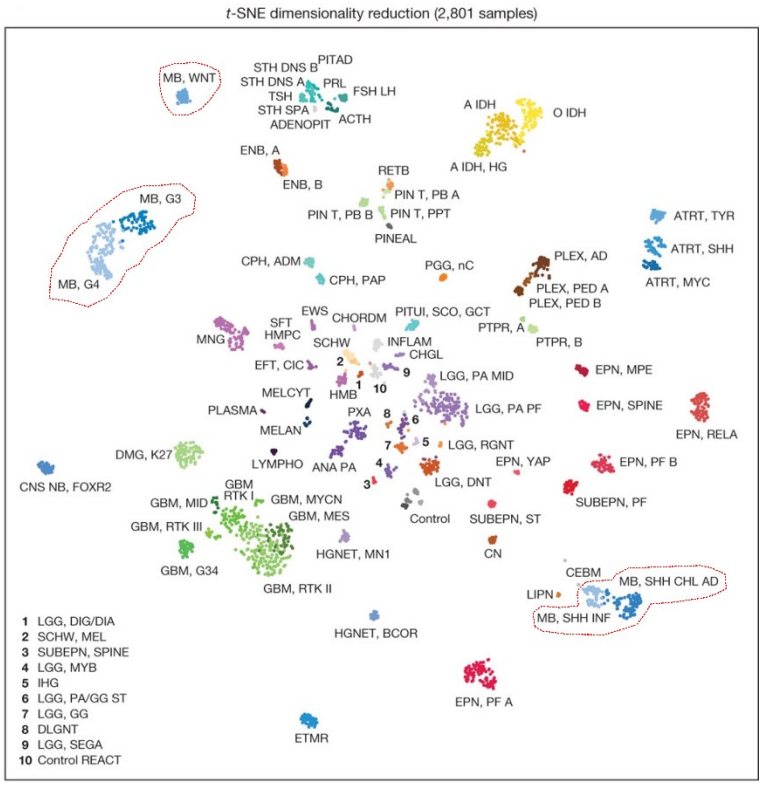

Figure 6 t-distributed stochastic neighbor embedding (TSNE) plot for pediatric CNS tumor and their subgroup classification based on methylation profiles. Each dot represents a separate sample. Colors represent tumor types. MB subgroups are encircled in red. Image adapted from Capper et al (2018)[7].

stochastic neighbour embedding, TSNE) plots, and are named after the respective altered pathways (Figure 6). The other two subgroups are called Group 3 and Group 4 and were initially described as distinct subgroups. However, as indicated by the lack of distinct separation in dimension reduction plots, Group 3 and 4 MB more likely represent a continuum, and the current consensus described them as Group 3/4 with up to 8 subtypes comprising both clear Group 3 or 4 subtypes as well as subtypes with a mixture of both.

WNT subgroup comprises around 10 % of all cases[14] and is considered a low risk MB[49] (Figure 7). WNT tumors are histologically classic MBs, they have a low rate of metastasis (12 %), are rarely recurrent and have a 98 % 5-year OS rate. WNT MBs occur mainly in children (3-10 years) and adolescents (10-17 years), rarely in adults (17+ years). This subgroup was divided into children and adult WNT in a publication by Cavalli et al (2017)[2], however, the current consensus does not specify WNT subtypes[1]. WNT MB molecular changes are described in section 1.1.3.2.

SHH subgroup is diagnosed in 30 % of all MBs[14] (Figure 7). Depending on specific molecular and histological features these tumors vary from low to (very) high risk (in particular, differentiated based on *TP53* status)[49]. SHH MBs are separated into 4 subtypes with distinct demographics and molecular features. SHHα MBs constitute 29 % of SHH tumors. They are observed in all histological groups, occur mainly in children and are more common in males. SHHα metastasize in 20 % of cases and have 70 % 5-year OS. SHHβ MBs comprise 16 % of SHH MB. These tumors have a preference to the infant (0-3 years) and children demographics, they show desmoplastic and classic histology and have 33 % chance to metastasize. The SHHβ MBs are considered as

Subgroup		WNT	SHH			
Frequency (of all MB)		10	30			
Recurrence		Rare; local or metastatic	Local			
Proposed cell or origin		Progenitor cells in the lower rhombic lip	Granule precursors of the external granule layer GNP-like cells			
Subtype			α	β	γ	δ
Demographics	Frequency (of subgroup)	100	29	16	21	34
	Age					
	Gender	♀ 55 45 ♂	♀ 37 63 ♂	♀ 53 47 ♂	♀ 45 55 ♂	♀ 31 69 ♂
Clinical features	Histology	Classic	Classic, desmoplastic, LC/A	Desmoplastic, classic	Desmoplastic, MBEN	Classic, desmoplastic
	Metastasis (%)	12	20	33	9	9
	5 year OS (%)	98	70	67	88	89
Molecular features	Cytogenetics	6-	9p+ 9q- 10q- 17p-	2+	9q-	9q- 14q-
	Driver events	CTNNB1, DDX3X or SMARCA4 mut	MYCN or GLI2 amp TP53 mut PTCH1 mut	PTCH1 or KMT2D mut SUFU mut/del PTEN del	PTCH1, SMO or BCOR mut PTEN del	PTCH1 mut TERT promoter mut

Subgroup		GROUP 3				GROUP 4			
Frequency (of all MB)		25				35			
Recurrence		Metastatic				Metastatic			
Proposed cell or origin		Early progenitor-like cells				UBC and GluCN progenitors			
Subtype		I	II	III	IV	V	VI	VII	VIII
Demographics	Frequency (of subgroup)	4	13	9	10	8	9	22	25
	Age								
	Gender	♀ 40 60 ♂	♀ 23 77 ♂	♀ 22 78 ♂	♀ 32 68 ♂	♀ 32 68 ♂	♀ 33 67 ♂	♀ 34 66 ♂	♀ 25 75 ♂
Clinical features	Histology	Classic, desmoplastic	LC/A, classic	Classic, LC/A	Classic	Classic	Classic	Classic	Classic
	Metastasis (%)	35	57	56	58	62	45	45	50
	5 year OS (%)	77	50	43	80	59	81	85	81
Molecular features	Cytogenetics	Balanced	8+ 1q+ i17q (less)	7+ i17q 10q-	14+ 7+ 8- 10- 11- 16-	7+ i17q 16q-	7+ i17q 8- 11-	7+ i17q (less) 8-	i17q
	Driver events	GFI1(B) OTX2amp	MYCamp GFI1(B) KBTB4, SMARCA4, CTDNEP1, KMT2D mut	MYCamp (less)	Ø	MYC or MYCN amp	PRDM6act MYCNamp	KBTBD4 mut	PRDM6act ZMYM3 or KMT2C mut

0-3 3-10 10-17 17+

Figure 7 MB molecular subgroup and subtype summary adapted from the review by Hovestadt and colleagues (2020)[1]. Upper panel shows WNT and SHH MBs, lower panel shows the intersection between Group 3 and Group 4 MB. Mut: mutation. Amp: amplification. Del: deletion. Act: activation. Subgroup frequency and cell-of-origin numbers are based on a review by Jurachka & Taylor (2019)[14].

high risk tumors and have 67 % 5-year OS probability. SHHγ MBs comprise 21 % of SHH group and can occur in any age group with a prevalence in infants. These tumors show desmoplastic, MBEN or classic histology. They mestatasize in 9 % of cases and have 88 % 5-year OS probability. Final SHH subtype is SHHδ which is the most common and takes 34 % of all SHH tumors. They usually have classic or desmoplastic histology, mainly occur in adolescents and adults and are more common in females. SHHδs metastasize in 9 % of cases and have 5-year OS probability of 89 %. SHH molecular alterations and development is discussed in section 1.1.3.3.

While WNT and SHH subgroups were named after the pathways that are altered in these tumors, **Group 3 and Group 4** were simply numbered or named "non-WNT/non-SHH" due to the lack of a unique pathway alteration[1]. Group 3 and 4 tumors are both highly metastatic, with incidence rate of 25 and 35 %, respectively[14] (Figure 7). Group 3 and 4 MBs are currently defined in terms of a gradient or continuum of molecular alterations and divided into subtypes I – VIII. These subtypes have distinct demographic, biological and molecular features. The subtypes with mostly Group 3 characteristics are mainly undifferentiated and expressing the stem cell markers in contrast to subtypes in prototypical Group 4. Some subtypes are considered as intermediate, thus showing a mixture of described cell types, namely progenitor-like undifferentiated cells and differentiated neurons with similar gene expression profiles to unipolar brush cells (UBC) and glutamatergic cerebellar nuclei (GluCN)[1,55,58].

Based on the Northcott et al (2017)[55] and Sharma et al (2019)[56] studies, subtypes II – IV show characteristics of canonical Group 3 MB. They mainly occur in infant and children age groups and are more common in males. These tumors show LC/A and classic histology. Metastases occur in on average 57 % of cases and 5-year OS probability is as low as 43 or 50 % in subtypes II and III or as high as 80 % in the subtype IV. Subtypes I, V and VII show and intermediate Group 3/4 phenotype, a preference for children and adolescent demographics and are more common in males. A classic histology is mainly observed in these tumors, with subtype I occasionally demonstrating desmoplastic features. The metastatic potential of Group 3/4 intermediate tumors varies from 35 % (subtype I) to 62 % (subtype V), which is reflected in the 5-year OS probability with 77 and 59 %, respectively. Finally, subtype VI and VIII tumors show Group 4 characteristics, are common in male children and adolescents (subtype VIII) and have a classic histology. Subtype VI and VIII tumors are metastatic in 45 and 50 % of cases, respectively, and both have

an 81 % 5-year OS probability. Molecular alterations of all 8 subtypes will be discussed in sections 1.1.3.4 and 1.1.3.5.

1.1.3.2. WNT pathway in MB

The WNT pathway regulates the expression of genes necessary for the early embryonic development and differentiation of the cells. It also has been closely associated with adult and pediatric cancers. For example, one of the WNT pathway regulators, adenomatous polyposis coli (*APC*) gene, a well-known tumor suppressor, is frequently mutated and inactivated in adult colorectal cancer[59]. Molecularly, WNT pathway regulates the cellular levels of β-catenin, a protein with dual activity, as it is involved in cell-to-cell communication (mainly adherens junctions) and gene expression regulation. When secreted WNT family glycoproteins are not present and the pathway is switched off, β-catenin is being sequestered by the destruction complex, consisting of scaffold protein axin, APC, GSK3 kinase and casein kinase (CK1) (Figure 8). In this complex, GSK3 phosphorylates β-catenin, thus subjecting it to ubiquitination by βTrCP[60] (not pictured) or FBXW7[61] E3-ubiquitin ligases and subsequent proteasomal degradation. In absence of β-catenin in the nucleus, a complex of TCF/LEF and Groucho (not pictured) proteins recruit histone deacetylases and thus suppress the expression of various genes including cell proliferation regulators MYC and cyclin D, as well as extracellular matrix proteins, like MMPs[62]. Once WNT is present in the extracellular space, it binds to the receptor Frizzled and its' co-receptor lipoprotein receptor-related protein (LRP6). LRP6 is then phosphorylated by GSK3 and CK1

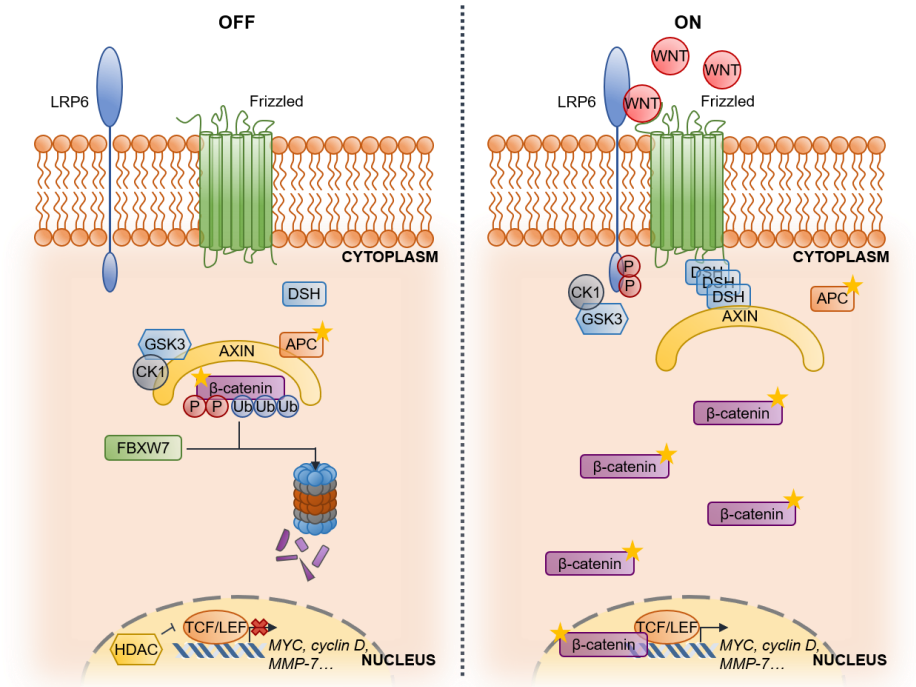

Figure 8 Canonic WNT pathway overview in OFF (left) and ON (right) mode. Stars show proteins frequently found mutated in WNT subgroup MB. Schematic was adapted from a review publication by Zhan, Rindtorff & Boutros[9] and Hovestadt et al (2020)[1].

kinases. This in turn recruits the disheveled (DSH) proteins to the plasma membrane, where they polymerize[63] and inactivate the destruction complex by sequestration. β-catenin then accumulates and enters the nucleus, where it forms an active complex with TCF/LEF thus inducing the expression of genes important for cell proliferation[9].

In WNT MBs, the WNT pathway is constantly activated, driving cellular proliferation. The most common somatic activating mutations (approximately 85 % of patients) are observed in the gene encoding β-catenin (*CTNNB1*)[64,65]. In addition, germline mutations of *APC* gene are also encountered leading to Turcot syndrome sometimes associated with MB[45]. Chromosome 6 monosomy is observed in most WNT MB cases[66] (Figure 7).

1.1.3.3. SHH pathway in MB

The sonic hedgehog (SHH) pathway is one of the key regulators of embryonic development, similar to the WNT pathway. Hedgehog (*Hh*), an *SHH* homologue in *Drosophila melanogaster* acts through a spatial gradient and is one of the main basic body plan regulators, determining the polarity of body segments[67].

In humans, the SHH pathway is involved mainly in stemness maintenance, as well as stem cell proliferation[68-70]. When the pathway is switched off (i.e. no SHH ligand is secreted), the transmembrane receptor Patched (PTCH) is suppressing the activation of the transmembrane receptor Smoothened (SMO) (Figure 9). Therefore, signalling to the cell is not transferred and the SUFU regulator remains bound to Gli1

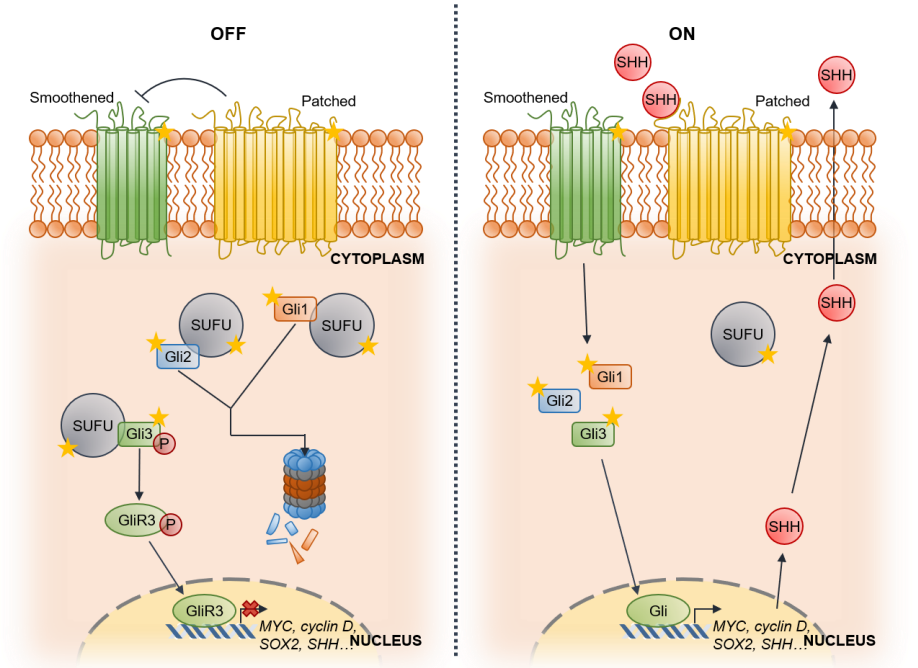

Figure 9 Canonic SHH pathway overview in OFF (left) and ON (right) mode. Stars show proteins frequently found mutated in SHH subgroup MB. Schematic was adapted from Rimkus et al (2016)[5], Jeng et al (2019)[6] and Hovestadt et al (2020)[1].

and Gli2, sequestrating them and eventually targeting them for degradation. In addition, SUFU bound to Gli3 subjects Gli3 to the protease-mediated cleavage leading to formation of the GliR3 transcription repressor. GliR3 is transported to the nucleus where it stops the transcription of various genes involved in proliferation. When the SHH ligand is present in the extracellular matrix, the pathway is in the ON mode (Figure 9). PTCH is bound by the ligand and is no longer inhibiting SMO. Therefore, Gli proteins accumulate and get transported into the nucleus where they activate the transcription of genes encoding proliferation-inductors, including Cyclin D, MYC and SOX2. In addition, the SHH pathway has a positive feedback loop[5,6].

In SHH MB, inactivating mutations or deletions in *PTCH1*, encoding Patched, are the most common molecular alterations irrespective of subtype. In addition, inactivating mutations of SUFU (SHHβ), activating mutations of Smoothened encoding gene *SMO* (most common in SHHγ) and amplifications of *GLI2* (most common in SHHα) are observed during the formation of tumor[55,71]. Various chromosome alterations are also present (Figure 7). In addition to SHH pathway-related alterations, mutations in various tumor drivers and suppressors are necessary for tumor formation (e.g. p53 or PTEN inactivation, TERT mutation). Mutations in *TP53* are particularly important. According to the 2016 WHO CNS tumor classification[49], *TP53*-mutated SHH MBs are considered to be high-risk. In fact, SHHα subtype (enriched for *TP53* alterations) when differentiated based on *TP53* status, show significantly lower 5-year OS probability when *TP53* is mutated (Figure 10)[2]. In addition to subtype differentiation, SHH MBs can be separated into three groups based on the age of patients, so called infant, children and adult SHH MB groups. Interestingly, *TP53* mutations are associated with children SHH MB[71].

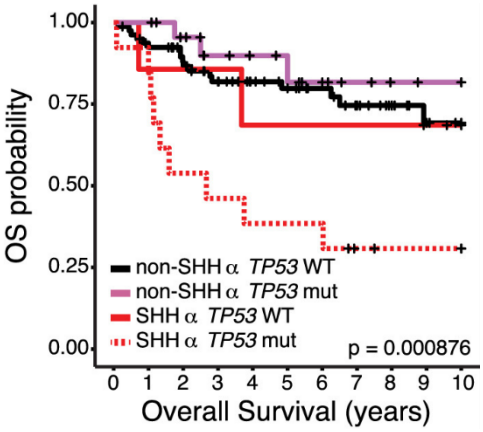

Figure 10 5-year OS probabilities comparing SHHα and other subtypes based on *TP53* status. Adapted from Cavalli et al (2017)[2].

1.1.3.4. Group 3 and group 4 subgroups and molecular alterations

As described previously Group 3 and 4 MBs form a continuum currently defined by 8 subtypes (I-VIII). These subtypes are characterized not only by different demographics, histology or risk profiles, but also by molecular alterations encountered in each of the subtypes. In fact, certain gene expression changes, copy number variations and chromosomal abnormalities correlate strongly with the survival profiles and risk levels (Figure 7)[1].

Taking together Group 3 and 4 MBs, the most prevalent cytogenetic alteration is the isochromosome 17q (i17q), encountered in around 50 % Group3/4 MB[55,66]. *MYC* amplification is the main driver event in the subtypes II-IV (Group 3). Since *MYC*-amplified MBs are a focus of this thesis, *MYC* amplification in MB will be described in detail in a separate section 1.1.3.5.

Other important alterations here include activation of the oncogenes *GFI1* and *GFI1B*. A relatively recently described protooncogene activation event called "enhancer hijacking" is taking place by juxta positioning the genomic sequence of either *GFI1* or *GFI1B* to close or remote active enhancers or super enhancers, thus inducing constant activation of these oncogenes[72]. Activated GFI1 or GFI1B forms a transcription repressive complex with chromatin remodelers and suppress genes important for neuronal differentiation[73].

Another important alteration found to some extent in all MB subgroups, but particularly important in Group3/4 MBs, is OTX2 amplification[74,75]. OTX2 is regulating stemness and differentiation expression programs, and therefore promotes tumor initiation and tumorigenesis when amplified[76].

Finally, a few other molecular alterations are present in the genomes of Group 3 and 4 MBs. Those include various epigenetic remodelers and members of the remodeling complexes, such as KDM6A, SMARCA4 or ZMYM3 (Figure 7), indicating the importance of the epigenome and epigenetic mechanisms (like "enhancer hijacking") for the formation of MB tumors.

1.1.3.5. MYC-amplification in MB

The oncogene *MYC* (or *MYCN*) are found overexpressed in MBs in practically every subgroup. *MYC*, which is associated to worse disease outcome is frequently overexpressed in the low risk WNT MBs. Here, *MYC* transcription is directly regulated by WNT pathway. Nonetheless, *MYC* is almost never amplified in WNT subgroup[66]. In SHH tumors, the MYC family member *MYCN* is found overexpressed, which is associated with worse prognosis[53]. In Group 4 MBs, *MYCN* overexpression is proposed to have a role in tumor maintenance[77].

MYC amplification has been mainly associated with Group 3 and is regarded as one of the hallmark features of the classical Group 3 MB. It is found in 10-17 % of Group 3 tumors[66] and is one of the most robust biomarkers for (very) high-risk MB[2]. Indeed, when comparing Group 3 subtypes as defined by Cavalli et al (2017)[2] based on *MYC* amplification, this alteration

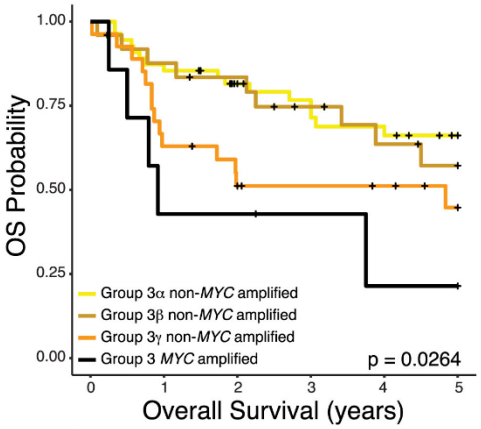

Figure 11 5-year OS probabilities comparing Group 3 subtypes depending on *MYC* status. Adapted from Cavalli et al (2017)[2].

significantly reduces the lowest 5-year OS probability of all subtypes (Group 3γ) from 50 % to below 25 % suggesting an extremely aggressive tumor behavior (Figure 11).

Due to their aggressiveness and comparatively easy transformation into the cell culture, *MYC*-amplified cell lines are enriched with Group 3 *in vitro* models [78]. On the other hand, *in vivo* model tumors do not form if only *MYC* amplification or overexpression is present. They require another genetic alteration event, namely *TP53* mutation, which is usually associated to *MYCN* amplification and SHH MB[79-81]. This suggests that in humans an additional genetic alteration is necessary for tumorigenesis when *MYC* amplification is present. For instance, glucose metabolic pathways and LDHA expression were proposed to be involved in tumor initiation[82].

1.1.4. Prognosis and therapeutic options

MB prognosis and risk assessment is currently based on both, evaluation of histology and of molecular subgroup and additional genetic alterations. In the 2016 World Health Organization (WHO) introduced molecular subgrouping and risk stratification recommendations for the first time into their tumor classification. For example, WNT MB with classic histology was determined to carry a low risk. In contrast, SHH MB with *TP53* mutation and large cell/anaplastic (LC/A) histology or Group 3 tumor with LC/A histology would be assigned to the high-risk group (Table 1). The therapeutic approach could be adjusted based on the risk profile of the tumor.

SOC MB treatment includes surgical resection of the tumor followed by cranio-spinal irradiation and chemotherapy. The goal of the surgery is maximal surgical resection of the tumor. The complete resection is sometimes not possible due to the sensitive tumor localization. Residual disease often correlates with the dismal outcome[83]. One of the most common complications of MB resection surgery is cerebellar mutism, or posterior fossa syndrome, observed in 25-29 % of patients[83-85]. Posterior fossa syndrome-affected patients are unable to pronounce words, become irritable, develop ataxia and hypotonia. Such complication development has been associated with further neurocognitive sequelae, often life-long[85,86].

Table 1 Risk assessment summary for MB molecular subgroups and MB histology. Adapted from Louis et al (2016)[49]. * (very) rare tumors. Mut: mutation. Wt: wild type.

Genetic profile	Histology	Prognosis
MB, WNT	Classic	Low risk
	LC/A*	Uncertain clinicopathological significance
MB, SHH, *TP53*mut	Classic	High risk
	LC/A	High risk
	Desmoplastic/nodular*	Uncertain clinicopathological significance
MB, SHH, *TP53*wt	Classic	Standard risk
	LC/A	Uncertain clinicopathological significance
	Desmoplastic/nodular	Low risk (infants)
	MBEN	Low risk
MB, Group 3	Classic	Standard risk
	LC/A	High risk
MB, Group 4	Classic	Standard risk
	LC/A*	Uncertain clinicopathological significance

Radiotherapy is a mainstay for MB treatment. Since MB tends to be highly metastatic and disseminates through the CSF, cranio-spinal irradiation is necessary. Based on the SIOP Europe Brain Tumor Committee MB Working Group developed Protocol 12.0 in 2017 (SIOP-PNET5), current recommended dose of radiotherapy for a standard risk MB patient is 23.4 Gy to the cranio-spinal axis (CSA) and 30.6 Gy to the posterior fossa. It is usually combined with adjuvant chemotherapy, as numerous studies have shown that adjuvant therapy significantly increases the progress-free survival (PFS) and OS in high-risk patients particularly[87,88].

Despite reduction of the radiation dose, unfortunately, various short- and long-term side effects dependent on radiotherapy are frequently observed. In addition to previously mentioned posterior fossa syndrome, other neurocognitive and neuropsychological sequelae are reported. This includes IQ reduction[89], emotional lability and other cognitive disabilities[90-93]. Endocrine system dysfunction and subsequent growth problems[94,95], as well as various organ dysfunctions and neuropathies[96] are common side effects, too.

Ever since driving mutations of MB were discovered, the hope for targeted therapy entering the routine clinical use for MB patients to reduce the potential long-term side effects persisted.

Unfortunately, until now none of the targeted drugs are used routinely. www.cinicaltrials.gov reports almost 100 active studies involving medulloblastoma. Some of them are evaluating new radiotherapy protocols or devices. Others are focused on bringing new therapeutic options to the clinic, including immunotherapy, small-molecule inhibitors and antibodies. Nonetheless, the scientists working on MB agree that a combination of different therapeutics in addition to SOC therapy will potentially make the most difference when applied to clinics. Therefore, the focus of this thesis is on potential combination therapy development for high risk MB.

1.2. MYC

C-MYC (in this thesis shortened as *MYC*, v-myc avian myelocytomatosis viral oncogene homolog) is a proto-oncogene considered to be one of the master regulators of various cellular processes, proposed to regulate up to 15 % of all genome[97]. *MYC* belongs to a family of genes also including *N-MYC* (*MYCN*) and *L-MYC* (*MYCL*), which have also been implicated in cancer development with *MYCL* involved in lung cancer[98] and *MYCN* strongly associated with pediatric neuroendocrine cancer neuroblastoma[99]. Nonetheless, the most studied family member remains *MYC*, shown to be overexpressed in the majority of human cancers and to contribute to the tumor development in at least 20 % of entities[100,101].

V-myc was discovered in the 2nd half of the 20th century as a transforming factor in the avian myelocytomatosis retrovirus-induced malignancies in chicken[102,103]. Later, scientists found v-myc homologues in humans with Burkitt's lymphoma[104-107] and pioneered the first efforts to understand the function of *MYC*, one of the most famous oncogenes with more than 38,000 mentions in PubMed database since the 1970s. In this section, MYC protein structure and function will be discussed in detail. MYC implications for tumorigenesis will be described, as well as current therapeutic targeting options and their (pre-)clinical development.

1.2.1. Structure, function and protein complexes

The *MYC* gene has 3 exons with over 4 kbp length in sum. Only the 2nd and 3rd exons end up translated, whereas the 1st exon has been proposed to be involved in mRNA stability regulation. The majority of *MYC* mRNAs in the cells are being transcribed from promoter P2. *MYC* mRNA includes the internal ribosome entry site (IRES) allowing translation when the 5' site is inaccessible for the ribosomes (e.g. during the viral infection)[108].

The MYC protein is 62 kDa large and composed of 439 amino acids. It belongs to a class of transcription factors containing a basic-helix-loop-helix-leucine-zipper (bHLH-LZ) motif as a part

of their structure. In addition to bHLH-LZ, MYC also has 4-5 conserved motifs named MYC homology box domains. Depending on the publication, either 4 (I, II, III and IV)[24] or 5 (I, II, IIIa, IIIb, IV)[18,109] domains are reported. In general, the MYC N-terminal domain (NTD) containing the homology boxes I, II, and III is a regulatory part of the protein and the C-terminal domain (CTD) containing the bHLH-LZ domain is required for DNA binding and dimerization with MAX, the main MYC binding partner (Figure 12).

The MYC regulatory part includes a transactivating domain (TAD) which in turn contains a degron domain (not pictured) where E3 ubiquitin ligases responsible for MYC turnover and proteasomal degradation bind. One of them is FBXW7 binding at the homology box I. This box contains MYC regulatory phosphorylation sites necessary for MYC transactivation and subsequent degradation (serine-62 and threonine-58). In addition to MYC regulatory proteins, modulators, required for transcription induction are also binding at the NTD. For example, histone acetyltransferase (HAT)

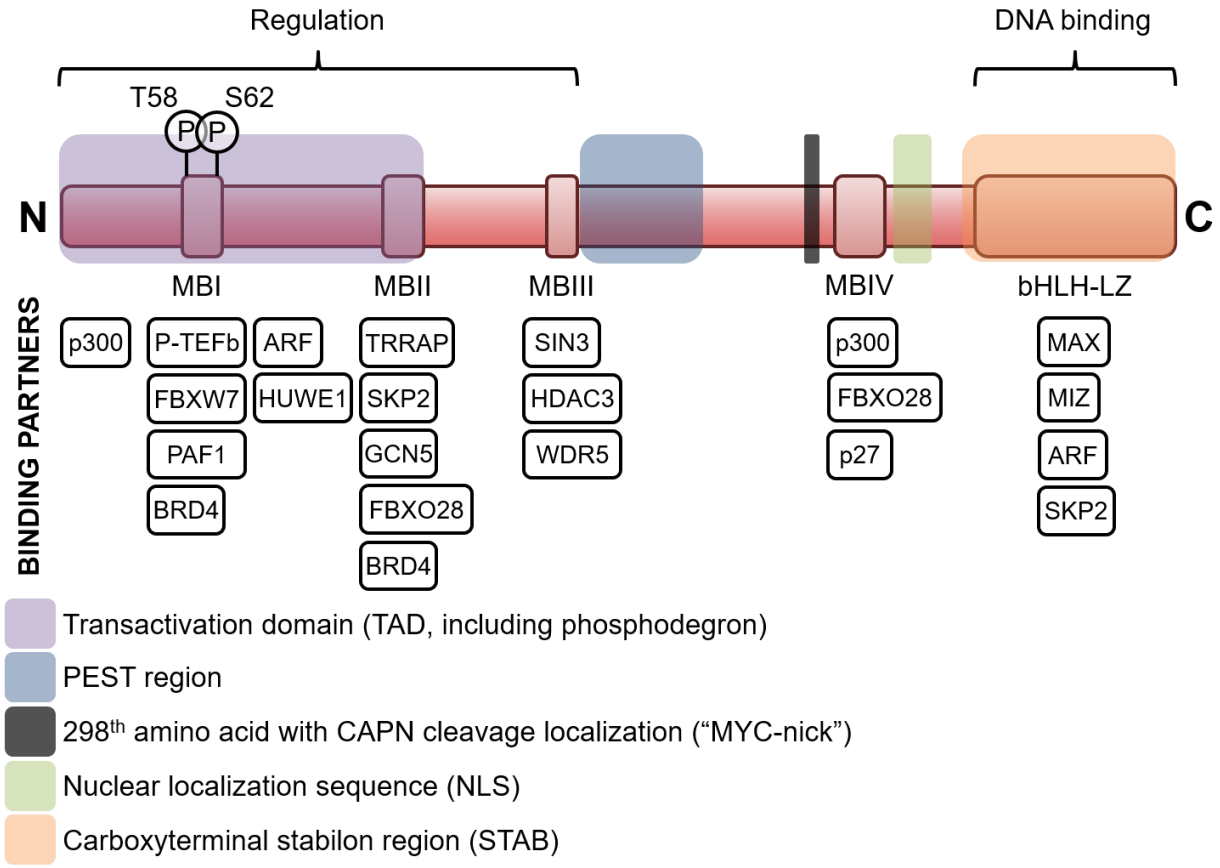

Figure 12 MYC protein structure, domains and binding partners. MB: MYC homology box. Adapted from Tu et al (2015)[18], Poole et al (2017)[24], Hydbring et al (2017)[30] and Thomas & Tansey (2011)[33].

p300, BRD4, a bromodomain protein, binding acetylated lysine residues, or p-TEFb, a CDK9-Cyclin T1 transcriptional pause-release complex.

The central part of MYC and the homology box III has been shown to be involved in transcriptional repression[110] and MYC destabilization[111]. Here, MYC repressor SIN3 and the histone deacetylase 3 (HDAC3) bind. In addition, the central part of the MYC protein also contains a PEST sequence enriched for classic disorder-promoting amino acids, proline (P), glutamate (E), serine (S) and threonine (T)[112]. The PEST region seems to be responsible for rapid MYC degradation independent of ubiquitination, since its' deletion increases the stability of the protein without affecting ubiquitin modification status and quantity[113]. The central part of the protein also contains another processing localization, namely a calpain (CAPN, calcium-activated neutral protease) cleaving site. This produces so-called "MYC-nick", a cytosolic version of MYC, interacting with HATs, promoting α-tubulin acetylation and microtubule regulation[114]. Finally, homology box IV, is required for MYC activity within the cell[115], with an adjacent nuclear localization signal (NLS).

The CTD of MYC protein, as mentioned above, is responsible for dimerization with MAX and MIZ-1 (MYC binding partner in transcription-repressing complex) and for DNA binding (LZ motif). The CTD also contains the so-called stabilon region (STAB), aiding with the stabilization of MYC. This is due to the association to MIZ-1, as well as allowing MYC to acquire metabolic stability[33,116].

In a normal cell, MYC is activated by mitogenic signal cascades and regulates transcription of genes involved in many necessary cellular processes, including but not limited to proliferation, cell growth, differentiation, and genomic stability. MYC and its' binding partner MAX bind to DNA sequences called E-boxes residing nearby gene regulatory elements, i.e. promoters and enhancers. The canonical E-box sequence is 5'-CACGTG-3'. However, MYC is also able to bind the non-canonical E- boxes, albeit with lower affinity. Upon binding a genome regulatory element, MYC recruits chromatin remodeler complexes (e.g. TRRAP) and other transcription elongation necessary proteins. MYC also induces BRD4-pTEFb-dependent phosphorylation of stalled RNA polymerase II[117-119]. This induces the start of elongation and proper transcription[12] (Figure 13a). In the case of transcriptional activation, MYC acts as a signal amplifier rather than as an initiator. That is, the genes that MYC is regulating are being expressed at a certain level. However, when mitogen signals are present in the cell and MYC protein levels are increasing, MYC is taking over every E-box (with a priority to canonical E-boxes in promoters) and amplifying the transcription[120].

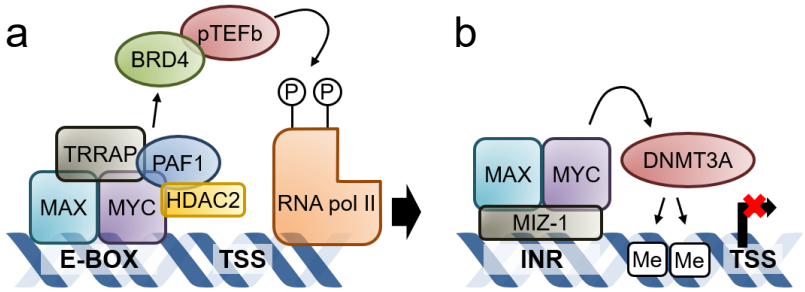

Figure 13 MYC protein as a member of transcription induction (a) and repression (b) complexes. TSS: transcription start site. INR: initiator. Adapted from Jaenicke et al (2016)[17], Chen et al (2018)[12], Stine et al (2015)[27], Gutierrez et al (2019)[29] and Adhikary & Eilers (2005)[31].

MYC is also a member of a transcriptional repressor complex. In this case when an initiator (INR) sequence is in the proximity of an E-box and MIZ-1 is bound to the INR, it can also bind the MYC/MAX complex. This leads to the recruitment of *de novo* DNA methyltransferase, which then methylates the DNA inducing the formation of the heterochromatin and repressing the transcription[29] (Figure 13b).

MYC's turnover and proteasomal degradation is an important and highly monitored mechanism (Figure 14). Activated or stabilized MYC has a phosphorylated serine-62 (S62), which in normal cells is phosphorylated by ERK family kinases, and at least partially by PLK1[121]. MYC's transcriptional activity increases upon S62 phosphorylation. S62 also primes MYC for further phosphorylation on the second residue within the phosphodegron domain, threonine-58 (T58), by GSK3β kinase[122]. This allows the removal of the stabilizing phosphorylation at S62 by the phosphatase PP2A. Phosphorylation at T58 without the stabilizing S62 phosphorylation is recognized by the FBXW7, which ubiquitinates MYC, thus targeting it to the proteasomal degradation[20,123]. In the cell, the turnover rate of MYC is very high. In addition to FBXW7, several other ubiquitin ligases have been implicated in MYC degradation and transcription induction processes depending on the cell cycle phase and other conditions. They all were reviewed in great detail by Farrell & Sears (2014)[20]. In addition, this work brought to light a "transcription factor licensing" concept, which indicates a dependency between transcription factor activation and degradation (i.e. MYC is activated only when phosphorylation priming the protein for degradation is in place).

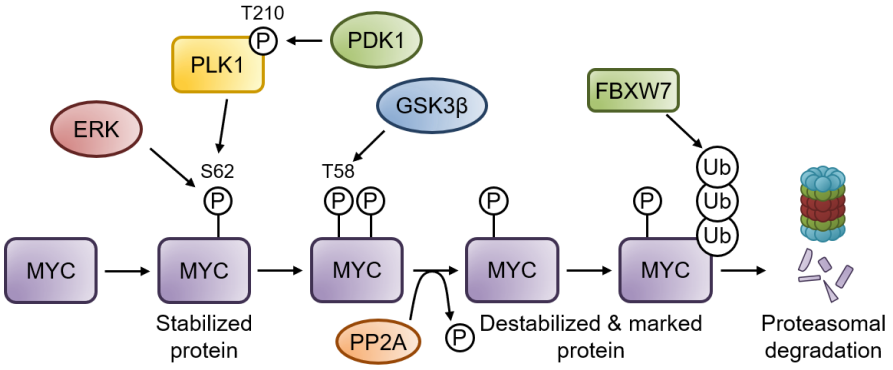

Figure 14 MYC protein stabilization and degradation process. S62: serine-62. T58: threonine-58. Adapted from Farrell & Sears (2014)[20] and Jozwiak et al (2014)[25].

1.2.2. Implications for tumorigenesis

All previously described MYC functions and targets show the importance of the protein and extensively regulated intricate mechanisms limiting its' activity. Even though MYC functions are precisely controlled, genetic and epigenetic alterations can cause MYC dysregulation. A certain pathway induction or the dysregulation of MYC degradation processes due to somatic or germline mutations can induce *MYC* overexpression. Examples are WNT pathway activation in WNT subgroup MB, where *MYC* is indeed upregulated, or FBXW7 ubiquitin ligase downregulation/inactivating mutation. In addition, *MYC* transcription can be induced by gene translocation to the proximity of the regulatory regions of highly expressed gene, for example in Burkitt's lymphoma[105]. Finally, increased *MYC* transcription in tumors is also achieved via amplification of the gene, found enriched in Group 3 MB and other cancers, both pediatric and adult (breast[124], prostate[125], lung[126] cancers, PDAC[127], etc). Of note, pan-cancer analyses of at least 12 cancer types found that *MYC* amplification frequency lies at around 14 %[128,129]. *MYC* amplification is almost always associated with dismal prognosis and extremely aggressive cancer.

In normal cells, *MYC* expression is induced by mitogen presence in the extracellular space. Therefore, MYC is involved in processes like cell proliferation and differentiation. As shown in Figure 15, the majority of those processes are deregulated in the tumor cells. Taking into account the hallmarks of cancer (a term coined by Hanahan & Weinberg in their famous reviews in 2000[130] and 2011[19]), MYC seems to be involved in each of the mechanisms driving tumorigenesis. For example, in addition to being able to sustain proliferative signalling, MYC is inducing ribosome biogenesis, which in turn is required for cell growth[131,132]. Also, MYC has been shown to interact and induce cyclin and CDK activation, fueling the cell cycle machinery and helping tumor cells evade growth suppressors[109,133,134]. MYC has been

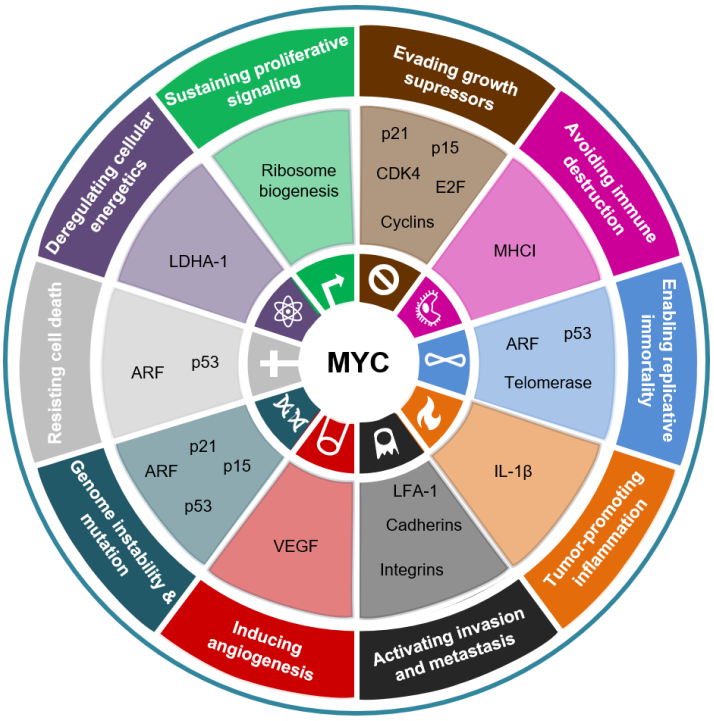

Figure 15 The hallmarks of cancer and MYC with MYC-regulated processes, binding partners and target genes. Adapted from Hanahan & Weinberg (2011)[19].

associated to immune system evasion[135], inflammation promotion[136], angiogenesis induction[137], metabolism deregulation[27], apoptosis deregulation[138] and genomic instability[139]. Thus it is no surprise that MYC has been dubbed as a "hallmark of tumor initiation and maintenance"[140] and is considered as one of the main targets in the fight against cancer. It is important to describe the concept of "oncogene addiction" in the discussion of MYC in tumorigenesis and before focusing on the targeting of MYC. This phenomenon has been shown in a panel of cancers and is quite often observed in *MYC*-amplified entities. Here, despite the genetic alterations and the complexity of transformed cellular machinery, the proliferation and growth of tumor cells could be impaired by inhibiting one oncogene[141]. Hence, a lot of research effort is directed at *MYC* and other oncogenes for therapeutic targeting. This topic is discussed in more detail in the following section.

1.2.3. Therapeutic targeting

MYC is a transcription factor, which makes it notoriously difficult to target directly. The reason is, that it lacks a specific active site which could be used for small molecule inhibitor targeting (in contrast to enzymes, such as kinases). An alternative approach could be targeting by a monoclonal antibody, which is rendered impractical due to MYC's inherent nuclear localization. Therefore, many other possibilities for MYC targeting have been proposed (Figure 16). Of note, in contrast to various reviews[12], in this thesis MYC/MAX dimerization targeting is considered direct as it is based on directly targeting MYC activity and not processes leading to MYC overactivation.

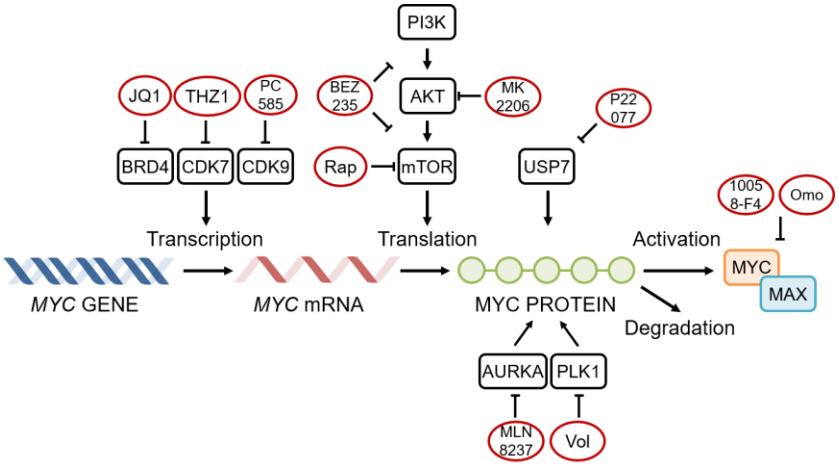

Figure 16 Direct and indirect MYC targeting on DNA, mRNA and protein levels. Rap: rapamycin. Omo: omomyc. Vol: volasertib. Adapted from Chen et al (2018)[12].

1.2.3.1. Direct targeting

As mentioned previously, due to inherent structural properties and lack of enzymatic activity, direct targeting of MYC protein historically has been shown to be problematic marking MYC as an "undruggable target"[109]. Nonetheless, targeting MYC expression/translation or MYC and MAX dimerization emerged as a substitute for actual direct targeting of the protein. The first option includes G-quadruplex stabilizers, antisense oligonucleotides and RNA interference with some

compounds eventually reaching phase I/II of clinical development. In particular, antisense oligonucleotide RESTEN-NG® has shown promise in oncology as well as in cardiology. However, apart from a successful clinical trial in cardiovascular patients in 2007[142] and a clinical trial in various solid neoplasms (NCT00343148), no developments have been reported.

Around the turn of the millennium, pioneered by Berg and colleagues[143], many groups interested in targeting MYC developed their own inhibitors to disrupt the MYC/MAX dimers. These included peptidomimetic inhibitors (e.g. omomyc, Figure 16), "credit-card" inhibitors, DNA-binding disrupting inhibitors and others (reviewed in great detail by Fletcher & Prochownik[144]). Unfortunately none of the MYC/MAX dimerization inhibitors reached the clinical development, although some of them have shown high efficacy *in vivo*[145] and potential to be used in combination with other therapeutic options[146].

1.2.3.2. Indirect targeting

Indirect MYC targeting has shown far more progress and potential compared to the direct expression/translation or dimerization/DNA binding targeting. In general, indirect targeting of MYC is based on inhibiting proteins inducing high levels of *MYC* expression and exists on several levels: transcription, translation and protein stability/degradation (Figure 16).

Indirect *MYC* transcription targeting aims at epigenetic regulator BRD4, shown to bind *MYC* super-enhancers and activate its' transcription[147], and transcription regulators cyclin-dependent kinases 7 and 9 (CDK7, CDK9). Despite potential toxicities due to the unspecific targeting of the whole genome, inhibitor off-target effects (namely BRD2/3 targeting) and other issues[148,149], inhibitors of BRD4 and other bromodomain proteins have shown potential alone and in combinations, reaching phase I/II of clinical development (Table 2). CDK7 and 9 are kinases regulating transcription initiation and elongation. Inhibition of CDK7 and 9 has been associated with *MYC* expression induction via binding to super-enhancers[150]. Inhibition of both kinases have been shown to substantially reduce *MYC* expression and promote anti-tumor effects[150,151]. Several CDK7 and CDK9 inhibitors have already been tested in clinics (first-in-human and phase I/II).

Targeting MYC translation is based on inhibiting proteins regulating PI3K/AKT/mTOR axis, generally regulating translation initiation. mTOR inhibitors have already been effective in MYC level reduction and have shown anti-tumor activity in multiple studies[152,153]. Some of the mTORi are already approved to use clinically, e.g. due to its' anti-angiogenic activity temsirolimus (a

Table 2 Summary of indirect MYC targeting mechanisms, the compounds and the clinical development phases. Adapted from Chen et al (2018)[12], Whitfield et al (2017)[145] and Alqahtani et al (2019)[154].

Mechanism	Targets	Compound examples	Example ref.	Clinical stage	Indications	Clinical trial examples
Transcription targeting	BRD4	JQ1	155-157	NA	NA	NA
		I-BET 762	158-160	Phase I/II	Various hematologic and solid cancers	NCT01943851 NCT01587703 NCT02964507
		MK-8628	161	Phase I/II	Various hematologic and solid cancers	NCT02698189 NCT02259114
	CDK7	THZ-1	150,162	NA	NA	NA
		SY-1365	163	Phase I/II	Advanced solid tumors	NCT03134638
	CDK9	PC585	151	NA	NA	NA
		AZD4573	164,165	Phase I/II	Hematologic malignancies	NCT03263637
Translation targeting	PI3K	BEZ-235	153,166	Phase I/II	Advanced solid tumors	NCT01343498 NCT01658436
		BKM-120	167-169	Phase I/II	Various hematologic and solid cancers	NCT01790932 NCT02301364 NCT01737450
	AKT	MK-2206	170,171	Phase I/II	Advanced solid tumors	NCT01169649 NCT00670488 NCT01283035
	mTOR	Temsirolimus	152,172,173	Approved	Renal cell carcinoma	NCT01206764 NCT00474786 NCT00410124
Protein stability (degradation) targeting	USP7	P22077	174,175	NA	NA	NA
	AURKA	MLN8237	176,177	Phase II/III	Various hematologic and solid cancers	NCT01482962 NCT01799278 NCT00807495
		LY3295668	178	Phase I	Advanced solid tumors	NCT03092934 NCT04106219
	PLK1	Described in section 1.4.4.				
Immune system targeting	BTK	Ibrutinib	179,180	Approved	CLL	NCT01804686 NCT02801578
	PD-L1/ CD47	Atezolizumab	181,182	Approved	Non-small cell lung cancer	NCT03285763

derivative of rapamycin) has been approved by FDA and EMEA in 2007 for use against renal cell carcinoma (RCC). PI3K inhibition was shown to synergize with histone deacetylase (HDAC)

inhibitors in MYC-dependent MB[168]. Multiple PI3K and AKT inhibitors are currently in various stages of clinical development (Table 2).

MYC stability and degradation pathways could be targeted by therapy. For example, USP7 (Figure 16) deubiquitinates MYC thus stabilizing the protein (as has been demonstrated in neuroblastomas[183]), in turn leads to the loss of transcriptional activity. Other ways of targeting MYC degradation pathways include targeting kinases regulating FBXW7 stability (PLK1[184]) and binding (AURKA[185]) with inhibitors in phase II/III clinical trials (Table 2).

Finally, targeting immune components overexpressed and necessary for MYC-dependent tumor survival often leads to MYC level downregulation and anti-tumor effects. This includes ibrutinib (approved for clinical use, in the market as Imbruvica®) targeting Bruton's Tyrosine Kinase (BTK)[180], and immune checkpoint inhibitors[135].

Taken together, targeting MYC is extremely challenging but, however, possible. In the last few years, a few combinations of previously mentioned inhibitors have been shown to have a lot of potential and act synergistically against MYC-addicted tumors via synthetic lethality or other mechanisms. This indicates that defeating MYC is achievable using combinatorial therapies.

1.3. Histone deacetylases

Histone deacetylases (HDACs) are a class of conserved chromatin remodelling enzymes catalyzing the removal of the acetyl group from the lysine residues of the histones and other target proteins. Together with other epigenetic modifiers (e.g. histone acetyltransferases, HATs, or methyltransferases, HMTs), HDACs regulate transcription machinery, DNA density and accessibility on a global genome level. According to the histone code theory, HDACs are considered to be "erasers", the enzymes removing the epigenetic marks, working opposite of "writers", in this case HATs.

Due to their global, genome-wide tightly regulated function and evident upregulation in some tumors, HDACs have been implicated in tumorigenesis of various cancer entities. In fact, HDAC inhibition has been shown to be anti-tumorigenic as early as the last decade of the 20th century[186]. Therefore, HDAC inhibitors were one of the biggest discoveries in anti-cancer therapy since early 2000s. In this section, HDAC structure, classification and biological function will be discussed. Moreover, HDACs' role in tumor development and the potential of HDAC inhibitors will be described in more detail.

1.3.1. Structure, function and classification

There are two major types of HDACs based on the co-factor required to carry out their enzymatic function, NAD^+-dependent sirtuins (will not be discussed here) and Zn^{2+}-dependent so-called "classical" HDACs. There are 11 "classical" HDACs. They all have a conserved catalytic deacetylase domain and are classified into 4 classes based on their structure (Figure 17).

Class I includes HDAC1, 2, 3 and 8. They are predominantly found in the nucleus and have been shown to be the class responsible for chromatin remodelling and deacetylating histones. HDACs 1 and 2 have been shown to take parts in transcriptional machinery repressor complexes, such as coREST[187], NuRD[188,189] and mSin3[190] in numerous publications. HDAC3 has been found in N-COR and SMRT nuclear-receptor co-repressor complex suggesting a role different from other class I HDACs[191]. In addition, of the class I HDACs, only HDAC3 has a nuclear export signal sequence (NES)[192] and can be shuttled to the cytoplasm, where it has been shown to de-acetylate STAT1[193], thus taking part in the regulation of signalling pathways of the cell. Based on various

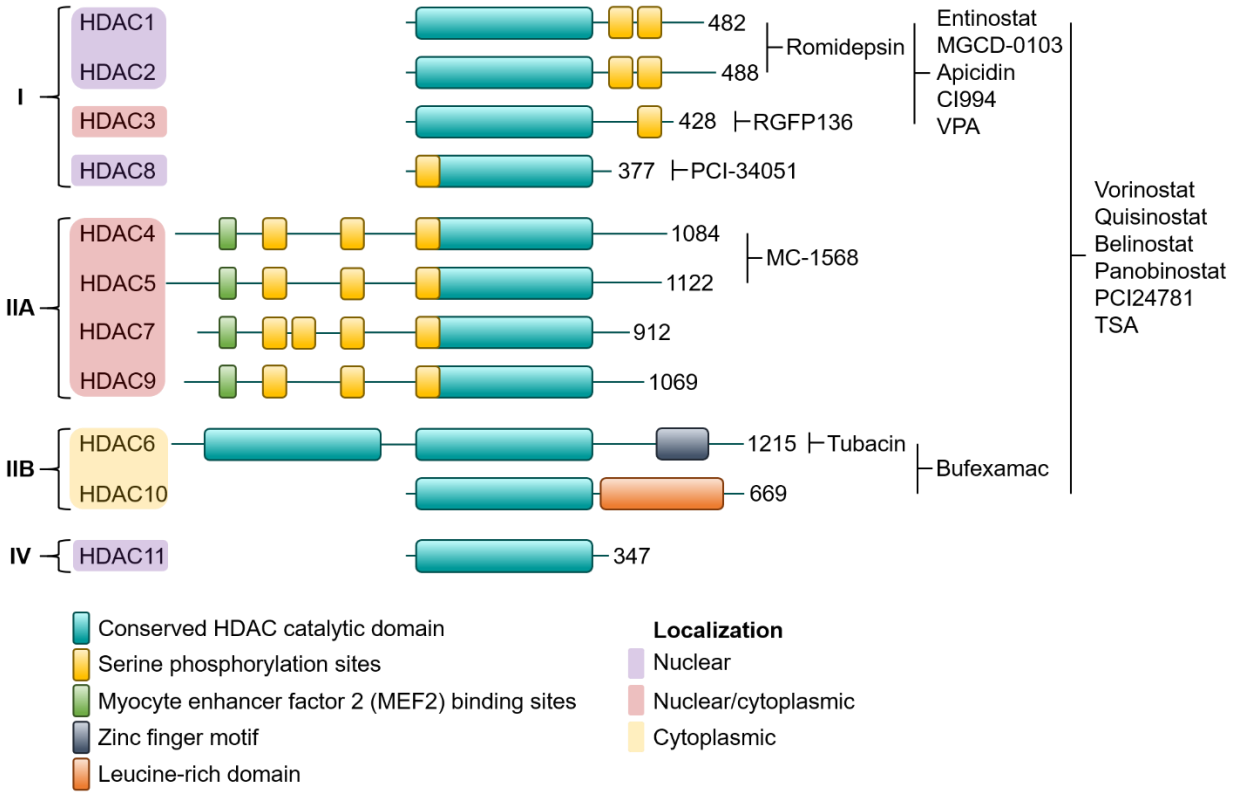

Figure 17 Summary of classical HDACs, including classification, structure, cellular localization and inhibitor specificity. Roman numbers indicate HDAC classes. Numbers next to the structures indicate a number of amino acids in the protein. Adapted from Witt et al (2009)[15], Haberland et al (2009)[26], Hessmann et al (2017)[28] and Wang et al (2015)[32].

studies conducted in the last two decades summarized in reviews[194,195], there are many doubts whether HDAC8's primary targets are histones[196]. Nonetheless, many other proteins with diverse physiological functions have been shown to be deacetylated by HDAC8, including SMC3[197], estrogen-related receptor α (ERR-α)[198] and p53[199]. HDAC1 and 2's involvement in transcriptional regulation and HDAC3 and 8's role in signalling pathways emphasize the class I HDAC implications for tumorigenesis and importance for HDAC inhibitor clinical application.

Class IIA includes 4 proteins: HDAC4, 5, 7 and 9. Compared to other HDACs, class IIA HDACs are expressed in specific organs and tissues (HDAC4, 5 and 9 in heart, brain and skeletal muscle, HDAC7 in vascular system, heart, skeletal muscle and brain[200,201]). Class IIA HDACs have a large N-terminal domain (NTD) necessary for shuttling between the nucleus and cytoplasm (NLS) and DNA binding. The NTD contains multiple highly conserved serine phosphorylation sites as well as MEF2 (Myocyte Enhancer Factor 2) family protein binding locations (Figure 17). These serines are regulating not only binding to the co-factor proteins, but also the sub-cellular localization and are phosphorylated as a response to stress[202,203]. MEF2 is a family of transcription factors controlling pleiotropic developmental pathways and response patterns. They are known to be involved in tumorigenesis and cardiological diseases. When bound to class IIA HDACs, MEF2 proteins act as repressors[201,204]. Class IIA HDACs also have a catalytic site amino acid residue substitute that substantially decreases the de-acetylation catalytic activity of class IIA HDACs[205].

Class IIB has two members, HDAC6 and 10. Both HDACs from class IIB are rather unusual due to their primarily cytoplasmic location (Figure 17, though occasionally residing in the nucleus[206]), indicating a different deacetylation target than histones. Indeed, a well-studied class IIB member HDAC6 has been shown to preferentially deacetylate a microtubule structural unit α-tubulin[207] and a chaperone heat shock protein 90 (Hsp90)[208], thus regulating the cell motility and protein homeostasis. HDAC6 also has a CTD-Zinc Finger motif binding free ubiquitin and ubiquitinated proteins[209,210]. Not much is known about the functions of HDAC10, however, its' role as polyamine deacetylase[211] and role in DNA repair and autophagy have been demonstrated[212,213].

Little is known about the only member of the **class IV**, HDAC11. Structurally, HDAC11 is similar to the other classic HDACs with approximately 80 % of its' sequence regarded to the catalytic domain[214]. HDAC11 has been reported to interact with HDAC6[215] and members of the cohesin complex[216], however, apart from its' function in immune response regulation[217,218], not much has been published on HDAC11's role in cellular processes.

As mentioned before, classic HDACs are Zn^{2+}-dependent enzymes, catalysing the removal of the acetyl- group from the lysine residues. In their catalytic domain, the zinc ion is chelated by two aspartate (Asp-178, Asp-267) and one histidine residue (His-180). The acetyl group bound by the lysine residue of the target protein binds the zinc ion causing electronic polarization. An adjacent water molecule is activated (deprotonated) by aspartate/histidine relay for the subsequent nucleophilic attack on the acetyl group (Figure 18a, left panel). A tetrahedral intermediate bound and stabilized by zinc ion and tyrosine is formed (Figure 18a, middle panel). Finally, the intermediate collapses forming the acetate and the de-acetylated lysine residue is protonated by adjacent histidine (Figure 18a, right panel)[219,220]. In general, as the catalytic domains of classic HDACs are conserved, the lysine deacetylation reaction is conducted by the same residues in all classes. However, as mentioned before, class IIA HDACs have a substitution of histidine residue instead of the stabilizing tyrosine, thus reducing their catalytic activity substantially[205].

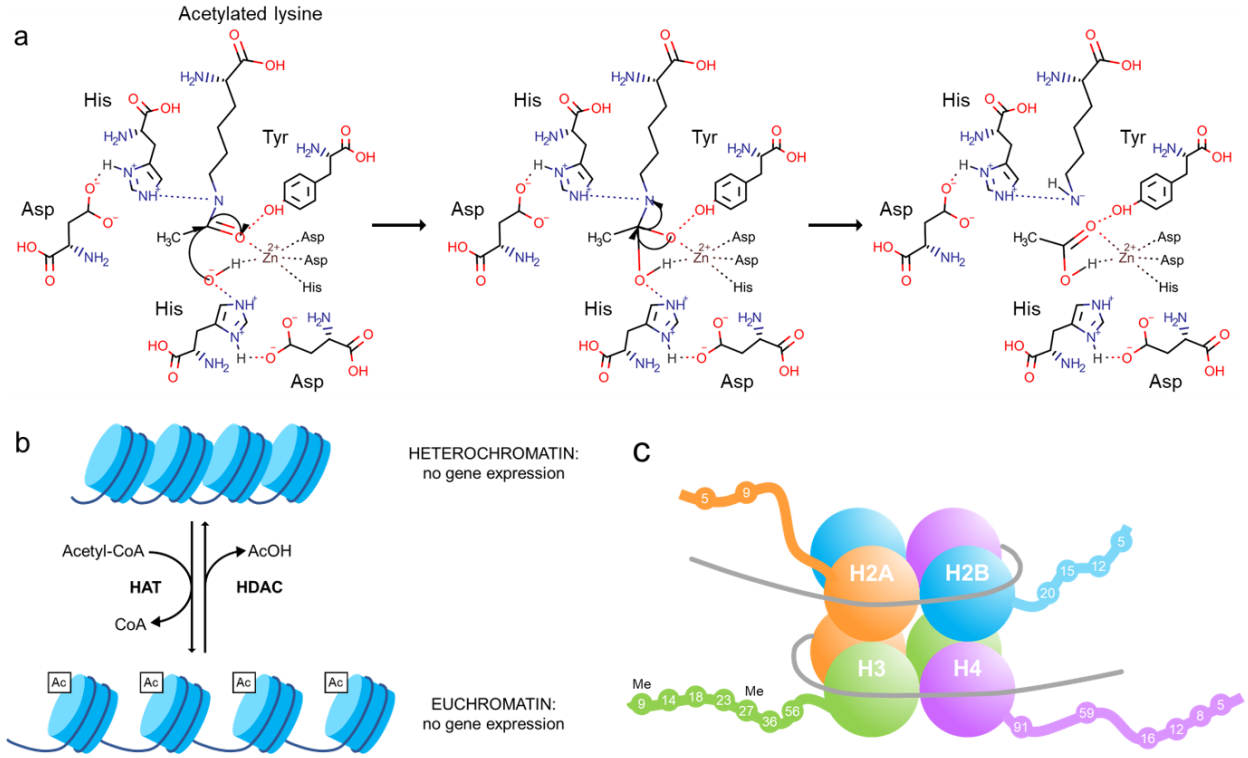

Figure 18 Histone deacetylation mechanisms. a – lysine deacetylation chemical reaction as catalyzed by classical HDACs, adapted from Lu (2013)[216]. b – Histone acetylation effect on chromatin density. c – Histone NTD residues found acetylated adapted from Dai & Wang (2014)[13]. Me: methylation.

As the name of the protein family suggests and as mentioned before, the protein targets for HDACs first discovered were histones. In particular, class I HDACs play a big role in histone deacetylation and chromatin density regulation. Generally, histone tails bear positive charge which allows them to tightly interact with negatively charged DNA. HATs, acetylating lysines

residing in the histone tails, neutralize their charge, thus allowing chromatin expansion, i.e. formation of euchromatin (Figure 18b). Sparse nucleosomes and accessible DNA allows transcription factor binding thus inducing gene expression. HDACs, removing acetyl group from the lysines of histone tails, and recruiting DNA methyltransferases (DNMTs) promote the formation of the denser version of chromatin, called heterochromatin. This version of chromatin does not allow gene expression[221,222].

Histone post-translational modifications (PTMs) play a major role in gene expression regulation. One of the most prominently researched marks is acetylation. There are multiple lysines shown to be acetylated in the histone tails. Most of them have been found in the tail of histone 3, which also has been the most studied histone of all (Figure 18c). Especially well known is the acetylation of histone 3 lysine 27 (H3K27ac) or lysine 9 (H3K9ac). Both residues can also be subjected to another PTM, methylation. Acetylated H3K9 and 27 are associated with enhancers and promoters of active genes. If both marks co-occur with histone 3 lysine 4 mono-methylation (H3K4me1), the sequence is most probably an enhancer, whereas promoter H3K4 is usually tri-methylated (H3K4me3). Acetylation on lysines 9 and 27 is contrasting to the methylation marks on the same residues. Methylated K9 and K27 indicate repressive signals and follows de-acetylation by HDACs in heterochromatin formation process[223].

1.3.2. Implications for tumorigenesis

As discussed in the previous section, deacetylating histones and being a part of various protein complexes important for transcription, classic HDACs regulate expression of various genes. Thus, it is not surprising that histone deacetylase expression has been shown to be deregulated in many different cancer entities, both children and adult, including, but not limited to neuroblastoma[212,224], MB[225,226], lung[227,228], liver[229,230], pancreatic[231,232], colorectal[233] malignancies, breast[234,235] and prostate[236] cancers. In addition HDAC expression is known to correlate with advanced stage and dismal outcome in various entities[224,237,238]. It is believed that classic HDACs have an oncogenic role, whether affecting transcription by deacetylating tumor suppressor gene promoters and thus silencing them or participating in the regulation of various signalling pathways and inducing known oncogenes. In addition, some cancer entities, such as melanoma[239], HDACs harbor inactivating somatic mutations. Furthermore, class II HDAC inhibition promotes angiogenesis[240], suggesting possible anti-tumor activities of HDACs.

Based on the wide variety of possible targets of HDACs including transcription and non-histone targets, just like MYC in the previous chapter, HDACs are involved in tumorigenic pathways of multiple hallmarks of cancer. The proliferation and division of cells are affected by HDACs via dysregulation of cell cycle DNA damage checkpoints, promotion of transcription of cyclins and cyclin-dependent kinases (CDK) or regulation of cell cycle proteins, such as p21 and p27[241-243]. For example, HDAC3 regulates mitotic entry by deacetylation of H3 in mitotic chromosomes which allows the Aurora B kinase (AURKB) to phosphorylate H3S10 (histone 3 serine 10), leading to dissociation of heterochromatin protein 1 (HP1) necessary for mitosis[244].

In addition to cell cycle and proliferation, HDACs have been shown to be highly involved in the regulation of extrinsic[245,246] and intrinsic apoptosis pathways[247-249]. Of note, the response to HDAC inhibitors dependence on *TP53* mutation status is an extensively debated topic[250]. Furthermore, HDACs have been demonstrated to influence the expression of DNA damage repair (DDR) genes and pathways[213,251-254], to regulate the epithelial-mesenchymal transition (EMT) via E-cadherin transcription[255,256], and to play a role in angiogenesis via direct HIF-1α[257] and Hsp90[256] acetylation. Alternatively, anti-angiogenic activity of HDACs has also been demonstrated[250]. Finally, HDACs are involved in the regulation of autophagy, a mechanism used by cells to discard damaged organelles, hijacked by cancer cells for drug efflux, promoting resistance to chemotherapy[212,213,258,259].

HDACs and the oncogene *MYC* have been shown to interact in normal and cancerous cells, providing a rationale for HDAC inhibitor use in MYC-addicted tumors. MYC recruits class I HDACs and thus induce transcriptional repression of genes regulating anti-tumorigenic cellular processes[110,260,261]. Additionally, MYC is a known non-histone target for deacetylation by HDACs, regulating MYC protein stability and thus, tumorigenesis[262]. Because of these implications, HDAC inhibitors have been widely researched alone and in combination for treatment of various MYC-driven cancers. The most clinically advanced HDAC inhibitors are discussed in section 1.3.3.

1.3.3. Therapeutic targeting

As outlined in the previous sections, HDACs make for interesting targets in cancer therapy. In fact, HDACs themselves were initially discovered as a potential target of a molecule inducing hyperacetylation of chromatin, cell cycle arrest and apoptosis in transformed cells[263]. Over decades of extensive research numerous HDAC inhibitors (HDACi) were discovered and used in pre-clinical and clinical studies (Table 3).

Table 3 Selected HDAC inhibitors and their clinical development description. *Depending on a report, some of the pan-HDACis also target HDAC11. AML: acute myeloid leukemia. NHL: non-Hodgkin's lymphoma.

Type	Drug	Target	Example Ref.	Clinical Stage	Indications	Clinical trial
Pan-HDACi	Vorinostat	Class I, II (IV*)	264-267	Approved	Cutaneous T-cell lymphoma	NCT00773747 NCT00128102 NCT00305773
				Phase II/III	Multiple myeloma, mesothelioma, AML	
	Panobinostat		268-271	Approved	Multiple myeloma	NCT01034163 NCT00777049 NCT00880269
				Phase II/III	Hodgkin's lymphoma, breast cancer, AML	
	Belinostat		272-275	Approved	Peripheral T-cell lymphoma	NCT00589290 NCT00357032 NCT00303953
				Phase I/II	AML, thymoma, NHL	
Class-selective HDACi	Entinostat	HDAC1 HDAC2 HDAC3	276-279	Phase II/III	Breast, colorectal cancer, Hodgkin's lymphoma	NCT02115282 NCT00866333 NCT01349959 NCT01105377
	Romidepsin		280-283	Approved	Cutaneous and peripheral T-cell lymphoma	NCT00112463 NCT00062075 NCT00085540
				Phase I/II	Soft tissue sarcoma, AML, high grade glioma	
	Bufexamac	Class IIB	284-286	Approved	Atopic eczema	NA
				Pre-clinical (as HDACi)	NA	
	Tubastatin A		212,287	Pre-clinical	NA	NA
Isoform-selective HDACi	Tubacin	HDAC6	288,289	Pre-clinical	NA	NA
	PCI-34051	HDAC8	290,291	Pre-clinical	NA	NA

In the beginning of the 2000s, due to HDAC upregulation across entities, HDACis were thought to be the ultimate weapon against a wide variety of cancers. Therefore, several pan-HDACis (targeting several classes of HDACs) were approved for clinical use. Today the success of

HDACis as monotherapeutics in the clinic seems questionable mainly due to global HDACi activity causing serious adverse effects, such as cardiac arrythmia, abnormal clotting or bone marrow depression[292]. Consequently, more and more isoform or class selective, so-called next generation HDACis are entering clinical trials with high hopes to increase the efficacy and to reduce the side effects (Table 3).

As mentioned before, the majority of HDACis are used in combination with drugs targeting other components of cellular processes important for tumorigenesis in various cancers, including MB[168], non-Hodgkin lymphoma[293], prostate cancer[294] and others. Importantly, a few years ago published studies have harnessed the genome-wide activity of HDACis to induce neo-antigens and use this for immunotherapy[295,296]. The focus of this thesis is on combining a selective HDAC inhibitor with a drug that potentially synergizes with it.

1.4. Polo-like kinases

Polo-like kinases (PLKs) are enzymes catalysing the phosphorylation of serine or threonine residues of regulated proteins. PLKs are well-known for their implications for cell cycle regulation, particularly mitotic entry, exit, spindle checkpoint and cytokinesis.

PLKs were first described in the last decades of the 20th century in *Drosophila melanogaster* mutants that had abnormal mitosis patterns[297,298]. Subsequently, PLKs were discovered in other organisms, including humans. Here, the most famous and well-studied PLK family member is PLK1, which, due to its' importance in cell cycle regulation, has been described as a potential target for anti-tumor therapy. In this section, cell cycle and PLK's regulatory functions will be described. In addition, protein structure and classification will be discussed, as well as PLKs' roles in tumorigenesis and efforts to target these proteins.

1.4.1. Cell cycle

The cell cycle is a sequence of events with a goal of producing two genetically identical daughter cells (i.e. the division of the mother cell). The mammalian cell cycle consists of two stages: the interphase and the mitotic phase (M-phase). Both are further subdivided into five cell cycle phases overall. The interphase has three phases termed G1 (G for "gap"), S and G2 (Figure 19). The M-phase is separated into mitosis and cytokinesis with the latter described as the last part of mitosis in some reports. Cells that are fully differentiated can stop their cycling and division by entering the G0 (or quiescent) phase. Here cells no longer grow or divide, although retaining their function

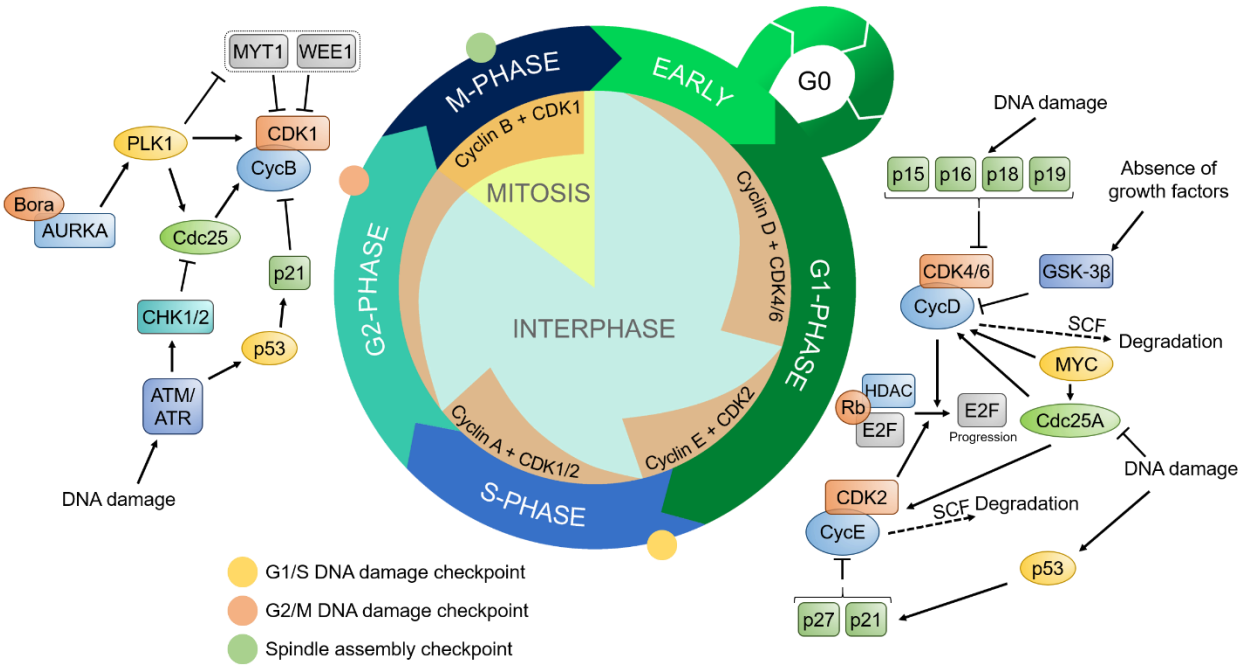

Figure 19 The schematic representation of the cell cycle with the key regulators of the restriction point/G1/S DNA damage checkpoint and G2/M DNA damage checkpoint. Cyc: cyclin. Information for the image: Nojima (2004)[22] and Cuddihy & O'Conell (2003)[300].

in the particular niche they occupy. The G0 phase is entered right after cytokinesis in an early G1 phase (Figure 19) and can be maintained indefinitely or for some time.

During the early **G1 phase**, cells make a commitment to start a cycle which will result in either cell division or apoptosis induction (if DNA damage is detected and self-monitoring mechanisms are intact). The main objective of the G1 phase is to accumulate biomass, check if the DNA is intact and prepare for DNA replication. The G1 phase is fuelled by external mitogenic signals inducing various signalling pathways in the cell. Generally, all these pathways lead to the transcription and translation of cyclin D (in humans there are 3 cyclins D, used depending on the context). Cyclin D binding to its' partner cyclin-dependent kinase (CDK) 4 or 6 activates the latter (Figure 19). Of note, all cyclin-CDK pairs are regulated by synthesis and degradation of the cyclin molecule, with unbound CDK being inactive. The cyclin D-CDK4/6 complex is activating the crossing of the restriction point (the point of commitment to enter the cell cycle) by phosphorylation of the Rb (retinoblastoma) protein, which, in turn, dissociates the repressor complex members from the E2F transcription factor. This induces transcription of a variety of genes, required for cell proliferation induction, cell growth and entering of the S phase. Cyclin E is expressed in the mid-late G1 phase, is mitogen-independent and binds CDK2. Both, cyclin D and E degradation can be induced by DNA damage and the p53 pathway through the CDK inhibitors p15, p16, p18, p19

(for the cyclin D-CDK4/6 complex) and p21 and p27 (for cyclin E-CDK2), which form the core responders for G1/S DNA damage checkpoint[22] (Figure 19). Of note, p16 is also well-known for its' role in induction of oncogene-induced senescence[299].

DNA replication occurs during the **S phase**. The pre-replication complexes are being assembled and positioned throughout G1, thus enabling DNA replication to start right after the G1/S checkpoint[300]. In addition to the double helix itself, many other building blocks of DNA need to be synthesized, thus in early S-phase before being degraded, cyclin E-CDK2 complex phosphorylates nuclear coactivator inducing the transcription of histones[301]. During mid-S phase cyclin A and CDK2 form a complex, which is active during the remaining S phase and early G2 phase, and assisting with the G2/M DNA damage point and mitosis entry.

The **G2 phase** takes place after DNA replication. During G2, cells increase their protein synthesis rate and grow rapidly to prepare for cell division, and microtubules start forming a spindle. Finally, the G2/M DNA damage checkpoint occurs allowing or restricting access to the mitotic phase. The G2/M DNA damage checkpoint is mainly regulated by the ATM/ATR/p53 protein axis (Figure 19). If DNA breaks are repaired or no DNA damage is detected, towards the end of G2 phase, the cyclin A-CDK2 complex phosphorylates Cdc25. PLK1 which is activated by AURKA-Bora phosphorylation also phosphorylates Cdc25. This activates Cdc25, which directly activates cyclin B-CDK1. Once cyclin B-CDK1 complex is active, cell enters the mitotic phase[302,303].

The **M (mitotic) phase** or mitosis is further divided into five sub-stages. These sub-stages are the prophase (condensation of chromatin to chromosomes, mitotic spindle formation and beginning of the breakdown of the nucleolus), prometaphase (attachment of microtubules to the kinetochores and nucleus breakdown), metaphase (centromere alignment on the metaphase plate), anaphase (movement of sister chromatids to the poles of the cell pulled by microtubules) and telophase with cytokinesis (reassembling of nuclear envelope and nucleolus, chromatin decondensation and disassembly of mitotic spindle with subsequent cytoplasmic division). During the prometaphase and metaphase, another checkpoint, namely spindle assembly checkpoint (SAC) takes place. SAC is responsible for halting the M phase if the kinetochores are not attached properly. If kinetochores are attached efficiently, Cdc20 activates the APC/C ubiquitin ligase complex, which in turn ubiquitinates cyclin B and securin. Destruction of cyclin B leads to the activation of mitotic exit network signalling. Proteolysis of securin releases separase, a protease cleaving cohesin, releasing the sister chromatids and allowing the anaphase entry[304].

1.4.2. Structure, function and classification

As mentioned previously PLKs are serine/threonine kinases with predominant function as cell cycle regulators. Structurally, PLKs are characterized by two conserved elements, N-terminal catalytic kinase domain and C-terminal regulatory polo-box domain. In humans, polo-like kinase family has five members, PLK1 through PLK5 (Figure 20).

The serine/threonine kinase domain is the most conserved part of the protein; however, it is active only in 4 members of PLK family, PLK1, 2, 3 and 4[11,305]. The catalytic kinase domain activity is regulated by phosphorylation of the T-loop. PLK1 function is regulated by the phosphorylation of threonine-210 (T210) by Aurora A kinase co-factor Bora (Figure 20)). Approximately a decade ago, a fifth member of the family, PLK5 was discovered[306]. The sequence of PLK5 was found disrupted by a stop codon at exon 6 with an open reading frame producing a truncated form of protein downstream. PLK5 is predicted to be catalytically inactive, nonetheless, it was described as a stress-induced protein involved in apoptosis, highly expressed in neurons and glia and downregulated in tumors[307].

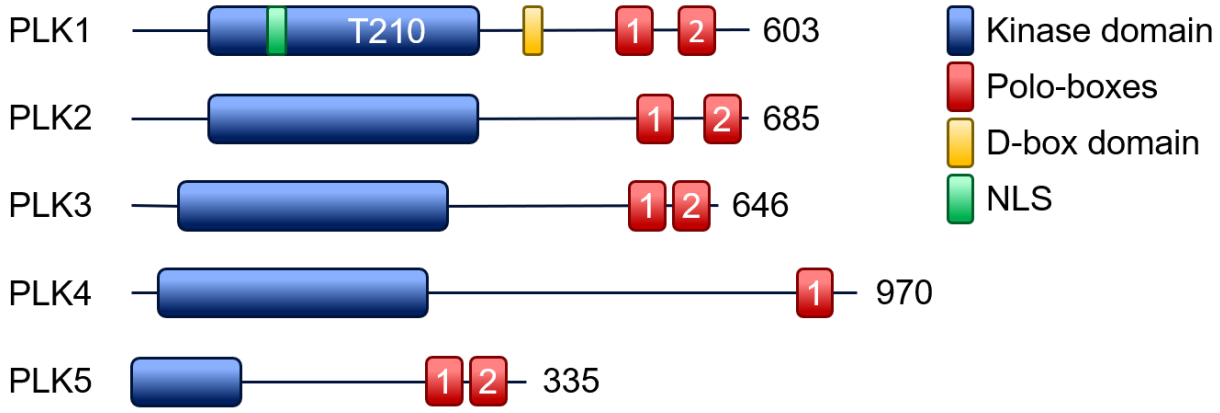

Figure 20 Summary of structural features of polo-like kinase family with amino acid sequence length shown. NLS: nuclear localization sequence. Adapted from Liu (2015)[11].

All PLKs have 2 polo-box domains, except for PLK4 with one polo-box. As mentioned previously, C-terminal polo-boxes act in a regulatory fashion and are less evolutionary conserved with approximately 70 amino acid core component shared among all family proteins[305]. The polo-box domain is a phosphopeptide-binding motif, suggesting a need of priming phosphorylation for PLK proteins to bind. Polo-boxes form a pocket for a primed target protein guiding the kinase domain[308,309]. Having only one polo-box motif, PLK4 needs an alternative mechanism, thus polo-box motif of PLK4 has been demonstrated to contribute to forming homodimers of the protein[310,311]. D-box motif (as shown for PLK1 in Figure 20) is essential for recognition by APC/C ubiquitin ligase and degradation in the mitotic exit[312].

Even though all catalytically active PLK family members are in some way associated to the cell cycle regulation, each of them has comparatively diverse and to some extent specific functions. PLK1 is the best studied PLK, which plays a key role in cell cycle regulation. As PLK1 is one of the main regulators of mitotic entry and spindle formation, the deficiency of PLK1 is embryonically lethal[313]. Mice embryos with deficient PLK1 exhibited abnormalities in mitotic spindle formation and developmental delays, which also points to the importance of PLK1 for cell cycle processes. As shown before (Figure 19), PLK1 phosphorylates Cdc25 that regulates the activation of cyclin B-CDK1 complex required for mitotic entry[314]. In addition, PLK1 is a negative regulator of MYT1 and WEE1 kinases inhibiting cyclin B complex[315,316]. This suggests a pivotal role of PLK1 in G2/M DNA damage checkpoint.

At the mitotic entry during the prophase one of the essential processes is the breakdown of the nuclear envelope. Here the most important part is carried out by microtubules and motor proteins. PLK1 has been shown to regulate one of the components of the dynein complex, $p150^{Glued}$, which when activated accumulates at the nuclear envelope[317] (Figure 21). During the prophase/prometaphase, PLK1 is recruited to the kinetochores[318] where it phosphorylates CLIP-170, directly promoting microtubule-kinetochore attachment[319]. Additionally, microtubule binding sites and correct attachment to kinetochore is regulated by another PLK1 target, Sgt1[320].

SAC, subsequent sister chromatid separation and cytokinesis are key features of late mitosis. Here also PLK1 has been shown to be involved, particularly in activation of ubiquitin ligase APC/C, which marks securin for destruction thus promoting chromatid separation[321]. Moreover, PLK1 negatively regulates Emi1, which represses the APC/C[322]. Finally, PLK1 localizes the central spindle[323] and facilitates the assembly of cleavage furrow formation complex[324]. PLK1 ubiquitination by APC/C complex and subsequent degradation is necessary for correct mitotic exit[312]. Further PLK1 functions and regulation of the protein have been reviewed by many including Liu (2015)[11], Lowery et al (2005)[305], van Vugt & Medema (2005)[325] and so on.

The functions of other members of PLK family are far less clear. PLK4 is the most similar to PLK1 functionally and the only PLK family member apart from PLK1 to be expressed only in dividing cells. Its' deficiency is embryonically lethal[326]. In addition, PLK4 was demonstrated to be involved in centriole duplication[327] and mitotic exit[326]. PLK2 and PLK3 are structurally similar to each other with their loss having no effect on PLK2/3 deficient animal viability[328,329]. PLK2 has been

demonstrated to assist PLK4 with centriole duplication in humans[330]. PLK3 was shown necessary during the G1/S transition activating the Cdc25[331] and supporting the DNA replication[332].

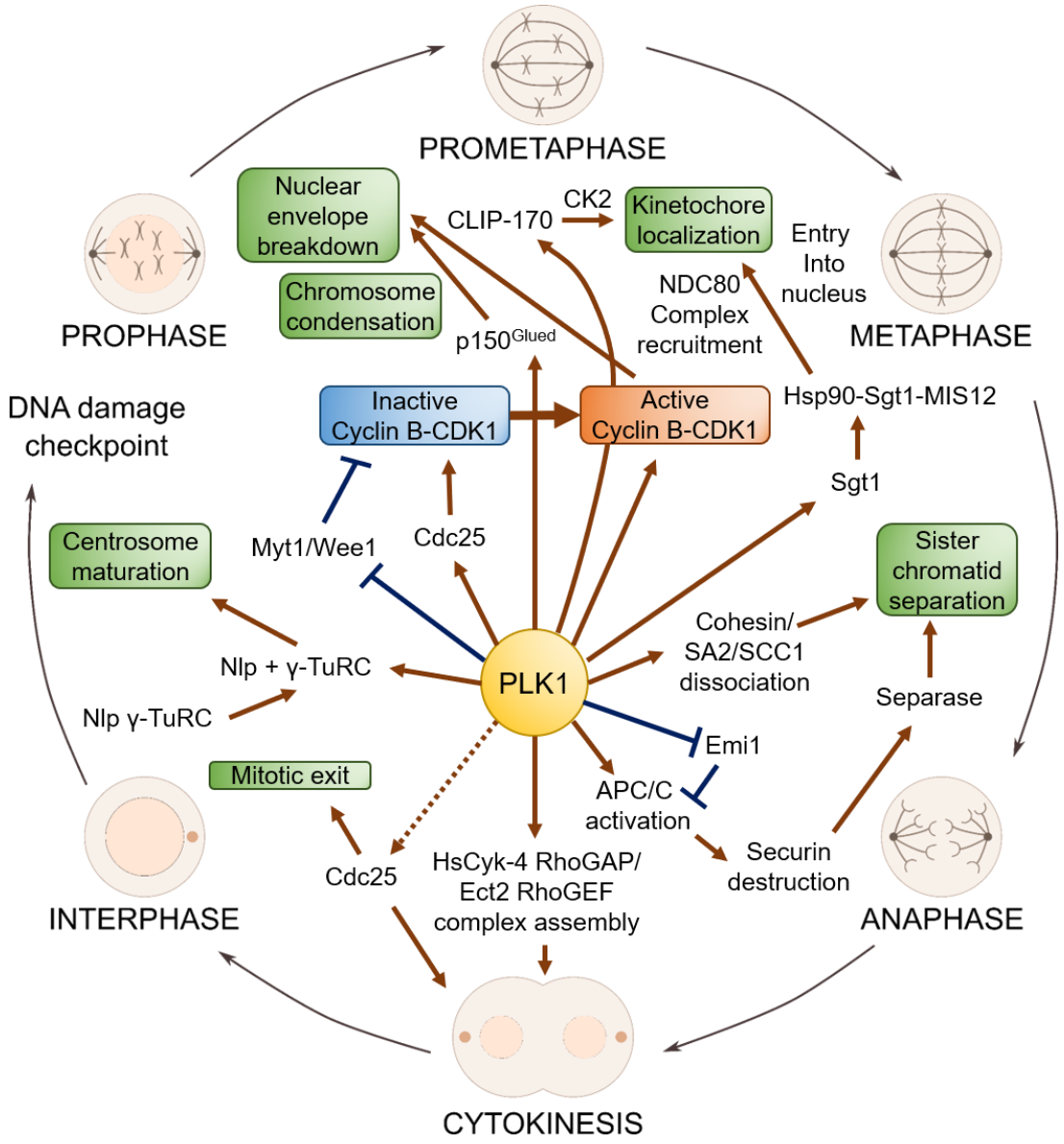

Figure 21 Summary of some of the PLK1 functions in the cell cycle regulation emphasizing mitotic phase. Image adapted from Liu (2015)[11].

1.4.3. Implications for tumorigenesis

As all PLK family members have an activity associated with cell cycle or cell differentiation, it is no surprise that their implications for tumor development have been well-studied. Interestingly, PLKs have been demonstrated to have two distinct and opposite roles depending on the entity and the driver of the tumor.

Classically, PLK1 and PLK4 are often upregulated in many different entities, including glioma, breast, prostate cancer, melanoma, lung cancer (PLK1, reviewed by Eckerdt et al (2005)[311] and Liu et al (2017)[333]) and colon and breast cancer (PLK4)[334]. Also, PLK1 overexpression is associated with aggressive tumors and poor prognosis in many entities (reviewed by Strebhardt (2010)[335]). Thus, these PLKs assume the role of the oncogenes.

Due to the diverse functions of PLK1, upregulation of its' expression potentially leads to the cell bypassing a G2/M DNA damage checkpoint[336,337] and abnormally entering the mitotic phase. Highly expressed PLK1 could also induce mistakes in centrosome duplication and aneuploidy[338,339]. In addition, PLK1 has been shown to induce the stabilization of MYC either by phosphorylating the transcription factor itself[340] or by targeting the FBXW7 ubiquitin ligase for degradation[184]. Interestingly, recently a concept of PLK1 as a tumor suppressor was suggested (reviewed by de Carcer (2019)[341]). It appears that in certain types of cancers PLK1 overexpression can be also associated with better prognosis and tumor regression (e.g. APC truncated colorectal cancer[342] or estrogen receptor (ER) negative/Her2 positive breast cancer[343]). Therefore, even though anti-PLK1 therapy has a lot of potential (as discussed in the section 1.4.4.), predictive biomarkers are essential for successful PLK1 inhibitor treatment development.

The expression of PLK2, 3 and 5 is reduced in various tumors, such as hematologic malignancies and ovarian cancer (PLK2)[344,345], lung and head and neck cancers (PLK3)[346,347], astrocytoma and glioblastoma (PLK5)[307]. Therefore, these members of the family are regarded to be tumor suppressors.

PLKs are furthermore involved in tumorigenesis by their crosstalk with the tumor suppressor p53[333]. The activity of PLK2 and PLK3 is induced by functional p53 in response to the DNA damage and other stresses[348,349]. On the other hand, it appears, that, when genotoxic stress is present, overexpressed PLK1 negatively regulates p53 protein stability and localization in the nucleus[350,351], leading to cell proliferation and in turn tumorigenesis. Additionally, PLK1 inhibition effect leading to programmed cell death was shown to be conducted via the p53 pathway[352,353]. PLK4 overexpression and epigenetic deregulation in the presence of genotoxic stress and hypoxia has been reported preferentially in p53-deficient cells[354].

Taken together, this data suggests a great therapeutic potential of PLK1 and PLK4 as targets in anti-cancer therapy, as discussed in the next section.

1.4.4. Therapeutic targeting

Due to their function as oncogenes and central role in cell cycle regulation and tumorigenesis a variety of PLK1 and PLK4 inhibitors have been developed for potential clinical use (Table 4). However, no PLK inhibitor has been approved for clinical use despite multiple phase III trials and volasertib being awarded a “breakthrough therapy” designation by the FDA in 2013. As in the case of HDACi, PLK inhibitors are now mainly tested in combinations with other agents striving to find synergistically acting combinations. Moderate success in clinics could be attributed to the dose limiting toxicities, limited efficacy[335,355] (both of which could be overcome by combinatorial therapy) or low intra-tumoral concentration of the drug in the patient[356].

Table 4 Summary of selected PLK1 and PLK4 inhibitors. AML: acute myeloid leukemia. MDS: myelodysplastic syndromes. *Rigosertib is PLK1 and PI3K inhibitor.

Target	Mode of Action	Drug	Example Ref.	Clinical Stage	Indications	Clinical Trials
PLK1	ATP-competitive	BI2536	357-360	Phase II	Solid tumors	NCT00526149
		Volasertib	361-364	Phase III	Solid tumors, AML, MDS	NCT01662505 NCT00969761 NCT01206816
		Onvansertib	365,366	Phase II	Solid tumors	NCT01014429
		GSK461364	367-369	Phase I	NHL	NCT00536835
		TAK-960	370,371	Phase I	Solid tumors	NCT01179399
		MLN0905	372,373	Pre-clinical	NA	NA
		Ro3280	374	Pre-clinical	NA	NA
	ATP-non-competitive	Rigosertib*	375,376	Phase III	Solid tumors, MDS	NCT01168011 NCT01241500
		HMN-176	377	Phase I	Solid tumors	378,379
		SBE 13 HCl	380,381	Pre-clinical	NA	NA
		Poloxin	382	Pre-clinical	NA	NA
PLK4	ATP-competitive	CFI-400945	383,384	Phase I/II	AML, MDS, prostate, breast cancer	NCT03187288 NCT03624543 NCT03385655
		YLT-11	385	Pre-clinical	NA	NA
	ATP-non-competitive	Centrinone	386,387	Pre-clinical	NA	NA

Generally, PLK inhibitors can be divided into two classes based on their mechanism of action, ATP-competitive and non-ATP-competitive (Table 4). ATP-competitive inhibitors target ATP-

binding groove in the catalytic kinase domain. Since the catalytic domain is the most conserved sequence in the PLK family, these inhibitors generally show problems with iso-enzyme selectivity and could potentially target other structurally related kinases. Currently many researchers develop non-ATP-competitive inhibitors binding polo-boxes (e.g. poloxin). This could provide necessary selectivity and eliminate the potential off-target effects. However, the only PLK1 inhibitors with non-ATP-competitive mode of action in clinical trials so far are rigosertib (affecting microtubule dynamics) and HMN-176/HMN-214 (interfering with the subcellular localization of the kinase)[335]. The latter was tested only in phase I in the beginning of the 2000s without further development[378].

1.5. Combination therapy

Drug interaction has been a highly discussed topic for the last century. Therefore, many models based of different definitions of dose-effect relationships have been developed. Drug interaction can be defined as synergistic (superadditive), additive and antagonistic. In a simplified manner, if two drugs are interacting synergistically, the same effect is reached with lower doses than expected (i.e. when single drug effects of those doses are added), thus reducing the potential of side effects in patients. When two drugs are interacting in an additive fashion, the combination effect equals the added effect (of note, this definition is an oversimplification; additivity can be explained using fractional product method developed by Chou & Talalay (1984)[388]). Antagonistic interaction points to two drugs reducing each other's effect. The quantitative determinant for assessing whether two drugs interact synergistically, additively or antagonistically is combination index (CI) calculated depending on the interaction model used.

The most commonly used model to determine drug interaction is Loewe's additivity model[389,390], graphically displayed in isobolograms[391]. Loewe's additivity is a dose-effect based strategy where additive effect of two drugs depends on the individual dose-response curves. This assumption leads to the calculation of combination index: $CI = \frac{a}{A} + \frac{b}{B}$ [388,392].The CI of additive relationship equals 1, thus underscoring the previously mentioned baseline for Loewe's theory. Graphically, the drug relationship is reflected by determining the concentrations of both drugs as single agents needed to achieve a certain effect (e.g. ED50, ED75 or ED90 as in Figure 22) and connecting them by a straight line (line of additivity). The concentrations needed to achieve the same effect

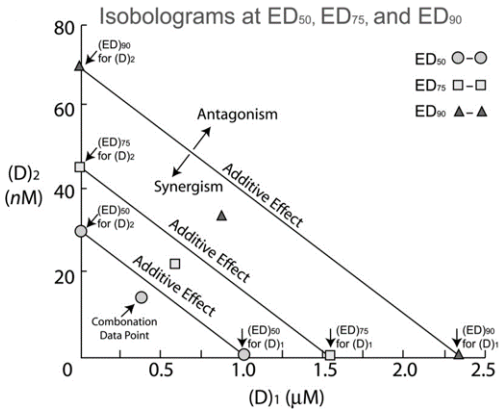

Figure 22 Isobolograms at ED50, ED75 and ED90 for drug A with concentration $(D)_1$ and drug B with concentration $(D)_2$. Image adapted from Chou (2006)[390].

when two drugs are combined are determined, which provides the coordinates for a combination data point (Figure 22). If the combination data point is below the line of additivity then drugs are interacting synergistically (CI < 1) and vice versa, when the data point is above the line, the drugs interact antagonistically (CI > 1). One of the most important limitations of the Loewe's additivity model is the fact that it relies on accurately estimated dose-response relationship which might be an issue in some biological assays[393,394].

Another model often used is the Bliss independence model[395]. It is an effect-based strategy assuming that drugs act independently of each other towards a common goal[393]. Following the Bliss model, observed combination effect is compared to the expected effect given the interaction is additive. The Bliss independence additivity score is calculated based on the single drug effects (E_A and E_B) and the effect of the combination treatment (E_{AB}): $E_A + E_B - E_A \times E_B$. If the effect of the combination of the drugs is larger than Bliss additivity score, the drugs interact synergistically. CI is calculated dividing the score by E_{AB}. The main limitation of Bliss model is the prerequisite for the drugs to act in an independent manner which is rather impossible in biological systems. Also, Bliss independence is calculated based on assumption that the dose-response relationship of the tested drugs is exponential. Finally, the effects that can be used in the Bliss model should be between 0 and 1[393]. Further limitations of both, Loewe's additivity and Bliss independence models have been discussed in detail by Goldoni & Johansson (2007)[396].

2. Aim

In this study we explore the combinatorial treatment options for patients with medulloblastoma (MB) and potentially other entities addicted to *MYC* or *MYCN* amplification. As mentioned above, *MYC*-amplified MB carries a dismal prognosis with surviving patients exhibiting long-term sequelae. This suggests a great need for targeted therapy.

The first component of the proposed combination therapy is entinostat, a class I selective HDAC inhibitor. Since HDAC inhibitors have frequently shown adverse effects upon treatment and limited efficacy, the combination with another drug could potentially improve the aforementioned limitations. Therefore, the goal of this study was to establish a clinically relevant combination therapy against MYC-driven medulloblastoma. In order to achieve this goal, four aims were set.

We first aimed to discover a target for a second component of the combination therapy. It was previously shown that HDAC2 and MYC reside in the same protein complex regulating transcription (Ecker, Thatikonda, et al, in revision). Therefore, in order to target one of the complex members, it was vital to determine the composition of the HDAC2-MYC protein complex.

Alternatively, we planned to examine the possibilities of indirectly targeting MYC in a protein complex-independent manner by discovering the target based on the transcriptional changes after entinostat treatment.

Secondly, we aimed to evaluate the potential of entinostat and the inhibitor determined in the first part of the project (i.e. PLK1 inhibitor) as monotherapeutics. Even though entinostat and PLK1is were previously evaluated in *MYC*-amplified background[184,226], the comprehensive analysis of response of MB cells to PLK1is has not been published.

The third aim was to examine whether the interaction between entinostat and PLK1i was synergistic. HDAC and PLK1 inhibitors have been shown to interact synergistically[293,397]. However, the role of *MYC*-amplification in the combination treatment is not known. Moreover, HDAC and PLK1 inhibitor combination and its' potential in clinical development has not been described in MB.

Finally, we aimed to analyze the interaction mechanism of entinostat and PLK1i as the mediators of HDAC and PLK1 inhibitor interaction are unknown.

3. Materials and methods

3.1. Materials

3.1.1. Cell lines and tissue culture

Table 5 Cell lines.

Cell line	Type	Origin	Supplier
MED8A	Adherent	Medulloblastoma, group 3, *MYC*-amplified	R. Gilbertson, St. Jude, Memphis, TN, USA
HD-MB03	Semi-adherent	Medulloblastoma, group 3, *MYC*-amplified	Developed in the CCU Pediatric Oncology, DKFZ, Heidelberg, Germany[398]
D458-Med	Semi-adherent	Medulloblastoma, group 3, *MYC*-amplified	Darell D. Bigner, Duke University, Durham, NC, USA
UW228-2	Adherent	Medulloblastoma, SHH	John R. Silber, University of Washington, Seattle, WA, USA
UW228-2-pMYC	Adherent	Medulloblastoma, SHH, DOX-inducible *MYC*	Parental cell line: John R. Silber, University of Washington, Seattle, WA, USA; inducible system: Developed in the CCU Pediatric Oncology, DKFZ, Heidelberg, Germany (Ecker, Thatikonda, et al, in revision)
ONS-76	Adherent	Meduloblastoma, SHH	Institute of Fermentation, Osaka, Japan
ONS-76-pMYC	Adherent	Medulloblastoma, SHH, DOX-inducible *MYC*	Parental cell line: Institute of Fermentation, Osaka, Japan; inducible system: Developed in the CCU Pediatric Oncology, DKFZ, Heidelberg, Germany (Ecker, Thatikonda, et al, in revision)
SK-N-BE(2)-C	Adherent	Neuroblastoma, *MYCN*-amplified	ECACC, Salisbury, UK
IMR-32	Adherent	Neuroblastoma, *MYCN*-amplified	DSMZ, Darmstadt, Germany
SK-N-AS	Adherent	Neuroblastoma	M. Schwab, DKFZ, Heidelberg, Germany
SH-SY5Y	Adherent	Neuroblastoma	DSMZ, Darmstadt, Germany
SK-N-FI	Adherent	Neuroblastoma	ATCC, Masassas, VA, USA
HSJD-GBM-001	Spheroids	Glioblastoma, *MYC*-amplified	A. M. Carcaboso, SJD, Barcelona, Spain
HSJD-DIPG-007	Spheroids	Diffuse Intrinsic Pontine Glioma, *MYC*-amplified	A. M. Carcaboso, SJD, Barcelona, Spain
SU-pcGBM2	Spheroids	Glioblastoma	M. Monje, Stanford University, Stanford, CA, USA
SU-DIPG-XXV	Spheroids	Diffuse Intrinsic Pontine Glioma, *MYC*-amplified	M. Monje, Stanford University, Stanford, CA, USA

SU-DIPG-XVII	Spheroids	Diffuse Intrinsic Pontine Glioma, *MYC*-amplified	M. Monje, Stanford University, Stanford, CA, USA
SU-DIPG-XIII	Spheroids	Diffuse Intrinsic Pontine Glioma, *MYCN*-amplified	M. Monje, Stanford University, Stanford, CA, USA

Table 6 Tissue culture media.

Medium		Additives	Cell lines
Dulbecco's Modified Eagle's Medium (DMEM)		10 % FCS	MED8A, UW228-2, ONS-76, SK-N-BE(2)-C, IMR-32, SK-N-AS, SH-SY5Y
Dulbecco's Modified Eagle's Medium (DMEM) supplemented with doxycycline		10 % FCS, 1 µg/mL doxycycline	UW228-2-pMYC, ONS-76-pMYC
RPMI 1640		10 % FCS	HD-MB03, SK-N-FI
Improved Minimum Essential Medium (IMEM)		10 % FCS	D458-Med
Tumor Stem Medium (TSM) Base	1:1 Neurobasal-A Medium and DMEM/F-12	10 mM HEPES, 1 mM sodium pyruvate, 1X MEM non-essential amino acids, 1X GlutaMax	-
TSM	TSM Base	2 % B-27, 2 µg/mL heparin, 20 ng/mL EGF, 20 ng/mL bFGF, 10 ng/mL PDGF-AA.	HSJD-GBM-001, HSJD-DIPG-007, SU-pcGBM2, SU-DIPG-XXV, SU-DIPG-XVII, SU-DIPG-XIII

Table 7 Tissue culture reagents.

Article	Cat. no.	Supplier
0.05 % Trypsin-EDTA	25300054	ThermoFisher Scientific, Waltham, MA, USA
Accumax Cell Aggregate Dissociation Medium	00-4666-56	ThermoFisher Scientific, Waltham, MA, USA
B-27 Supplement (50X)	17504044	ThermoFisher Scientific, Waltham, MA, USA
Deoxyribonuclease I	LS002007	ThermoFisher Scientific, Waltham, MA, USA
DMEM	41965039	ThermoFisher Scientific, Waltham, MA, USA
DMEM	BE12-604F/U1	LONZA, Basel, Switzerland
DMEM/F-12	11320074	ThermoFisher Scientific, Waltham, MA, USA
DMSO, cell culture grade	M6323.0100	Genaxxon bioscience, Ulm, Germany
Doxycycline	sc-337691	Santa Cruz, Dallas, TX, USA
FCS	F7524	Sigma-Aldrich, St. Louis, MO, USA
GlutaMax-I Supplement (100X)	35050038	ThermoFisher Scientific, Waltham, MA, USA
Heparin Solution (0.2 %)	H3149-10KU	Sigma Aldrich, St. Louis, MO, USA

HEPES Buffer Solution (1 M)	15630049	ThermoFisher Scientific, Waltham, MA, USA
H-PDGF-AA (10 µg/mL)	100-13A	Peprotech, Rocky, Hill, NJ, USA
IMEM	A1048801	ThermoFisher Scientific, Waltham, MA, USA
MEM non-essential amino acids 10 mM (100X)	11140035	ThermoFisher Scientific, Waltham, MA, USA
$MgCl_2$ (1 M)	AM9630G	ThermoFisher Scientific, Waltham, MA, USA
Neurobasal-A Medium	1088802	ThermoFisher Scientific, Waltham, MA, USA
PBS	D8537	Sigma-Aldrich, St. Louis, MO, USA
Recombinant human basic FGF (20 µg/mL)	AF-100-18B	Peprotech, Rocky Hill, NJ, USA
Recombinant human EGF (20 µg/mL)	AF-100-15	Peprotech, Rocky Hill, NJ, USA
RPMI 1640	21875034	ThermoFisher Scientific, Waltham, MA, USA
Sodium pyruvate (100 mM)	11360039	ThermoFisher Scientific, Waltham, MA, USA
Synth-a-Freeze Cryopreservation Medium	A1254201	ThermoFisher Scientific, Waltham, MA, USA
TrypLE Express Enzyme (1X)	12604013	ThermoFisher Scientific, Waltham, MA, USA
Trypsin-EDTA Solution (1X)	T3924-100ML	Sigma-Aldrich, St. Louis, MO, USA
Vi-Cell XR Cell Viability Analyzer™ solutions	B94987	Beckmann Coulter, Krefeld, Germany

3.1.2. Treatment reagents and drugs

Table 8 Reagents and drugs used for treatment.

Compound	Stock concentration	Solvent	Storage	Cat. no.	Supplier
Cycloheximide	100 mg/mL	DMSO	-20°C	sc-3508	Santa Cruz, Dallas, TX, USA
Entinostat (MS-275)	10 mM	DMSO	-20°C	S1053	BIOZOL, Eching, Germany
GSK461364	10 mM	DMSO	-20°C	S2193	BIOZOL, Eching, Germany
MG-132	100 mM	DMSO	-20°C	LKT-M2400.5	Biomol, Hamburg, Germany
Onvansertib (NMS-P937)	10 mM	DMSO	-80°C	T6247-1ml-TM	BioCat, Heidelberg, Germany
Rigosertib (ON-01910)	10 mM	DMSO	-20°C	S1362	BIOZOL, Eching, Germany
Thymidine	20 mM	H_2O	4°C	T9250-5G	Sigma-Aldrich, St. Louis, MO, USA

Volasertib (BI6727)	10 mM	DMSO	-80°C	S2235	BIOZOL, Eching, Germany

3.1.3. Bacteria

Table 9 Antibiotics used for bacterial selection.

Article	Dilution	Cat. no.	Supplier
Ampicillin sodium salt dissolved in sterile H_2O (100 mg/mL)	1:1000	sc-202951	Santa Cruz, Dallas, TX, USA

3.1.4. Primers

Table 10 Primers used for qRT-PCR assay.

Target	Product	Cat. no.	Supplier
ACTB	Hs_ACTB_2_SG QuantiTect Primer Assay	QT01680476	Qiagen, Hilden, Germany
GAPDH	Hs_GAPDH_2_SG QuantiTect Primer Assay	QT01192646	Qiagen, Hilden, Germany
MYC	Hs_MYC_1_SG QuantiTect Primer Assay	QT00035406	Qiagen, Hilden, Germany
MYCN	Hs_MYCN_1_SG QuantiTect Primer Assay	QT00201404	Qiagen, Hilden, Germany
PLK1	Hs_PLK1_1_SG QuantiTect Primer Assay	QT00049749	Qiagen, Hilden, Germany

3.1.5. Antibodies

Table 11 Primary antibodies used for western blotting.

Target	Host, type	Dilution	Cat. no.	Supplier
ac-H3 (K27)	Rabbit, polyclonal	1:1000	ab4729	Abcam, Cambridge, UK
ACTB	Mouse, monoclonal	1:10 000	A5441	Sigma-Aldrich, St. Louis, MO, USA
FBXW7	Rabbit, polyclonal	1:1000	ab109617	Abcam, Cambridge, UK
GAPDH	Mouse, monoclonal	1:10 000	MAB374	Merck, Darmstadt, Germany
H3	Rabbit, monoclonal	1:5000	4499S	Cell Signaling, Danvers, MA, USA
HDAC2	Mouse, monoclonal	1:1000	sc-81599	Santa Cruz, Dallas, TX, USA
MYC	Rabbit, monoclonal	1:10 000	ab32072	Abcam, Cambridge, UK
MYCN	Mouse, monoclonal	1:5000	sc-53993	Santa Cruz, Dallas, TX, USA

PARP1	Rabbit, monoclonal	1:5000	9532S	Cell Signaling, Danvers, MA, USA
p-FBXW7 (S176)	Rabbit	1:350	-	I. Hoffmann, DKFZ, Heidelberg, Germany
PLK1	Mouse, monoclonal	1:5000	ab17056	Abcam, Cambridge, UK
p-PLK1 (T210)	Rabbit, polyclonal	1:1000	5472S	Cell Signaling, Danvers, MA, USA
p-TCTP (S46)	Rabbit, polyclonal	1:1000	5251S	Cell Signaling, Danvers, MA, USA
TCTP	Rabbit, monoclonal	1:5000	ab133568	Abcam, Cambridge, UK

Table 12 Secondary antibodies used for western blotting.

Target species	Host, type	Conjugate	Dilution	Cat. no.	Supplier
Rabbit	Donkey, polyclonal	Horseradish peroxidase	1:5000	V795A	Promega, Madison, WI, USA
Mouse	Goat, polyclonal	Horseradish peroxidase	1:10 000	115-035-003	Dianova, Hamburg, Germany

Table 13 Antibodies used for immunoprecipitation.

Target	Host, type	Dilution	Cat. no.	Supplier
HDAC2	Mouse, monoclonal	1:40	sc-81599	Santa Cruz, Dallas, TX, USA
Normal IgG	Rabbit, polyclonal	1:400	2729S	Cell Signaling, Danvers, MA, USA
Normal IgG	Mouse	1:400	sc-2025	Santa Cruz, Dallas, TX, USA
MYC	Rabbit, monoclonal	1:40	ab32072	Abcam, Cambridge, UK

3.1.6. Plasmids

Table 14 Plasmids.

Article	Cat. no.	Supplier
pGIPZ non-silencing control	RHS4347	Horizon, Waterbeach, UK
pGIPZ PLK1 shRNA glycerol set	#1: RHS4430-200181617, clone ID: V2LHS_19709 #2: RHS4430-200201483, clone ID: V2LHS_241437 #3: RHS4430-200212626, clone ID: V2LHS_262328	Horizon, Waterbeach, UK

3.1.7. Restriction analysis

Table 15 Reagents for restriction analysis.

Article	Cat. no.	Supplier
Fast Digest SalI restriction enzyme	FD0644	ThermoFisher Scientific, Waltham, MA, USA
10X FastDigest Green Buffer	B72	ThermoFisher Scientific, Waltham, MA, USA

3.1.8. Biochemical reagents

Table 16 Biochemical reagents.

Article	Cat. no.	Supplier
Acetic acid	6755.1	Carl Roth, Karlsruhe, Germany
Acrylamide/Bis solution (40 % w/v)	10681.01	SERVA, Heidelberg, Germany
Agar	S210.3	Carl Roth, Karlsruhe, Germany
Agarose, low gelling temperature	A9414	Sigma-Aldrich, St. Louis, MO, USA
Albumin Standard (2 mg/mL)	23209	ThermoFisher Scientific, Waltham, MA, USA
APS	A3678	Sigma-Aldrich, St. Louis, MO, USA
Brilliant Blue G	27815	Sigma-Aldrich, St. Louis, MO, USA
Bromophenol Blue	A23331.0005	AppliChem, Darmstadt, Germany
BSA	A4612	Sigma-Aldrich, St. Louis, MO, USA
Citric acid	33114-1KG	Sigma-Aldrich, St. Louis, MO, USA
cOmplete™, Mini	11836153001	Sigma-Aldrich, St. Louis, MO, USA
DMP	D8388-250MG	Sigma-Aldrich, St. Louis, MO, USA
DTT	A1101	AppliChem, Darmstadt, Germany
ECL Primer Amersham	RPN2232	GE Healthcare Dharmacon, Lafayette, CO, USA
EDTA	1034	GERBU Biotechnik GmbH, Heidelberg, Germany
Ethanol, absolute	20821.321	VWR chemicals, Radnor, PA, USA
GelRed®	M3199.0500	Genaxxon bioscience, Ulm, Germany
Glycerol	15523	Honeywell Riedel-de-Haën, Seelze, Germany
Glycine	33226	Sigma-Aldrich, St. Louis, MO, USA
HCl	13-1683	Sigma-Aldrich, St. Louis, MO, USA
HEPES	9105.2	Carl Roth, Karlsruhe, Germany
Isopropanol	20842.330	VWR chemicals, Radnor, PA, USA
KCl	6781.1	Carl Roth, Karlsruhe, Germany
MassRuler DNA Ladder Mix, Ready-to-use	SMO403	ThermoFisher Scientific, Waltham, MA, USA
Methanol	M/4000/PC17	ThermoFisher Scientific, Waltham, MA, USA
Milk powder	T145.2	Carl Roth, Karlsruhe, Germany
Na_2HPO_4	28029.292	WR chemicals, Radnor, PA, USA

NaCl	BP358-1	ThermoFisher Scientific, Waltham, MA, USA
NaOH	30620	Sigma-Aldrich, St. Louis, MO, USA
Normal goat serum	5-000-121	Dianova, Hamburg, Germany
Peptone	8986	Carl Roth, Karlsruhe, Germany
PhosSTOP	49068450001	Sigma-Aldrich, St. Louis, MO, USA
Polyethylenimine (PEI)	23966-1	Polysciences Europe, Hirschberg an der Bergstrasse
Ponceau S solution	A2935.0500	AppliChem, Darmstadt, Germany
Precision Plus Protein™ Kaleidoscope™ prestained protein standard	1610375	Bio-Rad, Hercules, CA, USA
Propidium iodide	A2261.0025	WR chemicals, Radnor, PA, USA
Ribonuclease A	R6513-10MG	Sigma-Aldrich, St. Louis, MO, USA
RNaseZAP™	R2020-250ML	Sigma-Aldrich, St. Louis, MO, USA
SDS pellets	2326.1	Carl Roth, Karlsruhe, Germany
Sucrose	4621.1	Carl Roth, Karlsruhe, Germany
SYBR™ Green Platinum™ qPCR SuperMix-UDG	11733046	ThermoFisher Scientific, Waltham, MA, USA
TEMED	2367.3	Th. Geyer, Renningen, Germany
Triethanolamine	90279-100ML	Sigma-Aldrich, St. Louis, MO, USA
Tri-Sodium citrate dihydrate	27833.294	VWR chemicals, Radnor, PA, USA
Triton-X 100	A4975.0500	AppliChem, Darmstadt, Germany
Triton-X 100	A4975.0500	AppliChem, Darmstadt, Germany
Trizma Base	T1503	Sigma-Aldrich, St. Louis, MO, USA
Tween 20	500-018-3	MP Biomedicals, Santa Ana, CA, USA
Yeast extract	70161	Sigma-Aldrich, St. Louis, MO, USA
β-mercaptoethanol	39563	SERVA, Heidelberg, Germany

3.1.9. Buffers and solutions

Table 17 Recipes for used buffers and solutions.

Solution (storage)	Ingredients	Amount/volume	Final conc.
Agar solution (4 °C)	Agar	15 g	1.5 %
	LB medium	1 L	-
Antibody dilution buffer (4 °C)	Milk powder	4 g	2 %
	TBS-T	200 mL	-
APS (-20 °C)	APS	5 g	10 %
	De-ionized H_2O	50 mL	-
Blocking milk (-20 °C)	Milk powder	200 g	20 %
	BSA	30 g	3 %
	Normal goat serum (dissolved in sterile H_2O)	10 mL	1 %
	Tween 20	2 mL	0.2 %

	FCS (not inactivated)	200 mL	20 %
	PBS	Fill-up to 1 L	-
BSA antibody dilution buffer (-20 °C)	BSA	10 g	5 %
	TBS-T 0.1 %	200 mL	-
$CaCl_2$, sterile-filtered (-20 °C)	$CaCl_2$	27.7 g	2.5 M
	De-ionized H_2O	100 mL	-
Cell fractionation buffer (4 °C)	HEPES	238 mg	10 mM
	KCl	75 mg	10 mM
	$MgCl_2$	14.3 mg	1.5 mM
	Sucrose	11.6 g	0.34 M
	100 % glycerol	10 mL	10 %
	DTT 1 M	100 µL	1 mM
	cOmplete™, Mini	1 tablet/10 mL	-
	De-ionized H_2O	Fill-up to 100 mL	-
Cell fractionation buffer with Triton X-100 (4 °C)	HEPES	238 mg	10 mM
	KCl	75 mg	10 mM
	$MgCl_2$	14.3 mg	1.5 mM
	Sucrose	11.6 g	0.34 M
	100 % glycerol	10 mL	10 %
	DTT 1 M	100 µL	1 mM
	cOmplete™, Mini	1 tablet/10 mL	-
	Triton X-100	100 µL	0.1 %
	De-ionized H_2O	Fill-up to 100 mL	-
Deoxyribonuclease I, sterile-filtered (-80 °C)	Deoxyribonuclease I	100 mg	4.4 mg/mL
	$MgCl_2$	22.5 µL	1 mM
	PBS	22.5 mL	-
DMP solution	DMP	5.4 mg	20 mM
	Triethanolamine buffer	1 mL	-
Doxycycline 10X (-20 °C)	Doxycycline	100 mg	10 mg/mL
	Sterile H_2O	10 mL	-
Doxycycline 1X (-20 °C)	Doxycycline 10X	1 mL	1 mg/mL
	Sterile H_2O	9 mL	-
DTT 1 M (-20 °C)	DTT	1.54 g	1 M
	Autoclaved de-ionized H_2O	10 mL	-
FACS washing buffer (4 °C)	Sodium citrate buffer	3.8 mL	38 mM
	De-ionized H_2O	96.2 mL	-
FACS staining solution (per sample)	FACS washing buffer	400 µL	-
	PI stock	8 µL	50 µg/mL
	Ribonuclease A	2 µL	50 µg/mL
FCS (-20 °C)	Heat-inactivated at 56 °C for 30 min	-	-
IP bead storage buffer (4 °C)	Tween 20	100 µL	0.01 %
	NaN_3	0.9 mg	0.09 %
	PBS	Fill-up to 1 L	-
IP bead washing buffer pH 8.0 (4 °C)	Na_3PO_4	1.6 g	0.1 M
	De-ionized H_2O	Fill-up to 100 mL	-
	HCl	Dropwise to set pH	-

IP blocking buffer (4 °C)	BSA	1 g	0.5 %
	PBS	200 mL	-
IP elution buffer (4 °C)	Citric acid	1.92 g	0.1 M
	De-ionized H_2O	Fill-up to 100 mL	-
IP lysis buffer (-20 °C)	Trizma Base	360 mg	30 mM
	NaCl	70 mg	120 mM
	100 % glycerol	10 mL	10 %
	EDTA	58 mg	2 mM
	KCl	15 mg	2 mM
	Triton-X 100	1 mL	1 %
	cOmplete™, Mini	1 tablet/10 mL	-
	De-ionized H_2O	Fill-up to 100 mL	-
IP sample loading buffer (RT)	Trizma Base	1.5 g	125 mM
	20 % SDS	20 mL	4 %
	Glycerol	20 mL	20 %
	Bromphenol blue	4 mg	0.004 %
	De-ionized H_2O	Fill-up to 100 mL	-
IP washing buffer pH 5.0 (4 °C)	Citric acid	4.7 g	24 mM
	Na_2HPO_4	9.2 g	51.7 mM
	De-ionized H_2O	Fill-up to 1 L	-
	HCl	Dropwise to set pH	-
LB medium (4 °C)	NaCl	10 g	1 %
	Peptone	10 g	1 %
	Yeast extract	5 g	0.5 %
	De-ionized H_2O	1 L	-
PBS-T (RT)	PBS	200 mL	-
	Tween 20	40 µL	0.02 %
PEI working solution pH 7, sterile-filtered (4 °C)	PEI	1 g	1 µg/µL
	De-ionized H_2O, 80 °C	1 L	-
	HCl	Dropwise to set pH	-
PI stock (4 °C)	PI	25 mg	2.5 mg/mL
	De-ionized H_2O	10 mL	-
Ponceau S solution (RT)	Ponceau S	5 mL	-
	De-ionized H_2O	45 mL	-
Quenching solution pH 7.5 (4 °C)	Trizma Base	1.22 g	50 mM
	HCl	Dropwise to set pH	-
	De-ionized H_2O	200 mL	-
Running buffer 10X (RT)	Tris	30.3 g	25 mM
	Glycine	144.1 g	192 mM
	SDS pellets	10 g	0.1 %
	De-ionized H_2O	Fill-up to 1 L	-
Running buffer 1X (RT)	Running buffer 10X	100 mL	-
	De-ionized H_2O	900 mL	-
Running gel buffer pH 8.8 (RT)	Tris	36.34 g	1.5 M
	De-ionized H_2O	200 mL	-
	HCl	Dropwise to set pH	-
SDS lysis buffer mix (-20 °C)	Stacking gel buffer	12.4 mL	-
	20 % SDS	10 mL	2 %

	100 % glycerol	10 mL	10 %
	De-ionized H_2O	Fill-up to 100 mL	-
SDS lysis buffer (-20 °C)	SDS lysis buffer mix	10 mL	-
	PhosSTOP	1 tablet	-
	DTT 1 M	10 µL	-
	cOmplete™, Mini	1 tablet	-
Sodium citrate buffer (4 °C)	Tri-sodium citrate dihydrate	25.8 g	1 M
	De-ionized H_2O	100 mL	-
Stacking gel buffer pH 6.8 (RT)	Trizma Base	12.12 g	0.5 M
	De-ionized H_2O	200 mL	-
	HCl	Dropwise to set pH	-
SYBR Green mastermix (per sample)	2X SYBR Green	10 µL	-
	Primer mix	2 µL	-
	Nuclease-free H_2O	3 µL	-
TAE 50X (RT)	EDTA	18.612 g	50 mM
	Trizma Base	242 g	2M
	Acetic acid	57.1 mL	1M
	De-ionized H_20	Fill-up to 1 L	-
TAE 1X (RT)	TAE 50X	50 mL	1X
	De-ionized H_20	1 L	-
TBS 10X (RT)	Trizma Base	60 g	
	NaCl	440 g	
	De-ionized H_2O	Fill-up to 5 L	-
	HCl	Dropwise to set pH	-
TBS-T (RT)	TBS 10X	100 mL	-
	De-ionized H_2O	900 mL	-
	Tween 20	2 mL	0.2 %
TBS-T 0.1 % (RT)	TBS 10X	100 mL	-
	De-ionized H_2O	900 mL	-
	Tween 20	1 mL	0.1 %
Thymidine stock solution, sterile-filtered (4 °C)	Thymidine	484 mg	20 mM
	De-ionized H_2O	100 mL	-
Transfer buffer 10X (RT)	Trizma Base	58 g	480 mM
	Glycine	29.3 g	390 mM
	De-ionized H_2O	1 L	-
Transfer buffer 1X (RT)	Transfer buffer 10X	100 mL	-
	100 % Methanol	200 mL	-
	De-ionized H_2O	700 mL	-
Triethanolamine buffer pH 8.2 (4 °C)	Triethanolamine	2.64 mL	0.2 M
	PBS	100 mL	-
	HCl	Dropwise to set pH	-

3.1.10. Consumables

Table 18 Consumables.

Article	Supplier
Cell scraper	Sarstedt, Nürnbrecht, Germany
Chromatography paper "Whatman CHR 3mm"	Miltenyi Biotec, Bergisch Gladbach, Germany
Conical tubes, 15 mL and 50 mL	ThermoFisher Scientific, Waltham, MA, USA
Cryovials	Carl Roth, Karlsruhe, Germany
D300e Digital dispenser dispenshead casettes T8+	Tecan, Männerdorf, Switzerland
Dynabeads™ Protein G	ThermoFisher Scientific, Waltham, MA, USA
Falcon® 5mL round bottom polystyrene est tubes	ThermoFisher Scientific, Waltham, MA, USA
Glassware	SCHOTT AG, Mainz, Germany
Microplates, 96 well, F-bottom, black	Greiner Bio-One, Frickenhausen, Germany
Parafilm® M	Benis, Braine-l'Alleud, Belgium
PCR tube strips and domed caps	ThermoFisher Scientific, Waltham, MA, USA
Pipette filter tips, 10 µL, 20 µL, 100 µL, 200 µL, 1000 µL	Nerbe plus, Winsen/Luhe, Germany
PVDF membrane	Bio-Rad, Hercules, CA, USA
Safe-Lock reaction tubes, 0.5 mL, 1.5 mL, 2.0 mL	Eppendorf, Hamburg, Germany
Serological pipettes, 5 mL, 10 mL, 25 mL	Sigma-Aldrich, St. Louis, MO, USA
Stericup-GP sterile vacuum filtration system, 500 mL	Merck Millipore, Burlington, MA, USA
Sterile filter, 0.2 µm	Merck Millipore, Burlington, MA, USA
Syringe 10 mL	Terumo, Tokyo, Japan
Tissue culture dishes, 100 x 20 mm	ThermoFisher Scientific, Waltham, MA, USA
Tissue culture dishes, 145 x 20 mm	Greiner Bio-One, Frickenhausen, Germany
Tissue culture flasks (low attachment), 25 cm^2, 75 cm^2, 175 cm^2	Sarstedt, Nürnbrecht, Germany
Tissue culture flasks (ultra-low attachment), 75 cm^2	Corning, Kaiserslautern, Germany
Tissue culture flasks, 25 cm^2, 75 cm^2, 175 cm^2	Greiner Bio-One, Frickenhausen, Germany
Tissue culture plates (ultra-low attachment), 6 well, 96 well	Corning, Kaiserslautern, Germany
Tissue culture plates, 6 well, 96 well	Corning, Kaiserlautern, Germany
ViCell 4 mL tubes	Beckmann Coulter, Brea, CA, USA

3.1.11. Kits

Table 19 Commercial kits.

Article	Cat. no.	Supplier
Amersham ECL Prime Western Blotting Detection Reagent	RPN2232	GE Healthcare Dharmacon, Lafayette, CO, USA
Caspase-3 Fluorometric Assay Kit	K105	Biovision, Milpitas, CA, USA
Cell Counting Kit-8	CK04-13	Dojindo Laboratories, Kumamoto, Japan
Pierce™ BCA Protein Assay Kit	23227	ThermoFisher Scientific, Waltham, MA, USA
PlasmoTest™ Mycoplasma Detection Kit	Rep_ptrk	InvivoGen, San Diego, CA, USA
QIAGEN Plasmid Maxi Kit	12145	Qiagen, Hilden, Germany
QIAamp® DNA Mini Kit		Qiagen, Hilden, Germany
qPCR Mastermix for SYBR® Green I	4309155	ThermoFisher Scientific, Waltham, MA, USA
RevertAid First Strand cDNA Synthesis Kit	K1622	ThermoFisher Scientific, Waltham, MA, USA
RNeasy Mini Kit	74104	Qiagen, Hilden, Germany
Venor® GenM Classic Mycoplasma Detection Kit	11-1250	Minerva Biolabs, Berlin, Germany

3.1.12. Instruments and machines

Table 20 Equipment and instruments.

Instrument	Supplier
ABI 7500 real time PCR cycler	Applied Biosystems, Foster City, CA, USA
Analytical balance "BP 121S"	Sartorius, Göttingen, Germany
Azure c400 imaging system	Azure Biosystems, Dublin, CA, USA
Barnstead™ GenPure™ xCAD Plus Ultrapure water purification system	ThermoFisher Scientific, Waltham, MA, USA
BD FACS Canto II analyzer	Becton, Dickinson and Company, Heidelberg, Germany
Benchtop centrifuge Allegra X-12R	Beckmann Coulter, Brea, CA, USA
Biometra T3000 thermocycler	LabRepCo, Horsham, PA, USA
Blotting chamber TransBlot® SD Semi-Dry Transfer Cell	Bio-Rad, Hercules, CA, USA
Butane/Propane cartridge	Campingaz/Newell Brands, Hoboken, NJ, USA
CellMate® II Serological Pipette	Matrix Technologies Corporation, ThermoFisher Scientific, Waltham, MA, USA
Chemi-Smart 5000 Technology, chemiluminescence imaging system	Vilber Lourmat, Eberhardzell, Germany
Cryo freezing container Nalgene® Cryo 1°C "Mr. Frosty"	ThermoFisher Scientific, Waltham, MA, USA
D300e Digital dispenser	Tecan, Männerdorf, Switzerland
DynaMag™-2 magnet	ThermoFisher Scientific, Waltham, MA, USA

Electrophoresis chamber Mini-Protean® Tetra System	Bio-Rad, Hercules, CA, USA
Epson perfection V700 photo scanner	EPSON, Nagano, Japan
FLUOstar OPTIMA automated plate reader	BMC Labtech, Ortenberg, Germany
Hamilton Microliter™ #701	Hamilton, Reno, NV, USA
Heat sealer "Folio"	Severin Elektro, Sundern, Germany
Heating block Thermomixer® Comfort	Eppendorf, Hamburg, Germany
Incubator Heraeus B6420	Heraeus, Leverkusen, Germany
Light microscope CKX31	Olympus, Hamburg, Germany
Light microscope CKX41 with reflected fluorescence system	Olympus, Hamburg, Germany
Magnetic stirrer with heating MR-3001	Heidolph Instruments, Schwabach, Germany
Microcentrifuge 547 R; rotor F 45 24-11	Eppendorf, Hamburg, Germany
Micropipette PIPETMAN Neo® P10N, P20N, P100N, P200N, P1000N	Gilson, Limburg-Offheim, Germany
Microwave Severin MW 7869	Severin Elektro, Sundern, Germany
Multi-axle rotating mixer TRM 56	IDL GmbH, Nidderau, Germany
Nano-Drop ND-1000 spectrophotometer	PEQLab, Erlangen, Germany
pH meter SevenEasy	Mettler-Toledo, Gießen, Germany
Pipette controller Accu-jet® pro	BRAND, Wertheim, Germany
Power supply EV231	PEQLab, Erlangen, Germany
Power supply PowerPac™ Basic Power Supply	Bio-Rad, Hercules, CA, USA
Precision balance 440-47N	Kern & SOHN, Balingen, Germany
Refrigerator with freezer	Liebher, Biberach and der Riß, Germany
Rocking platform WT 16	Biometra, Göttinger, Germany
Test tube shaker Reax Top	Heidolph Instruments, Schwabach, Germany
Tissue culture incubator "C200"	Labotect, Rosdorf, Germany
Tissue culture sterile bench "Safe2020"	ThermoScientific, Waltham, MA, USA
Ultra-low temperature freezer	ThermoFisher Scientific, Waltham, MA, USA
Vi-CELL XR automated cell counter	Beckmann Coulter, Brea, CA, USA
Vortexer IKA VF2	IKA Janke & Kunkel, Staufen im Breisgau, Germany
Water bath	Memmert, Schwabach, Germany

3.1.13. Databases and datasets

Table 21 Databases.

Database	Website
MSigDB v7.1	https://www.gsea-msigdb.org/gsea/msigdb/index.jsp
NCBI	https://www.ncbi.nlm.nih.gov/
R2	https://hgserver1.amc.nl/cgi-bin/r2/main.cgi
UniProt	https://www.uniprot.org/

Table 22 Datasets. GEP: gene expression profiling. RNAseq: RNA sequencing. INFORM: Individualized Therapy For Relapsed Malignancies in childhood program.

Dataset	Author	Size (n)	Access code	Reference
Cerebellum GEP	Kool	10	-	-
Glioma GEP	French	284	GSE16011	[399]
INFORM	INFORM/Jones	1082	-	[400]
MB GEP	Gilbertson	76	GSE37418	[401]
MB GEP	Pfister	223	-	[55]
MB protein	Forget	41	-	[402]
MB protein	Archer	45	MSV000082644	[403]
MB RNAseq	Cavalli	763	GSE85217	[2]
NB GEP	Versteeg	88	GSE16476	[404]

3.1.14. Software

Table 23 Software.

Software	Supplier
ABI 7500 software v2.3	Applied Biosystems, ThermoFisher Scientific, Waltham, MA, USA
Azure c400 acquisition software	Azure Biosystems, Dublin, CA, USA
CellB 2.3 Soft imaging software	Olympus Biosystem GmbH, Shinjuku, Tokyo, Japan
Chemi-Capt 500	Vilber Lourmat, Eberhardzell, Germany
CompuSyn v1.0	ComboSyn, Paramus, NJ, USA
D300e Digital dispenser control software	Tecan, Männerdorf, Switzerland
Endnote X9	Clarivate Analytics, Philadelphia, PA, USA
FlowJo™ v10.6.1	FlowJo, LLC, Ashland, OR, USA
GraphPad Prism v5.01	GraphPad Software Inc, San Diego, CA, USA
ImageJ v1.52	National Institutes of Health
Inkscape v0.92.4	Open source
IrfanView v4.54	Irfan Skilijan
Microsoft Office 2010	Microsoft, Redmond, WA, USA
OPTIMA Microplate reader software v2.20R2	BMC Labtech, Ortenberg, Germany
R v3.5.3	The R Foundation, Vienna, Austria
RStudio v1.1.463	RStudio, Boston, MA, USA
Vi-CELL™ XR 2.03 software	Beckmann Coulter, Brea, CA, USA

3.2. Methods

3.2.1. Tissue culture

All cell lines outlined in Table 5 were maintained in a humidified atmosphere with 5 % CO_2 at 37 °C. Before any experiments were conducted, all cell lines were authenticated using the Multiplex Cell Line Authentication test (MCA)[405] and examined for contamination with Multiplex cell Contamination Test (McCT)[405]. Cells used for experiments were certified to be virus, bacteria and *Mycoplasma* contamination-free and without cross-contamination with other cell lines. Cells were also routinely tested for *Mycoplasma* contamination: weekly using the PlasmoTest™ Mycoplasma Detection Kit and monthly by PCR with the Venor® GeM Kit. Culture confluency and health were evaluated every two days by visual examination using light microscopy. Unless indicated otherwise, all experimental techniques described in this section were applied in a sterile working environment under laminar flow with sterile solutions (Table 6-8) and consumables (Table 18).

3.2.1.1. Cell thawing

Cryopreserved MB and NB cell lines were kept in -80 °C. Prior to thawing, 50 mL Falcon tube with 5 or 10 mL of respective toom temperature (RT) medium (Table 6) was prepared. Cells in cryovial were thawed under warm running H_2O until only a small piece of ice was remaining in the cryovial. The contents of the cryovial were transferred to a Falcon tube with medium, gently mixed and transferred to a 25 cm^2 (5 mL medium, semi-adherent cell lines) or 75 cm^2 (10 mL medium, adherent cell lines) flask. Medium was changed after 24 hours.

Cryopreserved glioma (DIPG and GBM) spheroid cell lines were kept in liquid nitrogen. TSM Base and TSM with additives (Table 6) were pre-warmed to 37 °C. Cells were thawed as described above. The contents of the cryovial were transferred to a 50 mL Falcon tube. 9 mL of pre-warmed TSM Base were added on the cells dropwise in order to prevent osmotic shock. The contents of Falcon tube were mixed gently and centrifuged at 1000 rpm for 5 minutes. After the removal of supernatant, cells were resuspended in 6 mL of pre-warmed TSM with additives and transferred to a 25 cm^2 low attachment flask. Medium was completely changed after 48 hours.

3.2.1.2. Cell propagation

MB and NB cells were expanded and cultured mainly in 175 cm^2 flasks with 25 mL of respective medium. Medium was replaced every 3-4 days. Upon reaching 70-80 % confluency (approximately once a week) and collection of supernatants (only in semi-adherent cell lines), dead cells and residual protein were washed away with PBS. Cells were detached by exposure

to trypsin-EDTA for 2-3 minutes at 37 °C. The enzymatic reaction was stopped with respective medium, cells were collected and centrifuged at 800 rpm for 5 minutes. Afterwards, cells were either counted and seeded for further experiments (described in 3.2.1.3) or split in a definite ratio based on experimental plan and cell line, resuspended in respective RT medium and transferred to a new flask. MB and NB cells were cultivated until they reached passages later than 90 (MB) or 30 (NB).

Stably transfected UW228-2-pMYC and ONS-76-pMYC cell lines with doxycycline-inducible *MYC* expression were cultivated in DMEM supplemented with 1 µg/mL doxycycline. Prior to any experiment, UW228-2-pMYC and ONS-76-pMYC were cultured in DMEM without doxycycline for 5 days in order to fully reduce *MYC* expression in the control cells. Re-exposure of the experimental cells supposed to express *MYC* to doxycycline coincided with cell seeding for experiments.

Glioma cell lines were cultured in 75 cm^2 low attachment (HSJD-GBM-001, HSJD-DIPG-007, SU-pcGBM2, SU-DIPG-XXV) or ultra-low attachment (SU-DIPG-XVII, SU-DIPG-XIII) flasks with 20 mL of TSM. Cells were fed every 6th day (alternating with subculturing) by transferring 10 mL medium from the flask to a 50 mL Falcon tube and centrifuging at 1000 rpm for 5 minutes. Supernatant was decanted, spheroids were resuspended in 10 mL of pre-warmed TSM with double concentration of additives and transferred to an original flask. Cells were subcultured every 6th day (alternating with feeding) by transferring 20 mL medium with spheroids to a 50 mL Falcon tube and centrifuging at 1000 rpm for 5 minutes. After decanting the supernatant, 1 mL of pre-warmed Accumax (HSJD-GBM-001, HSJD-DIPG-007, SU-pcGBM2, SU-DIPG-XXV) or TrypLE (SU-DIPG-XVII, SU-DIPG-XIII) was added, the pellet was dissociated and incubated at 37 °C for 5 minutes. For SU-DIPG-XIII TrypLE was supplemented with 10 µL of Deoxyribonuclease I solution and 1 µL $MgCl_2$ to dissolve aggregates of cells and DNA released from dying cells. After the incubation, the single cells and the dissociation reagents were diluted by adding 9 mL of pre-warmed TSM Base, cells were counted using Vi-Cell XR automatic cell counter, either aliquoted for experiments or split for subculturing (6×10^5 cells in 75 cm^2 flask) and centrifuged at 1000 rpm for 5 minutes. Subcultured cells were resuspended in pre-warmed TSM with additives and transferred to new flask. Cells were propagated until they reached passage 20.

3.2.1.3. Cell seeding and harvesting

For experiments, MB, NB and glioma cell lines were seeded in either 6-well, 96-well tissue culture plates or tissue culture dishes with diameter of 100- or 145-mm. For seeding, cells were detached with trypsin-EDTA or dissociated with Accumax/TrypLE (described above) and counted using the Vi-Cell XR automatic cell counter. Afterwards cells were aliquoted in an experiment-specific cell number (described separately for each method) and divided into respective plates or dishes. Any treatment was started 24 hours after seeding.

Unless stated otherwise in the description of the techniques below, cell harvesting for subsequent experiments was conducted in a non-sterile working environment. After cell detachment/dissociation, cells were centrifuged at 1000 rpm for 5 minutes. Supernatants were preserved for semi-adherent and glioma cell lines and for all cell lines in experiments involving cell viability (3.2.1.4) and cell death (3.2.4.2 and 3.2.3.4).

3.2.1.4. Treatment with HDACi and PLK1i

Entinostat and PLK1 inhibitors (Table 8) were purchased solved in DMSO at 10 mM. Entinostat, GSK461364 and rigosertib were stored at -20 °C. Volasertib and onvansertib were stored at -80 °C. All drugs were added in depicted concentrations that were chosen for each experiment based on treatment duration, cell line and read-out technique. Drugs were pre-diluted in order to avoid pipetting errors occurring with volumes lower than 1 µL. Solvent control was treated with the highest concentration of DMSO of the respective experiment.

3.2.1.5. Treatment with cycloheximide

In order to determine whether volasertib affects the stability of MYC protein, pulse-chase experiments with the translation inhibitor cycloheximide were conducted. 24 hours after seeding, MED8A and HD-MB03 cells were pre-treated with either 50 nM of volasertib or DMSO (solvent) for 1 hour. Afterwards, a pulse of cycloheximide (final concentration 300 µg/mL) was administered. Cells were “chased”, i.e. collected after 15 and 30 minutes, 1, 2, 3 hours and subjected to protein extraction for immunoblotting. Untreated and DMSO (without cycloheximide) controls were collected at 3 hours timepoint.

3.2.1.6. Treatment with MG132

In order to determine, whether MYC is being degraded in a proteasome-dependent manner upon volasertib treatment, the proteasome inhibitor MG132 was employed for a rescue experiment. 24

hours after seeding, MED8A and HD-MB03 cells were treated with DMSO (solvent), volasertib (25 nM) and MG132 (50 nM) alone or with their combination for 6 or 16 hours. Cells were collected as described previously and subjected to protein extraction for immunoblotting.

3.2.1.7. Cell viability

Trypan blue stains only the cells that are dead or dying, since their compromised membranes allow the dye to enter the cell. Therefore, the numbers of viable and dead cells in the culture were determined using Vi-Cell XR automatic cell counter using trypan blue exclusion. Cell numbers were determined per 1 mL.

In order to determine the cell growth rate, cells were seeded in 2 mL medium in 6-well plates in 2.5×10^5 cells/well. Because of increased sensitivity due to lack of cell-cell contacts when seeded at low density, HD-MB03 and D458 cell lines were seeded at higher density, i.e. in 5×10^5 cells/well. Cells were harvested with trypsin-EDTA or Accumax/TrypLE in a sterile environment in overall 1 mL (500 µL dissociation reagent + 500 µL medium) and counted once a day for 5 days (with day 1 representing 24 hours after seeding). Viable cell numbers were normalized to seeded cell number. Cell doubling time was calculated:

$$DoublingTime = \frac{Duration \times \log(2)}{\log(FinalConcentration) - \log(InitialConcentration)}$$

Viable and dying cell numbers were also determined in response to the treatment with entinostat, volasertib and/or their combination (Table 8). Cells were seeded in 2 mL medium in 6-well plates in 5×10^5 cells/well. 24 hours after seeding cells were either left untreated, treated with solvent (DMSO), single drugs or combination. Substances were pre-diluted in 500 µL in 5X concentration and administered to the cells. Untreated cells were mock treated with 500 µL of respective medium. 72 hours post-treatment, the cells were collected as described previously, resuspended in 1 mL fresh medium and counted. Viable and dead cell numbers were normalized to untreated control well cell numbers.

3.2.1.8. Cell synchronization

The cell synchronization protocol used for the experiments described in this thesis is based on a double-thymidine block protocol. High levels of the DNA nucleosides thymidine hinders nucleoside metabolic pathways and blocks DNA synthesis, thus halting cell cycle at early S phase. For culture synchronization MED8A and UW228-2 cell lines were seeded in 9 mL medium

in 100 mm dishes in 10^6 cells/dish for subsequent flow cytometry analysis (3.2.4.3) and in 2 mL medium in 6-well plates in 10^6 cells/well for gene (3.2.2.1, 3.2.2.2, 3.2.2.3) and protein (3.2.3.2, 3.2.3.3, 3.2.3.4) expression analysis. 24 hours after seeding 1st thymidine block was conducted (Figure 23): thymidine was diluted in 10X concentration in 1 mL medium (for 100 mm dishes) or 5X concentration in 500 µL (for 6-well plates) and administered to the cells. Final thymidine concentration on the cells was 2 mM. Untreated control was mock treated with media alone. The 1st thymidine block was continued for 18 hours and is used to bring to the S phase the cells that were in M and G1 phase in asynchronous culture. After the 1st thymidine block, cells were washed with media without supplements in order to completely wash-out any remaining thymidine. Fresh medium with supplements was added and cells were kept in the incubator for 9 hours. During this time cells that were synchronized at early S phase enter the cell cycle again and reach the M phase together with the cells that were in S and G2 phases in asynchronous culture.

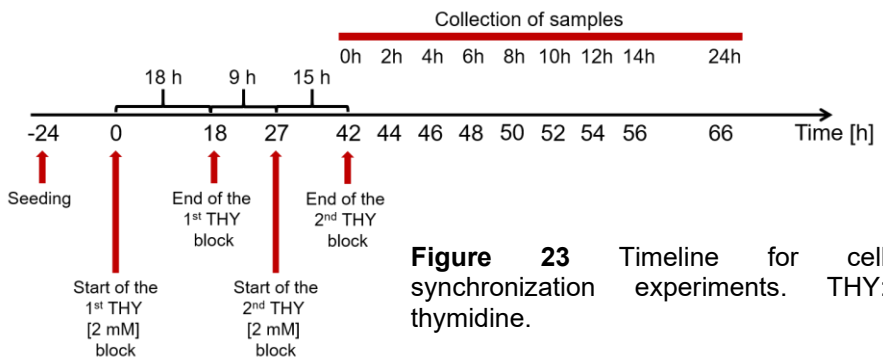

Figure 23 Timeline for cell synchronization experiments. THY: thymidine.

Following the 9-hour thymidine washout, the 2nd thymidine block is started as described before in 2 mM final concentration on the cells. The 2nd thymidine block is continued for 15 hours and brings to the early S phase the cells that reached M and G1 phases during the washout. After 15 hours cells are released in a synchronized culture by washing with medium without supplements and adding normal medium. Cells were collected every two hours as described above for 14 hours (Figure 23) with an additional sample collection 24 hours post-release. As mentioned, collected cells were further analysed by flow cytometry, qRT-PCR and immunoblotting.

3.2.1.9. Transient transfection

Cells were transfected using the pGIPZ plasmids containing either non-silencing shRNA or shRNA targeting PLK1 (Table 14). Polyethylenimine (PEI) working solution (Table 17) was used as a transfection reagent. As PEI aggregates DNA into positively charged particles, DNA is able to bind the negative cell surface. The DNA subsequently is capable of entering the cells via endocytosis and is released into the cytoplasm. 5×10^6 cells were seeded per 100 mm cell culture dish. 24 hours after seeding, medium was replaced. 42 µL of PEI working solution were added to 500 µL of the cell line-specific medium without the FCS. The plasmid DNA equivalent to 4 – 7 µg

(after optimization 7 µg were used) were added to 500 µL medium without FCS. Medium with PEI was added to DNA/medium vials, mixed and incubated for 20 minutes at RT. Medium with DNA:PEI complexes was added to the cells dropwise. As the transfection reagent is toxic to the cells, medium was replaced 16 hours post-transfection. Cells were monitored for GFP signal 24 and 48 hours after transfection and harvested (3.2.1.3) 48 hours after transfection for the evaluation of knockdown efficiency.

3.2.1.10. Cryopreservation

MB and NB cells were cryopreserved by detaching them and counting as described previously. 2 × 10^6 cells/cryovial were resuspended in 1 mL/cryovial medium supplemented with 10 % DMSO to prevent the formation of ice crystals. Cryovials with cells were transferred to the Mr. Frosty™ Freezing container which provides a gradual freezing process (-1 °C/min) due to the isopropanol surrounding the container. This reduces the damage for the cell membranes. After 48-72 hours cells were transferred to permanent cryopreservation location in the -80 °C freezer.

Glioma cells were cryopreserved as spheroids in order to enhance the culture re-establishment after cryopreservation. Medium with spheroids was transferred from the flasks to 50 mL Falcon tube and centrifuged at 1200 rpm for 5 minutes. Supernatant was decanted and spheroids were gently resuspended in 1 mL/cryovial Synth-a-Freeze cryopreservation medium. Cryovials with cells were immediately transferred to the Mr. Frosty™ Freezing container and after 48-72 hours, to the liquid nitrogen for permanent cryopreservation.

3.2.2. Nucleic acids

3.2.2.1. RNA isolation

RNA isolation was conducted using RNeasy® Mini Kit (Table 19) according to the manufacturers' instructions. 24 hours after seeding 2 × 10^6 cells/100 mm dish or following culture synchronization or treatment cells were harvested as described above. After the centrifugation step, cell pellets were lysed in 350 µL RLT highly denaturing guanidine-thiocyanate-containing buffer supplemented with 1 % β-mercaptoethanol. Lysates were mixed with an equal volume of 70 % ethanol, transferred to the RNeasy Mini Spin columns with 2 mL collection tubes and centrifuged at 10 000 rpm for 1 minute. The flow through was discarded and the columns were washed with 700 µL of RW1 buffer under vacuum suction and subjected to an on-column DNase digestion for 20 minutes at RT. Afterwards, columns were washed with 700 µL of RW1 buffer and twice with 500 µL of RPE buffer under vacuum suction. The remainder RPE buffer was removed by

centrifuging the columns placed in 2 mL collection tubes at 10 000 rpm for 1 minute. The RNA was eluted by placing the columns to 1.5 mL microcentrifuge tubes, adding 30 µL nuclease-free H_2O and centrifuging at 10 000 rpm for 2 minutes. In order to improve the yield of RNA, the eluate containing RNA was re-added to the column and centrifuged at 10 000 rpm for 2 minutes again. The RNA concentration was determined using the NanoDrop™ spectrophotometer measuring the light absorbance of nucleic acids at 260 nm. RNA purity was determined by measuring absorbance at 280 nm (proteins) and 230 nm (aromatic solvents). The RNA was considered pure when OD_{260}/OD_{280} ratio was 1.8-2.0 and OD_{260}/OD_{230} ratio was 2.0-2.2. RNA was stored at -80 °C.

3.2.2.2. cDNA synthesis

Complementary DNA (cDNA) was synthesized using RNA from 3.2.2.1 as a template. Reverse transcription was performed with RevertAid First Strand cDNA Synthesis Kit (Table 19) according to manufacturers' instructions. 0.5-1 µg of total RNA was transferred to a PCR tube and filled-up with nuclease-free H_2O to 10 µL. 1 µL/sample random hexamers were added and incubated at 70 °C for 5 minutes. Samples were transferred to ice and cooled. Subsequently, 7 µL/sample of reverse transcription master mix (per 1 sample: 4 µL 5X reaction buffer, 1 µL RiboLock RNase inhibitor, 2 µL 10 mM dNTPs) were added and incubated at 25 °C for 10 minutes. 2 µL/sample M-MuLV reverse transcriptase enzyme were added and incubated at 25 °C for 10 minutes followed by 37 °C for 60 minutes. The reaction was terminated at 70 °C for 10 minutes. Synthesized cDNA containing tubes were transferred to either -20 °C for short-term or to -80 °C for long-term storage.

3.2.2.3. Quantitative real-time RT-PCR

The quantitative real-time reverse-transcription polymerase chain reaction (qRT-PCR) technique allows to evaluate the absolute and relative levels of mRNA of gene of interest via the intermediate step of cDNA (3.2.2.2). When bound to double-stranded DNA, a fluorescent reporter molecule (in this case, SYBR® Green I), emits fluorescent light upon excitation. During PCR, DNA is amplified thus increasing the amount of bound reporter. Once the emitted fluorescence crosses a pre-defined threshold, a Cycle of Threshold (CT) is recorded.

The qPCR reaction was performed in a 96-well PCR plate with 15 µL/well gene-specific SYBR Green Mastermix (Table 17) consisting of 2X SYBR Green mastermix, commercially available reverse and forward primers (Table 10) and nuclease-free H_2O. cDNA from section 3.2.2.2 was

diluted with nuclease-free H_2O either 1:10 (when cDNA was synthesized of 1 µg of RNA) or 1:5 (when cDNA was synthesized of 0.5 µg of RNA). 5 µL of diluted cDNA was added to the mastermix with overall 20 µL per well in two technical replicates. The plate was subsequently covered with adhesive film and centrifuged at 800 rpm for 5 minutes.

The reaction was run on the ABI 7500 Real-Time PCR cycler with the ABI Software v2.3. The PCR was initiated at 50 °C for 2 minutes, followed by enzyme activation at 95 °C for 10 minutes. 40 cycles of DNA denaturation (95 °C 15 seconds) and primer annealing + DNA elongation (60 °C 1 minute) were run. Dissociation was carried out in 1 cycle of 95 °C for 15 seconds, 60 °C for 1 minute, 95 °C for 30 seconds and 60 °C 15 seconds. CT values of genes of interest were normalized to those of the housekeeping genes (constitutively expressed in the cell, here *ACTB* and *GAPDH*) and later calculated to fold change values comparing to the controls (untreated or solvent-treated cells).

3.2.2.4. Genomic DNA isolation

Genomic DNA was isolated prior to submitting the cell line samples for authentication (MCA)[405] and contamination (McCT)[405] testing as described above. DNA isolation was carried out using the QIAamp® DNA Mini Kit (Table 19) according to manufacturers' instructions. 24 hours after at least 10^6 cells/ 100 mm dish seeding, cells were harvested as described above and cell pellets were lysed in 180 µL of ATL buffer supplemented with 20 µL of proteinase K at 56 °C for 10 minutes. 200 µL of AL buffer were added to the mix and vortexed for 15 seconds. The mix was incubated at 70 °C for 10 minutes and shortly centrifuged. 200 µL of 100 % ethanol were added and mixed thoroughly by vortexing for 15 seconds. The mixture was applied to the QIAamp Mini Spin column in a 2 mL collection tube and centrifuged at 8000 rpm for 1 minute. The flow through was discarded and the column was washed with 500 µL of AW1 buffer followed by centrifugation at 8000 rpm for 1 minute. The column was washed for a second time with 500 µL of AW2 buffer and centrifuged at 14 000 rpm for 3 minutes. The column was transferred to new collection tube and centrifuged again at 8000 rpm for 1 minute. The DNA was eluted by transferring the column to the 1.5 mL microcentrifuge tube, adding 200 µL of nuclease-free H_2O, incubating for 5 minutes at RT and centrifuging at 8000 rpm for 1 minute. The eluate was re-added to the column and centrifuged again at 8000 rpm for 1 minute. The DNA concentration was determined using NanoDrop™ spectrophotometer measuring the light absorbance of nucleic acids at 260 nm. The DNA purity was determined by measuring absorbance at 280 nm (proteins) and 230 nm (aromatic solvents). DNA was considered pure when the OD_{260}/OD_{280} ratio was 1.8-2.0 and OD_{260}/OD_{230}

ratio was 2.0-2.2. For MCA and McCT testing DNA was diluted to 15-30 ng/µL and stored at -20 °C.

3.2.2.5. Plasmid DNA amplification and isolation

Commercially available pGIPZ vectors with PLK1-targeting shRNAs (Table 14) were delivered as *E. coli* glycerol stocks enabling in-house plasmid amplification and extraction. Plates with LB medium containing agar (Table 17) were prepared in advance and supplemented with ampicillin (Table 9) for bacterial selection. *E. coli* containing pGIPZ-shRNA were plated on pre-warmed agar plates in sterile working environment (next to the flame) after sterilization of plating instruments. Agar plates were incubated upside down (to avoid condensation) at 37 °C for 24 hours. Colonies were picked using sterile pipette tip and transferred to 3 mL LB medium (Table 17) supplemented with ampicillin. Bacteria were cultured for 24 hours at 37 °C on a shaking-block set at 220 rpm. 500 µL of suspension were transferred to 400 mL of LB medium with ampicillin and incubated for 24 hours at 37 °C in an orbital shaker at 220 rpm.

pGIPZ-shRNA plasmids were isolated using QIAGEN Plasmid Maxi Kit (Table 19) according to the manufacturers' instructions. Bacterial culture was harvested by centrifugation at 3000 rpm for 15 minutes at 4 °C. The bacterial pellet was resuspended in 10 mL of P1 buffer. 10 mL of P2 buffer was added and mixed by vigorously inverting tubes 6 times. The mixture was incubated at RT for 5 minutes. 10 mL of pre-chilled P3 buffer was added, mixed by vigorously inverting tubes 6 times and incubated on ice for 20 minutes. The mixture was centrifuged at 5000 rpm for 30 minutes at 4 °C, the supernatant was decanted and re-centrifuged at 5000 rpm for 15 minutes at 4 °C. In the meantime, a QIAGEN-tip 500 was equilibrated by applying 10 mL of QBT buffer and allowing to flow through by gravity flow. The supernatant of the bacterial mixture was applied to the QIAGEN-tip and allowed to enter the resin by gravity flow. The QIAGEN-tip was washed twice by 30 mL QC buffer allowing to move by gravity flow. DNA was eluted with 15 mL QF buffer into 50 mL Falcon tube by gravity flow. DNA was precipitated by adding 10.5 mL of isopropanol, mixing and centrifuging at 4500 rpm for 30 minutes at 4 °C. The supernatant was decanted and the DNA pellet was washed with 5 mL of 70 % ethanol and centrifuged at 4500 rpm for 10 minutes. After decanting the supernatant, the DNA pellet was air-dried for 10 minutes and dissolved in TE buffer. DNA concentration was determined using a NanoDrop™ spectrophotometer as described above.

3.2.2.6. Restriction analysis and electrophoresis

After plasmid DNA amplification (3.2.2.5) and extraction, the pGIPZ-shRNA identity was confirmed using SalI restriction enzyme (Table 15). The restriction digest followed by DNA electrophoresis allows to examine whether the plasmids are of correct size (and include the predicted restriction sites) and have not recombined during the amplification in bacteria. 2 µL of plasmid DNA diluted to 1 µg (total) was mixed with 15 µL of nuclease-free H_20, 2 µL of 10X FastDigest Green Buffer (Table 15) and 1 µL of SalI FastDigest restriction enzyme. The mix was incubated at 37 °C for 15 minutes and directly loaded to a 1 % agarose gel (in 1X TAE buffer (Table 17) mixed with Gel-Red). The gel was run at 45 V until the bands of the cut plasmid were separated (approximately 1 h). Gel images were captured using Azure c400 imaging system and software.

3.2.2.7. Gene expression profiling

Gene expression profiling (GEP) allows to evaluate global changes in the gene expression landscape following treatment. Here, 5×10^6 HD-MB03 cells/100 mm dish were seeded and, after 24 hours, were treated with 1 µM volasertib, 5 µM entinostat, the combination of both or the solvent for 6 hours. RNA was extracted as described above and submitted for Affymetrix U133 Plus 2.0 expression array analysis according to manufacturers' instructions. GEP was performed at the Genomics and Proteomics Core Facility, DKFZ, Heidelberg, Germany. Output data was pre-processed and analyzed in collaboration with Thomas Hielscher (Division of Biostatistics, DKFZ, Heidelberg, Germany). The analysis is described in 3.2.5.5.

3.2.3. Proteins

3.2.3.1. Cell fractionation and co-immunoprecipitation (co-IP)

Co-immunoprecipitation (co-IP) allows to evaluate whether two proteins are physically interacting in the cell. Here MYC and HDAC2 interaction was studied by incubating protein lysates with antibodies against MYC and evaluating the pull-down with immunoblotting for HDAC2 and mass spectrometry. Cell fractionation was employed for sample preparation in order to reduce background signal from cytoplasmic proteins.

5×10^6 of HD-MB03 cells were seeded per sample in a 145 mm tissue culture dish for subsequent cell fractionation and immunoprecipitation. Cells were harvested using trypsin-EDTA as described previously. The cell pellet was washed with PBS followed by centrifugation at 1000 rpm for 5 minutes twice. The cell pellet was resuspended in 200 µL of cell fractionation buffer supplemented

with Triton-X (Table 17) and incubated on ice for 8 minutes. Cells were fractionated by centrifugation at 1400 rpm for 5 minutes at 4°C yielding a supernatant fraction containing cytosolic content and a pellet fraction containing the nuclei. The supernatant was discarded, the pellet was resuspended in 500 µL of cell fractionation buffer (Table 17) and centrifuged at 1400 rpm for 5 minutes at 4 °C. The pellet was subsequently resuspended in 1 mL of IP lysis buffer (Table 17) and incubated rotating for 30 minutes at 4 °C. Whole cell lysates were also prepared to compare to the cell fractionation protocol. Here following cell harvesting, the pellet was resuspended in 1 mL of IP lysis buffer (Table 17) and incubated rotating for 1 hour at 4 °C.

Co-IP was carried out using Dynabeads™ protein G (Table 18) and DynaMag™-2 magnet (Table 20). Prior to the start of the co-IP, the magnetic beads were crosslinked to the antibodies in order to reduce their co-elution with precipitated proteins-of-interest and thus the background detection during mass spectrometry experiments. The beads were vortexed for at least 30 seconds. 50 µL beads/sample were transferred to 1.5 mL safe-lock reaction tubes and placed on the magnet. The supernatant was removed, the beads were incubated rotating with 200 µL antibodies diluted in PBS (Table 13) at RT for 10 minutes. Subsequently the complexes were gentle washed with 200 µL of PBS with the help of the magnet. Dynabeads™ Protein G-antibody complexes were washed twice in 1 mL of triethanolamine buffer (Table 17). The complexes were crosslinked in 1 mL of freshly made DMP solution (Table 17) by incubation for 30 minutes at 20 °C with gentle mixing. Upon the removal of the DMP solution, the reaction was stopped with 1 mL of quenching solution (Table 17) and incubation at RT for 15 minutes with rotation. The supernatant was removed and crosslinked bead-antibody complexes were washed 3 times with 1 mL of PBS-T (Table 17). The complexes were resuspended in IP blocking buffer (Table 17) and incubated rotating at 4 °C overnight. Before adding the samples, the complexes were washed 3 times with PBS.

Prior to adding to the beads, 1 % of nuclear or whole cell lysates were removed and kept as an “input 1” sample (i.e. crude lysate before the co-IP for comparison). The rest of the samples was added to the washed beads and incubated at RT for 10 minutes rotating. The samples were placed on the magnet, 1 % of supernatant was removed from each sample and kept as an “input 2” sample (i.e. the lysate of proteins that were not bound to pulled-down protein), the rest of the supernatant was discarded. The protein complexes bound to the bead-antibody complexes were gently washed 3 times with 200 µL of IP washing buffer, resuspended in 100 µL of IP washing buffer and transferred to fresh reaction tubes. Supernatant was removed and bead/protein complexes were either resuspended in 500 µL PBS (for mass spectrometry, stored at 4 °C) or

resuspended in a mix of 10 µL of IP elution buffer, 8 µL of IP sample loading buffer and 2 µL DTT (Table 17). 10 % of samples prepared for mass spectrometry analysis were removed and eluted for quality-control immunoblotting. Elution was conducted by incubating the mix at 70 °C for 10 minutes. The eluates were transferred to reaction tubes and stored at -20 °C until used in immunoblotting (3.2.3.4).

The beads were de-crosslinked by washing 5 times with IP bead washing buffer (Table 17), stored in IP bead storage buffer (Table 17) at 4 °C and used again up to 6 times.

3.2.3.2. Protein isolation for immunoblotting

In order to isolate proteins for subsequent immunoblotting the cells were seeded at a density of 0.5-1 × 10^6 cells/well of 6-well plates, treated with the compounds in the experiment-specific concentrations and harvested as described previously. Cell pellets were lysed in 200 µL of SDS lysis buffer (Table 17) containing protease and phosphatase inhibitors (preventing protein degradation and phosphorylation) as well as SDS, a strong detergent disrupting biological membranes. Protein tertiary structures were reduced by addition of DTT to the lysis buffer, since DTT is disrupting disulfide bridges formed between the thiol groups of cysteins. The protein samples in the SDS lysis buffer were subjected to denaturation by heat for 10 minutes at 95 °C. The denaturation was followed by centrifuging the samples for 1 minute at 14 000 rpm at 4 °C. Supernatants were transferred to new reaction tubes and either quantified (3.2.3.3) and used for immunoblotting (3.2.3.4) immediately or kept at -20 °C for short-term or -80 °C for long-term storage.

3.2.3.3. Protein quantification

The concentration of proteins in the lysates from 3.2.3.2 was quantified using the Pierce™ BCA Protein Assay Kit (Table 19) according to manufacturer's instructions. Bicinchoninic acid (BCA) assay requires alkaline environment and is based on two reactions: the peptide-bond-mediated reduction of Cu^{2+} ions to Cu^{+} (temperature-dependent and proportional to protein concentration reaction) and BCA-mediated Cu^{+} ion chelation leading to the formation of a purple complex absorbing at 562 nm. Protein concentrations are determined after the absorbance readout with FLUOstar OPTIMA plate reader and comparing to the standard curve.

Here, for protein quantification protein lysates were diluted 1:5 in SDS lysis buffer mix (Table 17, NB: no DTT added!) and 5 µL were transferred to the 96-well plate in two technical replicates. In order to enable the comparison to the standard curve, 5 µL of known concentration dilutions of

BSA (0-2000 µg/mL) were also added to the 96-well plate. 200 µL of freshly mixed Pierce™ BCA Protein Assay Kit buffers were added to the protein lysate samples. To allow the temperature-dependent BCA assay part to occur, the plate was incubated at 37 °C for 30 minutes. Subsequently, the absorbance was determined, and the sample protein concentrations were calculated based on the standard curve.

3.2.3.4. Gel electrophoresis and immunoblotting

SDS-polyacrylamide gel electrophoresis (SDS-PAGE) followed by immunoblotting allows for specific protein detection in a semi-quantitative manner. The first part of the method, namely SDS-PAGE, is a discontinuous electrophoretic system based on protein separation by polypeptide chain length in an electric field. In order to exclude the influence of protein structure, proteins are reduced and denatured (as described in 3.2.3.2). To eliminate the effect of natural protein charge and enable protein movement in the electric field, SDS binds the amino acids with its' 12-carbon tail, leaving the negatively-charged sulfate group outside, thus granting a negatively charged complex, able to move towards the anode. The discontinuous system is based on two different pH gels: the stacking gel helps to concentrate all proteins in one band before allowing the separation, and the running gel enabling the protein separation by weight. The stacking gel has 6.8 pH, where the glycine ions acquire a double charge, i.e. become zwitterions, and move very slowly in the electric field. Chloride ions are negatively charged thus moving towards the anode, sandwiching the proteins between glycine and chloride. The running gel has 8.8 pH where glycine acquires a negative charge and together with chloride move fast towards the anode leaving the proteins for separation by weight. The separation by weight is enabled by a porous nature of the gel of polymerized acrylamide, where larger proteins get stuck in the pores while smaller proteins move through the gel faster.

Here, the running gel was cast first at 10 or 12 % of final acrylamide concentration (Table 24, depending on the sizes of the proteins of interest) by pre-mixing the H_2O, the running gel buffer (Table 17) and 20 % SDS and adding acrylamide, 10 % APS (Table 17) and TEMED right before pouring the gel into ethanol-cleaned chamber. APS is a radical initiator and TEMED acts as a catalyst for the reaction of acrylamide polymerization. Isopropanol was added on top in order to remove bubbles at the meniscus and to protect the gel from radical scavenger oxygen. Isopropanol was removed following the polymerization of the gel (20-30 minutes), the running gel was carefully washed in order to remove any residual alcohol. The stacking gel was cast on top of the running gel at 4 % of final acrylamide concentration (Table 24). Again, the H_2O, the stacking

gel buffer (Table 17) and the 20 % SDS were pre-mixed with acrylamide, radical initiator APS and reaction catalyst TEMED added just before pouring the gel. 10 or 15-pocket combs were inserted and removed once the gel was polymerized.

The gels were assembled into the electrophoresis chamber, which was filled up with the 1X running buffer (Table 17). Prior to loading onto the gel, the protein samples from section 3.2.3.3 were diluted to 10-20 µg per gel (with the same protein amount in one gel) in SDS lysis buffer, mixed with 3 µL bromphenol blue (it allows to monitor the loading and the separation process) to the final volume of 20 µL and incubated at 95 °C for 5 minutes. The co-IP protein samples from the section 3.2.3.1 were loaded right after the elution described above. 5 µL of Precision Plus Protein™ Kaleidoscope™ (Table 16) protein standard was loaded together with the samples for a precise protein weight detection. The electrophoresis was run at 80 V until the proteins reached the running gel (approximately 15 minutes) and was set at 120 V until bromphenol blue band reached the end of the gel (approximately 1 hour 15 minutes).

Table 24 Running and stacking gel preparation and reagents.

Reagent	**Running gel**		**Stacking gel (4 %)**
	10 %	12 %	
De-ionized H_2O	2 mL	2.55 mL	1.538 mL
Running gel buffer (Table 17)	1.875 mL	1.875 mL	-
Stacking gel buffer (Table 17)	-	-	625 µL
20 % SDS	37.5 µL	37.5 µL	12.5 µL
Acrylamide/Bis solution (40 %)	2.5 mL	3 mL	335 µL
10 % APS	37.5 µL	37.5 µL	12.5 µL
TEMED	5 µL	5 µL	2.5 µL
Final volume/gel	**7.5 mL**	**7.5 mL**	**2.5 mL**

The second part of the method described in this section, is transfer followed by immunoblotting (i.e. western blotting). The western blotting technique is based on the transfer of the proteins separated by weight with SDS-PAGE onto the synthetic membrane using the electric field. Specific proteins can be detected by membrane incubation with antibodies.

Here, semi-dry blotting was used for the transfer of the proteins. Following the SDS-PAGE, the gel was removed from the chamber, the running gel was separated and transferred to the 1X transfer buffer (Table 17). In the blotting chamber, 6 transfer buffer pre-soaked Whatman chromatography papers (9 × 7 cm) were placed on the anode. The PVDF membrane (9 × 7 cm) was calibrated using methanol for 5 minutes, briefly soaked in the transfer buffer and placed on

top. The gel was placed on top and finally, 6 more pre-soaked Whatman chromatography papers were placed on the gel. The transfer was conducted at 35 mA/gel for 2 hours 15 minutes (12 % gel) or 2 hours 30 minutes (10 % gel). Following the transfer, the membrane was briefly soaked in methanol (2-3 minutes) and stained by Ponceau S solution (Table 17; 5 minutes) in order to ensure successful and uniform protein transfer. The gel was stained with Coomassie brilliant blue solution (Table 16) for 30 minutes followed by overnight de-staining with de-ionized H_2O to monitor the proteins left on the gel and thus the quality of transfer. Ponceau S and Coomassie brilliant blue dyes being negatively charged, bind all positive amino acids, thus staining all proteins. The excess of Ponceau S dye was washed away by de-ionized H_2O and the stained membrane was imaged by Epson perfection V700 Photo scanner. Subsequently, the membrane was placed in the 50 mL Falcon tube and blocked with the blocking milk (Table 17) rotating at RT for 1 hour. In the meantime, the antibodies for protein detection (Table 11) were diluted either in the antibody dilution buffer (Table 17) or the BSA antibody dilution buffer (Table 17; antibodies for pPLK1 or pTCTP detection). The incubation with 5 mL of primary antibody solution per tube was conducted on rotation device at 4 °C overnight.

The excess of primary antibody was washed away with 3 times rotating incubation with TBS-T (Table 17) at RT, each for 10 minutes. In the meantime, the horseradish-peroxidase-conjugated secondary antibodies (Table 12) were diluted in the antibody dilution buffer, transferred on the membranes and incubated rotating at RT for 1 hour. Afterwards, the membranes were TBS-T-washed 3 times rotating at RT for 10 minutes. The detection was conducted either using the Chemi-Smart imaging system and Chemi-Capt 5000 software or using the Azure c400 imaging system and software. Prior to placing the membranes into the imaging chambers, they were incubated for 2 minutes with 2 mL of Amersham™ ECL Prime chemiluminescent detection reagent mix in the dark. ECL Prime reagent-mediated protein detection is based on light emission upon luminol oxidation carried out by peroxidases conjugated to the secondary antibodies. Images were captured at automatic exposure times and adjusted-automatic exposure times (dependent on the emitted signal). The image signal quantification is described in section 3.2.5.6. The membranes were re-incubated with primary antibodies following wash-out of detection reagent with TBS-T for 10 minutes and provided that protein sizes were different enough to allow efficient detection. Membranes were sealed in autoclave bags and stored at -20 °C.

3.2.3.5. Mass spectrometry

Mass spectrometry of co-immunoprecipitated proteins from section 3.2.3.1 allows to obtain the information about what proteins are pulled down together with protein bound by the antibody (in this case, MYC and HDAC2). Here mass spectrometry and the analysis of the pulled down proteins were conducted by Dr. Gianluca Sigismondo in the lab of Prof. Dr. Jeroen Krijgsveld (Division of Proteomics of Stem Cells and Cancer, DKFZ, Heidelberg, Germany).

For mass spectrometry analysis, the samples bound on beads were washed with PBS and a sequential system of Tris-HCl buffers with increasing salt concentrations. Then beads were conditioned in 100 mM ammonium bicarbonate. Proteins were digested and de-salted by SP3 beads protocol[406]. Peptides were eluted in 0.1 % trifluoroacetic acid and loaded on a trap column. The peptides were separated over a 50 cm analytical column using a 70 min linear gradient of acetonitrile (6-40 %). Peptides were analyzed on an Orbitrap QExactive HF mass spectrometer operated in data dependent acquisition mode with HCD fragmentation.

Raw data was analyzed using MaxQuant free software including the Andromeda search Engine[407,408]. Peptides were identified using Uniprot database of *Homo Sapiens*. Match between runs option was active and both Label Free Quantification (LFQ) and intensity-Based Absolute Quantitation (iBAQ) scores were calculated.

3.2.4. Functional assays

3.2.4.1. Metabolic activity

In order to determine how cells respond to the HDAC and PLK1 inhibitors, a metabolic activity assay was employed. 5000 cells per well were seeded in 96-well tissue culture plates in 100 µL respective medium. Cells were treated after 24 hours with increasing concentrations of single drugs (in order to determine the 50 % inhibitory concentration (IC50); 3.2.5.3) or certain combinations (in order to determine whether the drugs are interacting synergistically; 3.2.5.4). The drugs were dispensed using D300e Digital dispenser (Table 20). Cells were incubated with the drugs for 72 hours. The metabolic activity was determined using a WST-8 assay with the Cell Counting Kit-8 (Table 19). The WST-8-based method is a colorimetric assay where tetrazolium salt is reduced by the dehydrogenases of metabolically active, i.e. viable, cells. This allows the formation of yellow formazan dye which absorbs at 450 nm and directly correlates with the number of living cells. Here, after 72 hours of treatment 10 µL of WST-8 reagent were added to the cells and incubated at 37 °C for 2 hours (4 hours for spheroids). Absorbance at 450 nm was measured

using FLUOstar OPTIMA plate reader (Table 20). All plates included solvent, untreated and background (only medium) controls. All metabolic activity measurements were carried out in technical triplicates.

3.2.4.2. Caspase-3-like activity

In order to differentiate whether the treatment is inducing apoptosis or another type of cell death, the Caspase-3 Fluorometric Assay Kit (Table) was used. Very mild cell lysis allows to retain the enzymatic activity of cleaved caspases that are induced by apoptosis induction signaling network. Caspases recognizing tetrapeptide DEVD (caspase-3 and -7) are able to cleave the provided substrate DEVD-AFC which emits 400 nm light when conjugated. Upon cleavage, free AFC emits light at 505 nm, which can be detected.

Here, 24 hours prior to treatment 10^6 cells/well were seeded in 6-well format. 16 hours before sample collection, apoptosis was induced in the positive control well with 20 second exposure to UV (35 mJ/cm^2). Cells were harvested using trypsin-EDTA as described previously. The cell pellets were collected by centrifugation at 1200 rpm for 5 minutes and lysed in the ice-cold Cell Lysis Buffer (provided with the kit). The lysates were incubated on ice for 10 minutes and the protein concentrations were measured using BCA protein quantification assay (3.2.3.3). 25-75 µg of proteins were diluted with lysis buffer to a final volume of 55 µL. The solution was mixed with 55 µL of 2X Reaction buffer and 10 mM DTT and distributed by 50 µL/well into 96-well black microplate in technical duplicates. 2.5 µL/well of 1:1 DEVD-AFC:DMSO substrate was added. The reaction was measured using FLUOstar OPTIMA (Table 20) plate reader at 37 °C with 380 nm excitation and 520 nm emission filter for 3 hours continuously. The slope/min output was determined based on the exponential part of the curves and normalized to the untreated control in order to obtain fold change values.

3.2.4.3. Flow cytometry

Flow cytometry or fluorescence activated cell sorting (FACS) allows cell counting based on various properties of the cells, including their size (forward scatter – FSC), granularity (side scatter – SSC), surface markers or expressed proteins. In this thesis flow cytometry was used to determine the percentage of cells in certain cell cycle phases upon staining with propidium iodide (PI). PI intercalates the DNA with no sequence preference, thus allowing a direct measurement of the amount of DNA and the cell cycle (Figure 24). Upon excitation PI emits orange-red light at 617 nm which can be detected using FACS cell analyzer (here BD FACS Canto II).

PI staining was carried out on the cells harvested after synchronization (3.2.1.8) and on the cells after HDACi and PLK1i single agent and combination treatment. For the latter, 10^6 cells/well were seeded and treated 24 hours after seeding. After the treatment, cells were harvested as described previously and resuspended in 10 mL of fresh medium. 1 mL was aliquoted for cell counting using Vi-Cell XR automatic cell counter. Cells were centrifuged at 1200 rpm for 5 minutes. The supernatant was decanted leaving 200 µL for the resuspension of the cell pellet in order to reduce the number of cells sticking to the walls of the Falcon tube during the fixation process. Cells were fixed and permeabilized (PI is not membrane permeable) by dropwise adding 1 mL of ice-cold 70 % ethanol while vortexing the cell suspension. The mix was incubated at 4 °C for 1-2 hours. Upon fixation cells were centrifuged at 1200 rpm for 5 minutes at 4 °C and washed with 1 mL of ice-cold FACS washing buffer (Table 17). Cells were centrifuged at 1400 rpm for 5 minutes at 4 °C, resuspended in 400 µL of FACS staining solution (Table 17) and incubated at 37 °C for 20 minutes in the dark with gentle shaking. Cells were centrifuged at 1400 rpm for 5 minutes at 4 °C, resuspended in 130 µL of PBS and subjected to measurement by BD FACS Canto II analyzer. PI fluorescence of 10 000 single cells was acquired using the PE filter setting and quantified using FlowJo® analysis software. FACS experiments were carried out at the Flow Cytometry Core Facility, DKFZ, Heidelberg, Germany.

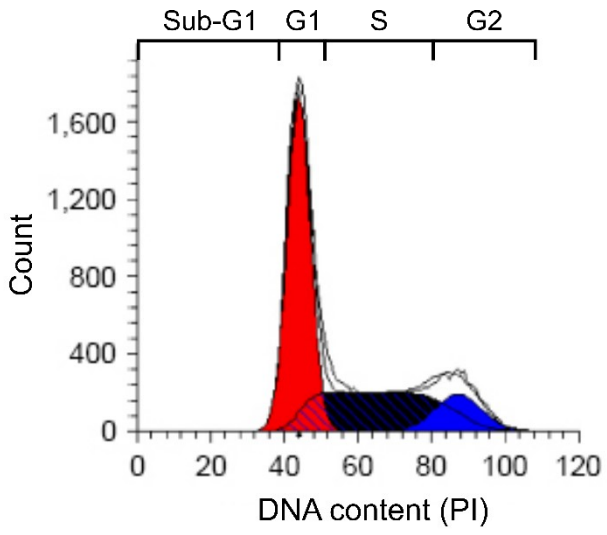

Figure 24 Exemplary histogram depicting normal cell cycle. Detected PI levels are directly proportional to the DNA content. Adapted from Han et al (2018)[4].

3.2.5. Statistical analysis and graphics

3.2.5.1. Expression and correlation analysis of publicly available datasets

The *MYC*, *MYCN* and *PLK1* gene log-transformed expression data from the publicly available datasets (Table 22) was downloaded from the R2 database (Table 21). The following probes were used: 202240_at (*PLK1*), 202431_s_st (*MYC*), 209757_s_at (*MYCN*). The MYC and PLK1 protein levels in MB (Table 22) were either supplied by the collaborators (Dr. Marc Remke and Daniel Picard, Düsseldorf University, Düsseldorf, Germany) or downloaded from the data repository. The expression values were plotted using *ggplot2* package[409] from RStudio v1.1.463. In order to

evaluate the correlation of *MYC* and *PLK1* or *MYCN* and *PLK1* mRNA expression, linear regression model and Pearson correlation coefficient were used.

3.2.5.2. Identification of significantly downregulated MYC target genes upon entinostat treatment

The publicly available (Ecker, Thatikonda, et al, in revision) datasets of GEP of HD-MB03 and MED8A cells treated with 5 µM of entinostat for 6 hours were obtained from the authors. The fold-change and adjusted p-values were determined using Bioconductor *limma* package[410] on the pre-normalized datasets. HALLMARK_MYC_TARGETS_V1 and V2[16] gene sets were downloaded from MSigDB molecular signatures database (Table 21). The genes from both gene sets were pooled. Only differentially expressed genes from the publicly available datasets that were also in the MYC target list were evaluated. The volcano plots were drawn with *ggplot2* package[409] with the significantly down- or up-regulated genes marked as genes of interest (due to short treatment time, log-transformed fold change values did not reach -2 or 2). The list of the genes of interest was further narrowed down based on the drugability of the potential targets (i.e. determining whether the selective inhibitor is available). Finally, the target with inhibitors in clinical development was chosen.

3.2.5.3. Dose-response curves and 50 % inhibitory concentrations (IC50)

The dose-response curves and IC50 calculations were based on metabolic activity assays of the cells exposed to a range of concentrations of HDAC and PLK1 inhibitors. Five-parameter logistic model was determined to be the best fit for the dose-response relationship studied in this thesis. The model was fitted using the *drc* package[411] in RStudio v1.1.463 and plotted with *ggplot2* package[409]. Relative and absolute IC50 were determined using GraphPad Prism v5.01.

3.2.5.4. Drug interaction: Chou-Talalay and Bliss Independence models

Drug interaction was evaluated using CompuSyn v1.0 software (Table 23; metabolic activity data evaluation) and Bliss Independence model (described in 1.5; other types of data).

With calculations established by Chou and Talalay, CompuSyn software is based on Loewe model (1.5) and calculates the combination index (CI) according to the Median Effect Equation[412] with median as the universal reference point. In order to be able to calculate the CI with CompuSyn, cells were treated with a range of concentrations of single HDACi and PLK1i, the range of concentrations of HDACi with IC50 concentration of PLK1i (and vice versa), the constant ratio with increasing concentrations of the drugs and a combination of inversed concentrations

(highest concentration of HDACi + lowest concentration of PLK1i and so on). The CI values below 0.9 we considered synergistic, CI between 0.9 and 1.1 indicates additivity, CI between 1.1 and 2 indicated buffer antagonism (associated to unsuitable ratio of concentrations of both drugs) and CI above 2 was determined to show hyper-antagonistic interaction. The calculations for Bliss Independence were based on the equation described in 1.5.

3.2.5.5. Gene expression profile analysis and gene set enrichment analysis

As stated above, the analysis of GEP and the gene set enrichment analysis (GSEA) were conducted in collaboration with Thomas Hielscher (Division of Biostatistics, DKFZ, Heidelberg, Germany). Affymetrix CEL files were GCRMA normalized and log-transformed. Differentially expressed probesets due to treatment were identified using the empirical Bayes approach based on moderated t-statistics as implemented in the Bioconductor package *limma*[410] accounting for paired samples. Gene set enrichment analysis was performed using the camera test[413]. In case a gene was represented by multiple probesets, the probeset with the strongest effect was selected for GSEA. p-values were adjusted for multiple testing using the Benjamini-Hochberg correction in order to control the false discovery rate. All analyses were performed with statistical software R 3.6.

3.2.5.6. Immunoblot quantification

The images from 3.2.3.4 were saved in *.tiff format, converted to *Grayscale* picture mode using IrfanView v4.54 and saved in *.jpeg format. The quantification of immunoblots was carried out using ImageJ v1.52 software. The region of interest (ROI) was defined separately for each of the blots based on the largest band present. The “Mean gray values” were measured for each lane. In addition, background values of each lane were determined and exported to the *.csv file. After the measured pixel density was inverted (subtracted from 255), the background values were subtracted in order to obtain the net values of the proteins. Finally, the values were normalized to the loading control (here, ACTB) and, in some experiments, to untreated/solvent control.

3.2.5.7. Experimental settings

Unless stated otherwise, all experimental data is depicted in mean ± standard deviation (SD). All experiments were carried out in at least 3 independent biological replicates. Technical replicates were used in some of the experiments, as described above. All data was visualized using RStudio v1.1.463 and Inkscape v0.92.4. Experimental data was compared using two-tailed unpaired Student’s t-test with or without Welch correction as appropriate. Comparisons between multiple

groups were conducted using two-way ANOVA. p-values lower than 0.05 were considered statistically significant.

4. Results

The main aim of this thesis was to elucidate potential therapeutic options for MYC-addicted medulloblastoma. As MYC activity is often dependent on its' partners in the transcriptional-activation and repression complexes, MYC-binding proteins in the MYC and HDAC2 complex were determined in the first part. This part is described in chapter 4.1.

As previous studies conducted in the laboratory suggested that class I HDACs are possible targets, the first combination therapy partner was the class I HDAC selective inhibitor entinostat. In the second part of the thesis (chapter 4.2), we elucidated another drug, PLK1i, indirectly targeting MYC that would have the potential to interact synergistically with HDAC inhibition. The cellular responses and mechanisms behind the synergistic behaviour were investigated, as well.

4.1. MYC multiprotein complex targeting

As discussed above, targeting of the MYC protein remains a challenge in anti-cancer therapy research. Therefore, other options are explored including targeting MYC binding partners in transcription-relevant protein complexes. As published previously (Ecker, Thatikonda, et al, in revision), HDAC2 and MYC are interacting in a protein complex in *MYC*-amplified MB cells, thus explaining preferential entinostat activity in a *MYC*-amplified background. Here we hypothesized that targeting another complex partner in addition to HDAC2 would synergistically inhibit the transcriptional activity of the HDAC2-MYC complex. In addition to increased efficacy, dual targeting of this complex could potentially reduce the toxicity of entinostat since lower doses are needed to achieve the same effect. In the following sections the optimization of the co-immunoprecipitation of the HDAC2-MYC complex is described, followed by the discussion of mass spectrometry results leading to identification of complex members.

4.1.1. Optimization of MYC-HDAC2 complex co-immunoprecipitation conditions

In order to elucidate the potential members of the HDAC2-MYC protein complex we pulled-down HDAC2 and MYC proteins separately, subjected the samples to mass spectrometry and determined the overlap between the identified lists of proteins as potential members of such complex.

First, we determined the optimal conditions of the co-immunoprecipitation (co-IP) of MYC and HDAC2 in the *MYC*-amplified MB cell line HD-MB03. The co-IP itself was conducted using Dynabeads™ protein G beads as described above. As published previously, HDAC2 and MYC

are indeed in a protein complex (Figure 25), as MYC protein signal was obtained in HDAC2 pull-down (Figure 25a) and vice-versa (Figure 25b). In addition, neither HDAC2 nor MYC was pulled down in negative and IgG controls. Interestingly, there was no visible difference between Input #1 (before co-IP) and #2 (lysate after co-IP), where we aimed to see the depletion of MYC or HDAC2, however, the sensitivity of immunoblot assay could be insufficient if the protein levels were low. The presence of unspecific bands and high unspecific signal in general in the MYC immunoblot after MYC co-IP and in HDAC2 immunoblot after HDAC2 co-IP indicated a necessity for further optimization of the protocol.

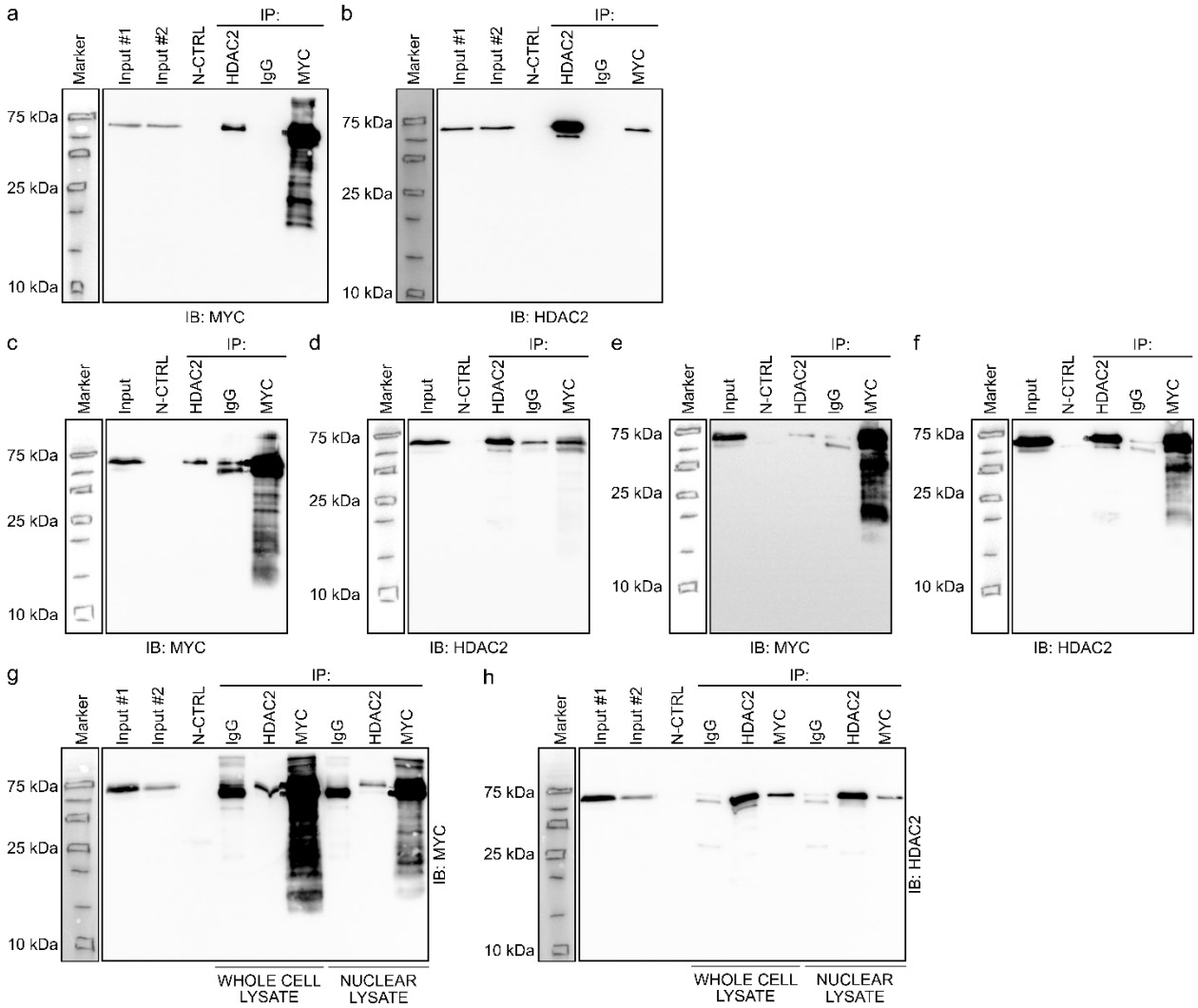

Figure 25 Co-immunopreciptation for HDAC2 and MYC followed by immunoblotting in HD-MB03 cell line. a – IB for MYC in whole cell lysate without bead crosslinking; b – IB for HDAC2 in whole cell lysate without bead crosslinking; c – IB for MYC in whole cell lysate without bead crosslinking; d – IB for HDAC2 in whole cell lysate without bead crosslinking; e – IB for MYC in nuclear lysate without bead crosslinking; f – IB for HDAC2 in nuclear lysate without bead crosslinking; g – IB for MYC after bead crosslinking; h - IB for HDAC2 after bead crosslinking. IP: immunoprecipitation. IB: immunoblot. Input #1: lysate before co-IP. Input #2: proteins remaining in discarded lysate after co-IP. N-CTRL: negative control (no proteins). IgG: IgG control.

Subsequently, in order to obtain lower levels of unspecific signal and because HDAC2 and MYC protein complex is most likely affecting transcription, we isolated the nuclei. We compared the co-IP of HDAC2 and MYC in nuclear fraction and whole cell lysates. Extracting the nuclei prior to co-IP reduced the amount of the proteins in the samples, but helped to obtain the co-IP signals with reduced unspecific binding (Figure 25c-f; the exposure times were increased in nuclear lysate immunoblots due to low protein levels). However, here even though MYC was pulled down with HDAC2 and vice versa, a number of unspecific bands and strong unspecific signals in the IgG control showed a necessity for further optimization.

For the final optimization step, we crosslinked the co-IP antibodies to the Dynabeads™ as described above in order to reduce the amount of antibodies eluted together with pulled down proteins and thus background signal. After extraction of the nuclei and the crosslinking step, the unspecific binding was further reduced, especially for the HDAC2 protein signal (Figure 25g and h). Furthermore, the MYC signal in the HDAC2 co-IP (Figure 25g) and vice-versa (Figure 25h) was evident, including the depletion of the proteins in the Input #2 samples.

The samples obtained after the co-IP of nuclear lysates with matched IgG controls were sent for mass spectrometry analysis, after the verification of correct co-IP using immunoblotting. The results of mass spectrometry are discussed in the following section.

4.1.2. Identification of MYC-HDAC2 complex proteins

As described in previous chapters, co-IP of MYC and HDAC2 was followed by mass spectrometry carried out by collaborators in the Division of Proteomics of Stem Cells and Cancer (Prof. Jeroen Krijgsveld). After the internal quality control, the label-free quantification (LFQ) of intensity of proteins in HDAC2/MYC co-IP samples over the respective IgG controls were plotted (Figure 26d). Thus, proteins enriched in both, HDAC2 and MYC co-IP were determined and ranked by their iBAQ scores (Figure 26b and c). Overall, 148 proteins were determined to be present in both, HDAC2 and MYC co-IPs, 135 (130 when applying more stringent cut-off) only in the MYC co-IP and 225 (214 when applying more stringent cut-off) only in the HDAC2 co-IP (Figure 26f). Some of the known HDAC2 and MYC interactors are also shown in green in Figure 26 (e.g. MYC interaction partner MAX, proteins of NuRD and NCOR complexes or YY1). All proteins bound to MYC and HDAC2 and their LFQ and iBAQ values are shown in the Supplementary table 1.

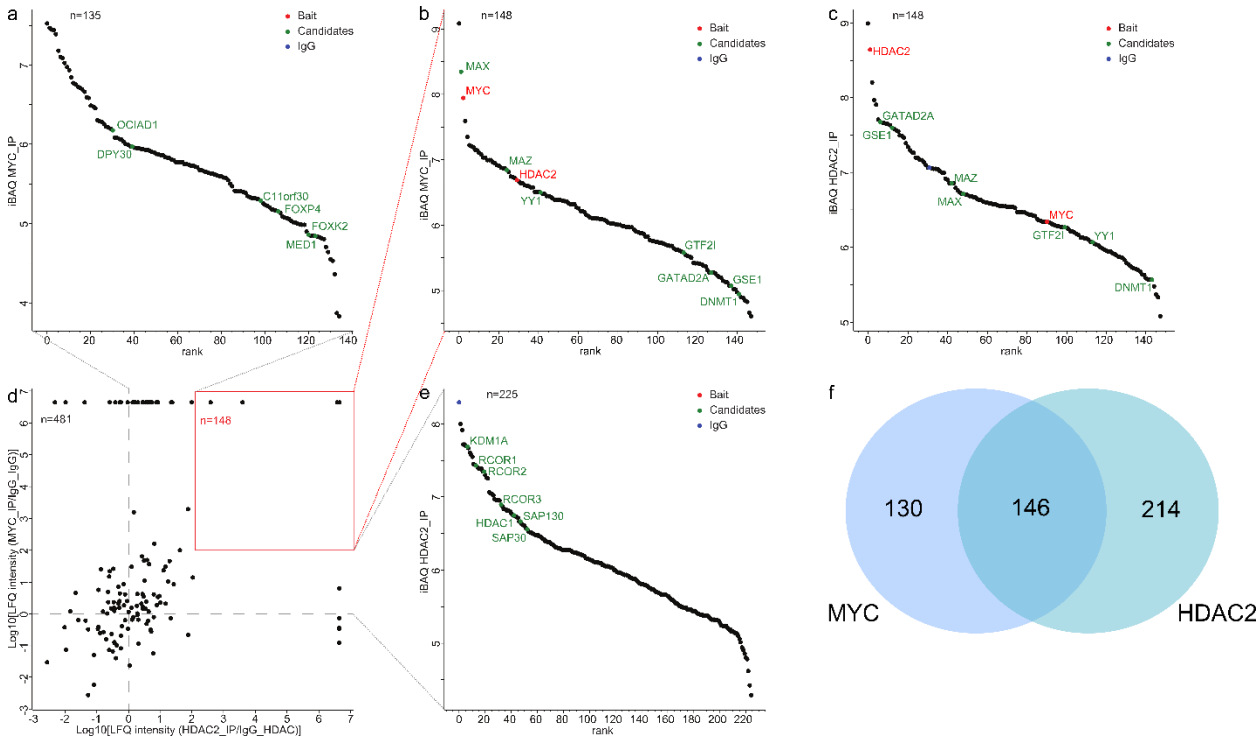

Figure 26 Summary of mass spectrometry results. a – proteins present only in MYC co-IP ranked by iBAQ; b – proteins present in both co-IPs ranked by MYC iBAQ; c - proteins present in both co-IPs ranked by HDAC2 iBAQ; d – LFQ intensities of HDAC2/HDAC2_IgG vs MYC/MYC_IgG; e - proteins present in only in HDAC2 co-IP ranked by iBAQ; f – Venn diagram showing the number of proteins potentially bound to HDAC2 and MYC vs proteins interacting to MYC and HDAC2 separately.

All proteins depicted in the red rectangle (Figure 26d) were then entered to the STRING protein-protein interaction web-tool which shows potential interactions and proteins known to bind together into complexes. Single nods were removed from further analysis with only high strength interactions left. As shown above, NuRD and coREST complex member proteins (NuRD: MTA2, CHD4, GATAD2A; coREST: ZNF217) were pulled down with MYC and HDAC2 (Figure 27). In addition, proteins involved in a variety of other processes, like DNA replication, mitochondrial respiratory chain regulation, mitotic apparatus, RNA processing, as well as protein biogenesis and homeostasis were found to be bound to MYC and HDAC2 in HD-MB03 cells. As we hypothesized targeting transcriptional HDAC2-MYC complex, we focused on the proteins depicted in top left corner of Figure 27. The top candidates identified were TBL1X, YY1 and DNMT1. TBL1X protein is involved in protein degradation and transcriptional regulation, known to bind HDAC3 in SMRT complex. YY1 is a multifunctional transcription factor known to direct HDACs and HATs to the target genes. Finally, DNMT1 is a maintenance DNA methyltransferase enzyme. All these proteins are bound to HDAC2 and MYC, are involved in transcriptional regulation and could potentially be targetable. However, no direct small molecule inhibitors

against TBL1X and YY1 have been reported. Regarding the third candidate, DNMT1, only general DNA methylation inhibitors (e.g. decitabine or 5-aza-cytidine) have been brought to the clinic, and direct methyltransferase inhibitors have not shown success in clinical trials. Thus, no direct targets for clinically applicable combination therapy were identified in the first part of the project.

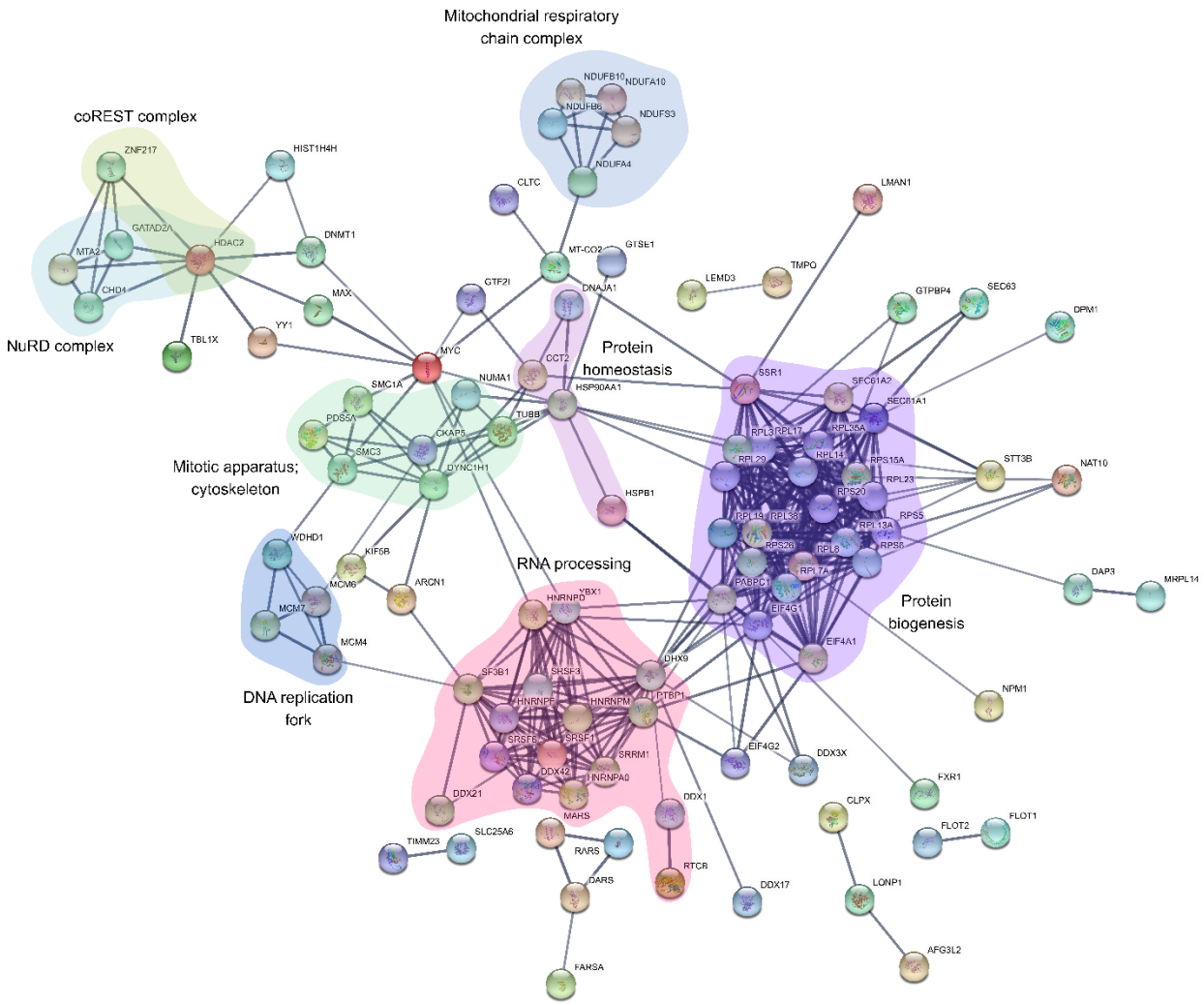

Figure 27 Known protein-protein interactions and protein functions mapped on both, HDAC2 and MYC, bound protein list. Bait proteins are shown in red. Single nods were removed. Only high strength interactions shown.

Taken together, we optimized the co-IP assay in *MYC*-amplified MB cells and confirmed that HDAC2 and MYC indeed form a protein complex (Ecker, Thatikonda, et al, in revision). We examined protein-protein interactions of HDAC2 and MYC with other proteins, and identified potential processes these interactors are involved in. Finally, we found three potential protein-candidates to be involved in transcription-regulatory HDAC2-MYC complex, however, none of them were suitable for clinically translatable combination targeting. Therefore, we focused the

study on indirect MYC targeting options and combining those compounds with entinostat as described in the next sections.

4.2. Indirect MYC targeting

As stated previously, indirect targeting of MYC has been proven to be successful in reducing both MYC protein levels as well as the effects of *MYC* overexpression in the cell. In MYC-addicted tumors, this downregulation of the transcription factor frequently leads to apoptosis and tumor mass reduction. Here, we are exploring a potential combination therapy indirectly targeting the MYC protein in two ways: the MYC-HDAC2-transcriptional complex (described in previous section), and the post-translational modification-mediated degradation pathway of MYC.

4.2.1. Entinostat selectivity for *MYC*-amplified background

Entinostat, an inhibitor specific for class I HDACs, has been previously shown as selective for *MYC*-amplified medulloblastoma cell lines. Prior to elucidating a potential combination partner for entinostat, in this section this data was confirmed by determination of metabolic activity, cell viability, cell cycle and cell death response to entinostat treatment in MB cell lines. The activity is also confirmed in neuroblastoma (NB) and high-grade glioma (HGG).

4.2.1.1. Entinostat IC50 estimation and on-target effect

The response to entinostat was determined by measuring metabolic activity of the cells after 72-hour treatment with a range of concentrations of entinostat. As evident in Figure 28a, the IC50s were lower in *MYC/N*-amplified compared to non-amplified cell lines in MB, HGG and NB (Table 25, Figure 28a-d). Moreover, some cells weakly respond to entinostat even at the highest concentrations (MB: UW228-2 and ONS-76, HGG: SU-DIPG-XVII and SU-pcGBM2, NB: SK-N-AS, SH-SY5Y), thus showing a possible resistance to HDAC inhibitors in general.

In order to validate the *MYC*-amplification and overexpression as a necessary factor for response to the entinostat treatment, a UW228-2 cell line stably expressing doxycycline-inducible MYC construct (Ecker, Thatikonda, et al, in revision) was used. Indeed, *MYC* overexpression reduced the IC50 1.3-times comparing ON and OFF cells (Figure 29).

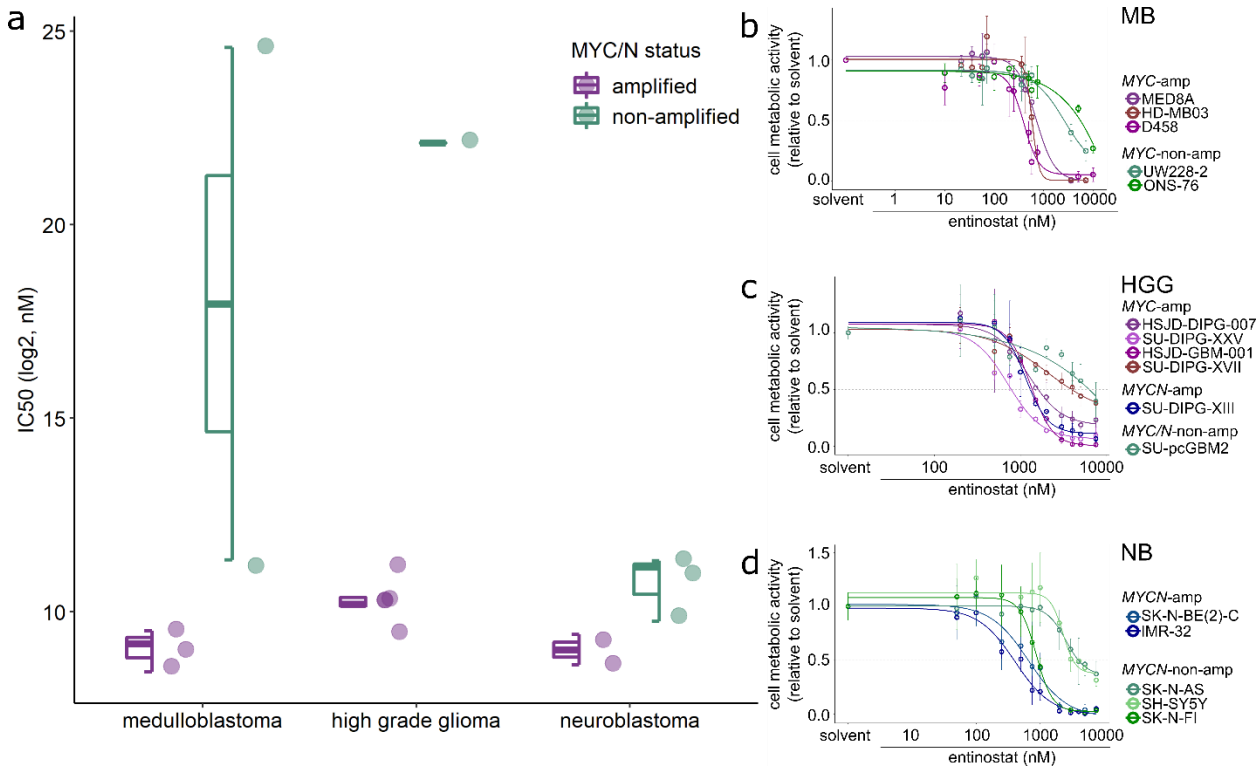

Figure 28 MB, HGG and NB cell line response to class I HDAC inhibitor entinostat. a – 50 % inhibitory concentrations (IC50) of cell lines in different entities; b (MB), c(HGG) and d (NB) – dose-response curves depicting cell response to a range of entinostat concentrations. Graphs show mean ±SD.

Table 25 50 % inhibitory concentrations (IC50) of entinostat in MB, HGG and NB *MYC/N*-amplification positive or negative cell lines.

Entity	Cell line	*MYC/N*-amp	Entinostat IC50 (nM)
Medulloblastoma (MB)	MED8A	*MYC*	730
	HD-MB03	*MYC*	580
	D458	*MYC*	350
	UW228-2	-	2600
	ONS-76	-	25×10^6
High-grade glioma (HGG)	HSJD-DIPG-007	*MYC*	1180
	SU-DIPG-XXV	*MYC*	687
	HSJD-GBM-001	*MYC*	1330
	SU-DIPG-XVII	*MYC*	2300
	SU-DIPG-XIII	*MYCN*	1140
	SU-pcGBM2	-	45.4×10^5
Neuroblastoma (NB)	SK-N-BE(2)-C	*MYCN*	686
	IMR-32	*MYCN*	396
	SK-N-AS	-	2560
	SH-SY5Y	-	2280
	SK-N-FI	-	867

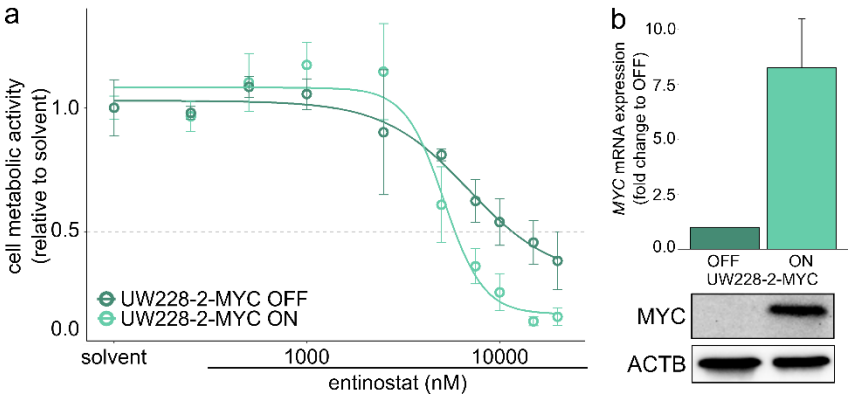

Figure 29 Doxycycline-inducible UW228-2-pMYC cell line response to entinostat. a – dose-response curve comparing ON and OFF cells. b – *MYC* mRNA and protein expression induced by doxycycline addition to the culture. Graphs show mean ±SD.

In order to confirm that entinostat is actually inhibiting class I HDACs, so-called on-target activity, we treated 3 representative MB cells lines (*MYC*-amplified: MED8A and HD-MB03, *MYC*-non-amplified UW228-2) with 500 nM and 1500 nM entinostat for 24 hours and monitored whether H3K27 acetylation mark levels were increasing. Indeed, acetylation compared to the solvent control increased 1.5 times (UW228-2), 5.8 times (HD-MB03) and 500 times (MED8A), respectively (Figure 30). This further underscored the difference between *MYC*-amplified and non-amplified cell response to the class I HDAC inhibition by entinostat and showed that entinostat is indeed targeting class I HDACs in these model cell lines in a dose-dependent manner.

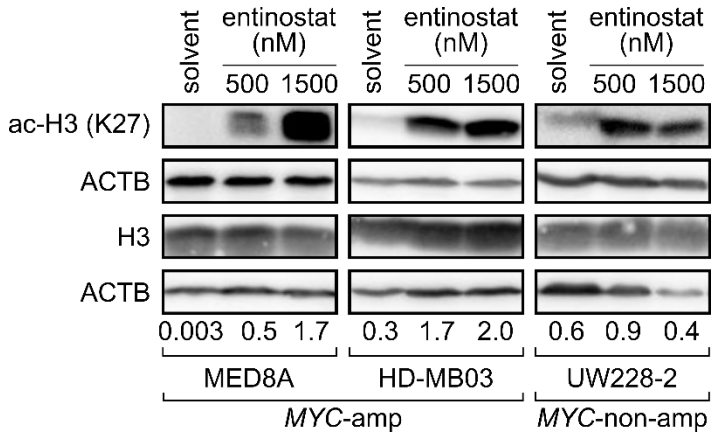

Figure 30 Entinostat on-target effect in MB cell lines. Acetylated H3 levels increased after 24-hour treatment with 500 nM or 1500 nM of entinostat in all cell lines.

4.2.1.2. Entinostat effect on cell viability, cell cycle and cell death

In order to confirm the results of the metabolic activity assay, the trypan blue exclusion technique was employed. This technique was used to determine the viable and dead cell numbers in the

MB, HGG and NB models. The cells were treated with a range of entinostat concentrations determined based on their metabolic activity IC50 for 72 hours, as indicated (Figure 31).

Entinostat significantly reduced the viable cell number in a concentration-dependent manner in all tested cell lines. A difference in viable cell number was evident in MB between *MYC*-amplified (MED8A and HD-MB03) and non-amplified (UW228-2) cell lines. After treatment with the highest concentration of entinostat, *MYC*-non-amplified cell line retained almost 50 % of viable cells (Figure 31a). No differences between *MYC/N*-amplified and non-amplified cell lines were observed in the models representing HGG (Figure 31b) and NB (Figure 31c).

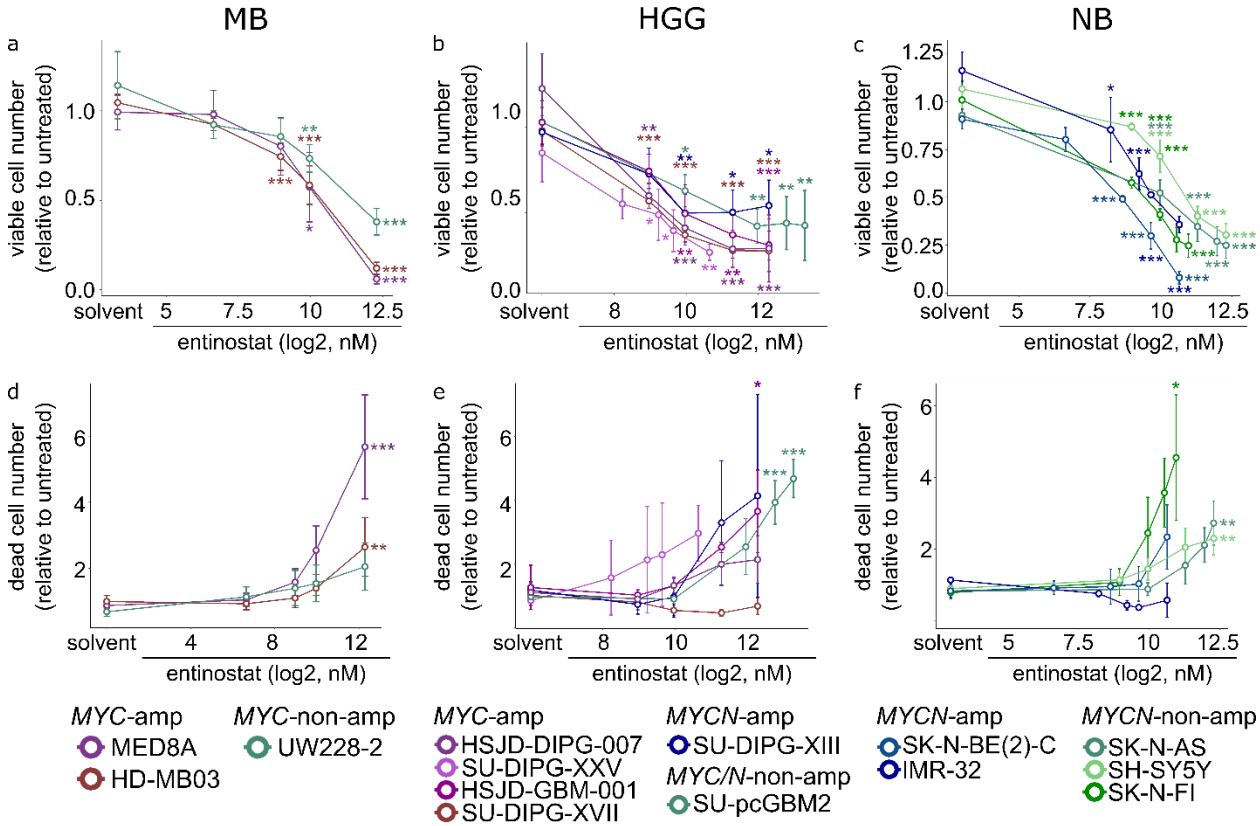

Figure 31 Relative viable and dead cell number after entinostat treatment for 72 hours. Viable (rel. to untreated) cells in MB (a), HGG (b) and NB (c) models. Dead (rel. to untreated) cells in MB (d), HGG (e) and NB (f) models. Graphs show mean ±SD. One-way ANOVA was used to compare to untreated control: *p < 0.05; **p < 0.01; ***p < 0.001

In concordance with reduction of viable cell number, the relative number of dead cells was increasing in the majority of tested cell lines. The numbers of dead cells were significantly higher compared to the solvent control after treatment with the highest concentration of entinostat in both

MYC-amplified cell lines (Figure 31d, 5-6-fold in MED8A and 3-fold in HD-MB03), but not in the non-amplified MB cell line.

No difference in relative dead cell numbers was detected between *MYC/N*-amplified and non-amplified HGG and NB cell lines. Of note, the *MYC/N*-amplified SU-DIPG-XVII (HGG) and IMR-32 (NB) cell lines did not show an increase in dead cell numbers (Figure 31e, f). As confirmed visually during the experiment process, entinostat indeed induced substantial cell death in both of those cell lines. This indicates that the cell death in SU-DIPG-XVII and IMR-32 cells has already occured at the 72-hour timepoint, therefore suggesting that earlier timepoint could be chosen for viability evaluation in these cell lines.

In order to study changes in cell cycle upon entinostat treatment, we used the n=3 representative MB cell lines, MED8A, HD-MB03 (both *MYC*-amplified) and UW228-2 (non-amplified). The cells were treated for 48 hours with three entinostat concentrations and subsequently cell cycle phases were determined by flow cytometry analysis after staining with propidium iodide. In both *MYC*-amplified cell lines (MED8A and HD-MB03), but not in the *MYC* non-amplified cell line (UW228-2) the treatment with entinostat significantly increased subG0/G1 cell fraction indicating cell death (Figure 32), in accordance with the results from the viability experiment (Figure 31). In addition to the subG0/G1 increase, a decrease in the S-phase was noted in *MYC*-amplified cells (significant differences only in HD-MB03), indicative of cell cycle arrest and cell death.

Finally, as the data from the analysis of the cell cycle and viability indicates that entinostat is promoting the cell death, we explored whether the cells are dying in an apoptotic manner. Upon 48-hour treatment with entinostat, we measured two hallmarks of apoptosis signalling, the caspase-3 activity and PARP1 cleavage.

Caspase-3 activity was induced in a concentration-dependent manner in both of *MYC*-amplified cell lies (MED8A and HD-MB03), but not in the *MYC* non-amplified (UW228-2) (Figure 32c). Furthermore, the full-length-to-cleaved PARP1 ratio was substantially reduced in *MYC*-amplified cells (particularly in HD-MB03), but not in UW228-2 (Figure 32d, e) confirming that entinostat treatment in MB cells is inducing apoptosis.

Taken together, the results presented in 4.2.1 confirm that the class I HDACi entinostat is selective to *MYC*-amplified MB cells reducing their metabolic activity and viability as well as arresting the cell cycle at the S-phase and inducing apoptosis. In addition, *MYC*-non-amplified cells also

respond to entinostat treatment, however, without inducing cell cycle arrest and cell death at comparable entinostat concentrations. Finally, in the cell lines tested from other entities, HGG and NB, the difference between *MYC/N*-amplified and non-amplified cells in terms of response to entinostat treatment was not linked to the *MYC/N* status as clearly as in the MB cells tested.

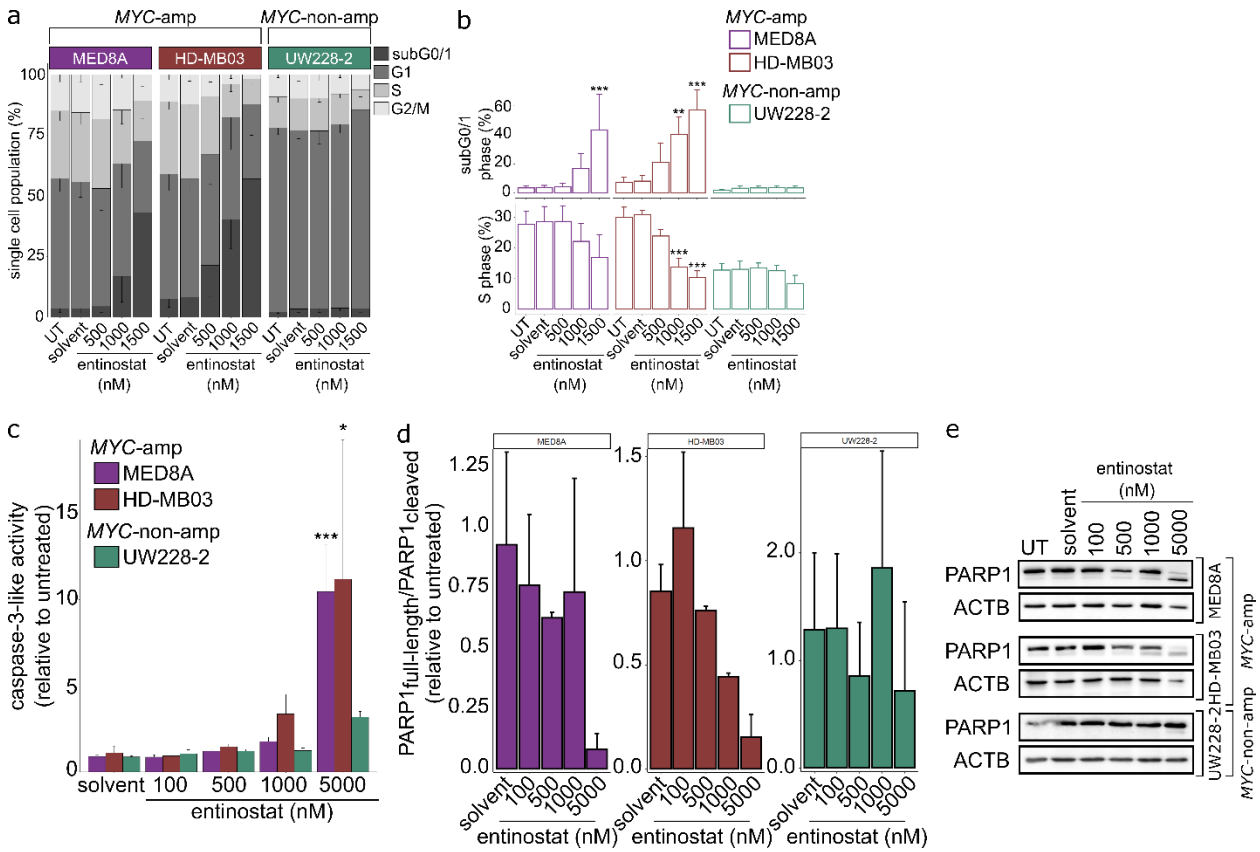

Figure 32 Entinostat activity on the cell cycle and cell death in MB cells. a – distribution of the cell cycle phases in MB after 48-hour treatment with entinostat; b – subG0/G1 and S-phase proportion; c – caspase-3-like activity induction; d – full-length and cleaved PARP1 ratio; e – representative immunoblots for PARP1. Graphs show mean ±SD. One-way ANOVA was used to compare to the untreated control: *p < 0.05; **p < 0.01; ***p < 0.001.

4.2.2. PLK1 as a target for combination therapy with entinostat

As mentioned previously, in this section we have elucidated a potential combination partner for entinostat using a previously generated dataset (Ecker, Thatikonda, et al, in revision). Here the filtering for potential combination partner target and its' expression in primary tumors and model cell lines are described.

4.2.2.1. *Identification of PLK1 as a potential target*

In order to elucidate potential targets for combination therapy with entinostat, we determined which MYC target genes, encoding proteins with cancer-therapy-targetable function, are significantly downregulated after entinostat treatment (Figure 33a). Generating a previously described dataset (Ecker, Thatikonda, et al, in revision), we used a *MYC*-amplified MB cell line HD-MB03 which treated for 6 hours in order to capture only a direct effect of entinostat on gene expression landscape. To achieve an observable effect, a high concentration of entinostat (5 µM) was used.

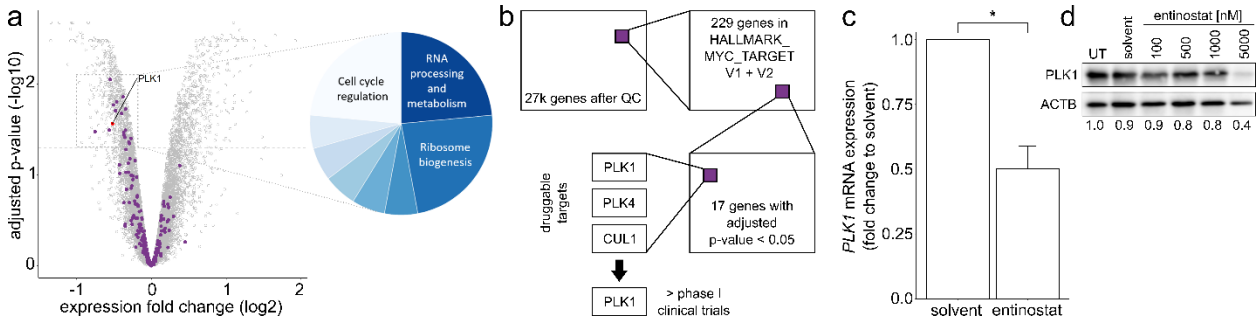

Figure 33 Entinostat combination partner target identification and validation. a – volcano plot with all differentially regulated genes after treatment with 5 µM entinostat for 6 hours with MYC-target genes shown in purple and separated in a pie chart by function; b – filtering scheme of determination of target for combination partner; c – *PLK1* downregulation upon 5 µM entinostat treatment for 6 hours on mRNA level; d – PLK1 protein level upon 24-hour entinostat treatment. Graph shows mean ±SD. t-test was used to compare solvent and entinostat-treated cells: *p < 0.05

27 thousand probes passing the quality control were filtered for MYC target genes summarized in HALLMARK_MYC_TARGET_V1 and V2 lists[16] (Figure 33b). HALLMARK_MYC_TARGET_V1 and V2 together are comprised of n=229 MYc target genes. 17/229 (7.4 %) of the MYC target genes were significantly downregulated after entinostat treatment (Supplementary table 2). Due to the fact that downregulated gene expression fold-change did not reach the usually applied threshold (-2 and 2) and strong changes were not expected due to the short timepoint selected, fold-change filtering was not applied. The majority of the downregulated genes were encoding proteins involved in cell cycle regulation, RNA metabolism and ribosome biogenesis in line with previously described MYC functions in cancer. 3/17 potential targets, PLK1, PLK4 and CUL1 (cullin-1, E3 ubiquitin ligase complex member), were druggable (i.e. with published inhibitors). PLK1 was chosen as a target, since PLK1is have advanced to phase III clinical trials and thus represent a highly translatable therapeutic option.

We validated that PLK1 is indeed downregulated upon 5 µM entinostat treatment for 6 hours on mRNA level (Figure 33c). We also observed the reduction of PLK1 protein levels after entinostat treatment for 48 hours (Figure 33d).

4.2.2.2. PLK1 mRNA and protein expression and function in cell lines

In order to evaluate target presence, *PLK1* mRNA expression was examined in MB, HGG and NB models with and without *MYC/N* amplification. *MYC/N* overexpression was confirmed in all models (Supplementary figure 1).

PLK1 mRNA is expressed significantly higher in all MB and HGG cell lines comparing to commercially available healthy cerebellum RNA (Figure 34). Since no commercially available healthy control for NB cells, *MYCN*-non-amplified cell line SK-N-AS was used as a reference. No clear difference between *MYC/N*-amplified and non-amplified MB, HGG, and NB cell lines was detected, both on mRNA and on protein level (MB only). In order to confirm this observation, we pooled all cell lines according to *MYC/N* status and compared the *PLK1* mRNA expression. It was slightly higher in *MYC/N*-amplified cells, however, the difference was not significant (Figure 34e). Overall, these results underscore the prevoiusly described general *PLK1* overexpression in cancer cells independent from *MYC/N* status.

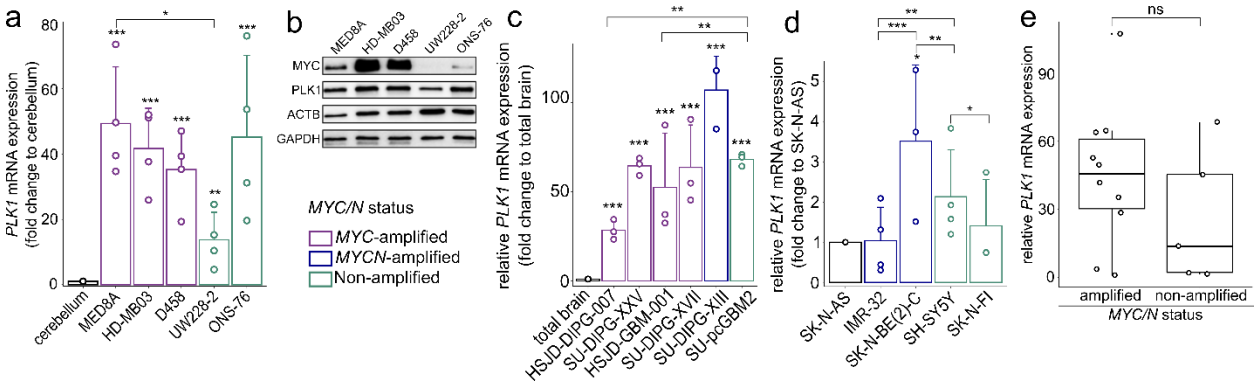

Figure 34 *PLK1* mRNA and protein expression evaluation. a – *PLK1* mRNA expression in MB cell lines; b – PLK1 protein expression in MB cell lines; c – *PLK1* mRNA expression in HGG cell lines; d – *PLK1* mRNA expression in NB cell lines; e – *PLK1* mRNA expression in MB, HGG and NB cell lines separated by *MYC/N*-amplification. Graphs show mean ±SD. One-way ANOVA was used to compare cell lines with healthy controls (a and c) or other cell lines; t-test was used to compare amplified and non-amplified cell lines: *p < 0.05; **p < 0.01; ***p < 0.001

To further understand what could be affecting *PLK1* mRNA expression and potentially the response to treatment with PLK1is, we analyzed the differences in doubling times between the cell lines. The *MYC/N*-amplified cell lines showed doubling times from 27.5 hours (MED8A, *MYC*-

amplified MB) to 61.9 hours (SU-DIPG-XIII, *MYCN*-amplified HGG). The *MYC/N*-non-amplified cell lines showed doubling times from 30.5 hours (ONS-76, MB) to 68.8 hours (SH-SY5Y, NB) (Table 26). In all entities, cell growth curves did not show separation based on *MYC/N*-amplification status (Figure 35). Taken together, no correlation between *MYC* status and cell doubling times could be established (Figure 35d). Hence the sensitivity of *MYC*-amplified cell lines towards PLK1is is not explained by higher doubling times (discussed in section 4.2.3.1).

Table 26 MB, HGG and NB cell doubling times.

Entity	Cell line	*MYC/N* status	Cell doubling time (hours)
Medulloblastoma	MED8A	*MYC* amplified	27.5
	HD-MB03	*MYC* amplified	40.7
	D458	*MYC* amplified	49.1
	UW228-2	Non-amplified	36.6
	ONS-76	Non-amplified	30.5
High-grade glioma	HSJD-DIPG-007	*MYC* amplified	38.2
	SU-DIPG-XXV	*MYC* amplified	37.7
	HSJD-GBM-001	*MYC* amplified	38.7
	SU-DIPG-XVII	*MYC* amplified	44.7
	SU-DIPG-XIII	*MYCN* amplified	61.9
	SU-pcGBM2	Non-amplified	55.4
Neuroblastoma	SK-N-BE(2)-C	*MYCN* amplified	45.9
	IMR-32	*MYCN* amplified	32
	SK-N-AS	Non-amplified	43.9
	SK-N-FI	Non-amplified	44.6
	SK-SY5Y	Non-amplified	68.8

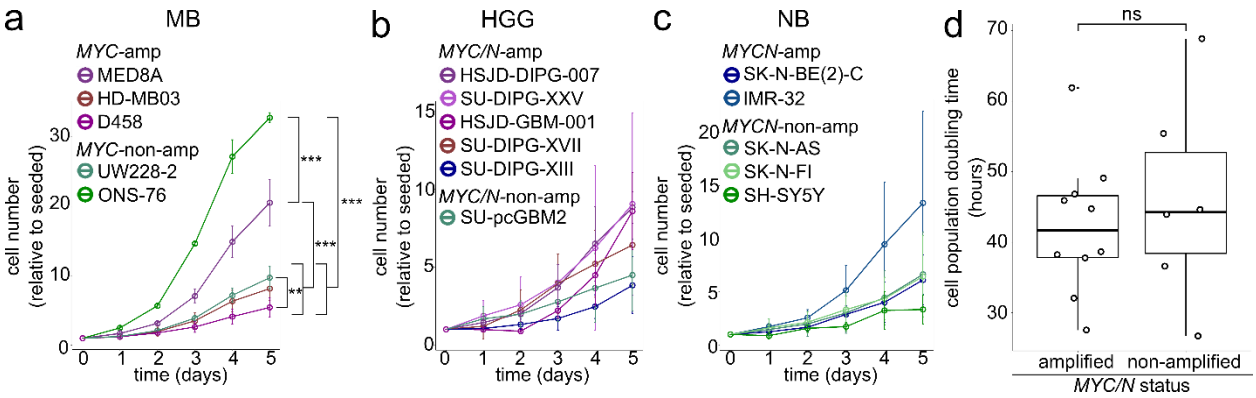

Figure 35 Cell lines growth curves and doubling time comparison based on *MYC/N*-status. Cell number increment in time in MB (a), HGG (b) and NB (c). d – cell doubling time in MB, HGG and NB cell lines separated by *MYC/N*-amplification status. Graphs show mean ±SD. One-way ANOVA was used to compare relative cell numbers at day 5: **p < 0.01; ***p < 0.001

In order to evaluate whether the overexpressed PLK1 retains its' normal function in *MYC*-amplified MB cell lines, we synchronized MED8A cells and determined whether *PLK1* mRNA expression changes dependent on the cell cycle phase and whether PLK1 kinase function remains intact.

The synchronization quality control was performed by analyzing the cell cycle of synchronized cells by propidium iodide staining and flow cytometry (Figure 36a). Subsequently, we determined that in the studied MED8A cell line the S phase takes approximately 4-5 hours, followed by G2 and M phases (approx. 4 hours). The cells go through one full cell cycle in over 14 hours (Figure 36a).

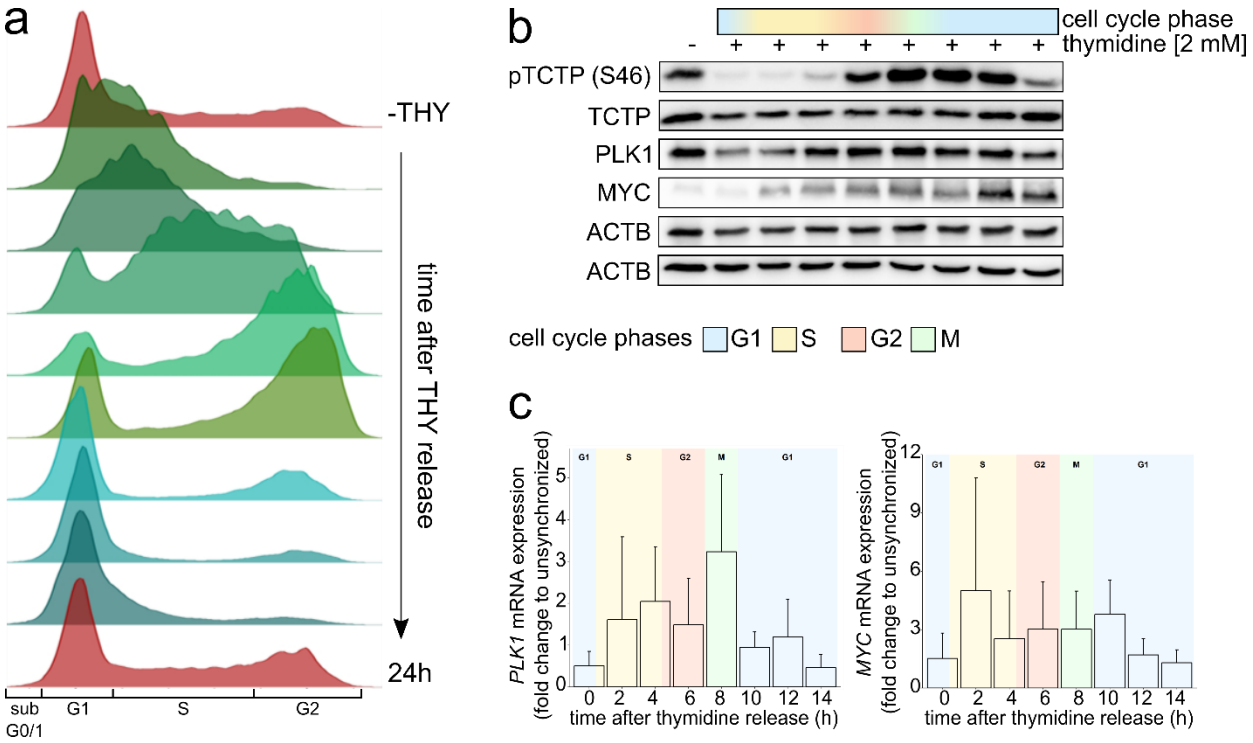

Figure 36 Evaluation of *PLK1* expression and function in different cell cycle phases in MED8A. a – cell cycle phase distribution in time after thymidine release; b – protein expression in cell cycle phases; c – *PLK1* (left) and *MYC* (right) mRNA expression in cell cycle phases. THY: thymidine. Graphs show mean ±SD.

As evident from phosphorylation of serine-46 of TCTP (a direct target of PLK1), PLK1 function in *MYC*-amplified MED8A cells is cell cycle-dependent despite general overexpression of *PLK1* (Figure 36b). Interestingly, MYC protein levels were comparatively low throughout the cycle and again increasing in G1, possibly pointing to MYC involvement in G1/S checkpoint. Alternatively, the observed increase in MYC protein levels could be due to the experimental setup and reflect a low cell density at seeding. Finally, neither *PLK1* nor *MYC* mRNA expression showed large

fluctuations during the cell cycle (Figure 36c) further underscoring the post-translational regulation of both proteins and high MYC protein turnover and lack of transcriptional regulation of the amplified gene.

4.2.2.3. PLK1 mRNA and protein expression in primary tumors

In the previous sections, PLK1 was shown as a potential target for combination therapy with entinostat and to be highly expressed in cell line models. In addition, cell line models were demonstrated to be suitable for PLK1 inhibition evaluation. We therefore proceeded to evaluate PLK1 as a target in primary tumors.

First, we analyzed several publicly available MB datasets comparing *PLK1* mRNA expression among subgroups and subtypes. *PLK1* mRNA expression was significantly higher in all MB subgroups compared to normal cerebellum (Figure 37a), and was the highest in SHH and Group 3. *PLK1* expression in SHH was significantly higher than in WNT and Group 4. In Group 3 *PLK1* expression was significantly higher than in Group 4. In order to evaluate whether *PLK1* mRNA expression is higher in *MYC*-amplification-associated subtypes, two other datasets were studied. The authors of publications where these datasets were first analysed proposed two alternative subtyping strategies for Group 3 and Group 4, Group 3 alpha, beta and gamma (*MYC*-amplification associated)[2] and subtypes I – VIII with subtype II mainly associated with *MYC*-amplification[55]. The latter eventually became the consensus subtyping strategy[56]. Nonetheless, *PLK1* expression is the highest in the subtype with *MYC*-amplification in both datasets, the gamma subtype (significant, Figure 37b) and subtype II (non-significant, Figure 37c) showing a potential relation between *PLK1* overexpression and *MYC*-amplification.

We examined *PLK1* mRNA expression in the INFORM dataset[400] to evaluate the potential for PLK1 targeting not only in primary tumors, but also in relapses (Table 22). Here, *PLK1* was significantly overexpressed in Group 3 MB compared to almost all other malignancies with exceptions of non-Hodgkin lymphoma (NHL), embryonic rhabdomyosarcoma (eRMS) and Wilms tumors (Figure 37d).

We validated *PLK1* overexpression in Group 3 MB tumors by examining two publicly available MB protein datasets separated by subgroups. PLK1 protein levels were again the highest in Group G3a (*MYC*-amplification-associated subgroup in Archer et al publication[403]) and in Group 3 with a significant difference compared to Group 4, in line with the mRNA dataset analysis (Figure 38).

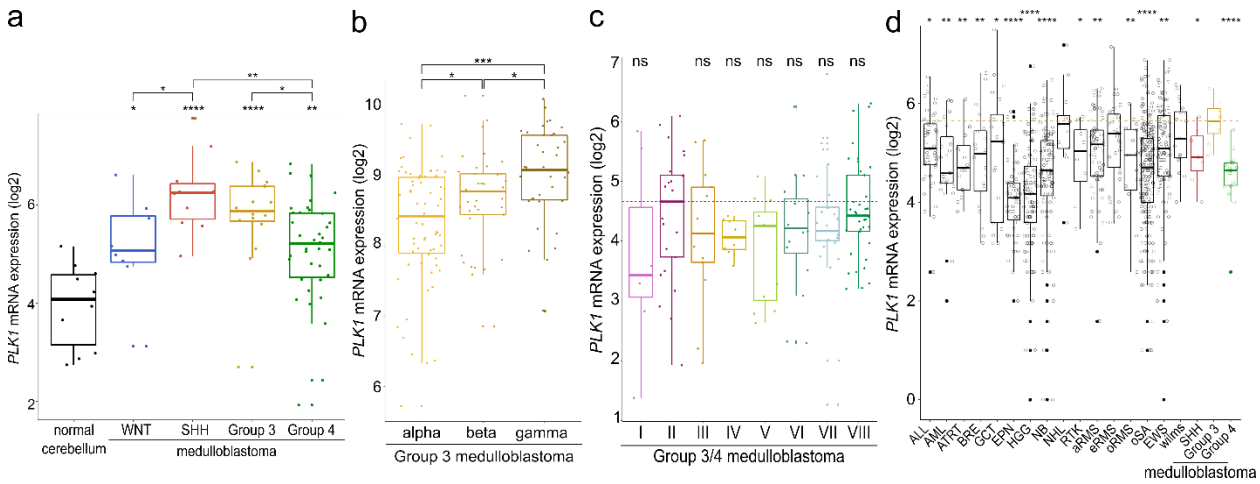

Figure 37 *PLK1* mRNA expression evaluation in tumors. a – *PLK1* mRNA expression in primary MB subgroups compared to normal cerebellum; b – *PLK1* mRNA expression in primary MB Group 3 subtypes; c – *PLK1* mRNA expression in primary MB Group3/4 subtypes; d – *PLK1* mRNA expression in relapsed pediatric malignancies. Significance was evaluated using one-way ANOVA: *p < 0.05; **p < 0.01; ***p < 0.001; ****p < 0.0001; ns = not significant. Dataset details are shown in Table 22.

Since in most of analyzed datasets *PLK1* mRNA expression was at least partly associated with *MYC*-amplification, we decided to inspect the largest MB mRNA dataset available (Cavalli, et al[2]) whether there was a correlation between *PLK1* and *MYC* mRNA expression in the MB subgroups. Indeed, *PLK1* and *MYC* mRNA expression correlated positively and significantly only in Group 3 ($r = 0.55$, $p < 0.05$, Figure 39c), which contains the *MYC*-amplified as well as MYC-driven MBs. No positive correlation was observed in the other subgroups except for weak correlation in Group 4 (Figure 39d, $r = 0.2$, $p < 0.05$; WNT, Figure 39a, $r = -0.21$, ns; SHH, Figure 39b, $r = -0.31$, $p < 0.05$).

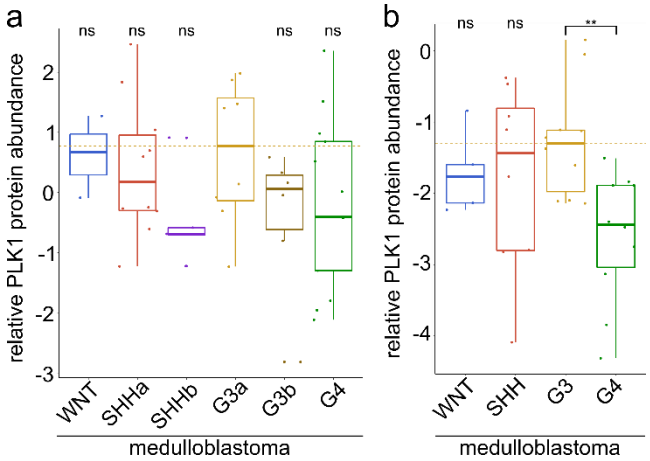

Figure 38 PLK1 protein expression in primary MB tumors. a – in Archer dataset and b – in Forget dataset. PLK1 protein levels in MB subgroups were compared by one-way ANOVA: **p < 0.01; ns = not significant. Details about datasets are shown in Table 22.

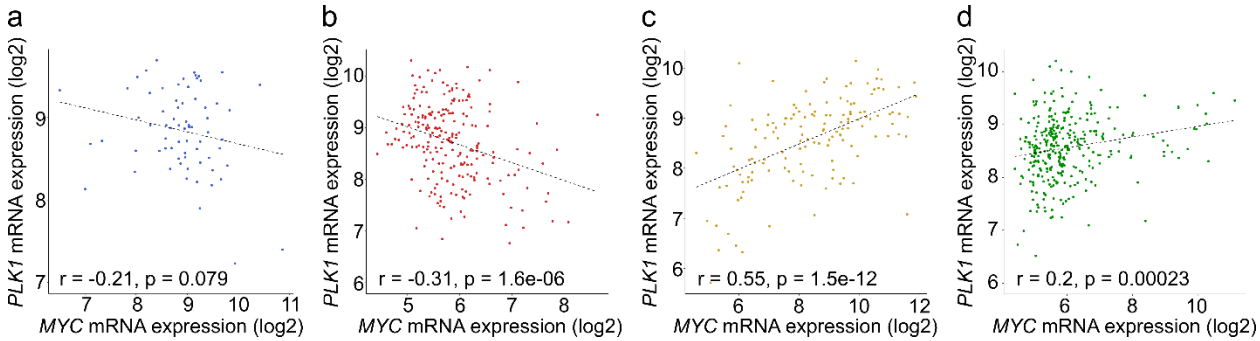

Figure 39 *PLK1* and *MYC* mRNA expression correlation analysis in primary MB tumor samples. Conducted in 4 subgroups separately: WNT (a), SHH (b), Group 3 (c) and Group 4 (d). Pearson correlation coefficient and p values are also depicted.

As before, we also included HGG and NB entities. We examined *PLK1* mRNA expression and the correlation of *PLK1/MYC/N* mRNA expression in published HGG and NB datasets. As no CNV-annotated glioma dataset is available (no *MYC/N* status was annotated), glioma samples were separated by grade. PLK1 mRNA was significantly overexpressed in higher grade tumors (Figure 40a), but was not correlated to *MYC* mRNA expression (Figure 40c, r = 0.023, ns). We also evaluated *MYCN* in glioma (data not shown) and obtained similar results. On the other hand, *PLK1* mRNA was expressed significantly higher in *MYCN*-amplified NB (Figure 40b), with a correlation of *PLK1* and *MYCN* mRNA expression r = 0.46 (Figure 40d, $p < 0.05$).

Taken together, the results presented in the section 4.2.2 show that PLK1 is one of MYC-target genes downregulated upon high-concentration entinostat treatment with available inhibitors. We chose PLK1 as a target for combination partner with entinostat. Furthermore, *PLK1* is upregulated in MB, HGG and NB cell lines and primary tumors. Finally, we show that despite overexpression, the function of PLK1 in and exemplary *MYC*-amplified MB cell line is intact, and that *MYC*-amplification does not influence the growth rate of the model cell lines used.

4.2.3. PLK1 inhibitor selectivity for *MYC*-amplified background

Upon confirmation of PLK1 expression in MB, HGG and NB model systems and primary tumors, we determined how cell lines with and without *MYC/N*-amplification respond to the treatment with different PLK1is. In this section, PLK1i dose-response relationships and validation are discussed.

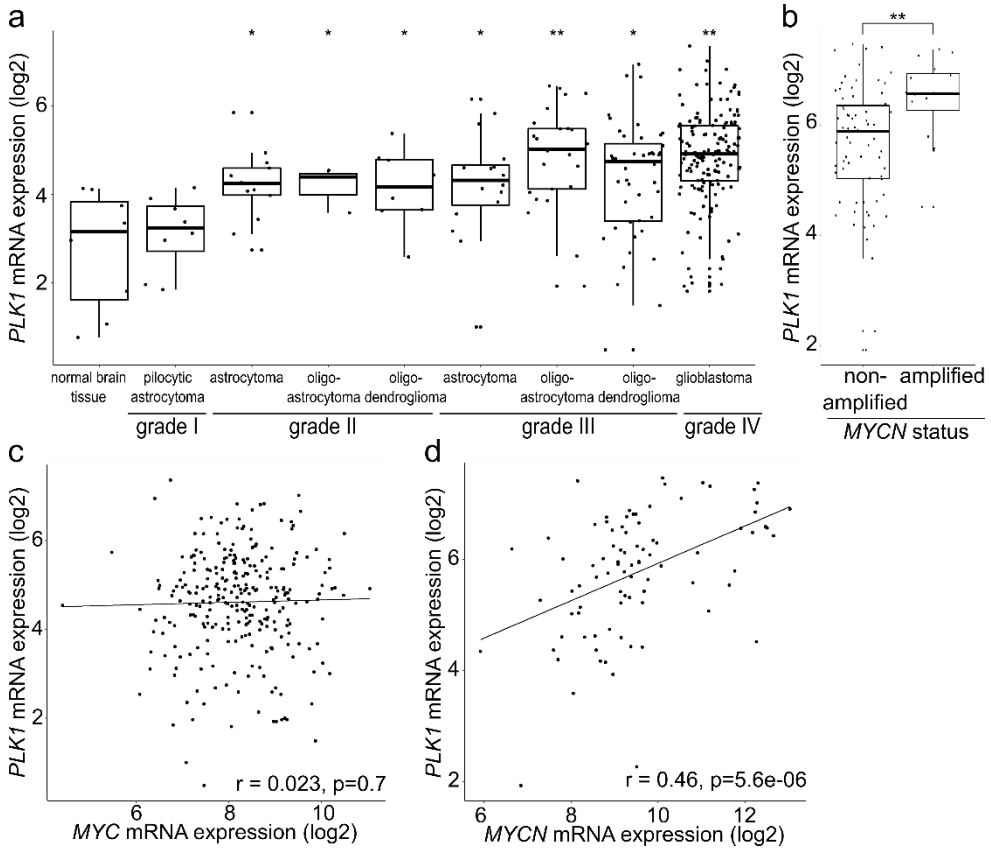

Figure 40 *PLK1* mRNA expression and correlation to *MYC/N* expression evaluation in glioma and NB. *PLK1* expression in gliomas (a) and NB (b). *MYC/N* and *PLK1* correlation in gliomas (c) and NB (d). Datasets are described in Table 22. One-way ANOVA and t-test were used for statistical evaluation: *p < 0.05; **p < 0.01. Pearson correlation coefficients are also depicted.

4.2.3.1. PLK1i IC50 estimation and on-target effect

The PLK1i dose-response relationship in *MYC*-amplified and non-amplified MB cells was evaluated by metabolic activity assay upon 72-hour treatment. Just as for entinostat treatment, *MYC*-amplified MB cell lines were more responsive to all ATP-competitive PLK1is tested with comparatively lower IC50s (Figure 41a, Table 27) and a clear separation in dose-response curve plots (Figure 41b, c, d). However, rigosertib, a non-ATP competitive PLK1i also active against PI3K, failed to show a similar pattern of response with regard to *MYC*-amplified vs non-amplified MB cells (Figure 41a, e). We therefore evaluated the on-target effect, i.e. whether rigosertib is indeed inhibiting PLK1 function in MB. We treated MB cell lines (MED8A, HD-MB03 and UW228-2) with a high concentration (1 µM, in order to achieve maximum inhibition) of each of the PLK1is for 20 minutes and performed immunoblotting for the phosphorylation of TCTP, a direct target of PLK1. Indeed, all ATP-competitive PLK1is (volasertib, GSK461364 and onvansertib) completely abolished the p-TCTP signal in all tested cell lines (Figure 42). Conversely, when cells were

treated with rigosertib, the p-TCTP signal remained as strong as in the control or even increased (in the UW228-2 cell line). As the PLK1 function was not reduced, indicated by the missing on-target effect, we excluded rigosertib from further experiments. This difference between ATP-competitive and non-competitive inhibitors could also indicate that direct inhibition of the PLK1 kinase function is important in the *MYC*-amplified or overexpressed background.

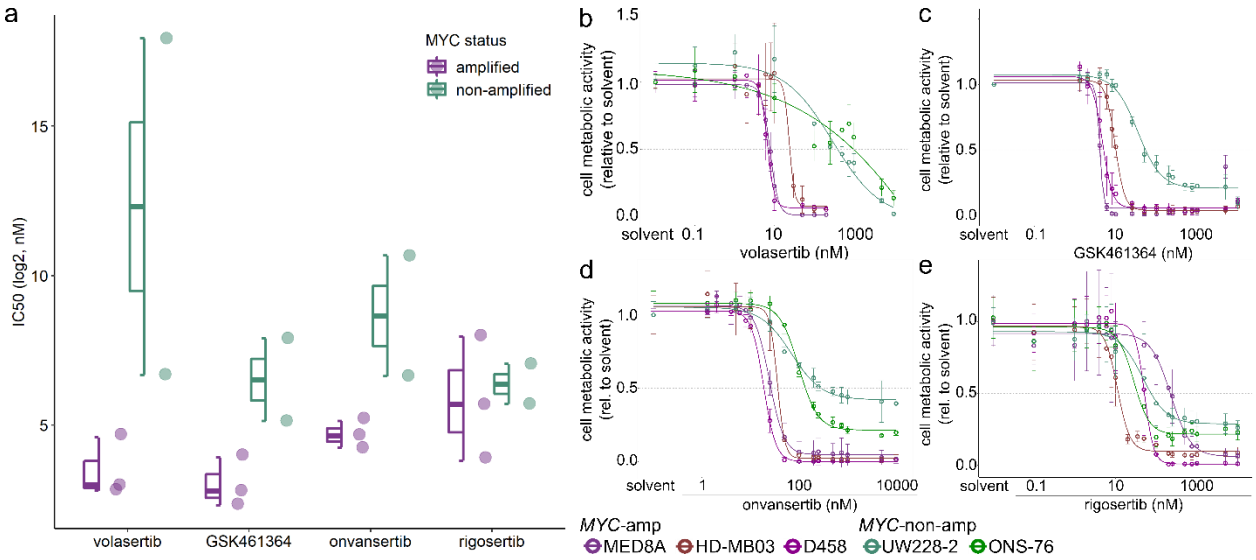

Figure 41 MB cell line response to a panel of PLK1 inhibitors. a – 50 % inhibitory concentrations (IC50) of different PLK1 inhibitors in MB cell lines. b (volasertib), c (GSK461364), d (onvansertib) and e (rigosertib) – dose-response curves depicting cell response to a range of PLK1i concentrations. Graphs show mean ±SD.

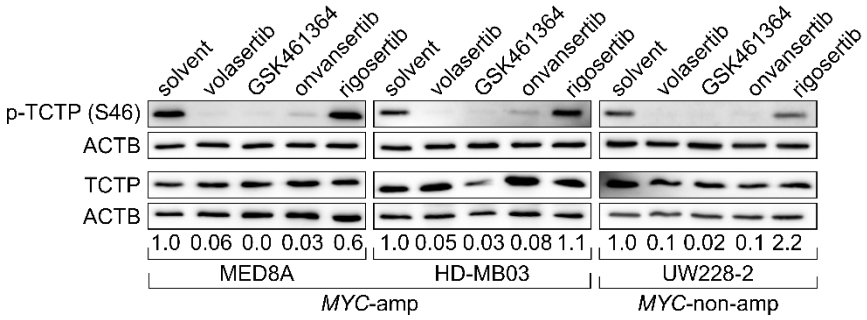

Figure 42 On-target effect of PLK1 inhibitors in MB cell lines. p-TCTP levels decreased after 20-minute treatment with 1 µM of ATP-competitive PLK1i, but not after rigosertib treatment.

In order to evaluate the combination of entinostat and PLK1i potential in other entities (HGG and NB), we examined the response of HGG and NB cell lines to the PLK1i volasertib. The IC50s were impossible to compare in terms of *MYC/N*-amplification in HGG due to the fact that only one *MYC/N*-non-amplified cell line (SU-pcGBM2) was included, and calculation of IC50 for the SU-pcGBM2 cell line was not possible (Figure 43a, Table 27). However, the higher sensitivity of

MYC/N-amplified HGG cells to volasertib was evident in the dose-response curves even without proper IC50 calculation (Figure 43b). *MYCN*-amplified IMR-32 was the most sensitive to volasertib NB cell line with IC50 at 8 nM (Figure 43a, c, Table 27). Another tested *MYCN*-amplified NB cell line SK-N-BE(2)-C showed similar response to the non-amplified NB cell lines. Therefore no *MYCN*-amplification-related sensitivity pattern was observed. Nonetheless, unlike the non-amplified NB cell lines, both *MYCN*-amplified cell lines reached zero relative metabolic activity at high concentrations indicating cytotoxic behaviour of volasertib only in the presence of *MYCN*-amplification.

Table 27 50 % inhibitory concentrations (IC50) of PLK1 inhibitors in MB, HGG and NB *MYC/N*-amplification positive or negative cell lines. *IC50 calculation was not possible using 5-parameter logistic model.

Entity	**Cell line**	**MYC/N-amp**	**IC50 (nM)**			
			Volasertib	**GSK461364**	**Onvansertib**	**Rigosertib**
Medulloblastoma (MB)	MED8A	*MYC*	8	7	19	52
	HD-MB03	*MYC*	24	15	35	14
	D458	*MYC*	7	5	25	249
	UW228-2	-	102	35	99	52
	ONS-76	-	25×10^4	239	1628	132
Hig-grade glioma (HGG)	HSJD-DIPG-007	*MYC*	13	6	-	-
	SU-DIPG-XXV	*MYC*	24	6	-	-
	HSJD-GBM-001	*MYC*	18	6	-	-
	SU-DIPG-XVII	*MYC*	27	10	-	-
	SU-DIPG-XIII	*MYCN*	96	13	-	-
	SU-pcGBM2	-	--*	--*	-	-
Neuroblastoma (NB)	SK-N-BE(2)-C	*MYCN*	28	-	-	-
	IMR-32	*MYCN*	8	-	-	-
	SK-N-AS	-	20	-	-	-
	SH-SY5Y	-	24	-	-	-
	SK-N-FI	-	26	-	-	-

In order to confirm that the response to PLK1i is dependent on *MYC*-amplification, we used a *MYC*-non-amplified MB cell line UW228-2 stably expressing an inducible *MYC* construct (UW228-2-pMYC) (Ecker, Thatikonda, et al, in revision). *MYC* expression is induced by the exposure to doxycycline (ON). Without added doxycycline, the cells express normal *MYC* levels of UW228-2 (OFF) (Figure 30b). We treated UW228-2-pMYC cells in ON and OFF with volasertib for 72 hours

and measured their metabolic activity. ON cells were more susceptible to volasertib treatment with almost 6-fold lower IC50 compared to the OFF cells (68.13 nM and 350 nM, respectively, Figure 44). To exclude the possibility that induced *MYC* expression accelerates the cell proliferation thus sensitizing the cells to the PLK1i, cell doubling times were measured (Ecker, Thatikonda, et al, in revision). *MYC*-induction did not significantly alter cell growth patterns within the time of treatment (data not shown). *MYC*-overexpression sensitizing the cells to the volasertib treatment underscores that *MYC*-overexpression could potentially act as a biomarker for the response to the PLK1i.

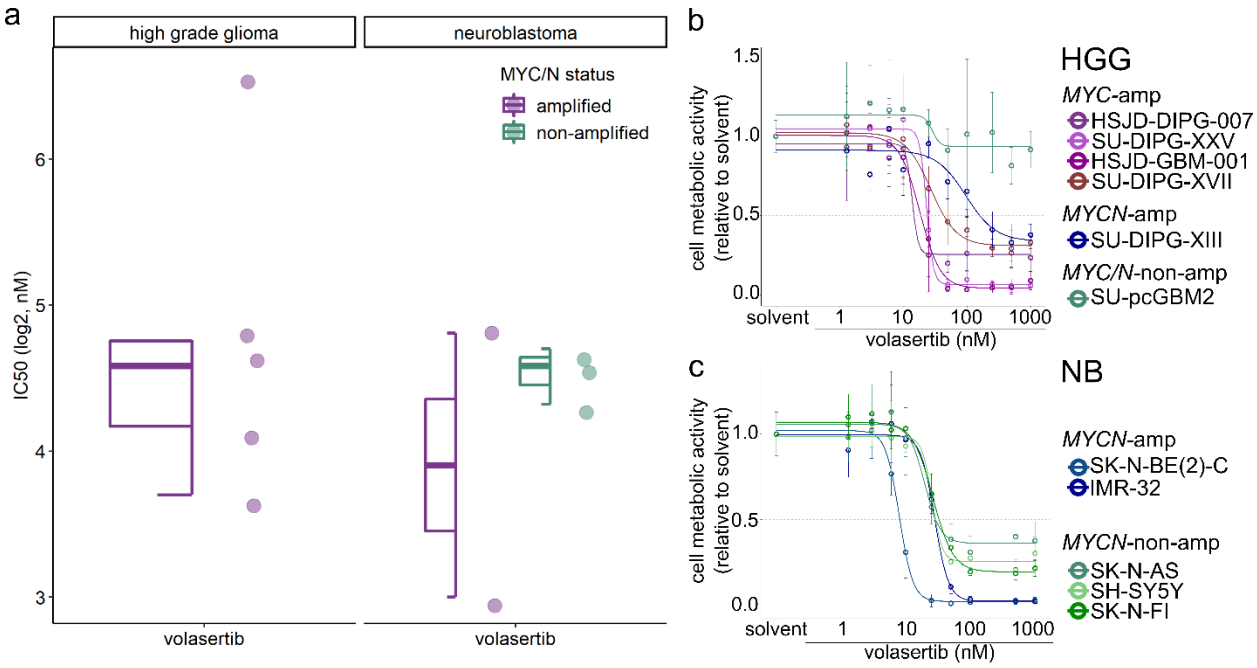

Figure 43 HGG and NB cell line response to volasertib. a – IC50 of volasertib in cell lines separated based on their *MYC/N*-status. b (HGG) and c (NB) – dose-response curves depicting cell response to volasertib. Graphs show mean ±SD.

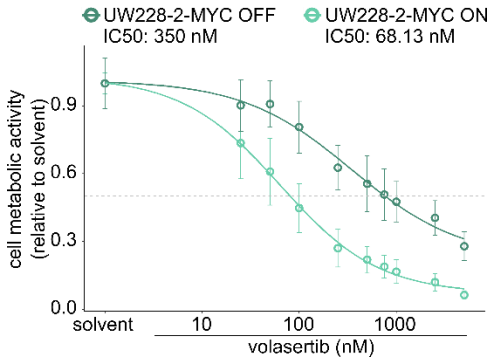

Figure 44 Doxycycline-inducible UW228-2-pMYC cell line response to volasertib. Graphs show mean ±SD.

4.2.3.2. Effect of the PLK1i volasertib on cell viability, cell cycle and cell death

To validate the data obtained in the metabolic activity assays (Figure 41 and 43), viable and dead cell numbers of MB, HGG and NB models after 72-hour treatment were quantified using the trypan blue exclusion assay. In concert with the metabolic activity data, the viable cell number was significantly reduced in *MYC*-amplified MB cell lines at lower concentrations (10 nM for MED8A and 25 nM for HD-MB03) compared to *MYC*-non-amplified cells (UW228-2; 50 nM) (Figure 45a). However, the number of dead cells after treatment with different volasertib concentrations was increasing only slightly (Figure 45d), with statistically significant differences only in *MYC*-amplified cells in the highest concentrations of volasertib. The viable cell number in the majority of *MYC*-amplified HGG cells was significantly decreasing at comparatively lower concentrations compared to *MYCN*-amplified or *MYC/N*-non-amplified cells (Figure 45b). The difference between amplified and non-amplified cell lines was also evident in the dead cell number induction (Figure 45e). In NB, the reduction of viable and increase in dead cells in IMR-32 was significant at much lower concentrations than another *MYCN*-amplified cell line SK-N-BE(2)-C (Figure 45c and f). Significant differences in viable and dead cell numbers were also observed in non-amplified NB cell lines. Thus no *MYCN* dependent difference in viable and dead cell measurement in response to volasertib treatment was detected in NB cells.

As we observed differences in response to volasertib between *MYC*-amplified and non-amplified MB cell lines and since PLK1 is strongly involved in cell cycle regulation, we also investigated the cell cycle response to volasertib treatment in both *MYC*-amplified and non-amplified cells. Here we assessed whether one of the hallmarks of PLK1 inhibition, namely G2/M phase arrest, occurs. Indeed, in all three MB cell lines, irrespective of their *MYC*-amplification status, cells arrested at G2 phase with significant increase in G2 populations in HD-MB03 and UW228-2 cell lines (Figure 46a and b). In addition, the cell population in subG0/G1 phase increased (Figure 46c) and the cell population in G1 phase decreased (Figure 46a) indicating a possible occurrence of cell death, and confirming previously measured decrease in cell viability after treatment with volasertib. Moreover, the subG0/G1 fraction increased at lower concentrations in *MYC*-amplified cell lines again showing differences between *MYC*-amplified and non-amplified cells.

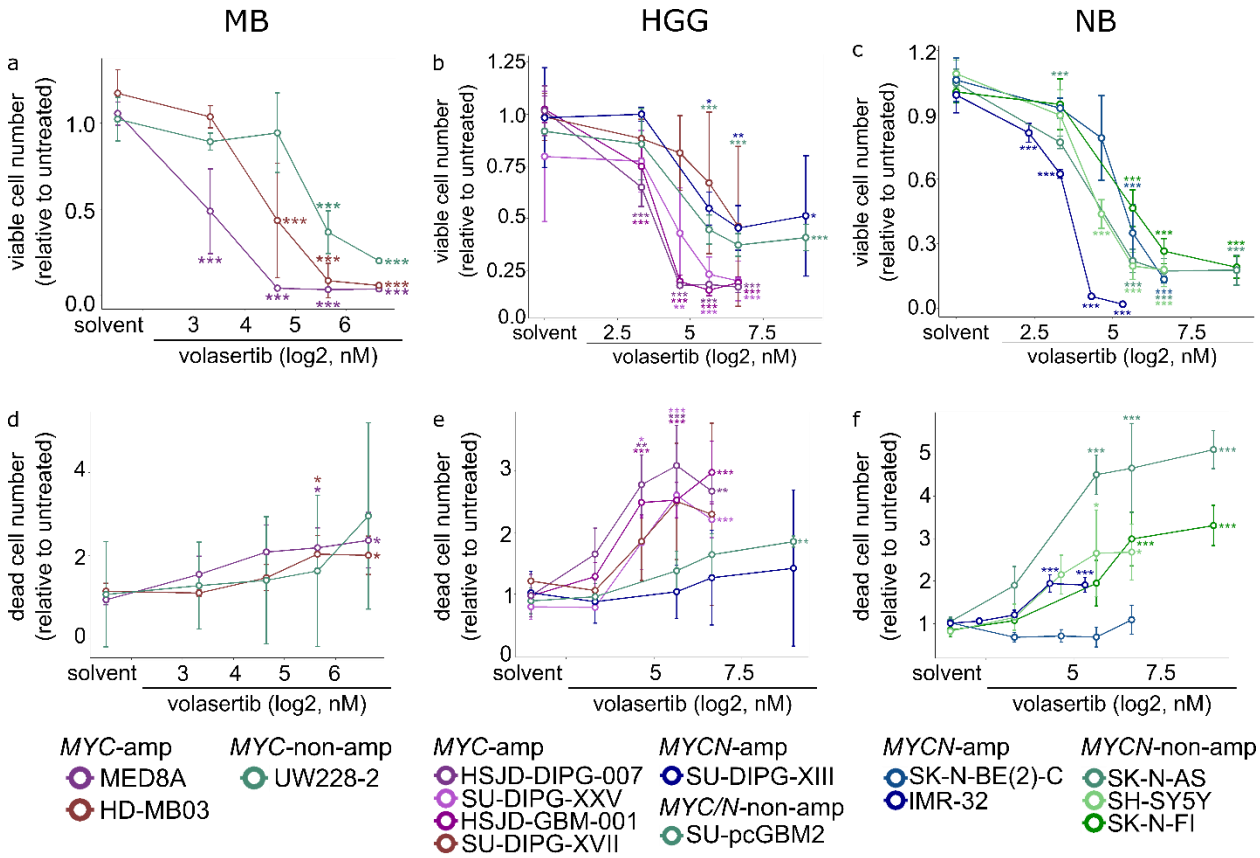

Figure 45 Relative viable and dead cell number after volasertib treatment for 72 hours. Viable (rel. to untreated) cells in MB (a), HGG (b) and NB (c) models. Dead (rel. to untreated) cells in MB (d), HGG (e) and NB (f) models. Graphs show mean ±SD. One-way ANOVA was used to compare to untreated control: *p < 0.05; **p < 0.01; ***p < 0.001

As our results of the viability and cell cycle analysis indicated a potential occurrence of cell death, we aimed to uncover whether the cells showed increased apoptosis signalling. For this aim, we treated MB cell lines with a range of volasertib concentrations for 24 hours and subsequently performed caspase-3 activity and PARP1 cleavage assays. As indicated in the previously discussed viability assays and cell cycle analyses, all three cell lines exhibited a high induction of caspase-3 activity showing activated apoptosis pathway irrespective of *MYC*-amplification status (Figure 46d). The caspase-3 induction was in fact the highest in *MYC*-non-amplified UW228-2 cell line. This could possibly be attributed to the general capacity of caspase-3 activity induction. Indeed, in UW228-2, UV-induced caspase-3 activity (positive control) was the highest of the tested cell lines (data not shown), indicating a high capacity of caspase-3 induction in this cell line. Surprisingly, even though PARP1 is a direct target of caspase-3, only a slight decrease in full length PARP1 without clear cleaved PARP1 was observed in UW228-2 (Figure 46f). Conversely, a clear cleaved PARP1 band was evident in *MYC*-amplified cell lines treated with 25

nM (MED8A) or 50 nM (HD-MB03) of volasertib as early as after 24-hour treatment (Figure 46e and f).

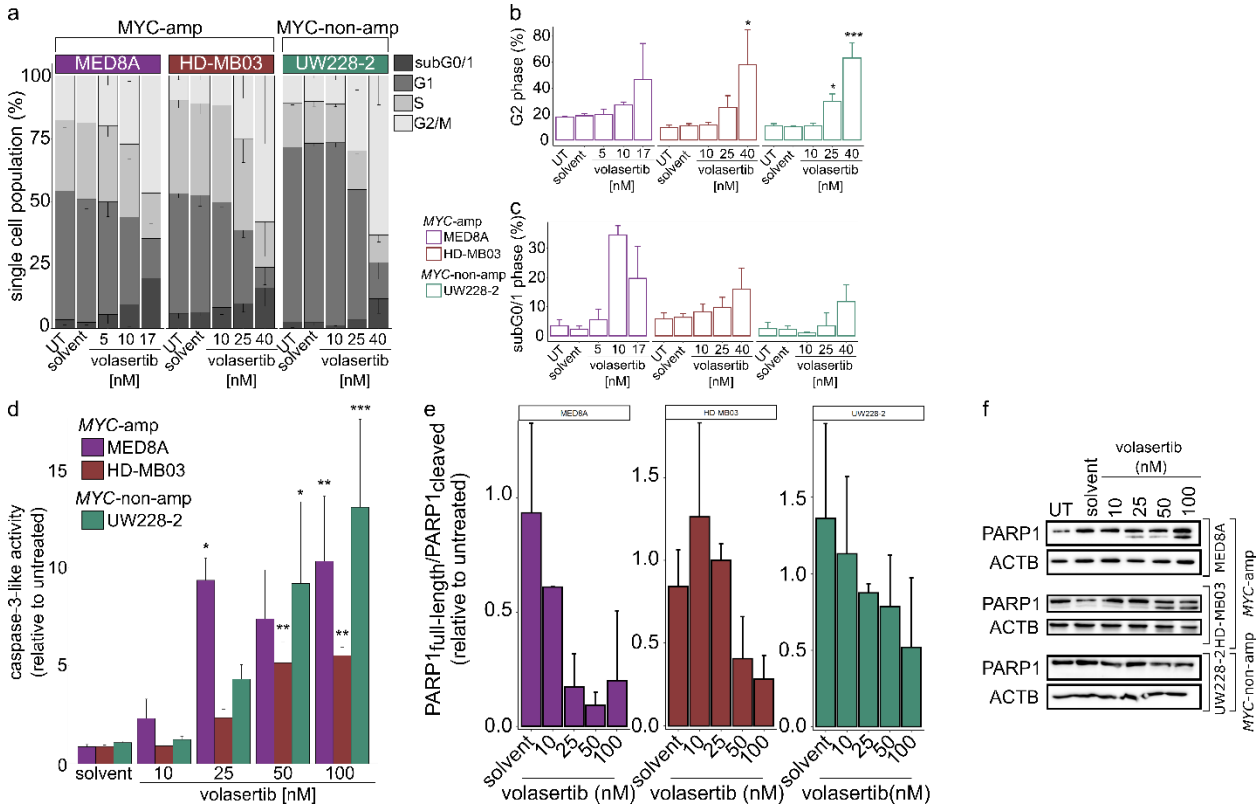

Figure 46 Volasertib activity on the cell cycle and cell death in MB cells. a – distribution of the cell cycle phases in MB after 24-hour treatment with volasertib; b – G2 and subG0/G1 proportion; c – caspase-3-like activity induction; d – full-length and cleaved PARP1 ratio; e – representative immunoblots for PARP1. Graphs show mean ±SD. One-way ANOVA was used to compare to the untreated control: *p < 0.05; **p < 0.01; ***p < 0.001.

Taken together, the results discussed in 4.2.3 section show that MB, HGG and NB cell line models respond to PLK1is at comparatively low concentrations. We show that *MYC*-amplification or overexpression sensitize MB cells to volasertib and other PLK1is. Moreover, we demonstrate the on-target effects of PLK1is, as well as clear *MYC*-amplification-dependent PLK1i activity on cell viability. Finally, volasertib induced cell cycle changes characteristic to PLK1 inhibition which leads to apoptotic cell death as indicated by caspase-3 activation and PARP1 cleavage.

4.2.4. Entinostat and PLK1 inhibitor interaction

Upon confirmation that both, entinostat and PLK1is act in *MYC/N*-amplification-dependent manner, we aimed to find out whether the inhibitors are interacting synergistically in *MYC/N*-amplified background, and whether this interaction is occurring at clinically relevant

concentrations. Here, we describe a metabolic activity drug interaction screen along with validation experiments in MB cells using volasertib as a representative PLK1i.

4.2.4.1. Combination index estimation in cell metabolic activity

In order to determine whether entinostat and PLK1is interact in a synergistic, additive or antagonistic manner, metabolic activity assay and subsequent combination index (CI) calculations using CompuSyn software were employed. Concentrations for the combination screen were chosen based on the IC50s determined previously. Entinostat and volasertib interacted synergistically in the majority of concentrations in all tested cell lines (Figure 47). However, the effect on cell metabolic activity and synergistic behaviour in clinically achievable concentrations was observed only in *MYC*-amplified MB cell lines. Combining volasertib concentration range and entinostat IC50 (Figure 47, Figure 48a, b, c) showing synergistic behaviour in MED8A, HD-MB03 and UW228-2 cell lines also underscores the difference between *MYC*-amplified and non-amplified cells. Here, despite being treated with substantially higher concentrations, UW228-8 relative metabolic activity does not decrease below 20 % even in the highest concentrations. Moreover, adding entinostat IC50 pushes the dose-response curves of *MYC*-amplified cells to a range that is indeed clinically achievable (Figure 48a and b, concentrations calculated based on reported c_{max}). Similar results are observed when adding volasertib IC50 to a range of entinostat concentrations (Supplementary figure 2a, b, c).

Comparing to volasertib, other PLK1is screened (GSK461364 and onvansertib) interact with entinostat in a less synergistic manner (Figure 47, 48d-i). Although CI indicates GSK461364 and entinostat synergy in UW228-2 and HD-MB03 cell lines, the assay evaluation presented a challenge due to comparatively low IC50 of GSK461364 compound in *MYC*-amplified cells and difficulties achieving a sigmoid-shaped dose-response curves. Comparing GSK461364 dose-response with and without added entinostat, the synergy can be observed albeit weaker copared to volasertib (Figure 48d, e, f, Supplementary figure 2d, e, f). On the other hand, onvansertib does not synergize with entinostat in lower concentrations (in *MYC*-amplified cell lines) in our measurements (i.e. buffer antagonism, Figure 47, 48g, h, i, Supplementary figure 2g, h, i).

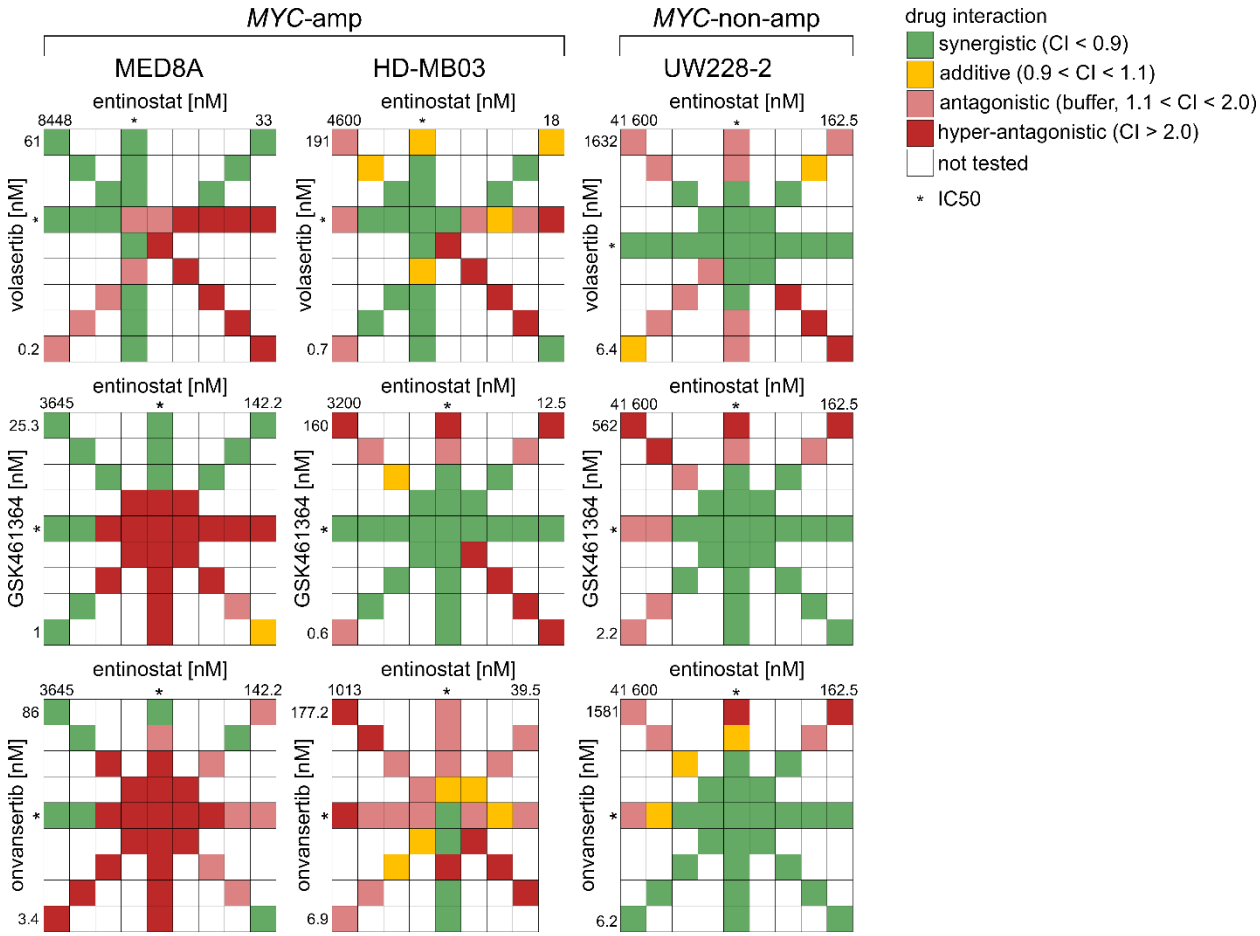

Figure 47 Summary of entinostat and PLK1i interaction screen in MB cell lines with and without *MYC*-amplification. Upper panel shows entinostat and volasertib combination. Middle panel shows entinostat and GSK461364 combination. Lower panel shows entinostat and onvansertib combination. Colors represent the interaction and combination indexes (CI) at particular concentration combination.

In HGG and NB, volasertib and entinostat interact synergistically across all tested cell lines (Figure 49), regardless of *MYC/N*-amplification status. However, here as in MB cell lines, synergistic interaction and effect on cell metabolic activity is achieved in lower concentrations in *MYC/N*-amplified cell lines. Also, as in MB screen, here addition of entinostat IC50 reduces cell metabolic activity substantially, shows synergistic behaviour and pushes dose-response curves to clinically achievable concentration range (Figure 50, Supplementary figure 3).

Taken together, CI estimation results suggest that volasertib and entinostat synergize in a selected range of concentrations in all tested cell lines. The drugs show synergistic interaction and similar effects on cell metabolic activity in lower concentrations in *MYC/N*-amplified cell lines underscoring the potential for clinical application.

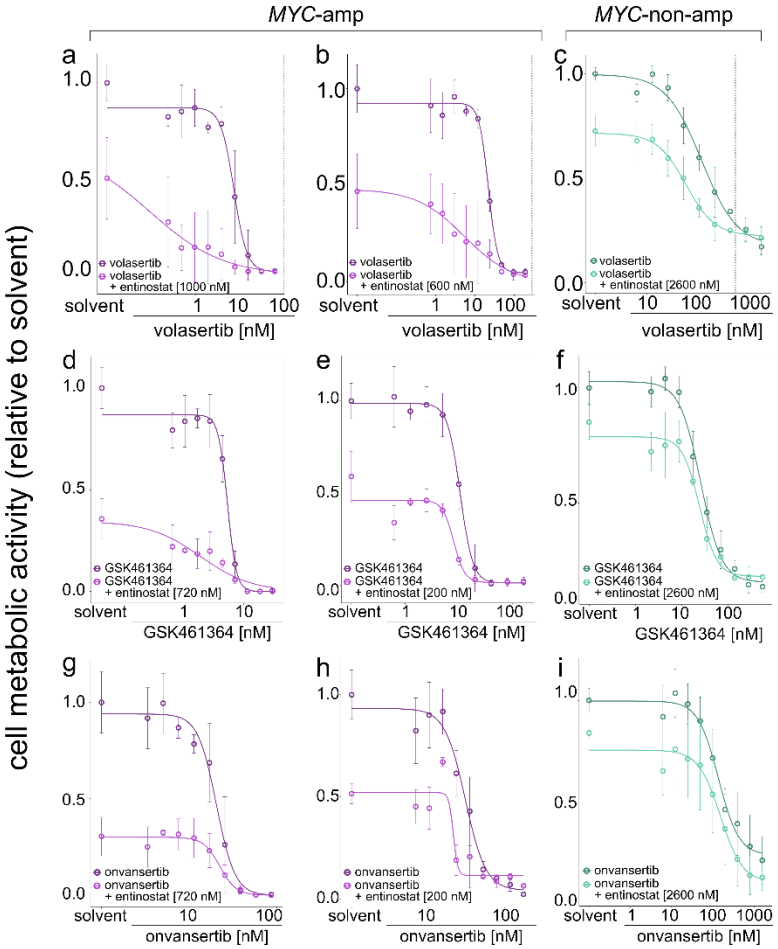

Figure 48 Dose-response curves of volasertib, GSK461364 or onvansertib alone vs combination with entinostat IC50 in MB. a, d, g – MED8A; b, e, h – HD-MB03; c, f, i – UW228-2. Grey dashed lines represent clinically achievable volasertib concentration. Graphs show mean ±SD. ←

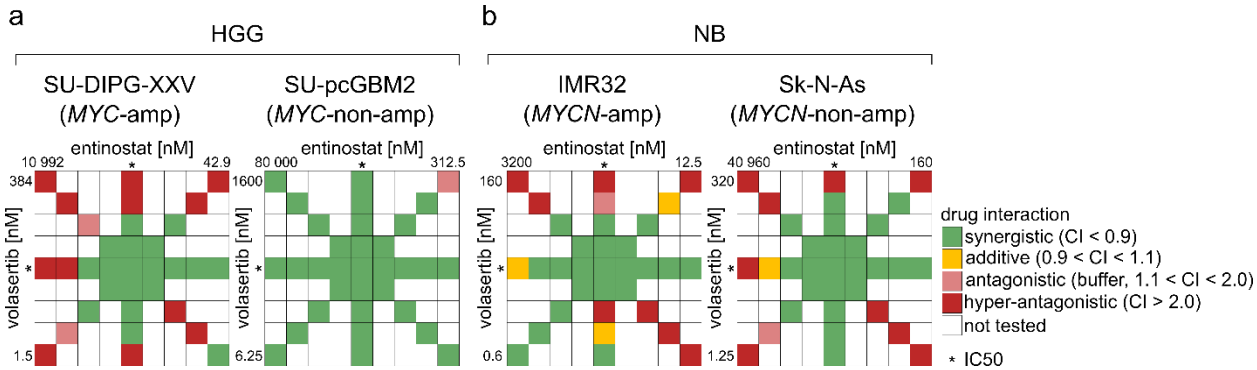

Figure 49 Summary of entinostat and volasertib interaction screen in HGG (a) and NB (b) cell lines with and without *MYC/N*-amplification. Colors represent the interaction and combination indexes (CI) at particular concentration combination.

Figure 50 Dose-response curves of volasertib alone vs combination with entinostat IC50 in HGG and NB. a – SU-DIPG-XXV; b – SU-pcGBM2; c – IMR-32; d – SK-N-AS. Grey dashed lines represent clinically achievable volasertib concentration. Graphs show mean ±SD. →

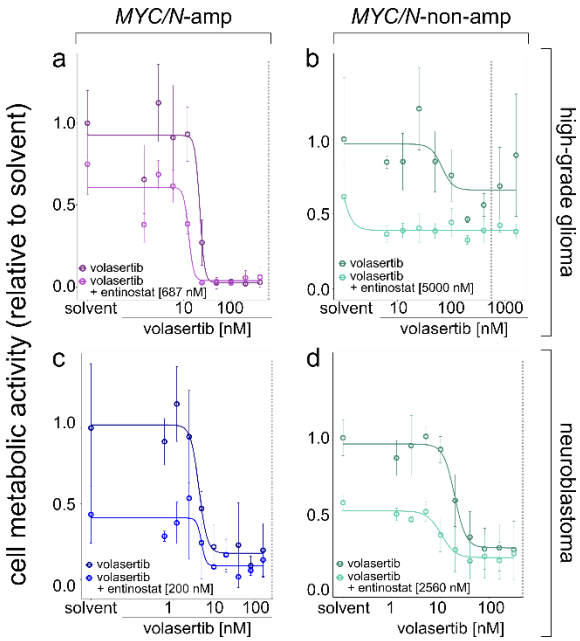

4.2.4.2. Validation of the interaction of entinostat and volasertib on cell viability, cell cycle and cell death induction

To confirm the synergy between entinostat and PLK1is, we performed validation experiments assessing cell viability, cell cycle and cell death responses to the combination of entinostat and volasertib. All validation experiments were carried out in MB cell lines with *MYC*-amplification, MED8A and HD-MB03 and without *MYC*-amplification, UW228-2. Concentrations used were empirically adjusted to the specific cell lines in order to be able to observe the given parameter at each treatment timepoint.

In order to assess whether the metabolic activity assay correctly estimated the cell viability response and drug interaction, we determined viable and dead cell numbers after 72-hour treatment using trypan-blue exclusion. Cells were treated with 500 nM entinostat, 10 (MED8A) or 15 (HD-MB03 and UW228-2) nM volasertib or their combination. The interaction was determined using the Bliss Independence model CI calculation.

In all three tested cell lines a reduction of relative viable cell number (Figure 51a) was observed upon combination treatment. However, in *MYC*-amplified cell lines the effect of combination was more substantial, as the viable cell number was significantly lower after combination treatment compared to single drug treatments. In contrast, no significant differences were observed between single-drug and combination-treated UW228-2 cell lines. Moreover, CI showed a synergistic interaction of entinostat and volasertib in *MYC*-amplified cells only.

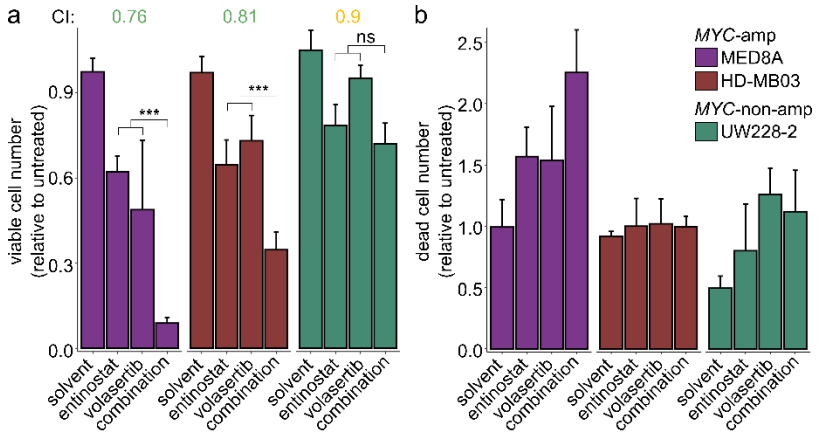

Figure 51 Relative viable (a) and dead (b) cell number in MB after 72-hour treatment. Entinostat: 500 nM, volasertib: 10 nM (MED8A) or 15 nM (HD-MB03 and UW228-2) or combination. CI calculated using Bliss Independence model (green: synergistic, yellow: additive). Graphs show mean ±SD. Differences were assessed for statistical significance using one-way ANOVA. ***$p < 0.001$; ns: not significant.

Examining the relative dead cell content in the same treating conditions showed an increase after single drug and combination treatment only in the MED8A cell line, but not in the other *MYC*-amplified cell line HD-MB03 (Figure 51b). Interestingly, comparing to the solvent control the dead cell number in treated UW228-2 cell line slightly increased. However, as the solvent control relative-to-untreated dead cell number is just above 0.5, there is no increase when comparing to untreated. Nonetheless, as discussed above, 72-hour treatment could have been too late for correct determination of dead cell content.

As substantial cell cycle alterations in the cells treated with single drugs were observed, we also examined the cell cycle phase cell populations in MB cell lines after 24, 48 and 72 hours of treatment with 1000 nM of entinostat, 10 (MED8A) or 15 (HD-MB03 and UW228-2) nM volasertib or their combination. After treatment of MED8A cells for 48 and 72 hours, the subG0/G1 fraction increased significantly in the samples treated with the combination compared to entinostat and control-treated cells (Figure 52). Interestingly, in MED8A the subG0/G1 percentage increase was observed mainly after treatment with volasertib or combination, whereas in HD-MB03 only after treatment with entinostat and combination. Also, in both *MYC*-amplified cell lines the number of cells in G2 was decreasing after combination treatment indicating a complete halt in cell proliferation (Figure 52a). No substantial changes in cell cycle composition were observed in treated UW228-2 cells. Synergism (MED8A, CI = 0.86) and additivity (HD-MB03, CI = 1) was detected in the *MYC*-amplified background and antagonism in the non-amplified background (UW228-2, CI = 1.73) (Figure 52b).

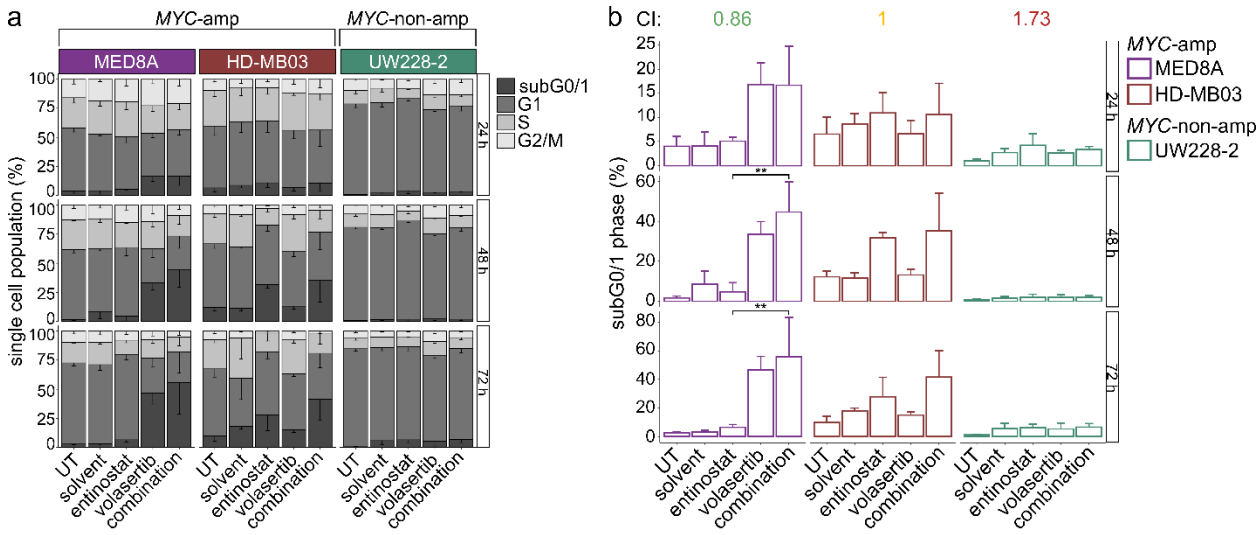

Figure 52 The distribution of the cell cycle phases in MB after 24, 48 and 72-hour treatment with entinostat, volasertib or their combination. Entinostat: 1000 nM, volasertib 10 (MED8A) and 15 (HD-MB03 and UW228-2) nM or combination. Single cell population composition (a). SubG0/G1-phase proportion (b). CI calculated using Bliss Independence model (green: synergistic, yellow: additive). Graphs show mean ±SD. One-way ANOVA: **p < 0.01.

After observing an increase in subG0/G1 phase in *MYC*-amplified cell lines, we also studied caspase-3 activity after 24 (MED8A) or 48-hour (HD-MB03 and UW228-2) treatment with the same concentrations as above. Here, in concordance with cell-cycle changes, caspase-3 activity was induced by volasertib in MED8A and by entinostat in HD-MB03 (Figure 53a). The combination of both drugs induced caspase-3 activity in both *MYC*-amplified cells showing CI < 1 and thus synergistic interaction. A small increase and antagonistic interaction were observed in treated UW228-2 cell line. In order to confirm that increased caspase-3 activity induces apoptosis, we analyzed whether PARP1 is being cleaved. Indeed, full-length/cleaved PARP1 ratio was reduced in an additive manner (MED8A CI = 1, HD-MB03 CI = 1.1, UW228-2 CI = 1.1) in both *MYC*-amplified cell lines, but not in the *MYC*-non-amplified cell line UW228-2 (Figure 53b, c).

Taken together, we confirm that entinostat and volasertib interact synergistically preferentially in *MYC*-amplified cell lines. We observed significant and synergistic decrease in viable cells, increase in subG0/G1 fraction in cell cycle analysis and synergistic/additive induction of apoptosis in *MYC*-amplified cell lines in the concentrations suggesting potential activity *in vivo*.

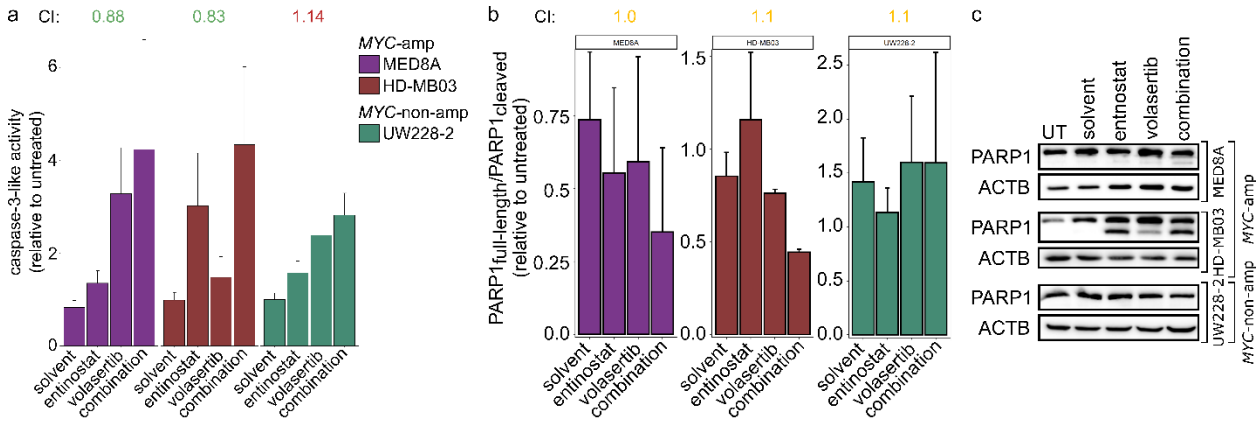

Figure 53 Apoptosis induction in entinostat, volasertib or combination-treated MB cell lines. Caspase-3-like activity induction after 24 (MED8A) or 48 (HD-MB03 and UW228-2) hours of treatment with 1000 nM entinostat, 10 (MED8A) or 15 (HD-MB03 and UW228-2) nM volasertib or combination (a). Full-length and cleaved PARP1 ratio (b) and representative immunoblots for PARP1 (c) after 48 hours of treatment with the same concentrations as in a. CI calculated using Bliss Independence model (green: synergistic, yellow: additive). Graphs show mean ±SD.

4.2.5. Investigation of volasertib's mechanism of action

We have previously shown that *MYC*-amplified cells are more sensitive to volasertib treatment. As PLK1 has been demonstrated to interact with FBXW7[184], the E3 ubiquitin ligase responsible for MYC turnover, we hypothesized that volasertib treatment induces MYC degradation pathway not only in NB (demonstrated by Xiao and colleagues[184]), but in MB as well. The resulting reduction of MYC levels then would lead to reduced proliferation and induced cell death. In this section, we investigate MYC protein stability after volasertib treatment and explore FBXW7 as a potential mediator of this process.

4.2.5.1. MYC levels in volasertib-treated cells

As *MYC*-amplified cells are more sensitive to volasertib treatment, we first determined whether *MYC* mRNA levels are changed after treatment with volasertib. We extracted the expression data from the gene expression profile generated after 6-hour treatment of HD-MB03 cell line with 1 µM of volasertib. *MYC* mRNA expression levels did not change after treatment comparing to the solvent control (Figure 54a). Subsequently we investigated whether MYC protein levels were changing in cells treated with volasertib. Here we used 25 nM volasertib and treated the MED8A and HD-MB03 cells for 6 and 16 hours. Indeed, MYC protein levels were reduced in the treated samples in concert with our hypothesis of volasertib inducing degradation of MYC (Figure 54b).

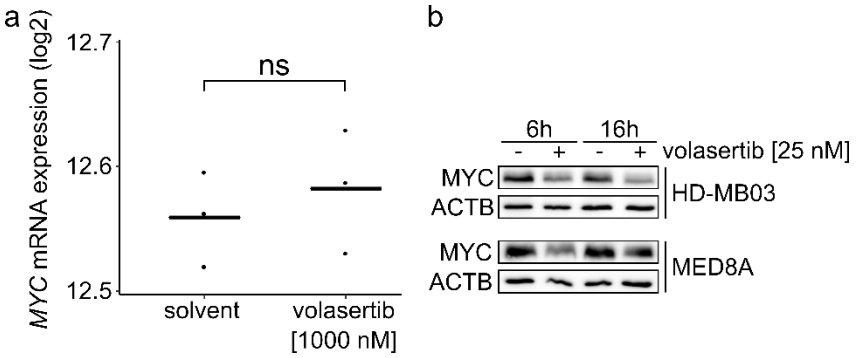

Figure 54 MYC levels in *MYC*-amplified MB cell lines after volasertib treatment. a – *MYC* mRNA expression in HD-MB03 cells after 1000 nM volasertib treatment for 6 hours; b – MYC protein levels in *MYC*-amplified MB cell lines after 25 nM volasertib treatment for 6 or 16 hours. Graph shows three independent replicates and a mean. Difference was assessed for statistical significance using t-test. ns: not significant.

4.2.5.2. MYC protein stability in volasertib-treated cells

In order to investigate the impact of volasertib on MYC protein stability we performed a cycloheximide (CHX) pulse-chase experiment in MED8A cell line with 1-hour pre-treatment with volasertib. Indeed, MYC degradation was faster in volasertib-treated samples compared to only CHX (Figure 55a), indicating the potential PLK1 involvement in MYC stability. This effect was only observed at a high volasertib concentration (1 µM), which was used to ensure maximum PLK1 activity suppression and maximum postulated effect on protein stability. No substantial difference between MYC degradation in volasertib and solvent-treated samples was observed when lower volasertib concentration (50 nM) was used (Figure 55b). This could indicate that either high inhibitor concdentrations are needed in our model to observe the PLK1i mediated MYC turnover, or that PLK1 influences MYC protein stability only indirectly (thus showing the need for higher volasertib concentration or longer treatment times), or potential off-target effects at high concentrations of volasertib reducing MYC protein stability.

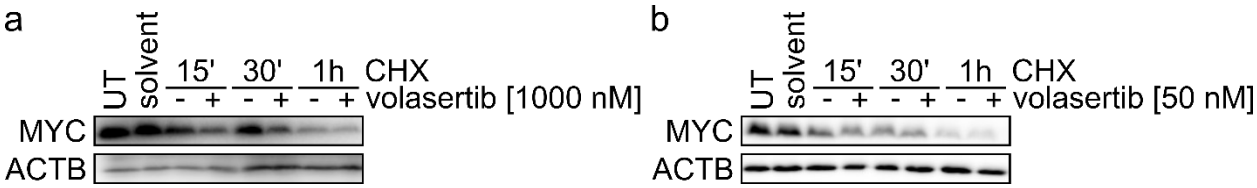

Figure 55 MYC protein degradation timeline in MED8A CHX pulse-chase assay. a – 1000 nM volasertib pre-treatment (1 h); b – 50 nM volasertib pre-treatment (1h). CHX: cycloheximide.

In order to confirm that MYC is indeed degraded via the proteasomal degradation pathway upon volasertib treatment, we investigated whether MYC levels could be rescued by addition of the proteasome inhibitor MG132. A rescue effect of MG132 was observed only in MED8A cell line after both, 6 and 16-hour treatment (Figure 56). However, MYC levels were only slightly increasing in MG132 co-treated HD-MB03 cells after 6 hours with no effect in 16-hour treated cells. Conversely, in HD-MB03 cells co-treatment with MG132 and volasertib strongly increased reduction of MYC levels.

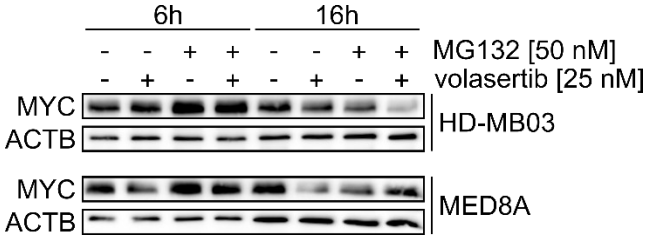

Figure 56 MYC protein levels in HD-MB03 and MED8A cells treated with volasertib, MG132 or both.

4.2.5.3. FBXW7 as a potential link between MYC and PLK1

Our experiments have shown inconclusive results regarding volasertib and MYC stability interaction. Previous publications have shown PLK1-dependent FBXW7 regulation. We therefore interrogated MB cell lines for FBXW7 overall and phosphorylated protein levels. FBXW7 protein expression was reduced in *MYC*-amplified MB cell lines MED8A and HD-MB03 compared to non-amplified cells (Figure 57). Phosphorylated FBXW7 (Figure 57, marked with *) was slightly higher in *MYC*-amplified cell lines in concert with the PLK1 expression upregulation demonstrated above. However, conclusions regarding p-FBXW7 differences should be drawn carefully as the custom-made p-FBXW7 antibody showed substantial unspecific binding.

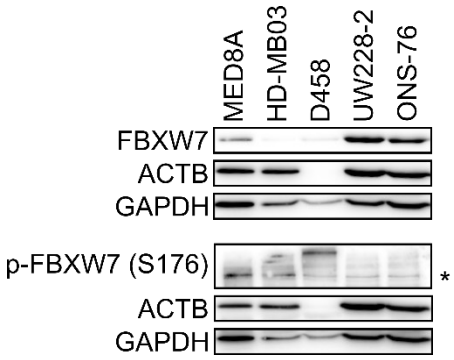

Figure 57 FBXW7 and p-FBXW7 levels in MB cell lines. *p-FBXW7 representing band.

PLK1-mediated FBXW7 phosphorylation should be targeting FBXW7 for auto-ubiquitination and subsequent degradation[184]. Thus, FBXW7 levels should be increasing when cells are treated with volasertib, mediated by increased stability of the protein. We therefore performed a CHX pulse-chase assay with MED8A cell line pre-treated with 1 µM volasertib for 1 hour and examined FBXW7 levels. However, no substantial increase in FBXW7 levels was noticed (Figure 58), thus pointing to either limitations of the assay (FBXW7 has a comparatively low turnover rate, which could be masking any effect of volasertib at short chase times) or indicating that FBXW7 is not the mediator of PLK1/MYC interaction in MB in contrast to other entities.

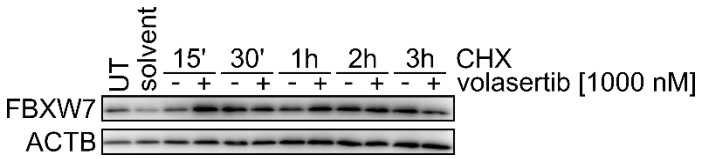

Figure 58 FBXW7 protein degradation timeline in MED8A CHX pulse-chase assay. CHX: cycloheximide.

Taken together, the results described in this section show that in *MYC*-amplified MB cells the mode of action of volasertib is mediated via targeting MYC. However, our results are inconclusive with regard to the effect of volasertib on the stability of MYC or FBXW7. The partial rescue of MYC levels by proteasome inhibition may indicate an effect on the MYC degradation pathway.

4.2.6. Investigation of entinostat and volasertib combination mechanism of action

We finally aimed to enhance our understanding of how entinostat and volasertib interact on the downstream level, and which pathways are regulated when MB cells are treated with the combination of volasertib and entinostat. We examined the expression of MYC target gene sets, and compared their expression in entinostat, volasertib or combination-treated HD-MB03 cells.

4.2.6.1. Identification of genes and pathways regulated after combination treatment

We performed a gene expression profiling (GEP) analysis in short-term high-dose-treated *MYC*-amplified HD-MB03 cells to obtain information on genes and pathways additively or over-additively (i.e. synergistically) activated in after combination treatment. The analysis of GEP data was carried out in cooperation with Thomas Hielscher, Division of Biostatistics, DKFZ.

Overall, the expression fold-change differences between cells treated with different inhibitors and solvent were low as in GEP analysis described above (section 4.2.2.1), possibly due to the short-term treatment. We identified 677 genes as significantly differentially expressed (Figure 59). Clusters of genes upregulated (upper part of Figure 59) and downregulated (middle part of Figure

59) in the combination-treated samples were identified. In addition, a cluster of genes downregulated mainly in volasertib-treated cells, but not in the combination-treated cells was identified (lower part of Figure 59).

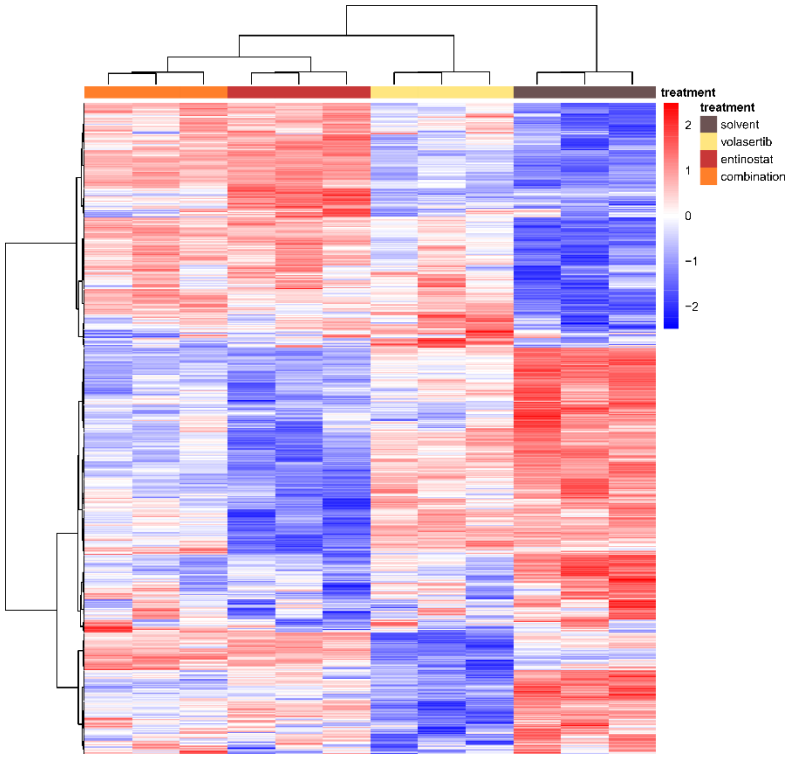

Figure 59 A heatmap showing significantly differentially expressed genes in HD-MB03 cells treated with solvent, volasertib, entinostat or their combination.

Subsequently, an analysis of possibly over-additive effects on gene expression profiles was carried out. We identified 14 genes significantly differentially expressed in an over-additive manner (Supplementary table 3). However, comparing to the solvent control, all of these genes were upregulated in entinostat and combination-treated cells and slightly downregulated in volasertib-treated cells, possibly showing that either entinostat had more influence on genome regulation (as an HDAC inhibitor) or that analysis had shortcomings identifying the downregulated genes, or the chosen timepoint was too short to identify any regulation influences by the PLK1 inhibition. The latter explanation would be the most credible as G2/M regulator genes activated by cyclin B/CDK1 complex, which is activated by PLK1 did not appear in the outcome of the analysis. Therefore, to better understand the pathways mediating the synergistic interaction of entinostat and volasertib one should either prolong the time of treatment or choose another possible readout, e.g. evaluation of (phospho-) proteome.

We also interrogated gene ontology (GO), KEGG and Reactome databases for pathways affected by combination treatment, however, none were identified as significantly and synergistically regulated further underscoring the limitations of chosen GEP conditions.

4.2.6.2. Comparison of MYC target gene set expression in combination-treated cells

The unsupervised analysis of pathways in GO, KEGG and Reactome databases was not conclusive. We therefore performed a supervised analysis using the dataset generated by GEP and MYC target gene sets HALLMARK_MYC_TARGET_V1 and V2[16], in order to analyze the effect of combination treatment on MYC transcriptional activity. As predicted by our previous experiments examining MYC levels after volasertib treatment, and by experiments examining MYC protein stability upon entinostat treatment (Ecker, Thatikonda, et al, in revision), the gene set HALLMARK_MYC_TARGETS_V1 was significantly downregulated after treatment with entinostat and volasertib alone, and the V2 gene set also significantly downregulated by volasertib treatment (Figure 60a and b). This indicates a reduction of MYC transcriptional activity upon PLK1i treatment. Interestingly, both gene sets were significantly downregulated by combination treatment with substantially higher enrichment scores. This shows evidence that the loss of MYC transcriptional activity and subsequent downregulation of MYC target genes could be responsible for phenotypic effects of the combination treatment.

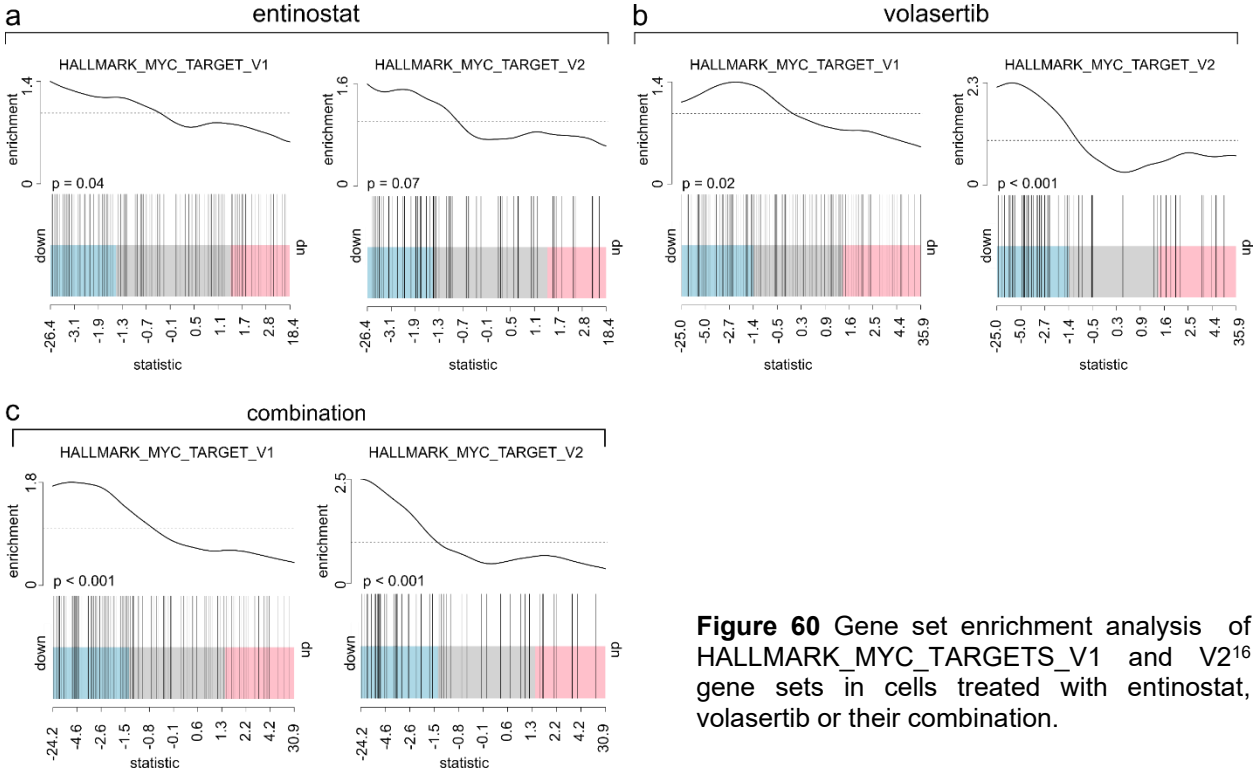

Figure 60 Gene set enrichment analysis of HALLMARK_MYC_TARGETS_V1 and V2[16] gene sets in cells treated with entinostat, volasertib or their combination.

We also determined whether MYC protein levels are reduced after combination treatment. Indeed, MYC levels were downregulated in MED8A cell line after as early as 24 hours of treatment (Figure 61). As entinostat has been shown (Ecker, Thatikonda, et al, in revision) to stabilize an inactive form of MYC, it is evident that volasertib is mainly responsible for MYC protein level downregulation depicted in Figure 61. The relative loss of MYC protein compared to solvent is evident after 24 h and 72 h of treatment with volasertib and combination (Figure 61).

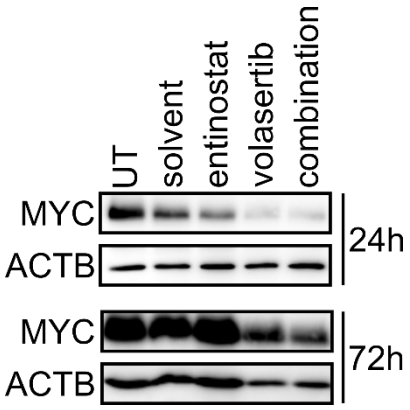

Figure 61 MYC protein levels in MED8A cells after entinostat (1000 nM), volasertib (15 nM) or combination treatment for 24 and 72 hours.

Taken together we here show the genes that were significantly downregulated in short-term single and combination treatments. We demonstrate what genes could potentially be involved in synergistic interaction between entinostat and volasertib. More importantly, we confirm that combination of entinostat and volasertib exert their activity via MYC, even in short-term-treated cells, thus at least partly validating our hypothesis that phenotypic effects on cell viability and cell cycle are induced by MYC downregulation.

5. Discussion

MYC is one of the best known and well-described oncogenes in cancer research. It acts as a potential regulator for 15 % of the genome[97] and has been shown to be involved in tumor initiation and maintenance in as many as 20 % of all cancer entities[100,101]. The transcription, translation and function of MYC are all precisely regulated by a well-orchestrated machinery hijacked during the tumorigenesis. It occurs mainly because MYC functions as a regulator of key cellular processes, such as cell proliferation, growth, metabolism, motility and others[18,140]. Therefore, ever since the discovery of MYC activation in Burkitt's lymphoma[104-107] in the end of 20th century, MYC targeting was the main objective of many research laboratories. Unfortunately, as a transcription factor, MYC is extremely difficult to pharmaceutically target directly, thus the majority of efforts in creating a MYC inhibitor failed[109]. In the last few decades, however, targeting of MYC transcription, translation, stability and degradation has shown promise even in clinical setting[12,145,154].

In this study, MYC targeting is described mainly in pediatric medulloblastoma (MB). Arising in the posterior fossa of the brain, MB is one of the most common CNS cancers in children. MB is divided into clinically, molecularly, pathologically and epidemiologically distinct subgroups and subtypes. MB Group 3[1,2,66] (subtype II[55,56]) is particularly enriched in *MYC*-amplification-harbouring tumors and is thus considered high-risk. In fact, *MYC*-amplification reduces the overall survival probability to less than 25 %[2] despite standard of care treatment (SOC, includes surgical resection, cranio-spinal irradiation and chemotherapy). And even though some of the patients reach a durable remission, the sequelae of the harsh treatment regimen[89-91,95,96] and the high risk for secondary malignancies[8] remain. Therefore, using targeted therapy against the driver of such tumor could potentially reduce the tumor mass more efficiently and diminish the side effects of the SOC therapy.

Here, the MYC-dependent potential of class I HDAC inhibitor entinostat was confirmed[226] and, as HDACis show a comparatively high toxicity in clinics, a combination therapy was assessed. Firstly, the members of hypothetical transcription-regulatory complex of HDAC2 and MYC were elucidated. As the data was deemed inconclusive, other options for combination therapy were evaluated. Here, polo-like kinase 1 (PLK1) was identified as a potential target in *MYC*-amplified MB. In order to reduce the aforementioned toxicity and to increase the achieved effect, PLK1 was inhibited together with entinostat treatment. We showed that entinostat and PLK1i volasertib interact synergistically reducing cell viability and inducing cell death in MB models in clinically relevant concentrations when *MYC*-amplification was present. As the synergistic activity of

entinostat and volasertib was exerted via the MYC axis, the *MYC*-amplification was proposed as a biomarker for this clinically promising combination therapy. Nonetheless, the potential of such therapy remains to be examined *in vivo*.

5.1. MYC-HDAC2 complex

As described above (section 1.2), the function of MYC is highly dependent on its' interaction partners[18]. For instance, the best described MYC function is transcriptional activation. After heterodimerizing with its' essential interaction partner MAX[414,415], MYC can bind to the E-boxes and thus modulate transcriptional activity. Apart from MAX, MYC has been known to interact with many other proteins and protein complexes, including TRRAP, a member of STAGA complex with HAT activity (mediated by GCN5)[416]. Another MYC interactor with epigenetic activity is p300/CBP HAT complex, shown to have dual functions in MYC regulation, i.e. acetylate MYC increasing MYC turnover and stabilizing MYC as its' cofactor[417,418]. HAT complexes and acetylation has been shown to have different effects both on MYC and on target gene activation, indicating that these complexes target MYC to specific subsets of genes in different cell populations[18]. These findings show how important the role of MYC acetylation, HATs and, possibly, histone deacetylases (HDACs) is.

One of MYC binding partners we recently identified in *MYC*-amplified MB cells (Ecker, Thatikonda, et al, in revision) is HDAC2. We have demonstrated that HDAC2 and MYC form a complex bound mainly on active state chromatin (marked by H3K27ac) capable of both, transcriptional activation and repression. We also proposed a hypothetical mechanism in concert with p300/CBP role of MYC acetylation and deactivation[417]. Here, in an HDAC2-MYC complex, MYC is de-acetylated by HDAC2, thus allowing transactivation of the protein (MYC activation is regulated by phosphorylation of two residues, S62 and T58 within the phosphodegron domain, that could potentially be prevented by acetylation of adjacent lysines). As we propose the HDAC2-MYC protein complex to regulate transcription of MYC target genes, the pharmaceutical inhibition potential was suggested. In the study described in this thesis, we aimed to determine what other proteins could be the members of such protein complex and whether they could be targeted with small molecule inhibitors in addition to HDAC2 targeting, thus reducing the concentrations needed to achieve a substantial effect on tumor mass reduction.

In this thesis, the HDAC2-MYC protein-protein interaction identity was confirmed in *MYC*-amplified MB model (section 4.1.1). Moreover, in concert with our previous study (Ecker,

Thatikonda, et al, in revision), we show that HDAC2-MYC complex is localized in the nucleus (Figure 25), thus validating its' suggested activity on transcriptional profiles. As described in the section 4.1.2 and shown in Figure 27, we identified proteins involved in reported MYC or HDAC2-influenced cellular processes, such as protein homeostasis[419], RNA processing[420] and DNA stability[421]. We also found the members of complexes known to be associated with HDAC2, such as coREST[422,423] and NuRD[424,425].

As we were aiming to elucidate the members of the transcriptional regulator complex, we focused on the proteins known to have functions relevant for the transcription regulation. Here our potential targets were filtered to 4: YY1, DNMT1, TBL1X and GTF2I. Two of these, namely YY1[426,427] and GTF2I[428], are well known MYC interactors, together with MYC regulating transcription (YY1 has also been reported to bind HDAC2[429]). TBL1X, which has been shown to bind HDAC2[284], as described above, is involved in protein degradation. In addition, due to its' role in the recruitment of proteasome complex, TBL1X was proposed to play a key role in transcriptional repressor complexes as a mediator of cofactor exchange[430]. Finally, DNMT1 maintains DNA methylation patterns on the CpG islands and has been shown to be binding HDAC2 in a repressor complex before[431]. In general, the biding partners highly suggest a repressive transcriptional function of the MYC-HDAC2 complex.

Due to the lack of suitable direct inhibitors of TBL1X, GTF2I and YY1, targeting these proteins in combination with entinostat was rendered impossible (excluding the indirect or non-specific inhibitors, such as nitric oxide for YY1, reviewed by Sarvagalla et al[432]). The only possible target among the potential complex members was DNMT1, which, as described above, has inhibitors only used in pre-clinical studies[433]. The only clinically relevant inhibitors so far are DNA dependent, thus do not directly inhibit DNMT1, just the DNA methylation in general. In addition, the toxicity profiles of compounds, such as 5-aza-cytidine and 5-aza-2'-deoxycytidine, are comparatively unfavourable, especially combined with another epigenetic inhibitor[434].

Even though this part of the study was not followed up, the hypothesis of targeting the MYC-HDAC2 complex from two directions remains to be examined. As this analysis was derived from one replicate only, the experiment should be repeated in order to confirm whether the proposed complex members are indeed binding MYC and HDAC2 and repressing the transcription in *MYC*-amplified MB cells. Finally, even though not directly targeting DNMT1, combination of DNA methylation and HDAC inhibitors have shown promise in other entities[435] also in clinical trials[436].

Possibly, a direct inhibition of DNMT1 could improve the effect achieved in previous studies as well as the toxicity profiles.

5.2. Indirect MYC targeting

While the development of small molecule inhibitors targeting MYC directly failed, the indirect targeting of MYC (transcription, translation, degradation, etc) has proven to be a major success. Inhibitors targeting BRD4, mTOR, AURKA and other proteins involved in MYC activity in various entities have already been used in clinical trials (summarized in Table 2).

We therefore aimed to elucidate a potential target with connection to MYC for combination therapy with entinostat. Since the majority of MYC-driven genes are involved in cell proliferation and regulate important tumorigenesis and tumor maintenance processes, we identified potential targets by filtering the entinostat-treatment-downregulated gene pool for druggable MYC targets encoding genes (depicted in Figure 33), namely PLK1, PLK4 and CUL1. As discussed in section 1.4, PLK1[311,333,335] and PLK4[334] are both known as oncogenes and are found upregulated in many different entities with PLK1 upregulation known as a general feature of tumorigenesis[437-442]. Also, as described above, PLK1 regulates MYC stability by phosphorylating E3 ubiquitin ligase FBXW7[184] which is responsible for MYC turnover[443]. Phosphorylation marks FBXW7 for ubiquitination and subsequent degradation, thus closing MYC and PLK1 in a feedback loop.

Due to the number of PLK1 inhibitors in clinical development and clear previous research data on PLK1 and MYC interaction, PLK1 was chosen as the main target for the second part of the study.

5.2.1. PLK1 in *MYC*-amplified medulloblastoma

As one of the cell cycle regulators and known tumor-promoting factors, PLK1 has been extensively investigated in many different entities, among them pediatric malignancies and medulloblastoma. PLK1is have been shown to reduce tumor cell proliferation and clonogenic potential alone[444,445] (to some extent), but more importantly in combination with radio or chemotherapy[445-449] as well as other small molecule inhibitors, e.g. BETi[450,451], showing a great importance of PLK1 in tumor development. In addition, PLK1 overexpression has been shown to be associated with worse prognosis, aggressive tumors[452-457] and metastatic behaviour[458,459] in a number of entities. In contrast to extensive research on PLK1 upregulation in p53-deficient tumors, where depletion of PLK1 was found particularly cytotoxic[352,353,460,461], the relationship of MYC and PLK1 expression has been studied relatively less. Apart from the identification of PLK1 as a MYC target gene, PLK1 and MYC were found overexpressed in diffuse large B-cell

lymphoma[462]. In another hematological malignancy, a double-hit lymphoma (DHL), *PLK1* and *MYC* mRNA expression correlates and is regarded to be a new hallmark indicating high-risk tumor behaviour[340,463].

In medulloblastoma, PLK1 has been previously mainly associated to SHH subgroup, where a "PLK1 signalling event" together with the FOXM1 network (one of transcription factors activating PLK1 transcription[464-466]) were identified to impact prognosis[467]. In addition, connections of PLK1 to MYCN, which is frequently upregulated in the SHH subgroup, have been documented before[184]. In a previously referenced study Park and colleagues[467] also observed that the most favourable prognosis for Group 3 MB patients correlates with the loss of "oncogenic core genes", among them *MYC* and *PLK1*, therefore emphasizing the potential of PLK1 targeting in Group 3 MB.

In concert with the described data, in this study, *PLK1* mRNA was found overexpressed in SHH and Group 3 subgroups of MB (Figure 37). We also observed similar effects when we compared PLK1 protein levels in MB subgroups (Figure 38) in two previously published datasets[402,403]. *PLK1* and *MYC* mRNA were correlating only in Group 3 (Figure 39), whereas *PLK1* and *FOXM1* mRNA expression correlated across the entire dataset (data not shown), suggesting that MYC and PLK1 connection in Group 3 MB could be either subgroup or genetic-alteration specific. In addition, this could indicate that MYC target gene set either expands or generally changes in different subgroups/subtypes of MB (i.e. with or without *MYC* amplification). *PLK1* expression was also found specifically upregulated in MB subtypes associated to *MYC* amplification, further reiterating the importance of genetic background in MB.

Accordingly, the data we acquired from MB cell line models was in concordance with expression values in primary tumors. In *MYC*-amplified MB cells *PLK1* mRNA expression and protein levels were only slightly higher and did not show substantial differences compared to SHH-derived *MYC*-non-amplified cell lines (Figure 34). Comparing the used cell lines to the models derived from Group 4 or WNT subgroups in terms of *PLK1* mRNA expression would potentially aid in model-primary tumor difference assessment, especially necessary when examining mitotic kinase inhibitors. Unfortunately, the enrichment of MB SHH and Group 3 models and lack of reliably identified Group 4 and WNT models[78] prevents the improvement of the cell line model panel used.

In agreement with data generated in adult malignant gliomas[468,469], *PLK1* mRNA expression was increased in high grade (and risk) gliomas compared to low-grade gliomas (Figure 40). As described above, *PLK1* expression upregulation can be recognized as a general feature in

tumorigenesis and tumor maintenance, as well as an indicator for poor prognosis. Also, as expected in an entity with comparatively low number of *MYC* amplifications, *MYC* and *PLK1* mRNA expression values did not correlate in the glioma dataset. We also did not observe any substantial differences in *PLK1* mRNA expression in cell line models with different *MYC* or *MYCN* status (Figure 34). This could indicate that *MYC* overexpression is a poor biomarker in high-grade glioma. However, previously described MYC and PLK1 protein interaction, as well as the importance of MYC post-translational regulation suggested that the PLK1 targeting could still have potential in a subset of such tumors. As no gene expression dataset with comparable copy number variation (CNV) data and enough samples was published to date, direct *MYC/N* amplification and *PLK1* expression relationship in glioma remains to be investigated.

PLK1 inhibition has been proven successful in neuroblastoma[444] and PLK1 and MYCN interaction has been studied before[184]. Therefore, as expected *MYCN* and *PLK1* mRNA expression values were highly correlated. In addition, *PLK1* mRNA expression was significantly higher in *MYCN*-amplified NB samples (Figure 40). Interestingly, no such clear difference was observed in cell lines (Figure 34), where *PLK1* was significantly upregulated only in SK-N-BE(2)-C cell line (with *MYCN* amplification), but not in IMR-32, suggesting that despite of *MYCN* amplification, different PLK1 regulatory mechanisms could be expressed in these cell lines.

As mentioned above, *PLK1* overexpression is related to poor disease outcome, which would indicate high *PLK1* expression in relapsed tumors. Surprisingly, *PLK1* overexpression is prominent only in Group 3 MB relapse samples compared to NB or HGG (Figure 37), suggesting that relapsed HGG and NB might not rely on *PLK1* and possibly *MYC/N* overexpression as much as Group 3 MB. Alternatively, due to high-risk profile and poor prognosis in general, Group 3 MB relapses could be overall enriched for samples harbouring *MYC* amplification.

5.2.2. *MYC*-amplified medulloblastoma and PLK1i

As *PLK1* mRNA expression was independently significantly associated to poor prognosis in SHH and Group 3 subgroups of MB, PLK1 was shown to be a valid target in those subgroups of MB as early as 2013[457]. Since then, many researchers have employed different strategies of combinatorial treatment including PLK1is. For example, Han and colleagues[450] as well as Timme et al[451] reported the potency of the combination of PLK1 and BRD4 inhibitors in preclinical models of (*MYC*-amplified) MB and other pediatric malignancies (neuroblastoma and rhabdomyosarcoma). In addition, PLK1i was shown to enhance the activity of radiotherapy: Pezuk

and colleagues[445] as well as Harris et al[449] demonstrated the potential of PLK1i as a radiosensitizer. Interestingly, even though some of these reports focused on *MYC*-amplified MB cells, none have previously discussed increased PLK1i-sensitivity of MYC-driven MB after treatment with single agent PLK1i.

Although PLK1is have been used in clinical trials before (Table 4, volasertib used mainly in hematological malignancies, phase III in AML NCT01721876, GSK461364 in phase I study on Non-Hodgkin lymphoma NCT00536835, onvansertib in multiple phase I/II trials), there are no reports on PLK1i clinical trials in pediatric oncology. Even in adult malignancies, PLK1i clinical application surveys seem to be halted due to the severe side effects of the therapy including neutropenia, thrombocytopenia and myelosuppression[357,368,369]. In fact, a recent letter in Trends in Cancer Opinion section by Yan and colleagues[470] calls out extensive mitotic kinase inhibitor development regardless of their clinical failures. Underscoring the on-target effects of mitotic kinase (including PLK1) inhibitors in healthy proliferating tissue and different proliferation indices in models compared to patients, they advocate for adjusting a common misconception about only malignant cells being able to proliferate and suggest reconsidering the use of such inhibitors in personalized medicine. As the therapeutic window for PLK1is in patients seems to be comparatively small, the reduction of effective dosage as well as development of effective biomarkers should be a priority. Therefore, in addition to examining the potential of PLK1i in MB, we here assessed *MYC*-amplification as a biomarker and propose a possibility to reduce the effective dose of PLK1i by combination therapy (section 5.2.3).

In contrast to the data published by Abbou et al[447] on MB cell lines and treatment with volasertib, we observed a clear difference between IC50 values when treating *MYC*-amplified and non-amplified MB cells (Figure 41, Table 27) with volasertib and other ATP-competitive PLK1is. This difference is not dependent (though it could be slightly influenced) on cell proliferation rate as there is no substantial difference between *MYC*-amplified and non-amplified cells in terms of cell growth (Figure 35). In fact, one of the most sensitive to PLK1i MB cell line MED8A divides at a significantly lower rate compared to the least sensitive ONS-76 cell line. In addition, we further demonstrate the MB cell line sensitizing to PLK1i by overexpressing *MYC* in non-amplified UW228-2 cell line reducing IC50 almost 6-fold (Figure 44). This further indicates that *MYC*-amplification indeed can predict MB cell line response to PLK1i.

PLK1 function is particularly important during the cell cycle transition to M phase[314-316] and for correct kinetochore attachment as well as chromosome separation[312,318,319,323] (discussed in the section 1.4.2). In addition, it was previously reported that PLK1 also takes part in the genome repair mechanism[471]. In fact, PLK1-upregulated tumors often are found to have abnormal chromosome separation and cell division[439], as well as an ability to overcome DNA damage-induced cell cycle arrest without actually repairing the DNA[472,473], which in turn promotes genome instability[439]. In line with known PLK1 functions, PLK1is in various cancer entities were shown to induce mitotic catastrophe and the G2 cell cycle arrest as well as increase the proportion of polyploid cell population, frequently resulting in cell death induction[446,474]. Interestingly, another outcome of PLK1 inhibition has also been reported. Here, Driscoll an colleagues[475] found that small molecule inhibitor-mediated inhibition of PLK1 results in double-strand breaks of DNA and, in some cell lines, induction of senescence signalling and phenotype.

In concert with the aforementioned reports, in this study we also demonstrate that PLK1 inhibition with volasertib resulted in G2-phase cell cycle arrest, which, in turn, induced apoptotic cell death (Figure 46). Interestingly, both, cell cycle arrest and caspase-3, were induced by comparable volasertib concentrations irrespective of *MYC*-amplification status of MB cells. However, *MYC*-non-amplified cell line UW228-2 did not have PARP1 cleaved even though PARP1 is a direct target of caspase-3. In addition, *MYC*-amplified cell lines demonstrated significant differences in viable cell numbers in lower concentrations of volasertib compared to the UW228-2 (Figure 45). This suggests either that volasertib effect is cytotoxic only in *MYC*-amplified MB and cytostatic in non-amplified cells or that caspase-3 activity quantification methodology has limitations in terms of direct comparison of cell lines with different general caspase-3 induction profiles. Moreover, one should take into account the fact that UW228-2 cell line is *TP53*-defficient[476], thus exhibiting abnormal response to DNA damage and apoptosis induction. In any case, additional non-amplified cell lines should be surveyed in order to fully understand, whether volasertib induces cell death in *MYC*-amplification-dependent manner in MB.

Comparably to MB data, in HGG the treatment with volasertib reduced metabolic activity in *MYC/N*-amplification-dependent manner (Figure 43). We also observed a similar effect assessing the viability of the cells (Figure 45), however, here volasertib effect was different in *MYC* and *MYCN*-amplified cells with *MYCN*-amplified cell line being largely unresponsive to PLK1 inhibition in lower concentrations. In contrast to a previous report about PLK1 inhibition reliably reducing *MYCN*-amplified NB cell line viability[184], a difference was also observed between two *MYCN*-

amplified NB cell lines in both metabolic activity and cell viability. This indicates that in *MYCN*-amplified cells other factors could also influence the response to PLK1 inhibition. For example, NB is known to be composed of cells with two phenotypes, mesenchymal and adrenergic, with different transcriptional landscapes[477], which could potentially affect the response to the treatment. However, in order to explain this phenomenon, a larger panel of *MYCN*-amplified NB cell lines should be evaluated.

5.2.3. Interaction of entinostat and PLK1 inhibitors

PLK1 inhibitors have been shown to induce the DNA damage and mitotic abnormalities[471,478], suggesting a complementary mechanism to that of HDAC inhibitors[479,480]. Therefore, PLK1 and HDAC inhibitors have already been proven to interact synergistically in Non-Hodgkin[293] and double-hit[481] lymphoma, leukemia[397] and prostate cancer[482]. All these studies reported combinatorial effects on the cell cycle, death and/or viability and used the pan-HDACis (e.g. vorinostat, belinostat, valproic acid) and BI2536 or volasertib as PLK1is. Interestingly, only the studies focused on lymphomas[293,481] reported that PLK1 and HDAC effects were related to the MYC-mediated signalling pathways and MYC protein, however, the authors did not suggest *MYC*-amplification or overexpression as a biomarker for HDAC and PLK1 inhibitor combination.

In this study, we demonstrate that the class I HDACi entinostat interacts synergistically with PLK1i volasertib in MB cell lines (Figure 47). In fact, entinostat and volasertib synergize in all tested cell lines irrespective of their *MYC*-amplification status. However, when comparing the concentrations used, it is evident that only in *MYC*-amplified MB cells, synergistic interaction is observed together with desired effect and comparatively lower concentrations. In addition, only in *MYC*-amplified MB cell lines, an addition of a second compound pushed the dose-response curves into the range of doses achievable in patients (Figure 48). This emphasizes the translational potential of the combination and *MYC*-amplification as a biomarker.

Additionally, in line with previously published data, in this study the combinatorial effect of entinostat and volasertib is shown to synergistically reduce the number of viable cells in *MYC*-amplified MB only (Figure 51, the effect is additive in the non-amplified cell line). We also demonstrate an at least additive interaction of entinostat and volasertib on the cell cycle (Figure 52) and the induction of apoptosis (caspase-3 activity and PARP1 cleavage, Figure 53) in *MYC*-amplified MB cells. Interestingly, in the measurements for apoptotic effects, the *MYC*-amplified cell lines reacted differently to entinostat and volasertib single treatments in line with the metabolic

activity IC50 concentrations (MED8A was more sensitive to volasertib, HD-MB03 to entinostat). Also, even though apoptosis in HD-MB03 after single and combination treatment was evident, the number of dead cells (Figure 51) did not increase, pointing out the importance of the timing of such experiments. As the effect on the cell death was measured after 48 hours of treatment, it is possible that in HD-MB03 culture the cells committed to apoptosis could no longer be detected after 72 hours when the cell viability was evaluated. This suggests that there is a population of cells responding to the treatment by arresting their cell cycle, but not proceeding with the cell death signalling while other cells become apoptotic. Provided such a hypothesis holds true, another factor besides *MYC*-amplification influencing the response to the combinatorial therapy should be elucidated.

In line with data shown on single agent treatments and in MB cell lines, entinostat and volasertib synergized in both tested HGG cell lines (Figure 49 and 50). However, similarly to MB, only in the *MYC*-amplified cell line SU-DIPG-XXV the compounds interacted synergistically in clinically achievable concentrations further underscoring the clinical potential of combination only in the presence of a biomarker, such as *MYC/N*-amplification. Similar effects were observed in NB cell lines. Importantly, even though in both, *MYC/N*-amplified and non-amplified cell lines the addition of the second drug dose equivalent to the IC50 pushed the dose-response curve towards the clinically achievable range, the IC50s of *MYC/N*-non-amplified cell lines exceeded the application-relevant concentrations more than 10-fold.

As the majority of the conclusions were drawn from the data generated in the cell lines derived from the CNS tumors, it is extremely important to take the pharmacokinetics of the drugs and their ability to penetrate the blood-brain barrier (BBB) into consideration. The BBB is a feature of the cerebral vasculature, where a layer of endothelial cells forming the walls of the vessels surrounding the brain is tightly regulating the homeostasis by restricting the access to the CNS. The BBB protects the brain form various toxins and infections, it also prevents the movement of various molecules, including the small molecule inhibitors[483]. Part of the BBB can sometimes be disrupted in the presence of tumor[484].

Due to its' chemical properties and molecular composition, volasertib is unlikely to cross the BBB. There is only a comparatively limited list of studies where PLK1is were assessed in terms of BBB penetrability. All of those studies determined how glioblastoma tumors or cells react to the inhibition of PLK1. Danovi and colleagues[485] reported that volasertib to some extent is able to cross the model BBB in vitro, however, other tested PLK1is had better permeability scores. On

the other hand, Dong & Park et al[448] showed that in their mouse model, single agent volasertib effect was negligible, only exhibiting anti-tumor properties when tumors were irradiated (radiotherapy has been reported to increase the permeability of the BBB[486,487]). The PLK1is that have been demonstrated to cross the BBB were BI2536[485,488] and GSK461364[485,489]. As BI2536 is a less potent PLK1i compared to volasertib, GSK461364 and onvansertib were screened in this study for synergistic interaction with entinostat. GSK461364 and entinostat interacted synergistically comparably to the treatment with volasertib (Figure 47). *MYC*-amplified HD-MB03 and non-amplified UW228-2 cell lines showed synergistic interaction in the majority of tested concentrations. However, again, the higher effect on cell metabolic activity was found in lower concentrations in the presence of *MYC*-amplification. Interestingly, the compounds did not synergize in another *MYC*-amplified cell line MED8A. This could be influenced by a number of factors, including the limitations of chosen concentrations and ratios, as well as a steep slope of GSK461364 dose-response curve in MED8A cells. Onvansertib synergized with entinostat only in the high concentration-treated *MYC*-non-amplified cell line, potentially pointing to the limitations of the methodology used in this study, different cell response to the compounds of different potency or another influencing factor, either biological or technical.

5.2.4. PLK1i, entinostat and MYC stability

PLK1 and HDAC inhibitor involvement in DNA damage and mitotic slippage induction is not the only potential mechanism of action of this combination. In fact, when *MYC* overexpression or amplification is present in the cells making them addicted to MYC, it is also likely that the combinatorial treatment effect is conducted via MYC.

As mentioned previously, PLK1 has been shown to be involved in MYC protein stability regulation via multiple pathways. For instance, Tan and colleagues[490] demonstrated that one of the sites regulating the stability and activation of MYC protein, S62, could be phosphorylated by PLK1. This was further reiterated in other studies, where the authors showed that PLK1i decreased the S62 phosphorylation[491] and the stability of MYCN protein[184] in T-ALL and neuroblastoma cells. In addition, the latter study showed that PLK1 also regulates the degradation of MYCN protein by already mentioned ubiquitin ligase FBXW7 phosphorylation.

In this study, volasertib reduced the levels of MYC protein in line with previously published work (Figure 54). However, in contrast to the conclusions by others, volasertib did not affect the stability of MYC protein in MED8A cells when used in a concentration where no off-target activity was

reported (Figure 55). This result indicates either the limitations of the experimental conditions used or points out the fact that in MB PLK1 and MYC could potentially interact indirectly or have other means of affecting each other, as volasertib treatment was selective for *MYC*-amplified cell lines (as discussed previously). Interestingly, the proteasomal inhibitor MG132 still managed to rescue the effect of volasertib on MYC protein levels in MED8A cell line, potentially underscoring the indirect interaction possibility (Figure 56). As we explored FBXW7 as a potential indirect mediator, we did not observe the increased stability of the protein upon PLK1 inhibition, thus contradicting the data reported by others (Figure 58). As the FBXW7-PLK1-MYC axis interaction was reported in another tumor entity, neuroblastoma[184], an entity- or genetic background-specific (*MYC* vs *MYCN* amplification) mode of action could be exerted. In fact, Jiang and colleagues[491] have recently discussed another mitotic kinase, AURKB and MYC, but not MYCN interaction as MYC and MYCN have different amino acid sequences in their transactivation domains affecting the activating phosphorylation patterns.

HDACis have been shown to be selective for *MYC*-amplified cells[168,226,260]. This effect is potentially exerted via inactivation and stabilization of the MYC protein upon co-localization of MYC and class I HDACs[261,492,493]. This in turn leads to a loss of MYC transcriptional activity and down-regulation of canonical MYC target genes (Ecker, Thatikonda, et al, in revision). In fact, in this study, as well as in others (Ecker, Thatikonda, et al, in revision) we report that HDAC2 and MYC co-localize in a protein complex in *MYC*-amplified MB cells further underscoring the potential of class I HDAC inhibitors.

Apart from the aforementioned hypotheses and a brief comment on HDAC and PLK1 combination inducing the generation of the reactive oxygen species (ROS)[397], the mechanism and the mediators of HDAC and PLK1 inhibition largely remain to be elucidated. Even the studies reporting the potential MYC involvement in the response to the combination failed to address the actual mechanism. Unfortunately, after assessing the transcriptional profile changes induced by entinostat and volasertib in *MYC*-amplified MB cells, we also did not succeed at elucidating the genes or patterns responsible for the phenotype changes after treatment. As both of the drugs are not directly targeting transcription factors and HDACs are acting genome-wide, the entinostat effect could potentially be masking the effect of volasertib at the chosen timepoint. This limitation of the study could be circumvented if different treatment times for entinostat and volasertib were employed. In addition, a single mechanism of action of the combination could be absent in general. Entinostat and volasertib could possibly be inducing the phenotype by affecting different

pathways of the cell and just due to the sheer potency of both drugs, the increased effect can be detected. However, this hypothesis, as well as ROS induction in the MB models remains to be examined.

Even though we failed to determine the precise mechanism of synergistic entinostat and volasertib interaction, we are the first to report that the effect is at least partially conveyed via MYC protein as MYC target gene sets are significantly downregulated upon treatment with both compounds. In addition, MYC protein is completely abolished in the combination-treated cells. In line with the hypothesis discussed above, faster acting volasertib could potentially indirectly (as indicated by our data) reduce the stability and in turn, the levels of MYC protein. Meanwhile the remaining MYC (as the MYC levels in *MYC*-amplified MB cells are enormous) could be trapped onto the chromatin in an inactive form by entinostat treatment (as reported by Ecker, Thatikonda, et al, in revision). The activity of both compounds on MYC in MYC-addicted cells thus is determined synergistic.

6. Conclusions and perspectives

The aim and focus of the study discussed in this dissertation was to develop a combination therapy against *MYC*-amplified medulloblastoma with potential for clinical application. Based on studies conducted previously, the class I HDAC inhibitor entinostat was chosen as the first component of the combination. Two methods for target discovery were assessed: targeting the MYC-HDAC2 complex members and the identification of target based on transcriptional profile of entinostat-treated cells. The compounds targeting the elucidated proteins were examined for single treatment response, as well as in combination with the HDACi. Finally, the mechanism behind the interaction of combination partners was analysed.

Aim 1: Target discovery

As determined by previous work, HDAC2 and MYC are residing in the same protein complex with potential function of repressing the transcription of target genes. Therefore, we aimed to identify the member of the protein complex. In this study, the other complex proteins were determined, however, none of them were targetable, thus a second hypothesis for target discovery was drawn. In future projects, the composition as well as the function of the complex could be further investigated. Moreover, the PTMs applied on MYC by the HDAC2 should be identified in order to fully comprehend the relationship between those proteins.

Based on the changes of the transcriptional landscape of MYC-target genes after entinostat treatment, polo-like kinase 1 (PLK1) was identified as the most promising candidate target for the combination therapy.

Aim 2: Evaluation of entinostat and PLK1i as monotherapeutics

In order to determine whether *MYC*-amplified and non-amplified MB cells respond to the treatment with entinostat and selected PLK1 inhibitors as monotherapeutics, cell metabolic activity, viability, cycle and death induction were evaluated. We confirmed that entinostat is inducing the cell cycle changes and apoptosis more efficiently in *MYC*-amplified MB cells. Moreover, *MYC*-amplified MB cell lines were more sensitive to volasertib, GSK461364 and onvansertib treatment compared to the non-amplified cells. Finally, volasertib was shown to arrest the cell cycle in G2/M phase in all cell lines, whereas inducing the cell death and reducing the number of viable cells only in the cells with *MYC*-amplification. Therefore, we conclude that volasertib acts cytotoxically in the cell lines harbouring *MYC*-amplification and cytostatically in non-amplified cell lines.

Aim 3: Examination of entinostat and PLK1 inhibitor interaction

The relationship between several PLK1 inhibitors and entinostat were evaluated and quantified as a combination index. In addition, the changes in cell cycle, viability and death were examined in the entinostat and volasertib combination-treated cell lines. In all tested cell lines entinostat and selected PLK1 inhibitors interacted in a synergistic manner. In addition, entinostat and volasertib combination was validated to induce the apoptosis and reduce the viable cell number in an over-additive manner. Even though the effects of combination were observed in all tested cell lines, we are the first to report that entinostat and volasertib interact in a synergistic manner reducing the number of viable cells in clinically achievable doses only in *MYC*-amplified cells. The viability of the non-amplified cells was reduced only in high concentrations bordering on the doses with off-target activity.

Aim 4: Analysis of the entinostat and volasertib interaction mechanism

As determined previously entinostat and volasertib interact synergistically. Therefore, our goal here was to find out how the synergy was conveyed from targeting the single proteins to phenotypical effect. Even though in this study, we failed to determine the definite gene expression patterns influencing the synergistic interaction, we demonstrated that entinostat and volasertib exert their monotherapeutic as well as the combination therapy effects via MYC protein further emphasizing the potential of *MYC*-amplification as a biomarker in MB system.

In order to fully examine the clinical potential of HDAC and PLK1 inhibitor combination, *in vivo* assay evaluating the on-target effect (and thus the BBB permeability) as well as survival after the combination treatment is planned. In addition, further assessment of the PLK1i mechanism of action in *MYC*-amplified cell lines is necessary, including the on-target activity validation by the PLK1 knock-down experiment. Finally, the PLK1 inhibition on the kinome of the *MYC*-amplified cell lines should be investigated.

7. Supplementary material

7.1. Supplementary figures

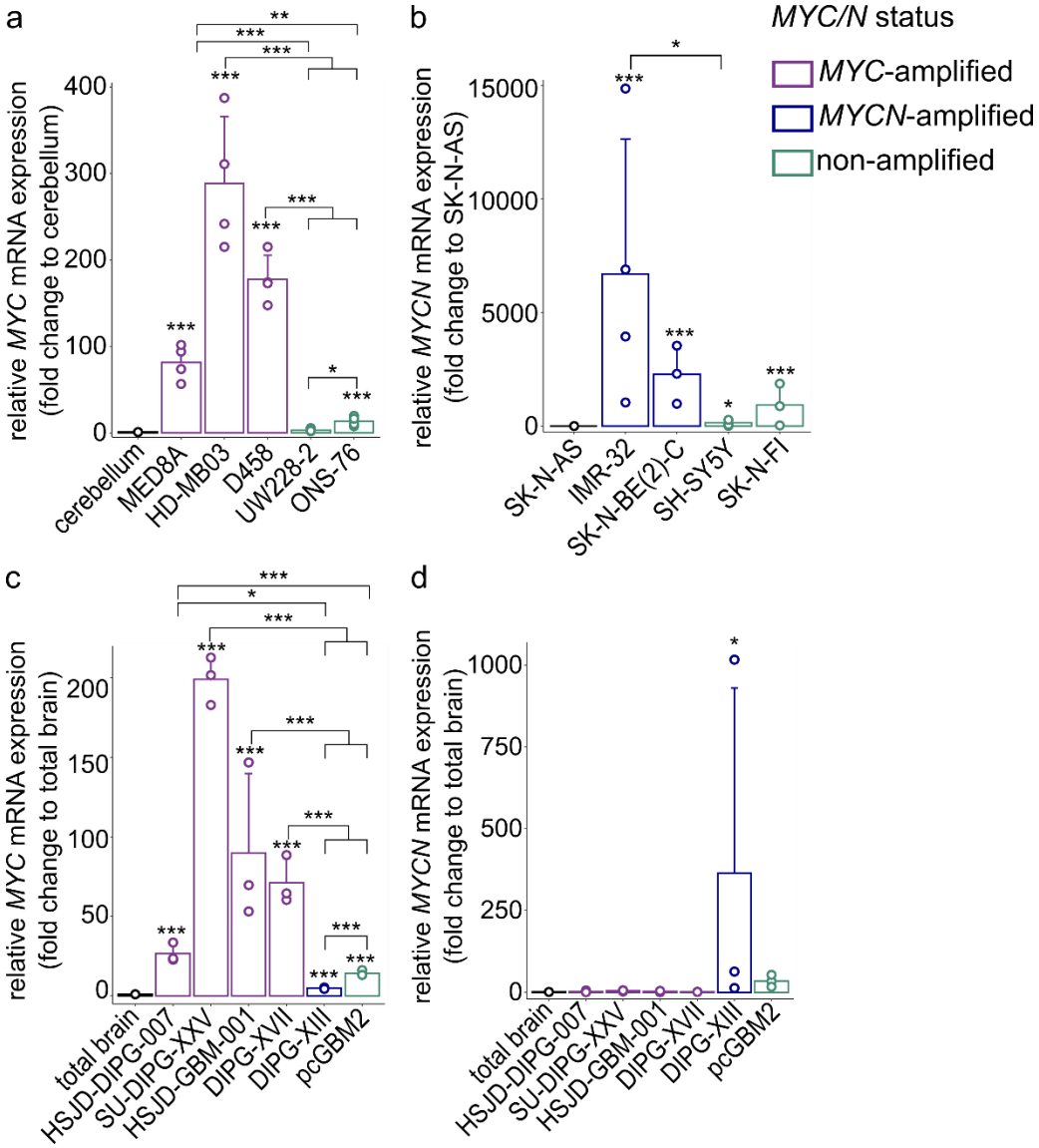

Supplementary figure 1 *MYC/N* mRNA expression levels in MB (a), NB (b) and HGG (c and d). Graph depicts mean of at least three biological replicates ± SD. One-way ANOVA was used to compare cell lines with healthy controls (a, c and d) or other cell lines: *p < 0.05; **p < 0.01; ***p < 0.001

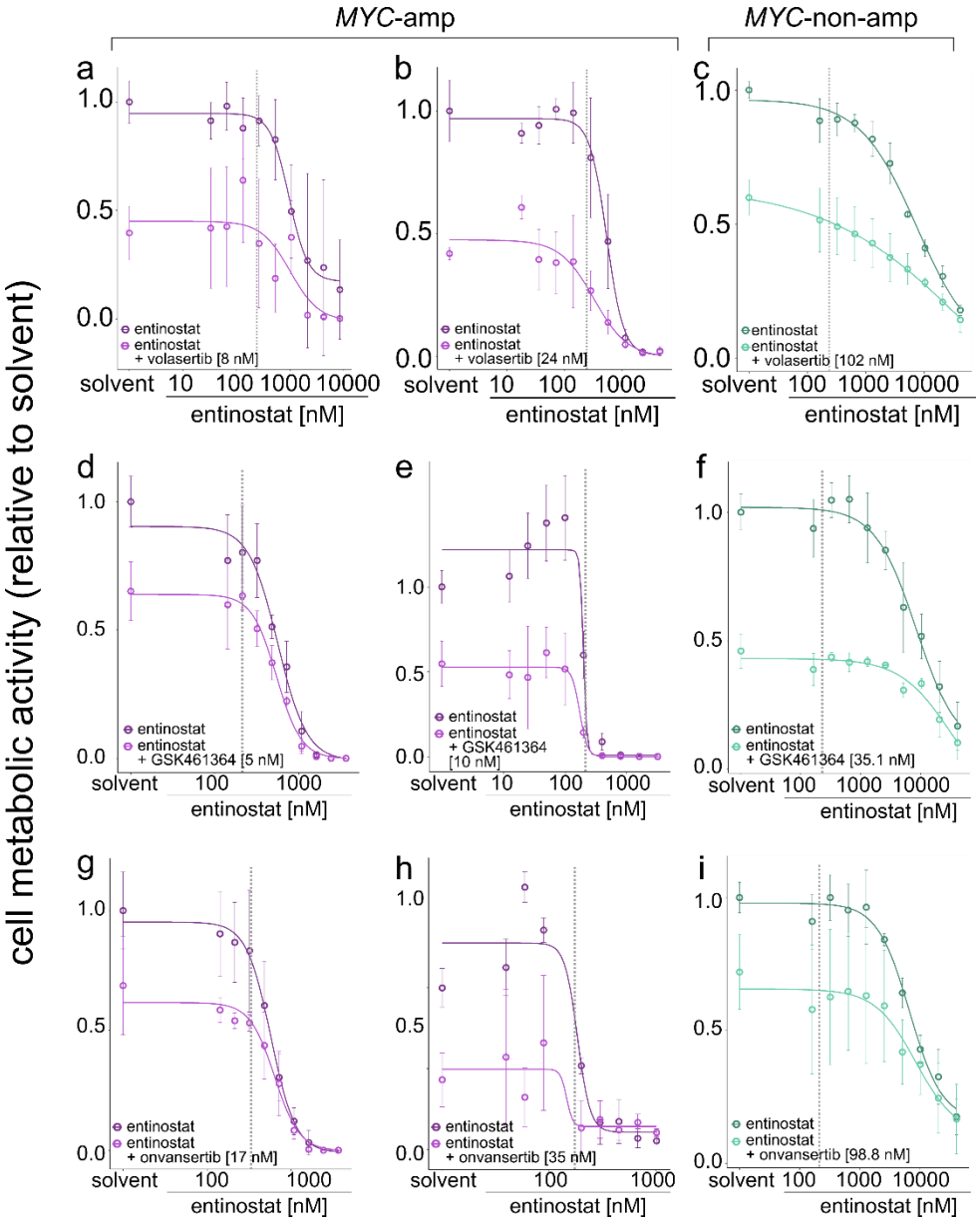

Supplementary figure 2 Dose-response curves of entinostat alone vs combination with volasertib (a-c), GSK461364 (d-f) or onvansertib (g-h) IC50 in MB. a, d, g – MED8A; b, e, h – HD-MB03; c, f, i – UW228-2. Graph depicts mean of at least three biological replicates ± SD. Grey dashed lines represent clinically achievable entinostat concentration.

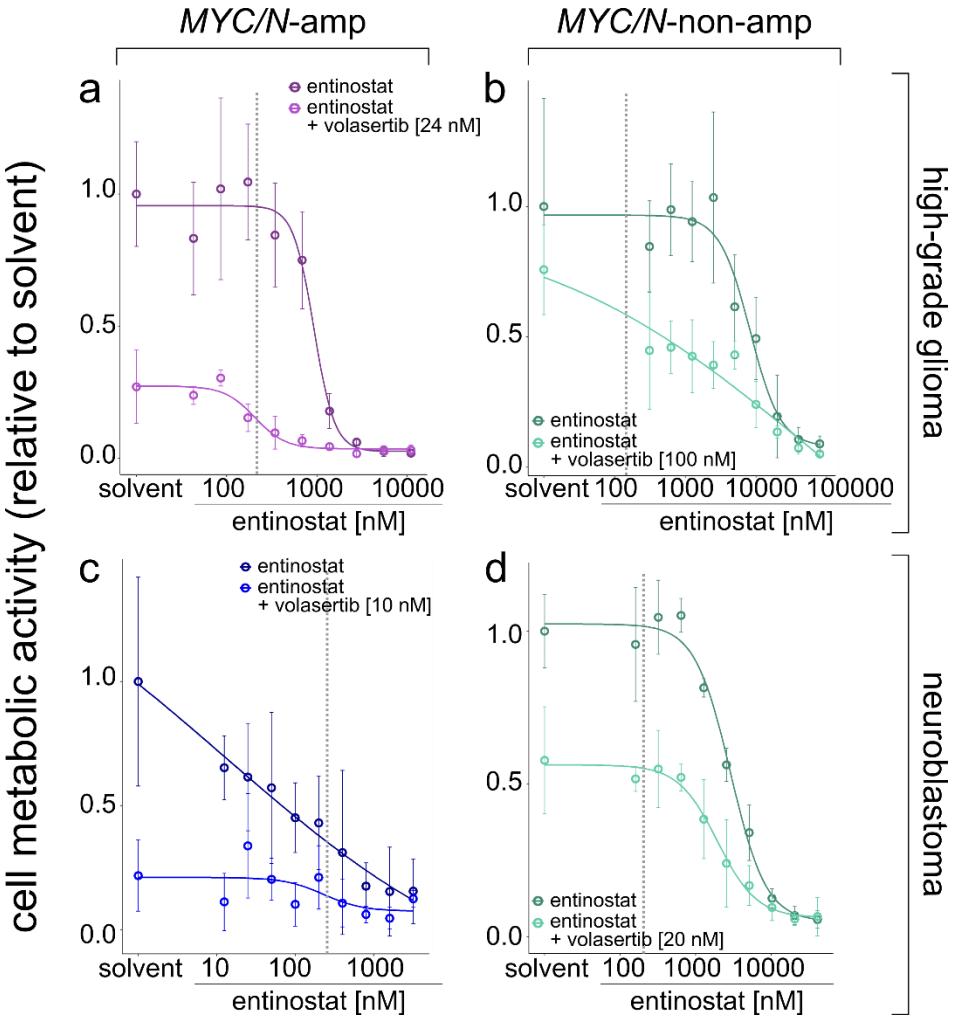

Supplementary figure 3 Dose-response curves of entinostat alone vs combination with volasertib IC50 in HGG and NB. a – SU-DIPG-XXV; b – SU-pcGBM2; c – IMR-32; d – SK-N-AS. Graph depicts mean of at least three biological replicates ± SD. Grey dashed lines represent clinically achievable entinostat concentration.

7.2. Supplementary tables

Supplementary table Proteins identified to bind HDAC2 and MYC with indicated label-free quantification intensities (LFQ) and iBAQ values.

Gene names	Log2 [LFQ intensity (MYC_IP/IgG_ MYC)]	Log2 [LFQ intensity (HDAC_IP/IgG_ HDAC)]	Log10 iBAQ HDAC_ IP	Log10 iBAQ IgG_ HDAC	Log10 iBAQ IgG_ MYC	Log10 iBAQ MYC_IP
RPL19	6.643856	6.643856	7.91	6.94	7.00	7.59
HDAC2	6.643856	6.584313	8.64	6.07	5.58	6.69
HIST1H4H	6.643856	6.643856	8.20	0.00	0.00	6.99
MAX	6.643856	6.643856	6.71	0.00	0.00	8.35
RPL14	6.643856	6.643856	7.71	6.57	6.62	7.20
RPL35A	6.643856	6.643856	7.65	6.36	5.74	7.19
USMG5	6.643856	6.643856	7.49	6.77	6.46	7.35
RPL29	6.643856	6.643856	7.66	0.00	0.00	7.15
VAPA	6.643856	6.643856	7.50	6.03	0.00	7.22
RPS6	6.643856	6.643856	7.47	6.03	5.79	7.15
SFRS3	6.643856	6.643856	7.66	6.03	5.09	6.95
RPL17	6.643856	6.643856	7.56	6.36	0.00	7.04
RPL8	6.643856	6.643856	7.59	6.65	0.00	6.96
RPL7A	6.643856	6.643856	7.64	6.58	6.53	6.87
RPL3	6.643856	3.594014	7.55	5.84	6.27	6.87
RPL38	6.643856	6.643856	7.35	6.66	6.68	7.04
RPS20	6.643856	6.643856	7.27	6.76	7.07	7.08
MYC	6.643856	6.643856	6.34	0.00	0.00	7.95
RPS5	6.643856	6.643856	7.26	6.58	5.20	7.00
NDUFA4	6.643856	6.643856	7.14	6.45	5.70	7.10
RPS26	6.643856	6.643856	7.30	6.69	6.46	6.92
SLIRP	6.643856	6.643856	7.20	6.31	6.07	6.87
TUBB	6.643856	6.643856	7.06	6.30	6.35	6.99
PGAM5	6.643856	6.643856	7.18	6.22	5.45	6.73
SSR1	6.643856	6.643856	7.04	6.00	0.00	6.81
SLC25A6	6.643856	6.643856	7.06	6.13	6.07	6.75
SRSF6	6.643856	6.643856	7.17	0.00	0.00	6.61
DNAJA1	6.643856	6.643856	6.85	6.32	5.37	6.91
RPL13A	6.643856	6.643856	7.19	6.81	5.95	6.51
MAZ	6.643856	6.643856	6.86	6.21	6.35	6.84
CHCHD6	6.643856	6.643856	7.02	0.00	0.00	6.67
COX2	6.643856	6.643856	7.05	6.70	6.88	6.64
LMAN1	6.643856	6.643856	7.10	6.03	6.00	6.58

HACD3	6.643856	6.643856	7.00	6.19	5.75	6.64
CYP1B1	6.643856	6.643856	7.00	5.16	0.00	6.59
IGLL5	6.643856	6.643856	7.06	0.00	0.00	6.51
RPS15A	6.643856	6.643856	7.05	0.00	0.00	6.48
CHD4	6.643856	6.643856	7.65	0.00	0.00	5.86
YBX1	6.643856	6.643856	6.92	5.47	6.06	6.58
MRPL14	6.643856	6.643856	6.76	0.00	0.00	6.72
MTA2	6.643856	6.643856	7.97	5.10	0.00	5.50
SFXN1	6.643856	6.643856	6.71	6.16	0.00	6.60
RPL23	6.643856	6.643856	6.72	5.78	5.82	6.50
ZNF217	6.643856	6.643856	7.39	4.89	4.14	5.76
HNRNPD	6.643856	6.643856	6.74	5.56	4.72	6.39
SLC25A1	6.643856	6.643856	6.90	5.30	5.50	6.22
MCM6	6.643856	6.643856	6.68	5.86	0.00	6.41
HNRNPA0	6.643856	6.643856	6.70	6.29	5.83	6.38
HSPB1	6.643856	6.643856	6.63	6.15	6.26	6.45
SRSF1	6.643856	6.643856	6.86	0.00	0.00	6.22
NDUFS3	6.643856	6.643856	6.68	0.00	0.00	6.37
NDUFB6	6.643856	6.643856	6.66	6.06	5.77	6.38
TIMM23	6.643856	6.643856	6.54	6.07	0.00	6.47
DPM1	6.643856	6.643856	6.60	0.00	0.00	6.39
PYCR1	6.643856	6.643856	6.54	6.14	6.26	6.45
HNRPF	6.643856	6.643856	6.52	0.00	0.00	6.43
GATAD2A	6.643856	6.643856	7.68	5.10	0.00	5.28
MCM7	6.643856	6.643856	6.61	5.40	0.00	6.32
RAB10	6.643856	6.643856	6.59	6.47	6.29	6.32
CSRP2	6.643856	6.643856	6.54	5.93	0.00	6.36
NCLN	6.643856	6.643856	6.55	0.00	4.97	6.33
SLC39A9	6.643856	6.643856	6.79	5.88	5.56	6.09
AFG3L2	6.643856	6.643856	6.56	5.47	0.00	6.32
GTSE1	6.643856	6.643856	6.47	6.57	6.52	6.36
PSPC1	6.643856	6.643856	6.45	0.00	0.00	6.25
UGT3A1	6.643856	6.643856	6.54	5.35	5.15	6.15
MTDH	6.643856	6.643856	6.59	5.66	4.50	6.10
G3BP2	6.643856	6.643856	6.60	0.00	0.00	6.08
HADHA	6.643856	6.643856	6.58	0.00	0.00	6.10
DDX21	6.643856	6.643856	6.48	0.00	0.00	6.20
GSE1	6.643856	6.643856	7.60	0.00	0.00	5.07
TBL2	6.643856	6.643856	6.64	0.00	0.00	6.02
FLOT1	6.643856	6.643856	6.58	5.33	5.29	6.03

B3GAT3	6.643856	6.643856	6.47	0.00	0.00	6.11
LONP1	6.643856	6.643856	6.54	5.63	4.77	6.03
RCN1	6.643856	6.643856	6.56	5.58	4.94	6.01
NPM1	6.643856	6.643856	6.63	0.00	0.00	5.93
YY1	6.643856	6.643856	6.07	0.00	0.00	6.50
RTCB	6.643856	6.643856	6.42	5.81	5.76	6.14
DARS	6.643856	6.643856	6.54	0.00	0.00	5.97
CABC1	6.643856	6.643856	6.42	0.00	5.54	6.07
SPATS2L	6.643856	6.643856	6.47	4.66	4.29	6.01
RARS	6.643856	6.643856	6.37	4.72	0.00	6.09
WDHD1	6.643856	2.001355	6.47	5.18	5.17	5.99
DDX17	6.643856	6.643856	6.44	5.51	0.00	6.02
MCM4	6.643856	6.643856	6.34	5.22	0.00	6.10
NDUFB10	6.643856	6.643856	6.35	0.00	0.00	6.01
SEC61A1	6.643856	6.643856	6.25	5.95	4.88	6.11
DDX1	6.643856	6.643856	6.31	5.01	4.54	5.98
FXR1	6.643856	6.643856	6.44	0.00	0.00	5.82
EIF4G1	6.643856	6.643856	6.36	5.12	3.91	5.90
TMPO	6.643856	6.643856	6.26	5.05	0.00	5.97
MATR3	6.643856	6.643856	6.27	0.00	0.00	5.89
THRAP3	6.643856	6.643856	6.13	0.00	0.00	5.96
FARSA	6.643856	6.643856	6.20	5.07	5.15	5.88
ASPH	6.643856	6.643856	6.29	5.23	5.19	5.76
RBM39	6.643856	6.643856	6.32	5.55	5.50	5.73
EIF4A1	6.643856	6.643856	6.67	5.34	0.00	5.38
MARS	6.643856	6.643856	6.29	4.81	0.00	5.73
SEPT7	6.643856	6.643856	6.03	0.00	0.00	5.97
BCLAF1	6.643856	6.643856	6.34	4.55	4.69	5.62
TBL1X	6.643856	6.643856	6.28	6.22	4.59	5.68
HNRNPM	6.643856	6.643856	6.22	5.14	0.00	5.72
FLOT2	6.643856	6.643856	6.10	5.44	0.00	5.82
GTF2I	6.643856	6.643856	6.27	0.00	0.00	5.58
SEC63	6.643856	6.643856	6.16	5.44	5.40	5.68
NDUFA10	6.643856	6.643856	5.96	5.19	0.00	5.88
SMC1A	6.643856	6.643856	6.13	0.00	0.00	5.70
EL52	6.643856	6.643856	6.12	5.87	4.98	5.64
STT3B	6.643856	6.643856	6.00	0.00	0.00	5.74
GTPBP4	6.643856	6.643856	6.27	0.00	0.00	5.41
CCT2	6.643856	6.643856	5.95	5.50	4.48	5.69
DHX9	6.643856	6.643856	6.02	0.00	0.00	5.59
PTBP1	6.643856	6.643856	5.86	5.20	0.00	5.74

DDX3X	6.643856	6.643856	5.99	0.00	0.00	5.61
ODR4	6.643856	6.643856	6.05	0.00	0.00	5.53
HDLBP	6.643856	6.643856	5.94	4.59	0.00	5.63
PABPC1	6.643856	6.643856	5.79	0.00	0.00	5.77
SF3B1	6.643856	6.643856	5.98	4.61	0.00	5.40
DYNC1H1	6.643856	2.590029	6.08	4.71	4.29	5.28
PDS5A	6.643856	6.643856	5.92	0.00	0.00	5.42
DDX42	6.643856	6.643856	6.18	0.00	0.00	5.15
SRRM1	6.643856	6.643856	6.12	4.77	4.91	5.20
LRRC41	6.643856	6.643856	5.87	0.00	0.00	5.42
NAT10	6.643856	6.643856	6.21	0.00	0.00	5.07
SUPT16H	6.643856	6.643856	5.75	0.00	0.00	5.52
CLTC	6.643856	6.643856	5.89	0.00	0.00	5.31
PRRC2C	6.643856	6.643856	5.64	5.53	5.77	5.54
CLPX	6.643856	6.643856	5.70	0.00	0.00	5.42
ZNF609	6.643856	6.643856	5.88	0.00	0.00	5.23
ARCN1	6.643856	6.643856	5.83	5.49	0.00	5.26
LEMD3	6.643856	6.643856	5.68	0.00	0.00	5.37
SMC3	6.643856	6.643856	5.91	0.00	0.00	5.13
C14orf166	6.643856	6.643856	5.72	0.00	0.00	5.27
EMC1	6.643856	6.643856	5.77	0.00	0.00	5.01
ATP13A1	6.643856	6.643856	5.58	4.83	4.02	5.20
DAP3	6.643856	6.643856	5.58	0.00	0.00	5.13
SMCHD1	6.643856	6.643856	5.73	4.41	4.23	4.85
CKAP5	6.643856	6.643856	5.57	0.00	0.00	4.98
KIF5B	6.643856	6.643856	5.63	0.00	0.00	4.89
DNMT1	6.643856	6.643856	5.57	4.39	4.78	4.94
EIF4G2	6.643856	6.643856	5.37	0.00	0.00	5.02
NUMA1	6.643856	6.643856	5.48	0.00	0.00	4.90
GTF3C1	6.643856	6.643856	5.71	0.00	0.00	4.66
DHX30	6.643856	6.643856	5.34	0.00	0.00	4.61
FASN	6.643856	6.643856	5.08	0.00	0.00	4.82

Supplementary table 1 Significantly regulated genes from the HALLMARK_MYC_TARGET_V1 and V2[16] gene sets upon entinostat treatment (5 µM; 6 hours). Blue: druggable targets.

Gene	LogFC	Adj.P.Val	Biological process	Druggable (y/n)	Clinical development
CCNA2	-0.5509	0.00891	Cell cycle; mitosis	n	NA
PLK4	-0.3791	0.01382	Cell cycle	y	P1/P2, in combination with immunotherapy
CDC20	-0.4651	0.01569	Cell cycle; mitosis	n	NA
NOP16	-0.5067	0.01701	Ribosome biogenesis	n	NA
MPHOSPH10	-0.3455	0.01886	Ribosome biogenesis	n	NA
SLC19A1	-0.4795	0.01968	Intra/Inter-cellular transport	n	NA
WDR74	-0.4001	0.02107	Ribosome biogenesis	n	NA
PLK1	-0.5207	0.0272	Cell cycle; mitosis	y	Up to P3
SRSF7	-0.5639	0.03212	RNA processing	n	NA
CUL1	-0.3478	0.03217	Protein ubiquitination	y	Pre-clinical
SRSF1	-0.7527	0.03343	RNA processing	n	NA
CTPS1	-0.3708	0.03418	Pyrimidine biosynthesis	n	NA
CSTF2	-0.3669	0.03637	RNA processing	n	NA
NIP7	-0.3553	0.03859	Ribosome biogenesis	n	NA
NDUFAF4	-0.2742	0.03959	Respiratory chain assembly	n	NA
SUPV3L1	-0.3021	0.04335	Mitochondrial RNA metabolism	n	NA
GRWD1	-0.2924	0.04508	DNA replication	n	NA

Supplementary table 2 Genes regulated in an over-additive manner in combination compared to entinostat (5 μM) or volasertib (1 μM) alone after 6 h treatment.

Gene	LogFC	Adj.P.Val
NAP1L5	0.91851531	4.62721E-05
STC1	0.938571605	0.000103577
BEND4	0.753955612	0.000225157
STEAP1	1.210785831	0.000229065
STC1	1.310648746	0.000450052
PTGS2	1.447406604	0.000685487
HLTF	0.348278375	0.000699949
SERTM1	1.245933345	0.000756935
FOXO6	0.650445676	0.000808459
ATL3	0.527391204	0.001033948
TMEM108	0.897791092	0.001370216
ADCK2	0.6217655	0.001427661
ENPP4	1.116914206	0.001605338
NAP1L5	0.91851531	4.62721E-05
STC1	0.938571605	0.000103577
BEND4	0.753955612	0.000225157

8. References

1 Hovestadt, V. *et al.* Medulloblastomics revisited: biological and clinical insights from thousands of patients. *Nature reviews. Cancer* **20**, 42-56, doi:10.1038/s41568-019-0223-8 (2020).

2 Cavalli, F. M. G. *et al.* Intertumoral Heterogeneity within Medulloblastoma Subgroups. *Cancer Cell* **31**, 737-754 e736, doi:10.1016/j.ccell.2017.05.005 (2017).

3 Steliarova-Foucher, E. *et al.* International incidence of childhood cancer, 2001-10: a population-based registry study. *Lancet Oncol* **18**, 719-731, doi:10.1016/S1470-2045(17)30186-9 (2017).

4 Han, H. *et al.* Inhibition of cell proliferation and migration through nucleobase-modified polyamidoamine-mediated p53 delivery. *International journal of nanomedicine* **13**, 1297-1311, doi:10.2147/ijn.S146917 (2018).

5 Rimkus, T. K., Carpenter, R. L., Qasem, S., Chan, M. & Lo, H. W. Targeting the Sonic Hedgehog Signaling Pathway: Review of Smoothened and GLI Inhibitors. *Cancers* **8**, doi:10.3390/cancers8020022 (2016).

6 Jeng, K. S. *et al.* Sonic Hedgehog signaling pathway as a potential target to inhibit the progression of hepatocellular carcinoma. *Oncology letters* **18**, 4377-4384, doi:10.3892/ol.2019.10826 (2019).

7 Capper, D. *et al.* DNA methylation-based classification of central nervous system tumours. *Nature* **555**, 469-474, doi:10.1038/nature26000 (2018).

8 Kaatsch, P., Grabow, D. & Spix, C. German Childhood Cancer Registry - Annual Report 2016 (1980-2015). (Institute of Medical Biostatistics, Epidemiology and Informatics (IMBEI) at the University Medical Center of the Johannes Gutenberg University Mainz, 2016).

9 Zhan, T., Rindtorff, N. & Boutros, M. Wnt signaling in cancer. *Oncogene* **36**, 1461-1473, doi:10.1038/onc.2016.304 (2017).

10 Polkinghorn, W. R. & Tarbell, N. J. Medulloblastoma: tumorigenesis, current clinical paradigm, and efforts to improve risk stratification. *Nature Clinical Practice Oncology* **4**, 295-304, doi:10.1038/ncponc0794 (2007).

11 Liu, X. Targeting Polo-Like Kinases: A Promising Therapeutic Approach for Cancer Treatment. *Translational oncology* **8**, 185-195, doi:https://doi.org/10.1016/j.tranon.2015.03.010 (2015).

12 Chen, H., Liu, H. & Qing, G. Targeting oncogenic Myc as a strategy for cancer treatment. *Signal Transduction and Targeted Therapy* **3**, 5, doi:10.1038/s41392-018-0008-7 (2018).

13 Dai, H. & Wang, Z. Histone Modification Patterns and Their Responses to Environment. *Current Environmental Health Reports* **1**, 11-21, doi:10.1007/s40572-013-0008-2 (2014).

14 Juraschka, K. & Taylor, M. D. Medulloblastoma in the age of molecular subgroups: a review. **24**, 353, doi:10.3171/2019.5.Peds18381 (2019).

15 Witt, O., Deubzer, H. E., Milde, T. & Oehme, I. HDAC family: What are the cancer relevant targets? *Cancer Letters* **277**, 8-21, doi:https://doi.org/10.1016/j.canlet.2008.08.016 (2009).

16 Liberzon, A. *et al.* The Molecular Signatures Database (MSigDB) hallmark gene set collection. *Cell Syst* **1**, 417-425, doi:10.1016/j.cels.2015.12.004 (2015).

17 Jaenicke, L. A. *et al.* Ubiquitin-Dependent Turnover of MYC Antagonizes MYC/PAF1C Complex Accumulation to Drive Transcriptional Elongation. *Molecular Cell* **61**, 54-67, doi:https://doi.org/10.1016/j.molcel.2015.11.007 (2016).

18 Tu, W. B. *et al.* Myc and its interactors take shape. *Biochimica et Biophysica Acta (BBA) - Gene Regulatory Mechanisms* **1849**, 469-483, doi:https://doi.org/10.1016/j.bbagrm.2014.06.002 (2015).
19 Hanahan, D. & Weinberg, R. A. Hallmarks of cancer: the next generation. *Cell* **144**, 646-674, doi:10.1016/j.cell.2011.02.013 (2011).
20 Farrell, A. S. & Sears, R. C. MYC degradation. *Cold Spring Harb Perspect Med* **4**, doi:10.1101/cshperspect.a014365 (2014).
21 Ostrom, Q. T. *et al.* CBTRUS Statistical Report: Primary Brain and Other Central Nervous System Tumors Diagnosed in the United States in 2012-2016. *Neuro Oncol* **21**, v1-v100, doi:10.1093/neuonc/noz150 (2019).
22 Nojima, H. G1 and S-phase checkpoints, chromosome instability, and cancer. *Methods in molecular biology (Clifton, N.J.)* **280**, 3-49, doi:10.1385/1-59259-788-2:003 (2004).
23 Ellison, D. W. Childhood medulloblastoma: novel approaches to the classification of a heterogeneous disease. *Acta Neuropathologica* **120**, 305-316, doi:10.1007/s00401-010-0726-6 (2010).
24 Poole, C. J. & van Riggelen, J. MYC-Master Regulator of the Cancer Epigenome and Transcriptome. *Genes* **8**, doi:10.3390/genes8050142 (2017).
25 Jóźwiak, P., Forma, E., Bryś, M. & Krześlak, A. O-GlcNAcylation and Metabolic Reprograming in Cancer. **5**, doi:10.3389/fendo.2014.00145 (2014).
26 Haberland, M., Montgomery, R. L. & Olson, E. N. The many roles of histone deacetylases in development and physiology: implications for disease and therapy. *Nat Rev Genet* **10**, 32-42, doi:10.1038/nrg2485 (2009).
27 Stine, Z. E., Walton, Z. E., Altman, B. J., Hsieh, A. L. & Dang, C. V. MYC, Metabolism, and Cancer. **5**, 1024-1039, doi:10.1158/2159-8290.CD-15-0507 %J Cancer Discovery (2015).
28 Hessmann, E., Johnsen, S. A., Siveke, J. T. & Ellenrieder, V. Epigenetic treatment of pancreatic cancer: is there a therapeutic perspective on the horizon? **66**, 168-179, doi:10.1136/gutjnl-2016-312539 %J Gut (2017).
29 García-Gutiérrez, L., Delgado, M. D. & León, J. MYC Oncogene Contributions to Release of Cell Cycle Brakes. **10**, 244 (2019).
30 Hydbring, P., Castell, A. & Larsson, L. G. MYC Modulation around the CDK2/p27/SKP2 Axis. *Genes* **8**, doi:10.3390/genes8070174 (2017).
31 Adhikary, S. & Eilers, M. Transcriptional regulation and transformation by Myc proteins. *Nature Reviews Molecular Cell Biology* **6**, 635-645, doi:10.1038/nrm1703 (2005).
32 Wang, Z. Y., Qin, W. & Yi, F. Targeting histone deacetylases: perspectives for epigenetic-based therapy in cardio-cerebrovascular disease. *Journal of geriatric cardiology : JGC* **12**, 153-164, doi:10.11909/j.issn.1671-5411.2015.02.010 (2015).
33 Thomas, L. R. & Tansey, W. P. in *Advances in Cancer Research* Vol. 110 (ed George Klein) 77-106 (Academic Press, 2011).
34 Kaatsch, P. Epidemiology of childhood cancer. *Cancer treatment reviews* **36**, 277-285, doi:10.1016/j.ctrv.2010.02.003 (2010).
35 Robison, L. L. & Hudson, M. M. Survivors of childhood and adolescent cancer: life-long risks and responsibilities. *Nature reviews. Cancer* **14**, 61-70, doi:10.1038/nrc3634 (2014).
36 Cancer Research UK. *Children's cancers mortality statistics*, <https://www.cancerresearchuk.org/health-professional/cancer-statistics/childrens-cancers/mortality#heading-One> (2019).
37 Howlader, N. *et al.* SEER Cancer Statistics Review, 1975-2016. (National Cancer Institute, Bethesda, MD, USA, 2019).

38 Crocetti, E. *et al.* Epidemiology of glial and non-glial brain tumours in Europe. *European Journal of Cancer* **48**, 1532-1542, doi:https://doi.org/10.1016/j.ejca.2011.12.013 (2012).
39 Curtin, S. C., Minino, A. M. & Anderson, R. N. Declines in Cancer Death Rates Among Children and Adolescents in the United States, 1999-2014. *NCHS data brief*, 1-8 (2016).
40 Wright, J. H. NEUROCYTOMA OR NEUROBLASTOMA, A KIND OF TUMOR NOT GENERALLY RECOGNIZED. *The Journal of experimental medicine* **12**, 556-561, doi:10.1084/jem.12.4.556 (1910).
41 BAILEY, P. & CUSHING, H. MEDULLOBLASTOMA CEREBELLI: A COMMON TYPE OF MIDCEREBELLAR GLIOMA OF CHILDHOOD. *Archives of Neurology & Psychiatry* **14**, 192-224, doi:10.1001/archneurpsyc.1925.02200140055002 %J Archives of Neurology & Psychiatry (1925).
42 Rubinstein, L. J. & Northfield, D. W. THE MEDULLOBLASTOMA AND THE SO-CALLED "ARACHNOIDAL CEREBELLAR SARCOMA". *Brain : a journal of neurology* **87**, 379-412, doi:10.1093/brain/87.2.379 (1964).
43 Northcott, P. A. *et al.* Medulloblastoma comprises four distinct molecular variants. *Journal of clinical oncology : official journal of the American Society of Clinical Oncology* **29**, 1408-1414, doi:10.1200/jco.2009.27.4324 (2011).
44 Kool, M. *et al.* Integrated genomics identifies five medulloblastoma subtypes with distinct genetic profiles, pathway signatures and clinicopathological features. *PloS one* **3**, e3088, doi:10.1371/journal.pone.0003088 (2008).
45 Kool, M. *et al.* Molecular subgroups of medulloblastoma: an international meta-analysis of transcriptome, genetic aberrations, and clinical data of WNT, SHH, Group 3, and Group 4 medulloblastomas. *Acta Neuropathol* **123**, 473-484, doi:10.1007/s00401-012-0958-8 (2012).
46 Pietsch, T. *et al.* Medulloblastomas of the desmoplastic variant carry mutations of the human homologue of Drosophila patched. *Cancer research* **57**, 2085-2088 (1997).
47 Kimonis, V. E. *et al.* Clinical manifestations in 105 persons with nevoid basal cell carcinoma syndrome. *American journal of medical genetics* **69**, 299-308 (1997).
48 Gururangan, S. *et al.* Gorlin syndrome and desmoplastic medulloblastoma: Report of 3 cases with unfavorable clinical course and novel mutations. *Pediatr Blood Cancer* **62**, 1855-1858, doi:10.1002/pbc.25560 (2015).
49 Louis, D. N. *et al.* The 2016 World Health Organization Classification of Tumors of the Central Nervous System: a summary. *Acta Neuropathol* **131**, 803-820, doi:10.1007/s00401-016-1545-1 (2016).
50 Taylor, M. D. *et al.* Molecular subgroups of medulloblastoma: the current consensus. *Acta Neuropathol* **123**, 465-472, doi:10.1007/s00401-011-0922-z (2012).
51 Gibson, P. *et al.* Subtypes of medulloblastoma have distinct developmental origins. *Nature* **468**, 1095-1099, doi:10.1038/nature09587 (2010).
52 Remke, M. *et al.* Adult Medulloblastoma Comprises Three Major Molecular Variants. **29**, 2717-2723, doi:10.1200/jco.2011.34.9373 (2011).
53 Ellison, D. W. *et al.* Medulloblastoma: clinicopathological correlates of SHH, WNT, and non-SHH/WNT molecular subgroups. *Acta Neuropathol* **121**, 381-396, doi:10.1007/s00401-011-0800-8 (2011).
54 Cho, Y. J. *et al.* Integrative genomic analysis of medulloblastoma identifies a molecular subgroup that drives poor clinical outcome. *Journal of clinical oncology : official journal of the American Society of Clinical Oncology* **29**, 1424-1430, doi:10.1200/jco.2010.28.5148 (2011).
55 Northcott, P. A. *et al.* The whole-genome landscape of medulloblastoma subtypes. *Nature* **547**, 311-317, doi:10.1038/nature22973 (2017).

56 Sharma, T. *et al.* Second-generation molecular subgrouping of medulloblastoma: an international meta-analysis of Group 3 and Group 4 subtypes. *Acta Neuropathol* **138**, 309-326, doi:10.1007/s00401-019-02020-0 (2019).
57 Schwalbe, E. C. *et al.* Novel molecular subgroups for clinical classification and outcome prediction in childhood medulloblastoma: a cohort study. *Lancet Oncol* **18**, 958-971, doi:10.1016/S1470-2045(17)30243-7 (2017).
58 Hovestadt, V. *et al.* Resolving medulloblastoma cellular architecture by single-cell genomics. *Nature* **572**, 74-79, doi:10.1038/s41586-019-1434-6 (2019).
59 Markowitz, S. D. & Bertagnolli, M. M. Molecular origins of cancer: Molecular basis of colorectal cancer. *N Engl J Med* **361**, 2449-2460, doi:10.1056/NEJMra0804588 (2009).
60 Latres, E., Chiaur, D. S. & Pagano, M. The human F box protein β-Trcp associates with the Cul1/Skp1 complex and regulates the stability of β-catenin. *Oncogene* **18**, 849-854, doi:10.1038/sj.onc.1202653 (1999).
61 Jiang, J. X. *et al.* Tumor suppressor Fbxw7 antagonizes WNT signaling by targeting β-catenin for degradation in pancreatic cancer. *Tumour biology : the journal of the International Society for Oncodevelopmental Biology and Medicine* **37**, 13893-13902, doi:10.1007/s13277-016-5217-5 (2016).
62 DeSouza, R.-M., Jones, B. R. T., Lowis, S. P. & Kurian, K. M. Pediatric Medulloblastoma – Update on Molecular Classification Driving Targeted Therapies. **4**, doi:10.3389/fonc.2014.00176 (2014).
63 Metcalfe, C., Mendoza-Topaz, C., Mieszczanek, J. & Bienz, M. Stability elements in the LRP6 cytoplasmic tail confer efficient signalling upon DIX-dependent polymerization. *J Cell Sci* **123**, 1588-1599, doi:10.1242/jcs.067546 (2010).
64 Thompson, M. C. *et al.* Genomics identifies medulloblastoma subgroups that are enriched for specific genetic alterations. *Journal of clinical oncology : official journal of the American Society of Clinical Oncology* **24**, 1924-1931, doi:10.1200/jco.2005.04.4974 (2006).
65 Ellison, D. W. *et al.* beta-Catenin status predicts a favorable outcome in childhood medulloblastoma: the United Kingdom Children's Cancer Study Group Brain Tumour Committee. *Journal of clinical oncology : official journal of the American Society of Clinical Oncology* **23**, 7951-7957, doi:10.1200/jco.2005.01.5479 (2005).
66 Northcott, P. A. *et al.* Subgroup-specific structural variation across 1,000 medulloblastoma genomes. *Nature* **488**, 49-56, doi:10.1038/nature11327 (2012).
67 Nüsslein-Volhard, C. & Wieschaus, E. Mutations affecting segment number and polarity in Drosophila. *Nature* **287**, 795-801, doi:10.1038/287795a0 (1980).
68 Bhardwaj, G. *et al.* Sonic hedgehog induces the proliferation of primitive human hematopoietic cells via BMP regulation. *Nature immunology* **2**, 172-180, doi:10.1038/84282 (2001).
69 Liu, S. *et al.* Hedgehog signaling and Bmi-1 regulate self-renewal of normal and malignant human mammary stem cells. *Cancer research* **66**, 6063-6071, doi:10.1158/0008-5472.CAN-06-0054 (2006).
70 Ahn, S. & Joyner, A. L. In vivo analysis of quiescent adult neural stem cells responding to Sonic hedgehog. *Nature* **437**, 894-897, doi:10.1038/nature03994 (2005).
71 Kool, M. *et al.* Genome sequencing of SHH medulloblastoma predicts genotype-related response to smoothened inhibition. *Cancer Cell* **25**, 393-405, doi:10.1016/j.ccr.2014.02.004 (2014).
72 Northcott, P. A. *et al.* Enhancer hijacking activates GFI1 family oncogenes in medulloblastoma. *Nature* **511**, 428-434, doi:10.1038/nature13379 (2014).
73 Lee, C. *et al.* Lsd1 as a therapeutic target in Gfi1-activated medulloblastoma. *Nature communications* **10**, 332, doi:10.1038/s41467-018-08269-5 (2019).

74 Boon, K., Eberhart, C. G. & Riggins, G. J. Genomic amplification of orthodenticle homologue 2 in medulloblastomas. *Cancer research* **65**, 703-707 (2005).
75 de Haas, T. *et al.* OTX1 and OTX2 expression correlates with the clinicopathologic classification of medulloblastomas. *Journal of neuropathology and experimental neurology* **65**, 176-186, doi:10.1097/01.jnen.0000199576.70923.8a (2006).
76 Stromecki, M. *et al.* Characterization of a novel OTX2-driven stem cell program in Group 3 and Group 4 medulloblastoma. *Mol Oncol* **12**, 495-513, doi:10.1002/1878-0261.12177 (2018).
77 Swartling, F. J. *et al.* Pleiotropic role for MYCN in medulloblastoma. *Genes & development* **24**, 1059-1072, doi:10.1101/gad.1907510 (2010).
78 Ivanov, D. P., Coyle, B., Walker, D. A. & Grabowska, A. M. In vitro models of medulloblastoma: Choosing the right tool for the job. *Journal of biotechnology* **236**, 10-25, doi:10.1016/j.jbiotec.2016.07.028 (2016).
79 Roussel, M. F. & Robinson, G. W. Role of MYC in Medulloblastoma. *Cold Spring Harb Perspect Med* **3**, a014308, doi:10.1101/cshperspect.a014308 (2013).
80 Pei, Y. *et al.* An Animal Model of MYC-Driven Medulloblastoma. *Cancer Cell* **21**, 155-167, doi:https://doi.org/10.1016/j.ccr.2011.12.021 (2012).
81 Kawauchi, D. *et al.* A Mouse Model of the Most Aggressive Subgroup of Human Medulloblastoma. *Cancer Cell* **21**, 168-180, doi:https://doi.org/10.1016/j.ccr.2011.12.023 (2012).
82 Tao, R. *et al.* MYC Drives Group 3 Medulloblastoma through Transformation of Sox2+ Astrocyte Progenitor Cells. **79**, 1967-1980, doi:10.1158/0008-5472.CAN-18-1787 %J Cancer Research (2019).
83 Martin, A. M., Raabe, E., Eberhart, C. & Cohen, K. J. Management of pediatric and adult patients with medulloblastoma. *Curr Treat Options Oncol* **15**, 581-594, doi:10.1007/s11864-014-0306-4 (2014).
84 Gudrunardottir, T., Sehested, A., Juhler, M. & Schmiegelow, K. Cerebellar mutism: incidence, risk factors and prognosis. *Child's nervous system : ChNS : official journal of the International Society for Pediatric Neurosurgery* **27**, 513-514; author reply 515, doi:10.1007/s00381-010-1383-8 (2011).
85 Robertson, P. L. *et al.* Incidence and severity of postoperative cerebellar mutism syndrome in children with medulloblastoma: a prospective study by the Children's Oncology Group. *Journal of neurosurgery* **105**, 444-451, doi:10.3171/ped.2006.105.6.444 (2006).
86 Palmer, S. L. *et al.* Neurocognitive outcome 12 months following cerebellar mutism syndrome in pediatric patients with medulloblastoma. *Neuro Oncol* **12**, 1311-1317, doi:10.1093/neuonc/noq094 (2010).
87 Evans, A. E. *et al.* The treatment of medulloblastoma. Results of a prospective randomized trial of radiation therapy with and without CCNU, vincristine, and prednisone. *Journal of neurosurgery* **72**, 572-582, doi:10.3171/jns.1990.72.4.0572 (1990).
88 Tait, D. M., Thornton-Jones, H., Bloom, H. J., Lemerle, J. & Morris-Jones, P. Adjuvant chemotherapy for medulloblastoma: the first multi-centre control trial of the International Society of Paediatric Oncology (SIOP I). *European journal of cancer (Oxford, England : 1990)* **26**, 464-469 (1990).
89 Grill, J. *et al.* Long-term intellectual outcome in children with posterior fossa tumors according to radiation doses and volumes. *International journal of radiation oncology, biology, physics* **45**, 137-145, doi:10.1016/s0360-3016(99)00177-7 (1999).

90 Lanier, J. C. & Abrams, A. N. Posterior fossa syndrome: Review of the behavioral and emotional aspects in pediatric cancer patients. *Cancer* **123**, 551-559, doi:10.1002/cncr.30238 (2017).
91 Szentes, A. *et al.* Cognitive deficits and psychopathological symptoms among children with medulloblastoma. *Eur J Cancer Care (Engl)* **27**, e12912, doi:10.1111/ecc.12912 (2018).
92 Christopherson, K. M. *et al.* Late toxicity following craniospinal radiation for early-stage medulloblastoma. *Acta Oncol* **53**, 471-480, doi:10.3109/0284186X.2013.862596 (2014).
93 Haldbo-Classen, L. *et al.* Long-term cognitive dysfunction after radiation therapy for primary brain tumors. *Acta Oncol* **58**, 745-752, doi:10.1080/0284186X.2018.1557786 (2019).
94 Adan, L. *et al.* Adult height after growth hormone (GH) treatment for GH deficiency due to cranial irradiation. *Medical and pediatric oncology* **34**, 14-19, doi:10.1002/(sici)1096-911x(200001)34:1<14::aid-mpo3>3.0.co;2-w (2000).
95 Bielamowicz, K. *et al.* Hypothyroidism after craniospinal irradiation with proton or photon therapy in patients with medulloblastoma. *Pediatr Hematol Oncol* **35**, 257-267, doi:10.1080/08880018.2018.1471111 (2018).
96 Packer, R. J. *et al.* Long-term neurologic and neurosensory sequelae in adult survivors of a childhood brain tumor: childhood cancer survivor study. *Journal of clinical oncology : official journal of the American Society of Clinical Oncology* **21**, 3255-3261, doi:10.1200/JCO.2003.01.202 (2003).
97 Li, Z. *et al.* A global transcriptional regulatory role for c-Myc in Burkitt's lymphoma cells. *Proceedings of the National Academy of Sciences of the United States of America* **100**, 8164-8169, doi:10.1073/pnas.1332764100 (2003).
98 Ikegaki, N., Minna, J. & Kennett, R. H. The human L-myc gene is expressed as two forms of protein in small cell lung carcinoma cell lines: detection by monoclonal antibodies specific to two myc homology box sequences. *The EMBO journal* **8**, 1793-1799 (1989).
99 Cheng, J. M. *et al.* Preferential amplification of the paternal allele of the N-myc gene in human neuroblastomas. *Nature genetics* **4**, 191-194, doi:10.1038/ng0693-191 (1993).
100 Nesbit, C. E., Tersak, J. M. & Prochownik, E. V. MYC oncogenes and human neoplastic disease. *Oncogene* **18**, 3004-3016, doi:10.1038/sj.onc.1202746 (1999).
101 Dang, C. V. c-Myc Target Genes Involved in Cell Growth, Apoptosis, and Metabolism. **19**, 1-11, doi:10.1128/MCB.19.1.1 %J Molecular and Cellular Biology (1999).
102 Sheiness, D. & Bishop, J. M. DNA and RNA from uninfected vertebrate cells contain nucleotide sequences related to the putative transforming gene of avian myelocytomatosis virus. *Journal of virology* **31**, 514-521 (1979).
103 Roussel, M. *et al.* Three new types of viral oncogene of cellular origin specific for haematopoietic cell transformation. *Nature* **281**, 452-455, doi:10.1038/281452a0 (1979).
104 Croce, C. M. *et al.* Transcriptional activation of an unrearranged and untranslocated c-myc oncogene by translocation of a C lambda locus in Burkitt. *Proceedings of the National Academy of Sciences of the United States of America* **80**, 6922-6926, doi:10.1073/pnas.80.22.6922 (1983).
105 Dalla-Favera, R. *et al.* Human c-myc onc gene is located on the region of chromosome 8 that is translocated in Burkitt lymphoma cells. *Proceedings of the National Academy of Sciences of the United States of America* **79**, 7824-7827, doi:10.1073/pnas.79.24.7824 (1982).
106 Taub, R. *et al.* Translocation of the c-myc gene into the immunoglobulin heavy chain locus in human Burkitt lymphoma and murine plasmacytoma cells. *Proceedings of the*

National Academy of Sciences of the United States of America **79**, 7837-7841, doi:10.1073/pnas.79.24.7837 (1982).
107 Varmus, H. E. THE MOLECULAR GENETICS OF CELLULAR ONCOGENES. **18**, 553-612, doi:10.1146/annurev.ge.18.120184.003005 (1984).
108 Dang, C. V. MYC on the path to cancer. *Cell* **149**, 22-35, doi:10.1016/j.cell.2012.03.003 (2012).
109 Meyer, N. & Penn, L. Z. Reflecting on 25 years with MYC. *Nature Reviews Cancer* **8**, 976-990, doi:10.1038/nrc2231 (2008).
110 Kurland, J. F. & Tansey, W. P. Myc-Mediated Transcriptional Repression by Recruitment of Histone Deacetylase. **68**, 3624-3629, doi:10.1158/0008-5472.CAN-07-6552 %J Cancer Research (2008).
111 Herbst, A. *et al.* A conserved element in Myc that negatively regulates its proapoptotic activity. *EMBO Rep* **6**, 177-183, doi:10.1038/sj.embor.7400333 (2005).
112 Rogers, S., Wells, R. & Rechsteiner, M. Amino acid sequences common to rapidly degraded proteins: the PEST hypothesis. *Science (New York, N.Y.)* **234**, 364-368, doi:10.1126/science.2876518 (1986).
113 Gregory, M. A. & Hann, S. R. c-Myc proteolysis by the ubiquitin-proteasome pathway: stabilization of c-Myc in Burkitt's lymphoma cells. *Molecular and cellular biology* **20**, 2423-2435, doi:10.1128/mcb.20.7.2423-2435.2000 (2000).
114 Conacci-Sorrell, M., Ngouenet, C. & Eisenman, R. N. Myc-nick: a cytoplasmic cleavage product of Myc that promotes alpha-tubulin acetylation and cell differentiation. *Cell* **142**, 480-493, doi:10.1016/j.cell.2010.06.037 (2010).
115 Cowling, V. H., Chandriani, S., Whitfield, M. L. & Cole, M. D. A conserved Myc protein domain, MBIV, regulates DNA binding, apoptosis, transformation, and G2 arrest. *Molecular and cellular biology* **26**, 4226-4239, doi:10.1128/MCB.01959-05 (2006).
116 Tworkowski, K. A., Salghetti, S. E. & Tansey, W. P. Stable and unstable pools of Myc protein exist in human cells. *Oncogene* **21**, 8515-8520, doi:10.1038/sj.onc.1205976 (2002).
117 Wu, J. Q. & Snyder, M. RNA polymerase II stalling: loading at the start prepares genes for a sprint. *Genome Biology* **9**, 220, doi:10.1186/gb-2008-9-5-220 (2008).
118 Cowling, V. H. & Cole, M. D. The Myc transactivation domain promotes global phosphorylation of the RNA polymerase II carboxy-terminal domain independently of direct DNA binding. *Molecular and cellular biology* **27**, 2059-2073, doi:10.1128/MCB.01828-06 (2007).
119 Gargano, B., Amente, S., Majello, B. & Lania, L. P-TEFb is a Crucial Co-Factor for Myc Transactivation. *Cell Cycle* **6**, 2031-2037, doi:10.4161/cc.6.16.4554 (2007).
120 Wolf, E., Lin, C. Y., Eilers, M. & Levens, D. L. Taming of the beast: shaping Myc-dependent amplification. *Trends Cell Biol* **25**, 241-248, doi:10.1016/j.tcb.2014.10.006 (2015).
121 Cunningham, J. T. & Ruggero, D. New Connections between Old Pathways: PDK1 Signaling Promotes Cellular Transformation through PLK1-Dependent MYC Stabilization. **3**, 1099-1102, doi:10.1158/2159-8290.CD-13-0581 %J Cancer Discovery (2013).
122 Gregory, M. A., Qi, Y. & Hann, S. R. Phosphorylation by glycogen synthase kinase-3 controls c-myc proteolysis and subnuclear localization. *The Journal of biological chemistry* **278**, 51606-51612, doi:10.1074/jbc.M310722200 (2003).
123 Welcker, M. *et al.* The Fbw7 tumor suppressor regulates glycogen synthase kinase 3 phosphorylation-dependent c-Myc protein degradation. **101**, 9085-9090, doi:10.1073/pnas.0402770101 %J Proceedings of the National Academy of Sciences (2004).

124 Curtis, C. *et al.* The genomic and transcriptomic architecture of 2,000 breast tumours reveals novel subgroups. *Nature* **486**, 346-352, doi:10.1038/nature10983 (2012).
125 The Molecular Taxonomy of Primary Prostate Cancer. *Cell* **163**, 1011-1025, doi:10.1016/j.cell.2015.10.025 (2015).
126 Vermunt, P. W. *et al.* Implementation of a lifestyle intervention for type 2 diabetes prevention in Dutch primary care: opportunities for intervention delivery. *BMC Fam Pract* **13**, 79, doi:10.1186/1471-2296-13-79 (2012).
127 Bailey, P. *et al.* Genomic analyses identify molecular subtypes of pancreatic cancer. *Nature* **531**, 47-52, doi:10.1038/nature16965 (2016).
128 Ciriello, G. *et al.* Emerging landscape of oncogenic signatures across human cancers. *Nature genetics* **45**, 1127-1133, doi:10.1038/ng.2762 (2013).
129 Beroukhim, R. *et al.* The landscape of somatic copy-number alteration across human cancers. *Nature* **463**, 899-905, doi:10.1038/nature08822 (2010).
130 Hanahan, D. & Weinberg, R. A. The hallmarks of cancer. *Cell* **100**, 57-70, doi:10.1016/s0092-8674(00)81683-9 (2000).
131 Ji, H. *et al.* Cell-type independent MYC target genes reveal a primordial signature involved in biomass accumulation. *PloS one* **6**, e26057, doi:10.1371/journal.pone.0026057 (2011).
132 van Riggelen, J., Yetil, A. & Felsher, D. W. MYC as a regulator of ribosome biogenesis and protein synthesis. *Nature reviews. Cancer* **10**, 301-309, doi:10.1038/nrc2819 (2010).
133 Lutz, W., Leon, J. & Eilers, M. Contributions of Myc to tumorigenesis. *Biochimica et Biophysica Acta (BBA) - Reviews on Cancer* **1602**, 61-71, doi:https://doi.org/10.1016/S0304-419X(02)00036-7 (2002).
134 Bretones, G., Delgado, M. D. & León, J. Myc and cell cycle control. *Biochimica et Biophysica Acta (BBA) - Gene Regulatory Mechanisms* **1849**, 506-516, doi:https://doi.org/10.1016/j.bbagrm.2014.03.013 (2015).
135 Casey, S. C., Baylot, V. & Felsher, D. W. The MYC oncogene is a global regulator of the immune response. *Blood* **131**, 2007-2015, doi:10.1182/blood-2017-11-742577 (2018).
136 Mantovani, A., Allavena, P., Sica, A. & Balkwill, F. Cancer-related inflammation. *Nature* **454**, 436-444, doi:10.1038/nature07205 (2008).
137 Baudino, T. A. *et al.* c-Myc is essential for vasculogenesis and angiogenesis during development and tumor progression. *Genes & development* **16**, 2530-2543, doi:10.1101/gad.1024602 (2002).
138 McMahon, S. B. MYC and the control of apoptosis. *Cold Spring Harb Perspect Med* **4**, a014407-a014407, doi:10.1101/cshperspect.a014407 (2014).
139 Kuzyk, A. & Mai, S. c-MYC-induced genomic instability. *Cold Spring Harb Perspect Med* **4**, a014373-a014373, doi:10.1101/cshperspect.a014373 (2014).
140 Gabay, M., Li, Y. & Felsher, D. W. MYC activation is a hallmark of cancer initiation and maintenance. *Cold Spring Harb Perspect Med* **4**, a014241, doi:10.1101/cshperspect.a014241 (2014).
141 Weinstein, I. B. & Joe, A. Oncogene Addiction. **68**, 3077-3080, doi:10.1158/0008-5472.CAN-07-3293 %J Cancer Research (2008).
142 Kipshidze, N. *et al.* First human experience with local delivery of novel antisense AVI-4126 with Infiltrator catheter in de novo native and restenotic coronary arteries: 6-month clinical and angiographic follow-up from AVAIL study. *Cardiovascular revascularization medicine : including molecular interventions* **8**, 230-235, doi:10.1016/j.carrev.2007.04.002 (2007).
143 Berg, T. *et al.* Small-molecule antagonists of Myc/Max dimerization inhibit Myc-induced transformation of chicken embryo fibroblasts. *Proceedings of the National Academy of*

Sciences of the United States of America **99**, 3830-3835, doi:10.1073/pnas.062036999 (2002).
144 Fletcher, S. & Prochownik, E. V. Small-molecule inhibitors of the Myc oncoprotein. *Biochimica et Biophysica Acta (BBA) - Gene Regulatory Mechanisms* **1849**, 525-543, doi:https://doi.org/10.1016/j.bbagrm.2014.03.005 (2015).
145 Whitfield, J. R., Beaulieu, M.-E. & Soucek, L. Strategies to Inhibit Myc and Their Clinical Applicability. *Front Cell Dev Biol* **5**, 10-10, doi:10.3389/fcell.2017.00010 (2017).
146 Han, H. *et al.* Small-Molecule MYC Inhibitors Suppress Tumor Growth and Enhance Immunotherapy. *Cancer Cell* **36**, 483-497.e415, doi:10.1016/j.ccell.2019.10.001 (2019).
147 Sengupta, D. *et al.* Disruption of BRD4 at H3K27Ac-enriched enhancer region correlates with decreased c-Myc expression in Merkel cell carcinoma. *Epigenetics* **10**, 460-466, doi:10.1080/15592294.2015.1034416 (2015).
148 Xu, Y. & Vakoc, C. R. Targeting Cancer Cells with BET Bromodomain Inhibitors. *Cold Spring Harb Perspect Med* **7**, a026674, doi:10.1101/cshperspect.a026674 (2017).
149 Andrieu, G., Belkina, A. C. & Denis, G. V. Clinical trials for BET inhibitors run ahead of the science. *Drug Discov Today Technol* **19**, 45-50, doi:10.1016/j.ddtec.2016.06.004 (2016).
150 Chipumuro, E. *et al.* CDK7 inhibition suppresses super-enhancer-linked oncogenic transcription in MYCN-driven cancer. *Cell* **159**, 1126-1139, doi:10.1016/j.cell.2014.10.024 (2014).
151 Garcia-Cuellar, M. P. *et al.* Efficacy of cyclin-dependent-kinase 9 inhibitors in a murine model of mixed-lineage leukemia. *Leukemia* **28**, 1427-1435, doi:10.1038/leu.2014.40 (2014).
152 Frost, P. *et al.* In vivo antitumor effects of the mTOR inhibitor CCI-779 against human multiple myeloma cells in a xenograft model. *Blood* **104**, 4181-4187, doi:10.1182/blood-2004-03-1153 (2004).
153 Chapuis, N. *et al.* Dual inhibition of PI3K and mTORC1/2 signaling by NVP-BEZ235 as a new therapeutic strategy for acute myeloid leukemia. *Clinical cancer research : an official journal of the American Association for Cancer Research* **16**, 5424-5435, doi:10.1158/1078-0432.Ccr-10-1102 (2010).
154 Alqahtani, A. *et al.* Bromodomain and extra-terminal motif inhibitors: a review of preclinical and clinical advances in cancer therapy. *Future Sci OA* **5**, FSO372-FSO372, doi:10.4155/fsoa-2018-0115 (2019).
155 Filippakopoulos, P. *et al.* Selective inhibition of BET bromodomains. *Nature* **468**, 1067-1073, doi:10.1038/nature09504 (2010).
156 Delmore, J. E. *et al.* BET bromodomain inhibition as a therapeutic strategy to target c-Myc. *Cell* **146**, 904-917, doi:10.1016/j.cell.2011.08.017 (2011).
157 Mertz, J. A. *et al.* Targeting MYC dependence in cancer by inhibiting BET bromodomains. *Proceedings of the National Academy of Sciences of the United States of America* **108**, 16669-16674, doi:10.1073/pnas.1108190108 (2011).
158 Nicodeme, E. *et al.* Suppression of inflammation by a synthetic histone mimic. *Nature* **468**, 1119-1123, doi:10.1038/nature09589 (2010).
159 Wyce, A. *et al.* BET inhibition silences expression of MYCN and BCL2 and induces cytotoxicity in neuroblastoma tumor models. *PloS one* **8**, e72967, doi:10.1371/journal.pone.0072967 (2013).
160 Chaidos, A. *et al.* Potent antimyeloma activity of the novel bromodomain inhibitors I-BET151 and I-BET762. *Blood* **123**, 697-705, doi:10.1182/blood-2013-01-478420 (2014).
161 Coudé, M. M. *et al.* BET inhibitor OTX015 targets BRD2 and BRD4 and decreases c-MYC in acute leukemia cells. *Oncotarget* **6**, 17698-17712, doi:10.18632/oncotarget.4131 (2015).

162 Kwiatkowski, N. *et al.* Targeting transcription regulation in cancer with a covalent CDK7 inhibitor. *Nature* **511**, 616-620, doi:10.1038/nature13393 (2014).
163 Hu, S. *et al.* Discovery and Characterization of SY-1365, a Selective, Covalent Inhibitor of CDK7. *Cancer research* **79**, 3479-3491, doi:10.1158/0008-5472.Can-19-0119 (2019).
164 Alcon, C., Manzano-Muñoz, A. & Montero, J. A New CDK9 Inhibitor on the Block to Treat Hematologic Malignancies. *Clinical cancer research : an official journal of the American Association for Cancer Research* **26**, 761-763, doi:10.1158/1078-0432.Ccr-19-3670 (2020).
165 Cidado, J. *et al.* AZD4573 Is a Highly Selective CDK9 Inhibitor That Suppresses MCL-1 and Induces Apoptosis in Hematologic Cancer Cells. *Clinical cancer research : an official journal of the American Association for Cancer Research* **26**, 922-934, doi:10.1158/1078-0432.Ccr-19-1853 (2020).
166 Sharma, N. *et al.* PI3K/AKT/mTOR and sonic hedgehog pathways cooperate together to inhibit human pancreatic cancer stem cell characteristics and tumor growth. *Oncotarget* **6**, 32039-32060, doi:10.18632/oncotarget.5055 (2015).
167 Naderali, E. *et al.* Positive Effects of PI3K/Akt Signaling Inhibition on PTEN and P53 in Prevention of Acute Lymphoblastic Leukemia Tumor Cells. *Advanced pharmaceutical bulletin* **9**, 470-480, doi:10.15171/apb.2019.056 (2019).
168 Pei, Y. *et al.* HDAC and PI3K Antagonists Cooperate to Inhibit Growth of MYC-Driven Medulloblastoma. *Cancer Cell* **29**, 311-323, doi:10.1016/j.ccell.2016.02.011 (2016).
169 Maira, S. M. *et al.* Identification and characterization of NVP-BKM120, an orally available pan-class I PI3-kinase inhibitor. *Molecular cancer therapeutics* **11**, 317-328, doi:10.1158/1535-7163.Mct-11-0474 (2012).
170 Hirai, H. *et al.* MK-2206, an allosteric Akt inhibitor, enhances antitumor efficacy by standard chemotherapeutic agents or molecular targeted drugs in vitro and in vivo. *Molecular cancer therapeutics* **9**, 1956-1967, doi:10.1158/1535-7163.Mct-09-1012 (2010).
171 Devlin, J. R. *et al.* AKT signalling is required for ribosomal RNA synthesis and progression of Eμ-Myc B-cell lymphoma in vivo. *The FEBS journal* **280**, 5307-5316, doi:10.1111/febs.12135 (2013).
172 Yu, K. *et al.* mTOR, a novel target in breast cancer: the effect of CCI-779, an mTOR inhibitor, in preclinical models of breast cancer. *Endocrine-related cancer* **8**, 249-258, doi:10.1677/erc.0.0080249 (2001).
173 Hidalgo, M. & Rowinsky, E. K. The rapamycin-sensitive signal transduction pathway as a target for cancer therapy. *Oncogene* **19**, 6680-6686, doi:10.1038/sj.onc.1204091 (2000).
174 Chen, C. *et al.* Synthesis and biological evaluation of thiazole derivatives as novel USP7 inhibitors. *Bioorganic & medicinal chemistry letters* **27**, 845-849, doi:10.1016/j.bmcl.2017.01.018 (2017).
175 Fan, Y. H. *et al.* USP7 inhibitor P22077 inhibits neuroblastoma growth via inducing p53-mediated apoptosis. *Cell death & disease* **4**, e867, doi:10.1038/cddis.2013.400 (2013).
176 Brockmann, M. *et al.* Small molecule inhibitors of aurora-a induce proteasomal degradation of N-myc in childhood neuroblastoma. *Cancer Cell* **24**, 75-89, doi:10.1016/j.ccr.2013.05.005 (2013).
177 Dauch, D. *et al.* A MYC-aurora kinase A protein complex represents an actionable drug target in p53-altered liver cancer. *Nature medicine* **22**, 744-753, doi:10.1038/nm.4107 (2016).
178 Du, J. *et al.* Aurora A-Selective Inhibitor LY3295668 Leads to Dominant Mitotic Arrest, Apoptosis in Cancer Cells, and Shows Potent Preclinical Antitumor Efficacy. *Molecular cancer therapeutics* **18**, 2207-2219, doi:10.1158/1535-7163.Mct-18-0529 (2019).

179 Smith, M. R. Ibrutinib in B lymphoid malignancies. *Expert opinion on pharmacotherapy* **16**, 1879-1887, doi:10.1517/14656566.2015.1067302 (2015).
180 Massó-Vallés, D., Jauset, T. & Soucek, L. Ibrutinib repurposing: from B-cell malignancies to solid tumors. *Oncoscience* **3**, 147-148, doi:10.18632/oncoscience.310 (2016).
181 Forde, P. M., Reiss, K. A., Zeidan, A. M. & Brahmer, J. R. What lies within: novel strategies in immunotherapy for non-small cell lung cancer. *The oncologist* **18**, 1203-1213, doi:10.1634/theoncologist.2013-0171 (2013).
182 Spigel, D. R. *et al.* Clinical activity, safety, and biomarkers of MPDL3280A, an engineered PD-L1 antibody in patients with locally advanced or metastatic non-small cell lung cancer (NSCLC). **31**, 8008-8008, doi:10.1200/jco.2013.31.15_suppl.8008 (2013).
183 Tavana, O. *et al.* HAUSP deubiquitinates and stabilizes N-Myc in neuroblastoma. *Nature medicine* **22**, 1180-1186, doi:10.1038/nm.4180 (2016).
184 Xiao, D. *et al.* Polo-like Kinase-1 Regulates Myc Stabilization and Activates a Feedforward Circuit Promoting Tumor Cell Survival. *Mol Cell* **64**, 493-506, doi:10.1016/j.molcel.2016.09.016 (2016).
185 Otto, T. *et al.* Stabilization of N-Myc is a critical function of Aurora A in human neuroblastoma. *Cancer Cell* **15**, 67-78, doi:10.1016/j.ccr.2008.12.005 (2009).
186 Li, X., Yoshida, M., Beppu, T. & Lotan, R. Modulation of growth and differentiation of human colon carcinoma cells by histone deacetylase inhibitory trichostatins. *International journal of oncology* **8**, 431-437, doi:10.3892/ijo.8.3.431 (1996).
187 You, A., Tong, J. K., Grozinger, C. M. & Schreiber, S. L. CoREST is an integral component of the CoREST- human histone deacetylase complex. *Proceedings of the National Academy of Sciences of the United States of America* **98**, 1454-1458, doi:10.1073/pnas.98.4.1454 (2001).
188 Zhang, Y. *et al.* Analysis of the NuRD subunits reveals a histone deacetylase core complex and a connection with DNA methylation. *Genes & development* **13**, 1924-1935, doi:10.1101/gad.13.15.1924 (1999).
189 Xue, Y. *et al.* NURD, a novel complex with both ATP-dependent chromatin-remodeling and histone deacetylase activities. *Mol Cell* **2**, 851-861, doi:10.1016/s1097-2765(00)80299-3 (1998).
190 Zhang, Y., LeRoy, G., Seelig, H.-P., Lane, W. S. & Reinberg, D. The Dermatomyositis-Specific Autoantigen Mi2 Is a Component of a Complex Containing Histone Deacetylase and Nucleosome Remodeling Activities. *Cell* **95**, 279-289, doi:https://doi.org/10.1016/S0092-8674(00)81758-4 (1998).
191 Wen, Y.-D. *et al.* The histone deacetylase-3 complex contains nuclear receptor corepressors. **97**, 7202-7207, doi:10.1073/pnas.97.13.7202 %J Proceedings of the National Academy of Sciences (2000).
192 Yang, W. M., Tsai, S. C., Wen, Y. D., Fejer, G. & Seto, E. Functional domains of histone deacetylase-3. *The Journal of biological chemistry* **277**, 9447-9454, doi:10.1074/jbc.M105993200 (2002).
193 Krämer, O. H. *et al.* A phosphorylation-acetylation switch regulates STAT1 signaling. *Genes & development* **23**, 223-235, doi:10.1101/gad.479209 (2009).
194 Chakrabarti, A. *et al.* HDAC8: a multifaceted target for therapeutic interventions. *Trends in Pharmacological Sciences* **36**, 481-492, doi:https://doi.org/10.1016/j.tips.2015.04.013 (2015).
195 Banerjee, S., Adhikari, N., Amin, S. A. & Jha, T. Histone deacetylase 8 (HDAC8) and its inhibitors with selectivity to other isoforms: An overview. *European Journal of Medicinal Chemistry* **164**, 214-240, doi:https://doi.org/10.1016/j.ejmech.2018.12.039 (2019).

196 Olson, D. E. *et al.* An Unbiased Approach To Identify Endogenous Substrates of “Histone” Deacetylase 8. *ACS Chemical Biology* **9**, 2210-2216, doi:10.1021/cb500492r (2014).
197 Dasgupta, T., Antony, J., Braithwaite, A. W. & Horsfield, J. A. HDAC8 Inhibition Blocks SMC3 Deacetylation and Delays Cell Cycle Progression without Affecting Cohesin-dependent Transcription in MCF7 Cancer Cells. *The Journal of biological chemistry* **291**, 12761-12770, doi:10.1074/jbc.M115.704627 (2016).
198 Wilson, B. J., Tremblay, A. M., Deblois, G. v., Sylvain-Drolet, G. & Giguère, V. An Acetylation Switch Modulates the Transcriptional Activity of Estrogen-Related Receptor α. *Molecular Endocrinology* **24**, 1349-1358, doi:10.1210/me.2009-0441 %J Molecular Endocrinology (2010).
199 Yan, W. *et al.* Histone deacetylase inhibitors suppress mutant p53 transcription via histone deacetylase 8. *Oncogene* **32**, 599-609, doi:10.1038/onc.2012.81 (2013).
200 Kao, H. Y., Downes, M., Ordentlich, P. & Evans, R. M. Isolation of a novel histone deacetylase reveals that class I and class II deacetylases promote SMRT-mediated repression. *Genes & development* **14**, 55-66 (2000).
201 Wright, L. H. & Menick, D. R. A class of their own: exploring the nondeacetylase roles of class IIa HDACs in cardiovascular disease. *Am J Physiol Heart Circ Physiol* **311**, H199-H206, doi:10.1152/ajpheart.00271.2016 (2016).
202 Harrison, B. C. *et al.* Protein kinase C-related kinase targets nuclear localization signals in a subset of class IIa histone deacetylases. *FEBS letters* **584**, 1103-1110, doi:10.1016/j.febslet.2010.02.057 (2010).
203 McKinsey, T. A., Zhang, C. L. & Olson, E. N. Identification of a signal-responsive nuclear export sequence in class II histone deacetylases. *Molecular and cellular biology* **21**, 6312-6321, doi:10.1128/mcb.21.18.6312-6321.2001 (2001).
204 Di Giorgio, E., Hancock, W. W. & Brancolini, C. MEF2 and the tumorigenic process, hic sunt leones. *Biochimica et Biophysica Acta (BBA) - Reviews on Cancer* **1870**, 261-273, doi:https://doi.org/10.1016/j.bbcan.2018.05.007 (2018).
205 Lahm, A. *et al.* Unraveling the hidden catalytic activity of vertebrate class IIa histone deacetylases. **104**, 17335-17340, doi:10.1073/pnas.0706487104 %J Proceedings of the National Academy of Sciences (2007).
206 Yang, C. J. *et al.* Nuclear HDAC6 inhibits invasion by suppressing NF-κB/MMP2 and is inversely correlated with metastasis of non-small cell lung cancer. *Oncotarget* **6**, 30263-30276, doi:10.18632/oncotarget.4749 (2015).
207 Hubbert, C. *et al.* HDAC6 is a microtubule-associated deacetylase. *Nature* **417**, 455-458, doi:10.1038/417455a (2002).
208 Kovacs, J. J. *et al.* HDAC6 Regulates Hsp90 Acetylation and Chaperone-Dependent Activation of Glucocorticoid Receptor. *Molecular Cell* **18**, 601-607, doi:https://doi.org/10.1016/j.molcel.2005.04.021 (2005).
209 Boyault, C. *et al.* HDAC6-p97/VCP controlled polyubiquitin chain turnover. *The EMBO journal* **25**, 3357-3366, doi:10.1038/sj.emboj.7601210 (2006).
210 Hook, S. S., Orian, A., Cowley, S. M. & Eisenman, R. N. Histone deacetylase 6 binds polyubiquitin through its zinc finger (PAZ domain) and copurifies with deubiquitinating enzymes. *Proceedings of the National Academy of Sciences of the United States of America* **99**, 13425-13430, doi:10.1073/pnas.172511699 (2002).
211 Hai, Y., Shinsky, S. A., Porter, N. J. & Christianson, D. W. Histone deacetylase 10 structure and molecular function as a polyamine deacetylase. *Nature communications* **8**, 15368-15368, doi:10.1038/ncomms15368 (2017).

212 Oehme, I. *et al.* Histone deacetylase 10 promotes autophagy-mediated cell survival. *Proceedings of the National Academy of Sciences of the United States of America* **110**, E2592-E2601, doi:10.1073/pnas.1300113110 (2013).
213 Ridinger, J. *et al.* Dual role of HDAC10 in lysosomal exocytosis and DNA repair promotes neuroblastoma chemoresistance. *Sci Rep* **8**, 10039-10039, doi:10.1038/s41598-018-28265-5 (2018).
214 Gao, L., Cueto, M. A., Asselbergs, F. & Atadja, P. Cloning and functional characterization of HDAC11, a novel member of the human histone deacetylase family. *The Journal of biological chemistry* **277**, 25748-25755, doi:10.1074/jbc.M111871200 (2002).
215 Cheng, F. *et al.* Divergent roles of histone deacetylase 6 (HDAC6) and histone deacetylase 11 (HDAC11) on the transcriptional regulation of IL10 in antigen presenting cells. **60**, 44-53 (2014).
216 Joshi, P. *et al.* The functional interactome landscape of the human histone deacetylase family. **9** (2013).
217 Villagra, A. *et al.* The histone deacetylase HDAC11 regulates the expression of interleukin 10 and immune tolerance. *Nature immunology* **10**, 92-100, doi:10.1038/ni.1673 (2009).
218 Yanginlar, C. & Logie, C. HDAC11 is a regulator of diverse immune functions. *Biochimica et Biophysica Acta (BBA) - Gene Regulatory Mechanisms* **1861**, 54-59, doi:https://doi.org/10.1016/j.bbagrm.2017.12.002 (2018).
219 Lu, D. Epigenetic modification enzymes: catalytic mechanisms and inhibitors. *Acta Pharmaceutica Sinica B* **3**, 141-149, doi:https://doi.org/10.1016/j.apsb.2013.04.007 (2013).
220 Smith, B. C. & Denu, J. M. Chemical mechanisms of histone lysine and arginine modifications. *Biochim Biophys Acta* **1789**, 45-57, doi:10.1016/j.bbagrm.2008.06.005 (2009).
221 Luger, K. & Richmond, T. J. The histone tails of the nucleosome. *Current Opinion in Genetics & Development* **8**, 140-146, doi:https://doi.org/10.1016/S0959-437X(98)80134-2 (1998).
222 Hayes, J. J. & Hansen, J. C. Nucleosomes and the chromatin fiber. *Current Opinion in Genetics & Development* **11**, 124-129, doi:https://doi.org/10.1016/S0959-437X(00)00168-4 (2001).
223 Strahl, B. D. & Allis, C. D. The language of covalent histone modifications. *Nature* **403**, 41-45, doi:10.1038/47412 (2000).
224 Oehme, I. *et al.* Histone Deacetylase 8 in Neuroblastoma Tumorigenesis. **15**, 91-99, doi:10.1158/1078-0432.CCR-08-0684 %J Clinical Cancer Research (2009).
225 Milde, T. *et al.* HDAC5 and HDAC9 in medulloblastoma: novel markers for risk stratification and role in tumor cell growth. *Clinical cancer research : an official journal of the American Association for Cancer Research* **16**, 3240-3252, doi:10.1158/1078-0432.CCR-10-0395 (2010).
226 Ecker, J. *et al.* Targeting class I histone deacetylase 2 in MYC amplified group 3 medulloblastoma. *Acta Neuropathol Commun* **3**, 22, doi:10.1186/s40478-015-0201-7 (2015).
227 Minamiya, Y. *et al.* Expression of histone deacetylase 1 correlates with a poor prognosis in patients with adenocarcinoma of the lung. **74**, 300-304 (2011).
228 Osada, H. *et al.* Reduced expression of class II histone deacetylase genes is associated with poor prognosis in lung cancer patients. **112**, 26-32 (2004).
229 Buurman, R. *et al.* Histone deacetylases activate hepatocyte growth factor signaling by repressing microRNA-449 in hepatocellular carcinoma cells. **143**, 811-820. e815 (2012).

230 Feng, G. *et al.* HDAC5 promotes cell proliferation in human hepatocellular carcinoma by up-regulating Six1 expression. **18**, 811-816 (2014).
231 Fritsche, P. *et al.* HDAC2 mediates therapeutic resistance of pancreatic cancer cells via the BH3-only protein NOXA. **58**, 1399-1409, doi:10.1136/gut.2009.180711 %J Gut (2009).
232 Li, D. *et al.* Histone deacetylase 6 and cytoplasmic linker protein 170 function together to regulate the motility of pancreatic cancer cells. **5**, 214-223 (2014).
233 Stypula-Cyrus, Y. *et al.* HDAC up-regulation in early colon field carcinogenesis is involved in cell tumorigenicity through regulation of chromatin structure. **8** (2013).
234 Seo, J. *et al.* Expression of histone deacetylases HDAC1, HDAC2, HDAC3, and HDAC6 in invasive ductal carcinomas of the breast. **17**, 323-331 (2014).
235 Müller, B. M. *et al.* Differential expression of histone deacetylases HDAC1, 2 and 3 in human breast cancer-overexpression of HDAC2 and HDAC3 is associated with clinicopathological indicators of disease progression. **13**, 215 (2013).
236 Weichert, W. *et al.* Histone deacetylases 1, 2 and 3 are highly expressed in prostate cancer and HDAC2 expression is associated with shorter PSA relapse time after radical prostatectomy. **98**, 604-610 (2008).
237 Weichert, W. *et al.* Expression of class I histone deacetylases indicates poor prognosis in endometrioid subtypes of ovarian and endometrial carcinomas. **10**, 1021 (2008).
238 Weichert, W. *et al.* Association of patterns of class I histone deacetylase expression with patient prognosis in gastric cancer: a retrospective analysis. **9**, 139-148 (2008).
239 Stark, M. & Hayward, N. Genome-wide loss of heterozygosity and copy number analysis in melanoma using high-density single-nucleotide polymorphism arrays. *Cancer research* **67**, 2632-2642, doi:10.1158/0008-5472.Can-06-4152 (2007).
240 Lv, Z. *et al.* Downregulation of HDAC6 promotes angiogenesis in hepatocellular carcinoma cells and predicts poor prognosis in liver transplantation patients. **55**, 1024-1033 (2016).
241 Zupkovitz, G. *et al.* The cyclin-dependent kinase inhibitor p21 is a crucial target for histone deacetylase 1 as a regulator of cellular proliferation. *Molecular and cellular biology* **30**, 1171-1181, doi:10.1128/mcb.01500-09 (2010).
242 Li, Y., Peng, L. & Seto, E. Histone Deacetylase 10 Regulates the Cell Cycle G2/M Phase Transition via a Novel Let-7-HMGA2-Cyclin A2 Pathway. *Molecular and cellular biology* **35**, 3547-3565, doi:10.1128/mcb.00400-15 (2015).
243 Fan, J. *et al.* Down-regulation of HDAC5 inhibits growth of human hepatocellular carcinoma by induction of apoptosis and cell cycle arrest. *Tumour biology : the journal of the International Society for Oncodevelopmental Biology and Medicine* **35**, 11523-11532, doi:10.1007/s13277-014-2358-2 (2014).
244 Li, Y. *et al.* A novel histone deacetylase pathway regulates mitosis by modulating Aurora B kinase activity. *Genes & development* **20**, 2566-2579, doi:10.1101/gad.1455006 (2006).
245 Schüler, S. *et al.* HDAC2 attenuates TRAIL-induced apoptosis of pancreatic cancer cells. *Molecular cancer* **9**, 80, doi:10.1186/1476-4598-9-80 (2010).
246 Riley, J. S. *et al.* Prognostic and therapeutic relevance of FLIP and procaspase-8 overexpression in non-small cell lung cancer. *Cell death & disease* **4**, e951, doi:10.1038/cddis.2013.481 (2013).
247 Jung, K. H. *et al.* HDAC2 overexpression confers oncogenic potential to human lung cancer cells by deregulating expression of apoptosis and cell cycle proteins. *Journal of cellular biochemistry* **113**, 2167-2177, doi:10.1002/jcb.24090 (2012).

248 Kim, J. K. *et al.* Targeted inactivation of HDAC2 restores p16INK4a activity and exerts antitumor effects on human gastric cancer. *Molecular cancer research : MCR* **11**, 62-73, doi:10.1158/1541-7786.Mcr-12-0332 (2013).
249 Zhang, Y., Adachi, M., Kawamura, R. & Imai, K. Bmf is a possible mediator in histone deacetylase inhibitors FK228 and CBHA-induced apoptosis. *Cell death and differentiation* **13**, 129-140, doi:10.1038/sj.cdd.4401686 (2006).
250 Li, Y. & Seto, E. HDACs and HDAC Inhibitors in Cancer Development and Therapy. *Cold Spring Harb Perspect Med* **6**, doi:10.1101/cshperspect.a026831 (2016).
251 Li, Z. & Zhu, W. G. Targeting histone deacetylases for cancer therapy: from molecular mechanisms to clinical implications. *International journal of biological sciences* **10**, 757-770, doi:10.7150/ijbs.9067 (2014).
252 Miller, K. M. *et al.* Human HDAC1 and HDAC2 function in the DNA-damage response to promote DNA nonhomologous end-joining. *Nature structural & molecular biology* **17**, 1144-1151, doi:10.1038/nsmb.1899 (2010).
253 Thurn, K. T., Thomas, S., Raha, P., Qureshi, I. & Munster, P. N. Histone deacetylase regulation of ATM-mediated DNA damage signaling. *Molecular cancer therapeutics* **12**, 2078-2087, doi:10.1158/1535-7163.Mct-12-1242 (2013).
254 Kao, G. D. *et al.* Histone deacetylase 4 interacts with 53BP1 to mediate the DNA damage response. *The Journal of cell biology* **160**, 1017-1027, doi:10.1083/jcb.200209065 (2003).
255 von Burstin, J. *et al.* E-cadherin regulates metastasis of pancreatic cancer in vivo and is suppressed by a SNAIL/HDAC1/HDAC2 repressor complex. *Gastroenterology* **137**, 361-371, 371.e361-365, doi:10.1053/j.gastro.2009.04.004 (2009).
256 Rhodes, L. V. *et al.* Suppression of triple-negative breast cancer metastasis by pan-DAC inhibitor panobinostat via inhibition of ZEB family of EMT master regulators. *Breast cancer research and treatment* **145**, 593-604, doi:10.1007/s10549-014-2979-6 (2014).
257 Yoo, Y. G., Kong, G. & Lee, M. O. Metastasis-associated protein 1 enhances stability of hypoxia-inducible factor-1alpha protein by recruiting histone deacetylase 1. *The EMBO journal* **25**, 1231-1241, doi:10.1038/sj.emboj.7601025 (2006).
258 Koeneke, E., Witt, O. & Oehme, I. HDAC Family Members Intertwined in the Regulation of Autophagy: A Druggable Vulnerability in Aggressive Tumor Entities. *Cells* **4**, 135-168, doi:10.3390/cells4020135 (2015).
259 Moresi, V. *et al.* Histone deacetylases 1 and 2 regulate autophagy flux and skeletal muscle homeostasis in mice. *Proceedings of the National Academy of Sciences of the United States of America* **109**, 1649-1654, doi:10.1073/pnas.1121159109 (2012).
260 Liu, T. *et al.* Activation of tissue transglutaminase transcription by histone deacetylase inhibition as a therapeutic approach for Myc oncogenesis. **104**, 18682-18687 (2007).
261 Zhang, X. *et al.* Myc represses miR-15a/miR-16-1 expression through recruitment of HDAC3 in mantle cell and other non-Hodgkin B-cell lymphomas. *Oncogene* **31**, 3002-3008, doi:10.1038/onc.2011.470 (2012).
262 Nebbioso, A. *et al.* c-Myc Modulation and Acetylation Is a Key HDAC Inhibitor Target in Cancer. **23**, 2542-2555, doi:10.1158/1078-0432.CCR-15-2388 %J Clinical Cancer Research (2017).
263 Witt, O. & Lindemann, R. HDAC inhibitors: magic bullets, dirty drugs or just another targeted therapy. *Cancer Lett* **280**, 123-124, doi:10.1016/j.canlet.2009.02.038 (2009).
264 Richon, V. *et al.* Second generation hybrid polar compounds are potent inducers of transformed cell differentiation. **93**, 5705-5708 (1996).
265 Richon, V. M. *et al.* A class of hybrid polar inducers of transformed cell differentiation inhibits histone deacetylases. **95**, 3003-3007 (1998).

266 Kelly, W. K. *et al.* Phase I clinical trial of histone deacetylase inhibitor: suberoylanilide hydroxamic acid administered intravenously. **9**, 3578-3588 (2003).
267 Marks, P. A. & Breslow, R. Dimethyl sulfoxide to vorinostat: development of this histone deacetylase inhibitor as an anticancer drug. *Nature Biotechnology* **25**, 84-90, doi:10.1038/nbt1272 (2007).
268 George, P. *et al.* Combination of the histone deacetylase inhibitor LBH589 and the hsp90 inhibitor 17-AAG is highly active against human CML-BC cells and AML cells with activating mutation of FLT-3. *Blood* **105**, 1768-1776, doi:10.1182/blood-2004-09-3413 (2005).
269 Giles, F. *et al.* A phase I study of intravenous LBH589, a novel cinnamic hydroxamic acid analogue histone deacetylase inhibitor, in patients with refractory hematologic malignancies. *Clinical cancer research : an official journal of the American Association for Cancer Research* **12**, 4628-4635, doi:10.1158/1078-0432.Ccr-06-0511 (2006).
270 Maiso, P. *et al.* The histone deacetylase inhibitor LBH589 is a potent antimyeloma agent that overcomes drug resistance. *Cancer research* **66**, 5781-5789, doi:10.1158/0008-5472.Can-05-4186 (2006).
271 Wang, H., Cao, Q. & Dudek, A. Z. J. A. r. Phase II study of panobinostat and bortezomib in patients with pancreatic cancer progressing on gemcitabine-based therapy. **32**, 1027-1031 (2012).
272 Plumb, J. A. *et al.* Pharmacodynamic response and inhibition of growth of human tumor xenografts by the novel histone deacetylase inhibitor PXD101. *Molecular cancer therapeutics* **2**, 721-728 (2003).
273 Qian, X. *et al.* Activity of PXD101, a histone deacetylase inhibitor, in preclinical ovarian cancer studies. *Molecular cancer therapeutics* **5**, 2086-2095, doi:10.1158/1535-7163.Mct-06-0111 (2006).
274 Steele, N. L. *et al.* A phase 1 pharmacokinetic and pharmacodynamic study of the histone deacetylase inhibitor belinostat in patients with advanced solid tumors. *Clinical cancer research : an official journal of the American Association for Cancer Research* **14**, 804-810, doi:10.1158/1078-0432.Ccr-07-1786 (2008).
275 Gimsing, P. *et al.* A phase I clinical trial of the histone deacetylase inhibitor belinostat in patients with advanced hematological neoplasia. *European journal of haematology* **81**, 170-176, doi:10.1111/j.1600-0609.2008.01102.x (2008).
276 Saito, A. *et al.* A synthetic inhibitor of histone deacetylase, MS-27-275, with marked in vivo antitumor activity against human tumors. *Proceedings of the National Academy of Sciences of the United States of America* **96**, 4592-4597, doi:10.1073/pnas.96.8.4592 (1999).
277 Lee, B. I. *et al.* MS-275, a histone deacetylase inhibitor, selectively induces transforming growth factor beta type II receptor expression in human breast cancer cells. *Cancer research* **61**, 931-934 (2001).
278 Jaboin, J. *et al.* MS-27-275, an inhibitor of histone deacetylase, has marked in vitro and in vivo antitumor activity against pediatric solid tumors. *Cancer research* **62**, 6108-6115 (2002).
279 Ryan, Q. C. *et al.* Phase I and pharmacokinetic study of MS-275, a histone deacetylase inhibitor, in patients with advanced and refractory solid tumors or lymphoma. *Journal of clinical oncology : official journal of the American Society of Clinical Oncology* **23**, 3912-3922, doi:10.1200/jco.2005.02.188 (2005).
280 Ueda, H., Nakajima, H., Hori, Y., Goto, T. & Okuhara, M. Action of FR901228, a novel antitumor bicyclic depsipeptide produced by Chromobacterium violaceum no. 968, on Ha-ras transformed NIH3T3 cells. *Bioscience, biotechnology, and biochemistry* **58**, 1579-1583, doi:10.1271/bbb.58.1579 (1994).

281 Nakajima, H., Kim, Y. B., Terano, H., Yoshida, M. & Horinouchi, S. FR901228, a potent antitumor antibiotic, is a novel histone deacetylase inhibitor. *Experimental cell research* **241**, 126-133, doi:10.1006/excr.1998.4027 (1998).
282 Furumai, R. *et al.* FK228 (depsipeptide) as a natural prodrug that inhibits class I histone deacetylases. *Cancer research* **62**, 4916-4921 (2002).
283 Marshall, J. L. *et al.* A phase I trial of depsipeptide (FR901228) in patients with advanced cancer. *Journal of experimental therapeutics & oncology* **2**, 325-332, doi:10.1046/j.1359-4117.2002.01039.x (2002).
284 Bantscheff, M. *et al.* Chemoproteomics profiling of HDAC inhibitors reveals selective targeting of HDAC complexes. *Nat Biotechnol* **29**, 255-265, doi:10.1038/nbt.1759 (2011).
285 King, K., Hauser, A. T., Melesina, J., Sippl, W. & Jung, M. Carbamates as Potential Prodrugs and a New Warhead for HDAC Inhibition. *Molecules (Basel, Switzerland)* **23**, doi:10.3390/molecules23020321 (2018).
286 Schölz, C. *et al.* Acetylation site specificities of lysine deacetylase inhibitors in human cells. *Nat Biotechnol* **33**, 415-423, doi:10.1038/nbt.3130 (2015).
287 Butler, K. V. *et al.* Rational design and simple chemistry yield a superior, neuroprotective HDAC6 inhibitor, tubastatin A. *Journal of the American Chemical Society* **132**, 10842-10846, doi:10.1021/ja102758v (2010).
288 Haggarty, S. J., Koeller, K. M., Wong, J. C., Grozinger, C. M. & Schreiber, S. L. Domain-selective small-molecule inhibitor of histone deacetylase 6 (HDAC6)-mediated tubulin deacetylation. *Proceedings of the National Academy of Sciences of the United States of America* **100**, 4389-4394, doi:10.1073/pnas.0430973100 (2003).
289 Deskin, B. *et al.* Inhibition of HDAC6 Attenuates Tumor Growth of Non-Small Cell Lung Cancer. *Translational oncology* **13**, 135-145, doi:10.1016/j.tranon.2019.11.001 (2020).
290 Balasubramanian, S. *et al.* A novel histone deacetylase 8 (HDAC8)-specific inhibitor PCI-34051 induces apoptosis in T-cell lymphomas. *Leukemia* **22**, 1026-1034, doi:10.1038/leu.2008.9 (2008).
291 Rettig, I. *et al.* Selective inhibition of HDAC8 decreases neuroblastoma growth in vitro and in vivo and enhances retinoic acid-mediated differentiation. *Cell death & disease* **6**, e1657, doi:10.1038/cddis.2015.24 (2015).
292 Bruserud, O., Stapnes, C., Ersvaer, E., Gjertsen, B. & Ryningen, A. J. C. p. b. Histone deacetylase inhibitors in cancer treatment: a review of the clinical toxicity and the modulation of gene expression in cancer cells. **8**, 388-400 (2007).
293 Nguyen, T. *et al.* Synergistic interactions between PLK1 and HDAC inhibitors in non-Hodgkin's lymphoma cells occur in vitro and in vivo and proceed through multiple mechanisms. *Oncotarget* **8**, 31478-31493, doi:10.18632/oncotarget.15649 (2017).
294 Yin, L. *et al.* PARP inhibitor veliparib and HDAC inhibitor SAHA synergistically co-target the UHRF1/BRCA1 DNA damage repair complex in prostate cancer cells. *Journal of experimental & clinical cancer research : CR* **37**, 153, doi:10.1186/s13046-018-0810-7 (2018).
295 Brocks, D. *et al.* DNMT and HDAC inhibitors induce cryptic transcription start sites encoded in long terminal repeats. *Nature genetics* **49**, 1052-1060, doi:10.1038/ng.3889 (2017).
296 Daskalakis, M. *et al.* Reactivation of endogenous retroviral elements via treatment with DNMT- and HDAC-inhibitors. *Cell Cycle* **17**, 811-822, doi:10.1080/15384101.2018.1442623 (2018).
297 Sunkel, C. E. & Glover, D. M. J. J. o. c. s. polo, a mitotic mutant of Drosophila displaying abnormal spindle poles. **89**, 25-38 (1988).
298 Llamazares, S. *et al.* polo encodes a protein kinase homolog required for mitosis in Drosophila. **5**, 2153-2165 (1991).

299 Serrano, M., Lin, A. W., McCurrach, M. E., Beach, D. & Lowe, S. W. Oncogenic ras provokes premature cell senescence associated with accumulation of p53 and p16INK4a. *Cell* **88**, 593-602, doi:10.1016/s0092-8674(00)81902-9 (1997).
300 Takeda, D. Y. & Dutta, A. DNA replication and progression through S phase. *Oncogene* **24**, 2827-2843, doi:10.1038/sj.onc.1208616 (2005).
301 DeRan, M., Pulvino, M., Greene, E., Su, C. & Zhao, J. Transcriptional Activation of Histone Genes Requires NPAT-Dependent Recruitment of TRRAP-Tip60 Complex to Histone Promoters during the G₁/S Phase Transition. **28**, 435-447, doi:10.1128/MCB.00607-07 %J Molecular and Cellular Biology (2008).
302 Vigneron, S. *et al.* The master Greatwall kinase, a critical regulator of mitosis and meiosis. *The International journal of developmental biology* **60**, 245-254, doi:10.1387/ijdb.160155tl (2016).
303 Cuddihy, A. R. & O'Connell, M. J. in *International Review of Cytology* Vol. 222 99-140 (Academic Press, 2003).
304 Musacchio, A. & Salmon, E. D. The spindle-assembly checkpoint in space and time. *Nature Reviews Molecular Cell Biology* **8**, 379-393, doi:10.1038/nrm2163 (2007).
305 Lowery, D. M., Lim, D. & Yaffe, M. B. Structure and function of Polo-like kinases. *Oncogene* **24**, 248-259, doi:10.1038/sj.onc.1208280 (2005).
306 Andrysik, Z. *et al.* The novel mouse Polo-like kinase 5 responds to DNA damage and localizes in the nucleolus. *Nucleic Acids Research* **38**, 2931-2943, doi:10.1093/nar/gkq011 %J Nucleic Acids Research (2010).
307 de Cárcer, G. *et al.* Plk5, a Polo Box Domain-Only Protein with Specific Roles in Neuron Differentiation and Glioblastoma Suppression. **31**, 1225-1239, doi:10.1128/MCB.00607-10 %J Molecular and Cellular Biology (2011).
308 Elia, A. E., Cantley, L. C. & Yaffe, M. B. Proteomic screen finds pSer/pThr-binding domain localizing Plk1 to mitotic substrates. *Science (New York, N.Y.)* **299**, 1228-1231, doi:10.1126/science.1079079 (2003).
309 Cheng, K. Y., Lowe, E. D., Sinclair, J., Nigg, E. A. & Johnson, L. N. J. T. E. j. The crystal structure of the human polo-like kinase-1 polo box domain and its phospho-peptide complex. **22**, 5757-5768 (2003).
310 Leung, G. C. *et al.* The Sak polo-box comprises a structural domain sufficient for mitotic subcellular localization. *Nature Structural Biology* **9**, 719-724, doi:10.1038/nsb848 (2002).
311 Eckerdt, F., Yuan, J. & Strebhardt, K. Polo-like kinases and oncogenesis. *Oncogene* **24**, 267-276, doi:10.1038/sj.onc.1208273 (2005).
312 Lindon, C. & Pines, J. Ordered proteolysis in anaphase inactivates Plk1 to contribute to proper mitotic exit in human cells. *The Journal of cell biology* **164**, 233-241, doi:10.1083/jcb.200309035 (2004).
313 Lu, L.-Y. *et al.* Polo-like kinase 1 is essential for early embryonic development and tumor suppression. **28**, 6870-6876 (2008).
314 Roshak, A. K. *et al.* The human polo-like kinase, PLK, regulates cdc2/cyclin B through phosphorylation and activation of the cdc25C phosphatase. **12**, 405-411 (2000).
315 Watanabe, N. *et al.* Cyclin-dependent kinase (CDK) phosphorylation destabilizes somatic Wee1 via multiple pathways. **102**, 11663-11668, doi:10.1073/pnas.0500410102 %J Proceedings of the National Academy of Sciences of the United States of America (2005).
316 Nakajima, H., Toyoshima-Morimoto, F., Taniguchi, E. & Nishida, E. Identification of a consensus motif for Plk (Polo-like kinase) phosphorylation reveals Myt1 as a Plk1 substrate. *The Journal of biological chemistry* **278**, 25277-25280, doi:10.1074/jbc.C300126200 (2003).

317 Li, H. *et al.* Polo-like kinase 1 phosphorylation of p150Glued facilitates nuclear envelope breakdown during prophase. **107**, 14633-14638 (2010).
318 Kang, Y. H. *et al.* Self-regulated Plk1 recruitment to kinetochores by the Plk1-PBIP1 interaction is critical for proper chromosome segregation. **24**, 409-422 (2006).
319 Li, H. *et al.* Phosphorylation of CLIP-170 by Plk1 and CK2 promotes timely formation of kinetochore–microtubule attachments. **29**, 2953-2965 (2010).
320 Liu, X. S. *et al.* Plk1 phosphorylates Sgt1 at the kinetochores to promote timely kinetochore-microtubule attachment. **32**, 4053-4067 (2012).
321 Golan, A., Yudkovsky, Y. & Hershko, A. J. J. o. b. c. The cyclin-ubiquitin ligase activity of cyclosome/APC is jointly activated by protein kinases Cdk1-cyclin B and Plk. **277**, 15552-15557 (2002).
322 Hansen, D. V., Loktev, A. V., Ban, K. H. & Jackson, P. K. J. M. b. o. t. c. Plk1 regulates activation of the anaphase promoting complex by phosphorylating and triggering SCFβTrCP-dependent destruction of the APC inhibitor Emi1. **15**, 5623-5634 (2004).
323 Neef, R. *et al.* Choice of Plk1 docking partners during mitosis and cytokinesis is controlled by the activation state of Cdk1. **9**, 436-444 (2007).
324 Wolfe, B. A., Takaki, T., Petronczki, M. & Glotzer, M. J. P. b. Polo-like kinase 1 directs assembly of the HsCyk-4 RhoGAP/Ect2 RhoGEF complex to initiate cleavage furrow formation. **7** (2009).
325 van Vugt, M. A. T. M. & Medema, R. H. Getting in and out of mitosis with Polo-like kinase-1. *Oncogene* **24**, 2844-2859, doi:10.1038/sj.onc.1208617 (2005).
326 Hudson, J. *et al.* Late mitotic failure in mice lacking Sak, a polo-like kinase. **11**, 441-446 (2001).
327 Habedanck, R., Stierhof, Y.-D., Wilkinson, C. J. & Nigg, E. A. The Polo kinase Plk4 functions in centriole duplication. *Nature Cell Biology* **7**, 1140-1146, doi:10.1038/ncb1320 (2005).
328 Ma, S., Charron, J., Erikson, R. L. J. M. & Biology, C. Role of Plk2 (Snk) in mouse development and cell proliferation. **23**, 6936-6943 (2003).
329 Yang, Y. *et al.* Polo-like kinase 3 functions as a tumor suppressor and is a negative regulator of hypoxia-inducible factor-1α under hypoxic conditions. **68**, 4077-4085 (2008).
330 Warnke, S. *et al.* Polo-like kinase-2 is required for centriole duplication in mammalian cells. **14**, 1200-1207 (2004).
331 Bahassi el, M., Hennigan, R. F., Myer, D. L. & Stambrook, P. J. Cdc25C phosphorylation on serine 191 by Plk3 promotes its nuclear translocation. *Oncogene* **23**, 2658-2663, doi:10.1038/sj.onc.1207425 (2004).
332 Zimmerman, W. C. & Erikson, R. L. Finding Plk3. *Cell Cycle* **6**, 1314-1318, doi:10.4161/cc.6.11.4275 (2007).
333 Liu, Z., Sun, Q. & Wang, X. PLK1, A Potential Target for Cancer Therapy. *Translational oncology* **10**, 22-32, doi:https://doi.org/10.1016/j.tranon.2016.10.003 (2017).
334 Macmillan, J. C., Hudson, J. W., Bull, S., Dennis, J. W. & Swallow, C. J. J. A. o. s. o. Comparative expression of the mitotic regulators SAK and PLK in colorectal cancer. **8**, 729-740 (2001).
335 Strebhardt, K. Multifaceted polo-like kinases: drug targets and antitargets for cancer therapy. *Nature Reviews Drug Discovery* **9**, 643-660, doi:10.1038/nrd3184 (2010).
336 Smits, V. A. *et al.* Polo-like kinase-1 is a target of the DNA damage checkpoint. **2**, 672-676 (2000).
337 Syljuåsen, R. G., Jensen, S., Bartek, J. & Lukas, J. J. C. r. Adaptation to the ionizing radiation–induced G2 checkpoint occurs in human cells and depends on checkpoint kinase 1 and Polo-like kinase 1 kinases. **66**, 10253-10257 (2006).

338 Mundt, K. E., Golsteyn, R. M., Lane, H. A., Nigg, E. A. J. B. & communications, b. r. On the regulation and function of human polo-like kinase 1 (PLK1): effects of overexpression on cell cycle progression. **239**, 377-385 (1997).
339 Meraldi, P., Honda, R. & Nigg, E. A. J. T. E. j. Aurora-A overexpression reveals tetraploidization as a major route to centrosome amplification in p53−/− cells. **21**, 483-492 (2002).
340 Ren, Y. *et al.* PLK1 stabilizes a MYC-dependent kinase network in aggressive B cell lymphomas. *The Journal of clinical investigation* **128**, 5517-5530, doi:10.1172/jci122533 (2018).
341 de Cárcer, G. The Mitotic Cancer Target Polo-Like Kinase 1: Oncogene or Tumor Suppressor? *Genes* **10**, doi:10.3390/genes10030208 (2019).
342 Raab, M. *et al.* PLK1 has tumor-suppressive potential in APC-truncated colon cancer cells. *Nature communications* **9**, 1106, doi:10.1038/s41467-018-03494-4 (2018).
343 de Cárcer, G. *et al.* Plk1 overexpression induces chromosomal instability and suppresses tumor development. *Nature communications* **9**, 3012, doi:10.1038/s41467-018-05429-5 (2018).
344 Syed, N. *et al.* Transcriptional silencing of Polo-like kinase 2 (SNK/PLK2) is a frequent event in B-cell malignancies. **107**, 250-256 (2006).
345 Coley, H. M. *et al.* Polo like kinase 2 tumour suppressor and cancer biomarker: new perspectives on drug sensitivity/resistance in cancer. **3**, 78 (2012).
346 Li, B. *et al.* Prk, a cytokine-inducible human protein serine/threonine kinase whose expression appears to be down-regulated in lung carcinomas. **271**, 19402-19408 (1996).
347 Dai, W. *et al.* PRK, a cell cycle gene localized to 8p21, is downregulated in head and neck cancer. **27**, 332-336 (2000).
348 Burns, T. F. *et al.* Silencing of the novel p53 target gene Snk/Plk2 leads to mitotic catastrophe in paclitaxel (taxol)-exposed cells. **23**, 5556-5571 (2003).
349 Xie, S. *et al.* Plk3 functionally links DNA damage to cell cycle arrest and apoptosis at least in part via the p53 pathway. **276**, 43305-43312 (2001).
350 Yang, X. *et al.* Plk1-mediated phosphorylation of Topors regulates p53 stability. **284**, 18588-18592 (2009).
351 Liu, X. S., Li, H., Song, B. & Liu, X. J. E. r. Polo-like kinase 1 phosphorylation of G2 and S-phase-expressed 1 protein is essential for p53 inactivation during G2 checkpoint recovery. **11**, 626-632 (2010).
352 Liu, X. & Erikson, R. L. J. P. o. t. N. A. o. S. Polo-like kinase (Plk) 1 depletion induces apoptosis in cancer cells. **100**, 5789-5794 (2003).
353 Guan, R. *et al.* Small interfering RNA–mediated Polo-like kinase 1 depletion preferentially reduces the survival of p53-defective, oncogenic transformed cells and inhibits tumor growth in animals. **65**, 2698-2704 (2005).
354 Ward, A. & Hudson, J. W. J. P. o. p53-Dependent and cell specific epigenetic regulation of the polo-like kinases under oxidative stress. **9** (2014).
355 Degenhardt, Y. & Lampkin, T. Targeting Polo-like Kinase in Cancer Therapy. **16**, 384-389, doi:10.1158/1078-0432.CCR-09-1380 %J Clinical Cancer Research (2010).
356 Haupenthal, J. *et al.* Reduced efficacy of the Plk1 inhibitor BI 2536 on the progression of hepatocellular carcinoma due to low intratumoral drug levels. **14**, 410-IN410 (2012).
357 Steegmaier, M. *et al.* BI 2536, a potent and selective inhibitor of polo-like kinase 1, inhibits tumor growth in vivo. **17**, 316-322 (2007).
358 Mross, K. *et al.* Phase I dose escalation and pharmacokinetic study of BI 2536, a novel Polo-like kinase 1 inhibitor, in patients with advanced solid tumors. **26**, 5511-5517 (2008).

359 Mross, K. *et al.* A randomized phase II trial of the novel polo-like kinase 1 inhibitor BI 2536 in chemonaïve patients with unresectable advanced pancreatic cancer: a study in cooperation with the CESAR network of investigators. **19** (2008).
360 Von Pawel, J. *et al.* Randomized phase II trial of two dosing schedules of BI 2536, a novel Plk-1 inhibitor, in patients with relapsed advanced or metastatic non-small-cell lung cancer (NSCLC). **26**, 8030-8030 (2008).
361 Rudolph, D. *et al.* BI 6727, a Polo-like kinase inhibitor with improved pharmacokinetic profile and broad antitumor activity. **15**, 3094-3102 (2009).
362 Schöffski, P. *et al.* A phase I, dose-escalation study of the novel Polo-like kinase inhibitor volasertib (BI 6727) in patients with advanced solid tumours. **48**, 179-186 (2012).
363 Lin, C. C. *et al.* A phase I study of two dosing schedules of volasertib (BI 6727), an intravenous polo-like kinase inhibitor, in patients with advanced solid malignancies. *British Journal of Cancer* **110**, 2434-2440, doi:10.1038/bjc.2014.195 (2014).
364 Döhner, H. *et al.* Randomized, phase 2 trial of low-dose cytarabine with or without volasertib in AML patients not suitable for induction therapy. *Blood* **124**, 1426-1433, doi:10.1182/blood-2014-03-560557 %J Blood (2014).
365 Beria, I. *et al.* NMS-P937, a 4,5-dihydro-1H-pyrazolo[4,3-h]quinazoline derivative as potent and selective Polo-like kinase 1 inhibitor. *Bioorganic & medicinal chemistry letters* **21**, 2969-2974, doi:10.1016/j.bmcl.2011.03.054 (2011).
366 Valsasina, B. *et al.* NMS-P937, an orally available, specific small-molecule polo-like kinase 1 inhibitor with antitumor activity in solid and hematologic malignancies. *Molecular cancer therapeutics* **11**, 1006-1016, doi:10.1158/1535-7163.Mct-11-0765 (2012).
367 Emmitte, K. A. *et al.* Discovery of thiophene inhibitors of polo-like kinase. **19**, 1018-1021 (2009).
368 Olmos, D. *et al.* Phase I first-in-human study of the polo-like kinase-1 selective inhibitor, GSK461364, in patients with advanced solid tumors. **27**, 3536-3536, doi:10.1200/jco.2009.27.15_suppl.3536 (2009).
369 Gilmartin, A. G. *et al.* Distinct concentration-dependent effects of the polo-like kinase 1–specific inhibitor GSK461364A, including differential effect on apoptosis. **69**, 6969-6977 (2009).
370 Hikichi, Y. *et al.* TAK-960, a novel, orally available, selective inhibitor of polo-like kinase 1, shows broad-spectrum preclinical antitumor activity in multiple dosing regimens. *Molecular cancer therapeutics* **11**, 700-709, doi:10.1158/1535-7163.Mct-11-0762 (2012).
371 Nie, Z. *et al.* Discovery of TAK-960: an orally available small molecule inhibitor of polo-like kinase 1 (PLK1). *Bioorganic & medicinal chemistry letters* **23**, 3662-3666, doi:10.1016/j.bmcl.2013.02.083 (2013).
372 Duffey, M. O. *et al.* Discovery of a potent and orally bioavailable benzolactam-derived inhibitor of Polo-like kinase 1 (MLN0905). *Journal of medicinal chemistry* **55**, 197-208, doi:10.1021/jm2011172 (2012).
373 Shi, J. Q. *et al.* MLN0905, a small-molecule plk1 inhibitor, induces antitumor responses in human models of diffuse large B-cell lymphoma. *Molecular cancer therapeutics* **11**, 2045-2053, doi:10.1158/1535-7163.Mct-11-1036 (2012).
374 Wang, N. N. *et al.* Molecular targeting of the oncoprotein PLK1 in pediatric acute myeloid leukemia: RO3280, a novel PLK1 inhibitor, induces apoptosis in leukemia cells. *International journal of molecular sciences* **16**, 1266-1292, doi:10.3390/ijms16011266 (2015).
375 Gumireddy, K. *et al.* ON01910, a non-ATP-competitive small molecule inhibitor of Plk1, is a potent anticancer agent. **7**, 275-286 (2005).

376 Jimeno, A. *et al.* Phase I study of ON 01910.Na, a novel modulator of the Polo-like kinase 1 pathway, in adult patients with solid tumors. *Journal of clinical oncology : official journal of the American Society of Clinical Oncology* **26**, 5504-5510, doi:10.1200/jco.2008.17.9788 (2008).
377 Tanaka, H. *et al.* HMN-176, an active metabolite of the synthetic antitumor agent HMN-214, restores chemosensitivity to multidrug-resistant cells by targeting the transcription factor NF-Y. **63**, 6942-6947 (2003).
378 Garland, L. L., Taylor, C., Pilkington, D. L., Cohen, J. L. & Von Hoff, D. D. A phase I pharmacokinetic study of HMN-214, a novel oral stilbene derivative with polo-like kinase-1-interacting properties, in patients with advanced solid tumors. *Clinical cancer research : an official journal of the American Association for Cancer Research* **12**, 5182-5189, doi:10.1158/1078-0432.Ccr-06-0214 (2006).
379 Hoff, D. D. V., Taylor, C., Rubin, S., Cohen, J. & Garland, L. A Phase I and pharmacokinetic study of HMN-214, a novel oral polo-like kinase inhibitor, in patients with advanced solid tumors. **22**, 3034-3034, doi:10.1200/jco.2004.22.90140.3034 (2004).
380 Keppner, S. *et al.* Biological impact of freezing Plk1 in its inactive conformation in cancer cells. *Cell Cycle* **9**, 761-773, doi:10.4161/cc.9.4.10644 (2010).
381 Lange, L., Keppner-Witter, S., Grigat, J. & Spänkuch, B. Combinatorial inhibition of Plk1 and PKCβ in cancer cells with different p53 status. *Oncotarget* **5**, 2263-2275, doi:10.18632/oncotarget.1897 (2014).
382 Reindl, W. *et al.* Inhibition of polo-like kinase 1 by blocking polo-box domain-dependent protein-protein interactions. **15**, 459-466 (2008).
383 Mason, J. M. *et al.* Functional characterization of CFI-400945, a Polo-like kinase 4 inhibitor, as a potential anticancer agent. **26**, 163-176 (2014).
384 Kawakami, M. *et al.* Polo-like kinase 4 inhibition produces polyploidy and apoptotic death of lung cancers. **115**, 1913-1918 (2018).
385 Lei, Q. *et al.* YLT-11, a novel PLK4 inhibitor, inhibits human breast cancer growth via inducing maladjusted centriole duplication and mitotic defect. *Cell death & disease* **9**, 1066, doi:10.1038/s41419-018-1071-2 (2018).
386 Wong, Y. L. *et al.* Reversible centriole depletion with an inhibitor of Polo-like kinase 4. **348**, 1155-1160 (2015).
387 Suri, A. *et al.* Evaluation of protein kinase inhibitors with PLK4 cross-over potential in a pre-clinical model of cancer. **20**, 2112 (2019).
388 Chou, T. C. & Talalay, P. Quantitative analysis of dose-effect relationships: the combined effects of multiple drugs or enzyme inhibitors. *Advances in enzyme regulation* **22**, 27-55, doi:10.1016/0065-2571(84)90007-4 (1984).
389 Loewe, S. t. & Muischnek, H. J. N.-S. A. f. e. P. u. P. Über kombinationswirkungen. **114**, 313-326 (1926).
390 Loewe, S. The problem of synergism and antagonism of combined drugs. *Arzneimittel-Forschung* **3**, 285-290 (1953).
391 Greco, W. R., Bravo, G. & Parsons, J. C. The search for synergy: a critical review from a response surface perspective. *Pharmacological reviews* **47**, 331-385 (1995).
392 Berenbaum, M. J. C. & immunology, e. Synergy, additivism and antagonism in immunosuppression. A critical review. **28**, 1 (1977).
393 Foucquier, J. & Guedj, M. Analysis of drug combinations: current methodological landscape. **3**, e00149, doi:10.1002/prp2.149 (2015).
394 Chou, T.-C. Theoretical Basis, Experimental Design, and Computerized Simulation of Synergism and Antagonism in Drug Combination Studies. **58**, 621-681, doi:10.1124/pr.58.3.10 %J Pharmacological Reviews (2006).

395 Bliss, C. J. A. o. a. b. The toxicity of poisons applied jointly 1. **26**, 585-615 (1939).
396 Goldoni, M. & Johansson, C. A mathematical approach to study combined effects of toxicants in vitro: Evaluation of the Bliss independence criterion and the Loewe additivity model. *Toxicology in Vitro* **21**, 759-769, doi:https://doi.org/10.1016/j.tiv.2007.03.003 (2007).
397 Dasmahapatra, G., Patel, H., Nguyen, T., Attkisson, E. & Grant, S. PLK1 inhibitors synergistically potentiate HDAC inhibitor lethality in imatinib mesylate-sensitive or -resistant BCR/ABL+ leukemia cells in vitro and in vivo. *Clinical cancer research : an official journal of the American Association for Cancer Research* **19**, 404-414, doi:10.1158/1078-0432.CCR-12-2799 (2013).
398 Milde, T. *et al.* HD-MB03 is a novel Group 3 medulloblastoma model demonstrating sensitivity to histone deacetylase inhibitor treatment. *Journal of neuro-oncology* **110**, 335-348, doi:10.1007/s11060-012-0978-1 (2012).
399 Gravendeel, L. A. *et al.* Intrinsic gene expression profiles of gliomas are a better predictor of survival than histology. *Cancer research* **69**, 9065-9072, doi:10.1158/0008-5472.Can-09-2307 (2009).
400 Worst, B. C. *et al.* Next-generation personalised medicine for high-risk paediatric cancer patients - The INFORM pilot study. *European journal of cancer (Oxford, England : 1990)* **65**, 91-101, doi:10.1016/j.ejca.2016.06.009 (2016).
401 Robinson, G. *et al.* Novel mutations target distinct subgroups of medulloblastoma. *Nature* **488**, 43-48, doi:10.1038/nature11213 (2012).
402 Forget, A. *et al.* Aberrant ERBB4-SRC Signaling as a Hallmark of Group 4 Medulloblastoma Revealed by Integrative Phosphoproteomic Profiling. *Cancer Cell* **34**, 379-395.e377, doi:10.1016/j.ccell.2018.08.002 (2018).
403 Archer, T. C. *et al.* Proteomics, Post-translational Modifications, and Integrative Analyses Reveal Molecular Heterogeneity within Medulloblastoma Subgroups. *Cancer Cell* **34**, 396-410.e398, doi:10.1016/j.ccell.2018.08.004 (2018).
404 Molenaar, J. J. *et al.* Sequencing of neuroblastoma identifies chromothripsis and defects in neuritogenesis genes. *Nature* **483**, 589-593, doi:10.1038/nature10910 (2012).
405 Schmitt, M. & Pawlita, M. High-throughput detection and multiplex identification of cell contaminations. *Nucleic Acids Res* **37**, e119, doi:10.1093/nar/gkp581 (2009).
406 Hughes, C. S. *et al.* Single-pot, solid-phase-enhanced sample preparation for proteomics experiments. *Nature protocols* **14**, 68-85, doi:10.1038/s41596-018-0082-x (2019).
407 Cox, J. *et al.* Accurate proteome-wide label-free quantification by delayed normalization and maximal peptide ratio extraction, termed MaxLFQ. *Molecular & cellular proteomics : MCP* **13**, 2513-2526, doi:10.1074/mcp.M113.031591 (2014).
408 Tyanova, S., Temu, T. & Cox, J. The MaxQuant computational platform for mass spectrometry-based shotgun proteomics. *Nature protocols* **11**, 2301-2319, doi:10.1038/nprot.2016.136 (2016).
409 Wickham, H. *ggplot2: elegant graphics for data analysis*. (Springer, 2009).
410 Smyth, G. K. in *Bioinformatics and Computational Biology Solutions Using R and Bioconductor* (eds Robert Gentleman *et al.*) 397-420 (Springer New York, 2005).
411 Ritz, C., Baty, F., Streibig, J. C. & Gerhard, D. Dose-Response Analysis Using R. *PloS one* **10**, e0146021, doi:10.1371/journal.pone.0146021 (2015).
412 Chou, T. C. Derivation and properties of Michaelis-Menten type and Hill type equations for reference ligands. *Journal of theoretical biology* **59**, 253-276, doi:10.1016/0022-5193(76)90169-7 (1976).
413 Wu, D. & Smyth, G. K. Camera: a competitive gene set test accounting for inter-gene correlation. *Nucleic Acids Res* **40**, e133, doi:10.1093/nar/gks461 (2012).

414 Mao, D. Y. *et al.* Analysis of Myc bound loci identified by CpG island arrays shows that Max is essential for Myc-dependent repression. **13**, 882-886 (2003).
415 Amati, B. *et al.* Transcriptional activation by the human c-Myc oncoprotein in yeast requires interaction with Max. **359**, 423-426 (1992).
416 Grant, P. A. *et al.* Yeast Gcn5 functions in two multisubunit complexes to acetylate nucleosomal histones: characterization of an Ada complex and the SAGA (Spt/Ada) complex. **11**, 1640-1650 (1997).
417 Zhang, K., Faiola, F., Martinez, E. J. B. & communications, b. r. Six lysine residues on c-Myc are direct substrates for acetylation by p300. **336**, 274-280 (2005).
418 Faiola, F. *et al.* Dual regulation of c-Myc by p300 via acetylation-dependent control of Myc protein turnover and coactivation of Myc-induced transcription. **25**, 10220-10234 (2005).
419 Carystinos, G. D., Kandouz, M., Alaoui-Jamali, M. A. & Batist, G. Unexpected induction of the human connexin 43 promoter by the ras signaling pathway is mediated by a novel putative promoter sequence. *Molecular pharmacology* **63**, 821-831, doi:10.1124/mol.63.4.821 (2003).
420 Agrawal, P., Yu, K., Salomon, A. R. & Sedivy, J. M. Proteomic profiling of Myc-associated proteins. *Cell Cycle* **9**, 4908-4921, doi:10.4161/cc.9.24.14199 (2010).
421 Gupta, R. *et al.* DNA Repair Network Analysis Reveals Shieldin as a Key Regulator of NHEJ and PARP Inhibitor Sensitivity. *Cell* **173**, 972-988.e923, doi:10.1016/j.cell.2018.03.050 (2018).
422 Hauri, S. *et al.* A High-Density Map for Navigating the Human Polycomb Complexome. *Cell reports* **17**, 583-595, doi:10.1016/j.celrep.2016.08.096 (2016).
423 Thillainadesan, G. *et al.* Genome analysis identifies the p15ink4b tumor suppressor as a direct target of the ZNF217/CoREST complex. *Molecular and cellular biology* **28**, 6066-6077, doi:10.1128/mcb.00246-08 (2008).
424 Kloet, S. L. *et al.* Towards elucidating the stability, dynamics and architecture of the nucleosome remodeling and deacetylase complex by using quantitative interaction proteomics. *The FEBS journal* **282**, 1774-1785, doi:10.1111/febs.12972 (2015).
425 Hoffmeister, H. *et al.* CHD3 and CHD4 form distinct NuRD complexes with different yet overlapping functionality. *Nucleic Acids Res* **45**, 10534-10554, doi:10.1093/nar/gkx711 (2017).
426 Vernon, E. G., Gaston, K. J. B. e. B. A.-G. S. & Expression. Myc and YY1 mediate activation of the Surf-1 promoter in response to serum growth factors. **1492**, 172-179 (2000).
427 Vella, P., Barozzi, I., Cuomo, A., Bonaldi, T. & Pasini, D. J. N. a. r. Yin Yang 1 extends the Myc-related transcription factors network in embryonic stem cells. **40**, 3403-3418 (2012).
428 Roy, A. L., Carruthers, C., Gutjahr, T. & Roeder, R. G. Direct role for Myc in transcription initiation mediated by interactions with TFII-I. *Nature* **365**, 359-361, doi:10.1038/365359a0 (1993).
429 Tang, W. *et al.* The p300/YY1/miR-500a-5p/HDAC2 signalling axis regulates cell proliferation in human colorectal cancer. *Nature communications* **10**, 663, doi:10.1038/s41467-018-08225-3 (2019).
430 Oberoi, J. *et al.* Structural basis for the assembly of the SMRT/NCoR core transcriptional repression machinery. *Nature structural & molecular biology* **18**, 177-184, doi:10.1038/nsmb.1983 (2011).
431 Rountree, M. R., Bachman, K. E. & Baylin, S. B. DNMT1 binds HDAC2 and a new co-repressor, DMAP1, to form a complex at replication foci. *Nature genetics* **25**, 269-277, doi:10.1038/77023 (2000).

432 Sarvagalla, S., Kolapalli, S. P. & Vallabhapurapu, S. The Two Sides of YY1 in Cancer: A Friend and a Foe. *Front Oncol* **9**, 1230-1230, doi:10.3389/fonc.2019.01230 (2019).
433 Miletić, V., Odorčić, I., Nikolić, P. & Svedružić Ž, M. In silico design of the first DNA-independent mechanism-based inhibitor of mammalian DNA methyltransferase Dnmt1. *PloS one* **12**, e0174410, doi:10.1371/journal.pone.0174410 (2017).
434 Christman, J. K. 5-Azacytidine and 5-aza-2'-deoxycytidine as inhibitors of DNA methylation: mechanistic studies and their implications for cancer therapy. *Oncogene* **21**, 5483-5495, doi:10.1038/sj.onc.1205699 (2002).
435 Topper, M. J. *et al.* Epigenetic Therapy Ties MYC Depletion to Reversing Immune Evasion and Treating Lung Cancer. *Cell* **171**, 1284-1300.e1221, doi:10.1016/j.cell.2017.10.022 (2017).
436 O'Connor, O. A. *et al.* Oral 5-azacytidine and romidepsin exhibit marked activity in patients with PTCL: a multicenter phase 1 study. *Blood* **134**, 1395-1405, doi:10.1182/blood.2019001285 (2019).
437 Salvatore, G. *et al.* A cell proliferation and chromosomal instability signature in anaplastic thyroid carcinoma. *Cancer research* **67**, 10148-10158, doi:10.1158/0008-5472.Can-07-1887 (2007).
438 Liu, L., Zhang, M. & Zou, P. Expression of PLK1 and survivin in diffuse large B-cell lymphoma. *Leukemia & lymphoma* **48**, 2179-2183, doi:10.1080/10428190701615918 (2007).
439 Yamamoto, Y. *et al.* Overexpression of polo-like kinase 1 (PLK1) and chromosomal instability in bladder cancer. *Oncology* **70**, 231-237, doi:10.1159/000094416 (2006).
440 Liu, L., Zhang, M. & Zou, P. Polo-like kinase 1 as a new target for non-Hodgkin's lymphoma treatment. *Oncology* **74**, 96-103, doi:10.1159/000139137 (2008).
441 Kanaji, S. *et al.* Expression of polo-like kinase 1 (PLK1) protein predicts the survival of patients with gastric carcinoma. *Oncology* **70**, 126-133, doi:10.1159/000093003 (2006).
442 Weichert, W. *et al.* Expression patterns of polo-like kinase 1 in human gastric cancer. *Cancer science* **97**, 271-276, doi:10.1111/j.1349-7006.2006.00170.x (2006).
443 Sato, M. *et al.* MYC is a critical target of FBXW7. *Oncotarget* **6**, 3292-3305, doi:10.18632/oncotarget.3203 (2015).
444 Pajtler, K. W. *et al.* The GSK461364 PLK1 inhibitor exhibits strong antitumoral activity in preclinical neuroblastoma models. *Oncotarget* **8**, 6730-6741, doi:10.18632/oncotarget.14268 (2017).
445 Pezuk, J. A., Brassesco, M. S., Ramos, P. M. M., Scrideli, C. A. & Tone, L. G. Polo-Like Kinase 1 Pharmacological Inhibition as Monotherapy or in Combination: Comparative Effects of Polo-Like Kinase 1 Inhibition in Medulloblastoma Cells. *Anti-cancer agents in medicinal chemistry* **17**, 1278-1291, doi:10.2174/1871520617666170213112904 (2017).
446 Higuchi, F. *et al.* PLK1 Inhibition Targets Myc-Activated Malignant Glioma Cells Irrespective of Mismatch Repair Deficiency-Mediated Acquired Resistance to Temozolomide. *Molecular cancer therapeutics* **17**, 2551-2563, doi:10.1158/1535-7163.Mct-18-0177 (2018).
447 Abbou, S. *et al.* Polo-like Kinase Inhibitor Volasertib Exhibits Antitumor Activity and Synergy with Vincristine in Pediatric Malignancies. *Anticancer research* **36**, 599-609 (2016).
448 Dong, J. *et al.* The polo-like kinase 1 inhibitor volasertib synergistically increases radiation efficacy in glioma stem cells. *Oncotarget* **9**, 10497-10509, doi:10.18632/oncotarget.24041 (2018).
449 Harris, P. S. *et al.* Polo-like kinase 1 (PLK1) inhibition suppresses cell growth and enhances radiation sensitivity in medulloblastoma cells. *BMC cancer* **12**, 80, doi:10.1186/1471-2407-12-80 (2012).

450 Han, Y. *et al.* Synergistic activity of BET inhibitor MK-8628 and PLK inhibitor Volasertib in preclinical models of medulloblastoma. *Cancer Lett* **445**, 24-33, doi:10.1016/j.canlet.2018.12.012 (2019).
451 Timme, N. *et al.* Small-Molecule Dual PLK1 and BRD4 Inhibitors are Active Against Preclinical Models of Pediatric Solid Tumors. *Translational oncology* **13**, 221-232, doi:10.1016/j.tranon.2019.09.013 (2020).
452 Holtrich, U. *et al.* Induction and down-regulation of PLK, a human serine/threonine kinase expressed in proliferating cells and tumors. *Proceedings of the National Academy of Sciences of the United States of America* **91**, 1736-1740, doi:10.1073/pnas.91.5.1736 (1994).
453 Yuan, J. *et al.* Polo-like kinase, a novel marker for cellular proliferation. *The American journal of pathology* **150**, 1165-1172 (1997).
454 Wolf, G. *et al.* Prognostic significance of polo-like kinase (PLK) expression in non-small cell lung cancer. *Oncogene* **14**, 543-549, doi:10.1038/sj.onc.1200862 (1997).
455 Knecht, R. *et al.* Prognostic significance of polo-like kinase (PLK) expression in squamous cell carcinomas of the head and neck. *Cancer research* **59**, 2794-2797 (1999).
456 Ramani, P., Nash, R., Sowa-Avugrah, E. & Rogers, C. High levels of polo-like kinase 1 and phosphorylated translationally controlled tumor protein indicate poor prognosis in neuroblastomas. *Journal of neuro-oncology* **125**, 103-111, doi:10.1007/s11060-015-1900-4 (2015).
457 Triscott, J. *et al.* Personalizing the treatment of pediatric medulloblastoma: Polo-like kinase 1 as a molecular target in high-risk children. *Cancer research* **73**, 6734-6744, doi:10.1158/0008-5472.Can-12-4331 (2013).
458 Shin, S. B., Jang, H. R., Xu, R., Won, J. Y. & Yim, H. Active PLK1-driven metastasis is amplified by TGF-β signaling that forms a positive feedback loop in non-small cell lung cancer. *Oncogene* **39**, 767-785, doi:10.1038/s41388-019-1023-z (2020).
459 Cai, X. P. *et al.* PLK1 promotes epithelial-mesenchymal transition and metastasis of gastric carcinoma cells. *American journal of translational research* **8**, 4172-4183 (2016).
460 Liu, X., Lei, M. & Erikson, R. L. Normal cells, but not cancer cells, survive severe Plk1 depletion. *Molecular and cellular biology* **26**, 2093-2108, doi:10.1128/mcb.26.6.2093-2108.2006 (2006).
461 Takeshita, T. *et al.* High expression of polo-like kinase 1 is associated with TP53 inactivation, DNA repair deficiency, and worse prognosis in ER positive Her2 negative breast cancer. *American journal of translational research* **11**, 6507-6521 (2019).
462 Oon, M. L. *et al.* The contribution of MYC and PLK1 expression to proliferative capacity in diffuse large B-cell lymphoma. *Leukemia & lymphoma* **60**, 3214-3224, doi:10.1080/10428194.2019.1633629 (2019).
463 Hassan, Q. N., 2nd, Alinari, L. & Byrd, J. C. PLK1: a promising and previously unexplored target in double-hit lymphoma. *The Journal of clinical investigation* **128**, 5206-5208, doi:10.1172/JCI124919 (2018).
464 Costa, R. H. FoxM1 dances with mitosis. *Nat Cell Biol* **7**, 108-110, doi:10.1038/ncb0205-108 (2005).
465 Dibb, M. *et al.* The FOXM1-PLK1 axis is commonly upregulated in oesophageal adenocarcinoma. *Br J Cancer* **107**, 1766-1775, doi:10.1038/bjc.2012.424 (2012).
466 Zhang, Z., Zhang, G. & Kong, C. FOXM1 participates in PLK1-regulated cell cycle progression in renal cell cancer cells. *Oncology letters* **11**, 2685-2691, doi:10.3892/ol.2016.4228 (2016).

467 Park, A. K. *et al.* Subgroup-specific prognostic signaling and metabolic pathways in pediatric medulloblastoma. *BMC cancer* **19**, 571, doi:10.1186/s12885-019-5742-x (2019).
468 Cheng, M. W., Wang, B. C., Weng, Z. Q. & Zhu, X. W. Clinicopathological significance of Polo-like kinase 1 (PLK1) expression in human malignant glioma. *Acta histochemica* **114**, 503-509, doi:10.1016/j.acthis.2011.09.004 (2012).
469 Xi, X. *et al.* Joint bioinformatics analysis of underlying potential functions of hsa-let-7b-5p and core genes in human glioma. *Journal of translational medicine* **17**, 129, doi:10.1186/s12967-019-1882-7 (2019).
470 Yan, V. C. *et al.* Why Great Mitotic Inhibitors Make Poor Cancer Drugs. *Trends in Cancer*, doi:10.1016/j.trecan.2020.05.010.
471 Yata, K. *et al.* Plk1 and CK2 act in concert to regulate Rad51 during DNA double strand break repair. *Mol Cell* **45**, 371-383, doi:10.1016/j.molcel.2011.12.028 (2012).
472 Spoerri, L. *et al.* A novel ATM-dependent checkpoint defect distinct from loss of function mutation promotes genomic instability in melanoma. *Pigment cell & melanoma research* **29**, 329-339, doi:10.1111/pcmr.12466 (2016).
473 Benada, J., Burdová, K., Lidak, T., von Morgen, P. & Macurek, L. Polo-like kinase 1 inhibits DNA damage response during mitosis. *Cell Cycle* **14**, 219-231, doi:10.4161/15384101.2014.977067 (2015).
474 Ueda, A. *et al.* Therapeutic potential of PLK1 inhibition in triple-negative breast cancer. *Laboratory investigation; a journal of technical methods and pathology* **99**, 1275-1286, doi:10.1038/s41374-019-0247-4 (2019).
475 Driscoll, D. L. *et al.* Plk1 inhibition causes post-mitotic DNA damage and senescence in a range of human tumor cell lines. *PloS one* **9**, e111060, doi:10.1371/journal.pone.0111060 (2014).
476 Künkele, A. *et al.* Pharmacological activation of the p53 pathway by nutlin-3 exerts anti-tumoral effects in medulloblastomas. **14**, 859-869 (2012).
477 van Groningen, T. *et al.* Neuroblastoma is composed of two super-enhancer-associated differentiation states. *Nature genetics* **49**, 1261-1266, doi:10.1038/ng.3899 (2017).
478 Raab, M. *et al.* Mitotic arrest and slippage induced by pharmacological inhibition of Polo-like kinase 1. *Mol Oncol* **9**, 140-154, doi:10.1016/j.molonc.2014.07.020 (2015).
479 Stevens, F. E., Beamish, H., Warrener, R. & Gabrielli, B. Histone deacetylase inhibitors induce mitotic slippage. *Oncogene* **27**, 1345-1354, doi:10.1038/sj.onc.1210779 (2008).
480 Gaymes, T. J. *et al.* Histone deacetylase inhibitors (HDI) cause DNA damage in leukemia cells: a mechanism for leukemia-specific HDI-dependent apoptosis? *Molecular cancer research : MCR* **4**, 563-573, doi:10.1158/1541-7786.Mcr-06-0111 (2006).
481 Kikuchi, H. *et al.* Generation and characteristics of a novel "double-hit" high grade B-cell lymphoma cell line DH-My6 with MYC/IGH and BCL6/IGH gene arrangements and potential molecular targeted therapies. *Oncotarget* **9**, 33482-33499, doi:10.18632/oncotarget.26060 (2018).
482 Wissing, M. D. *et al.* Targeting prostate cancer cell lines with polo-like kinase 1 inhibitors as a single agent and in combination with histone deacetylase inhibitors. *FASEB J* **27**, 4279-4293, doi:10.1096/fj.12-222893 (2013).
483 Daneman, R. & Prat, A. The blood-brain barrier. *Cold Spring Harb Perspect Biol* **7**, a020412-a020412, doi:10.1101/cshperspect.a020412 (2015).
484 Sarkaria, J. N. *et al.* Is the blood-brain barrier really disrupted in all glioblastomas? A critical assessment of existing clinical data. *Neuro-oncology* **20**, 184-191, doi:10.1093/neuonc/nox175 (2018).

485 Danovi, D. *et al.* A high-content small molecule screen identifies sensitivity of glioblastoma stem cells to inhibition of polo-like kinase 1. *PloS one* **8**, e77053-e77053, doi:10.1371/journal.pone.0077053 (2013).
486 van Vulpen, M., Kal, H. B., Taphoorn, M. J. & El-Sharouni, S. Y. Changes in blood-brain barrier permeability induced by radiotherapy: implications for timing of chemotherapy? (Review). *Oncology reports* **9**, 683-688 (2002).
487 Parrish, K. E., Sarkaria, J. N. & Elmquist, W. F. Improving drug delivery to primary and metastatic brain tumors: strategies to overcome the blood-brain barrier. *Clinical pharmacology and therapeutics* **97**, 336-346, doi:10.1002/cpt.71 (2015).
488 Lerner, R. G. *et al.* Targeting a Plk1-Controlled Polarity Checkpoint in Therapy-Resistant Glioblastoma-Propagating Cells. *Cancer research* **75**, 5355-5366, doi:10.1158/0008-5472.Can-14-3689 (2015).
489 Tandle, A. T. *et al.* Inhibition of polo-like kinase 1 in glioblastoma multiforme induces mitotic catastrophe and enhances radiosensitisation. *European journal of cancer (Oxford, England : 1990)* **49**, 3020-3028, doi:10.1016/j.ejca.2013.05.013 (2013).
490 Tan, J. *et al.* PDK1 Signaling Toward PLK1–MYC Activation Confers Oncogenic Transformation, Tumor-Initiating Cell Activation, and Resistance to mTOR-Targeted Therapy. **3**, 1156-1171, doi:10.1158/2159-8290.CD-12-0595 %J Cancer Discovery (2013).
491 Jiang, J. *et al.* Direct Phosphorylation and Stabilization of MYC by Aurora B Kinase Promote T-cell Leukemogenesis. *Cancer Cell* **37**, 200-215.e205, doi:10.1016/j.ccell.2020.01.001 (2020).
492 Kurland, J. F. & Tansey, W. P. Myc-mediated transcriptional repression by recruitment of histone deacetylase. *Cancer Res* **68**, 3624-3629, doi:10.1158/0008-5472.CAN-07-6552 (2008).
493 Liu, T. *et al.* Activation of tissue transglutaminase transcription by histone deacetylase inhibition as a therapeutic approach for Myc oncogenesis. *Proc Natl Acad Sci U S A* **104**, 18682-18687, doi:10.1073/pnas.0705524104 (2007).